Contents

Introduction

Since the mid-20th century, Ni-based superalloys have been the dominant material of choice in the high temperature region of gas turbine engines. This working environment demands high temperature, stress, pressure and environmental resistance from the alloys used. The Ni-based superalloy structures advanced from polycrystalline, to directionally solidified single crystals. The alloys also underwent several critical alloying development stages such as the additions of Re and Ru in the latest generation superalloys to achieve higher temperature capabilities. These materials have thus far served their purpose well with increasing temperature capabilities to meet industry needs, now however further advances of their high temperature capabilities are not possible, as Turbine Entry Temperatures (TET) are expected to increase well beyond the melting temperature of Ni in future gas turbines. Current TETs are ≈ 1600 °C and Ni-based superalloy melting temperatures are ≈ 1350 °C, in order to operate at these TETs cooling channels within the turbine blades and thermal barrier coatings (TBC) are needed to maintain the surface temperature ~1150 °C.

Due to environmental and operational requirements the TET will increase towards at least ~1900 °C and Ni-based superalloys will be inadequate for operation at these temperatures. New, higher temperature alloys must be developed to meet the future requirements of gas turbine engines. High temperature alloys that have gained interest are those based on the silicides of refractory metals Nb, Mo, Ta and W however, their silicides have poor toughness in their monolithic form (Bewlay et al. 1997). Table 1.1 lists and compares the properties of the refractory metals (Grill & Gnadenberger 2006).

Table 1.1 Properties of refractory metals (Grill & Gnadenberger 2006)

	Niobium	Tantalum	Molybdenum	Tungsten
Melting point (°C)	2470	2996	2610	3410
Boiling point (°C)	3300	6100	4800	6700
Crystal structure	Cubic body centred	Cubic body centred	Cubic body centred	Cubic body centred
Density (g/cm^3)	8.57	16.6	10.2	19.3
Young's modulus (GPa)	110	186	290	358
Coefficient of thermal expansion (1/K)	7.1×10^{-6}	5.9×10^{-6}	5.4×10^{-6}	4.5×10^{-6}
Thermal conductivity (W/m K)	52	54	142	166
Electrical resistance (ohm m)	14.8×10^{-8}	13.5×10^{-8}	5.2×10^{-8}	5.5×10^{-8}
Workability at room temperature	Good	Good	Middle[a]	Bad[a]
Ductile/brittle transition temperature (°C)	−150	−260	−20	300
Softening temperature (°C)	Ca. 1000	Ca. 1400	Ca. 1300	Ca. 1600
Corrosion resistance	High	Very high	Low	Low

The inherent brittleness of the silicides in their unalloyed form can be overcome by alloying to give a combination of the refractory metal silicide along with a toughening solid solution phase. This dual phase microstructure can increase the toughness of the alloy and improve its mechanical properties (Bewlay et al. 1997). Both Nb and Mo silicide based alloys have been deemed as promising. The Nb_5Si_3 has the second highest melting temperature (2520 °C) of the 5-3 refractory metal silicides. Nb/Nb_5Si_3 based alloys have densities lower than those of Ni-based superalloys (<9 g/cm^3) (Lewandowski & Rigney 1996a) and Mo silicide based alloys (<10 g/cm^3) and a lower ductile to brittle transition temperature (DBTT) than the latter. These attributes are among the reasons that Nb silicide alloys and are currently receiving much attention as potential replacements for the N—based superalloys in high pressure gas turbines.

These new alloys, which are also known as Nb *in situ* composites owing to the *in situ* formation of the silicide phase during solidification or PM processing, must offer a balance of room and elevated temperature properties with oxidation resistance at low (< 800 °C), intermediate (800 < T < 1100 °C) and high (1100 °C < T < 1400 °C) temperatures. Oxidation resistance with high temperature (> 1150 °C) strength and creep behaviour are key requirements. Oxidation behaviour is critical given the pest oxidation of Nb intermetallics and the susceptibility of Nb to contamination by interstitials. The new alloys must have "acceptable" inherent oxidation resistance and will be protected by TBC type (i.e., bond coat(s) + thermally grown oxide(s) + ceramic top coat(s)) coatings in service, like the Ni based superalloys.

The word composite implies that these new materials can be either of the metal matrix type (higher than 50% volume fraction of the solid solution phase Nb_{ss}) or intermetallic matrix type (higher than 50% volume fraction of intermetallic compounds like Nb_3Si, Nb_5Si_3, $NbCr_2$ and others depending on alloy chemistry). At room temperature their toughness is controlled by the Nb_{ss} (chemistry, spatial distribution, size, vol%) and their strength by the intermetallics (type, chemistry, vol%) and the Nb_{ss} (chemistry-solid solution strengthening, vol%). At all temperatures their oxidation behaviour is controlled by the Nb_{ss} (chemistry, spatial distribution, size, vol%) and the intermetallics (type, chemistry, spatial distribution, vol%) and their mechanical properties by the Nb_{ss} (chemistry-solid solution strengthening, vol%) and the intermetallics (type, chemistry, vol%).

The new alloys belong to Nb-Si-Ti-X-Y systems where X is sd electronic configuration (i.e., transition metal TM, for example Cr, and/or transition-refractory metal (RM), for example Mo) and Y is sp electronic configuration metal (for example Al, or metalloid). Alloying additions that are expected to benefit oxidation behaviour are Al, Cr, Si and Ti. With the exception of Si, the other elements have solid solubility in Nb_{ss} that increases as its Ti content increases. The solid solubilities of Al and Cr in the Nb silicides are low, particularly for the latter, but that of Ti is high. The Al and Cr are considered desirable owing to the properties of alumina and chromia but the concentrations of these two elements are limited by their effects on DBTT and liquidus temperature, respectively. Titanium is desirable because it significantly improves the oxidation of $(Nb,Ti)_{ss}$ and Si, as the element responsible for the formation of silicide intermetallics, is expected to form silica. Thus, the "basis" for developing the new alloys has been the Nb-Si-Ti-Al-Cr system (Zelenitsas & Tsakiropoulos 2006b; Subramanian 1997).

Other alloying additions that have been shown to benefit oxidation behaviour are B, Ge, Hf and Sn. Hafnium is soluble in the Nb_{ss} and its solubility increases with the Ti content of the latter. Hafnium is expected to benefit oxidation via a "reactive element effect" by scavenging oxygen and to control environmental embrittlement (Grammenos & Tsakiropoulos 2010b; Grammenos & Tsakiropoulos 2010a; Grammenos & Tsakiropoulos 2011).

Titanium is the alloying addition that benefits the toughness of the Nb_{ss} and Nb_5Si_3. The Al, Cr and Si have an adverse effect on the toughness of the Nb_{ss}, which critically depends on the Al + Cr and Ti contents of Si free Nb_{ss} (Davidson & Chan 1999). Thus, research on alloys of the Nb-Si-Ti-Al-Cr system has sought to optimise the $(Nb,Al,Cr,Si,Ti)_{ss}$ chemistry (Bewlay et al. 1997; Mathieu et al. 2012; Bewlay et al. 1996; Grammenos & Tsakiropoulos 2010a; Zelenitsas & Tsakiropoulos 2005; Geng, Tsakiropoulos, et al. 2006a). Formation of Si free Nb_{ss} in "simple" Nb-Si-RM alloys is controlled by the type(s) of refractory metal(s) in the alloy, but the oxidation behaviour of the alloys is poor. The RMs form continuous solid solutions with the Nb and offer significant solid solution strengthening on their own or in synergy (Sha, H. Hirai, et al. 2003; Kim et al. 2002). The RM solid solubility in the Nb_5Si_3 is small. Elevated temperature strength and creep behaviour benefit from the effects of RM(s) on the

properties of the Nb_{ss}. However, the additions of Al, Cr, Hf and Ti tend to have an adverse effect on elevated temperature strength and creep behaviour.

The research described in this thesis is part of a wider R&D effort that aims to develop Nb silicide based alloys (Nb *in situ* composites) with a balance of properties at room and elevated temperatures. The same was therefore the aim of this research. The objective of this research was to understand how Sn and Hf affect the properties of Nb-18Si silicide based alloys in the presence of RM(s) and/or TMs. The tactics to achieve the objective of the research were the following:

(i)   To investigate the effect of alloying with Hf on the properties on the "basic" alloy composition Nb-18Si-24Ti-5Al-5Cr.

(ii)   To investigate the effect of the synergy of Hf and Sn with RM(s) by controlling the type of sp and sd electronic configuration elements and the concentration of the latter in the alloy. In this research the sp and sd elements of the studied alloys respectively were the Al, Si and Sn and Cr, Hf, Mo, Nb, Ti and W.

Phase equilibria data was the key for the design and selection of the alloys for this research. Phase equilibria was available only for some subsystems of the Nb-Si-Ti-Al-Cr-Hf-Mo-Sn-Ti-W either via commercial database(s) or internal (i.e., research group) work. The available phase equilibria relevant to this research are briefly reviewed in section 2.1. The processing of Nb silicide based alloys poses numerous challenges owing to the different melting points of the alloying elements (from 232 °C for Sn to 660 °C for Al, to 1414 °C for Si, to 1668 °C for Ti, to 2477 °C for Nb, to 3422 °C for W) and the sluggish solid state kinetics. Solidification processing is the preferred route as early research demonstrated that it is possible to cast DS alloys (and thus the potential to cast single crystal (SX) alloys with/out internal cooling). PM route processing has also been considered to produce near net shape components. The processing of Nb silicide based alloys in briefly reviewed in section 2.2 The properties of developmental alloys are briefly reviewed in section 2.3 (oxidation) and 2.5 (mechanical properties).

Literature review

The following section discusses the general topic surrounding this body of work and covers the major areas of interest.

2.1   Phase equilibria

Alloy design and development requires a good understanding of phase equilibria so that phase selection and stability can be understood and exploited towards obtaining the desired properties.

2.1.1   The Nb-Ti-Si system

The addition of Ti to Nb-silicide based alloys is vital to the improvement of the room temperature fracture toughness and oxidation resistance of the alloy. Figure 2.1 shows (a) the binary phase diagram of the Nb-Si system, (b) the binary phase diagram of the Ti-Si system and (c) the 3D ternary phase diagram of the Nb-Si-Ti system. In the binary Nb-Si system there is a eutectic at ~ 18 at% Si. This is the concentration of Si in higher order alloys with optimum creep performance. Solidification of alloys with 18 at% Si can result in Nb_{ss}-Nb_3Si_3 or metastable Nb_{ss}-Nb_5Si_3 eutectics depending on alloy chemistry. The Nb_3Si can transform eutectiodally to $Nb_{ss} + \alpha Nb_5Si_3$ and the stability of the latent microstructure can be controlled via alloying.
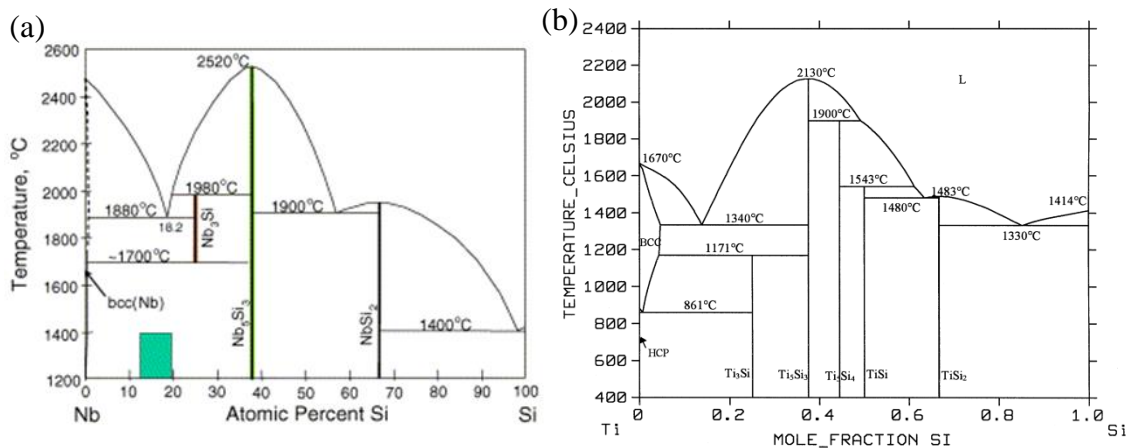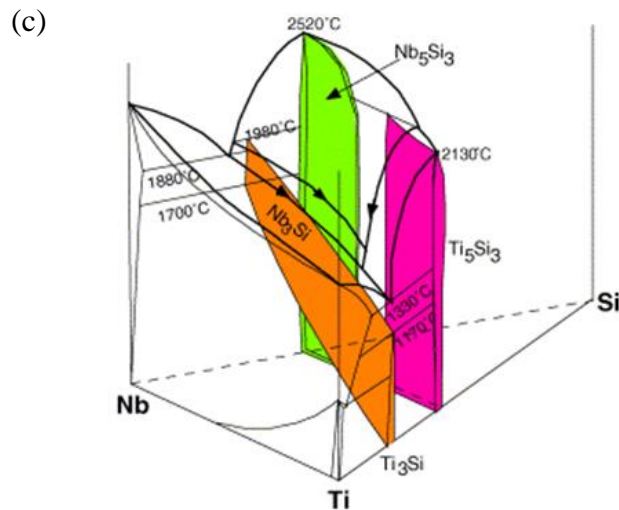
Figure 2.1 (a) the Nb-Si binary phase diagram (Zhao et al. 2004), (b) the Ti-Si binary phase diagram (Liang 1999) and (c) the Nb-Ti-Si 3D ternary phase diagram (Zhao et al. 2004).

Figure 2.1 (c) shows the Nb-Ti-Si system with 4 main intermetallic phases; Nb_3Si, Nb_5Si_3, Ti_3Si and Ti_5Si_3. Table 2.1 shows the crystal structures for the main phases in the Nb-Ti-Si system. The Nb_3Si and Ti_3Si are isomorphous, as both have the *t*P32 structure and the Ti_3Si is stable to room temperature, see Figure 2.1(b). Therefore as the Ti content increases, the L → Nb_{ss} + Nb_3Si eutectic is shifted from 1880 °C in the Nb-Si binary to lower temperatures and the Nb_3Si is stabilised below 1700 °C.

The αNb_5Si_3 (*t*I32) and Ti_5Si_3 (*h*P16) are not isomorphous. The Ti, which promotes the formation of the hexagonal phase Ti_5Si_3 tends to stabilise the tetragonal βNb_5Si_3 (owing to the stabilisation of Nb_3Si to lower temperature, the transformation βNb_5Si_3 + Nb_3Si →αNb_5Si_3 is also shifted to lower temperatures thus the stability of βNb_5Si_3 is extended to temperatures below 1940 °C) and the hexagonal γNb_5Si_3. The stabilisation of Nb_3Si and γNb_5Si_3, and the formation of Ti_5Si_3 mean that the amount of Ti used in the alloy must be chosen carefully owing to the adverse effect of high Ti on the melting temperature of the alloy and the formation of Ti_5Si_3 at high Ti contents in the 5-3 silicide. The Ti_5Si_3 has lower melting temperature than Nb_5Si_3 and thus is undesirable owing to its adverse effect on the creep properties of the alloy. The amount of Ti is limited to below 25 at% so that the alloy melting temperature is kept above

1700 °C and the formation of Ti_5Si_3 is supressed (Bewlay et al. 2004). As well as being stabilised by Ti, the γNb_5Si_3 is also stabilised by impurities, especially C.

Table 2.1 Crystal structures of phases in the Hf-Ti-Si, Nb-Ti-Si, Nb-Hf-Si and Nb-Ti-Hf-Si systems (Yang, B.P. Bewlay, et al. 2007).

Phase symbol	Thermodynamic model	Pearson symbol	Phase description
Hf-Ti-Si			
(Nb)	$(\mathbf{Hf},\mathbf{Ti},Si)_1(Va)_3$	$cI2$	Ternary solid solution with the bcc_A2 structure
Hf_2Si	$(\mathbf{Hf},Ti)_2Si$	$tI12$	Ternary solid solution based on the Hf_2Si
$(Hf,Ti)_5Si_3$	$(\mathbf{Hf},Ti)_5Si_3$	$hP16$	Ternary solid solution based on the Hf_5Si_3 and Ti_5Si_3
Ti_3Si	$(Hf,\mathbf{Ti})_3Si$	$tP32$	Ternary solid solution based on the Nb_3Si and Ti_3Si
Nb-Ti-Si			
(Nb)	$(\mathbf{Nb},\mathbf{Ti},Si)_1(Va)_3$	$cI2$	Ternary solid solution with the bcc_A2 structure
Ti_5Si_3	$(Nb,\mathbf{Ti})_5Si_3$	$hP16$	Ternary solid solution based on the Ti_5Si_3
$(Nb,Ti)_3Si$	$(\mathbf{Nb},\mathbf{Ti})_3Si$	$tP32$	Ternary solid solution based on the Nb_3Si and Ti_3Si
αNb_5Si_3	$(\mathbf{Nb},Ti)_5Si_3$	$tI32$	Ternary solid solution based on the low temperature form of $Nb_5Si_3(D8l)$
βNb_5Si_3	$(\mathbf{Nb},Ti)_5Si_3$	$tI32$	Ternary solid solution based on the high temperature form of $Nb_5Si_3(D8m)$
Nb-Hf-Si			
(Nb)	$(\mathbf{Nb},\mathbf{Hf},Si)_1(Va)_3$	$cI2$	Ternary solid solution with the bcc_A2 structure
Hf_2Si	$(Nb,\mathbf{Hf})_2Si$	$tI12$	Ternary solid solution based on the Hf_2Si
Hf_5Si_3	$(Nb,\mathbf{Hf})_5Si_3$	$hP16$	Ternary solid solution based on the Hf_5Si_3
Nb_3Si	$(\mathbf{Nb},Hf)_3Si$	$tP32$	Ternary solid solution based on the Nb_3Si
αNb_5Si_3	$(\mathbf{Nb},Hf)_5Si_3$	$tI32$	Ternary solid solution based on the low temperature form of $Nb_5Si_3(D8l)$
βNb_5Si_3	$(\mathbf{Nb},Hf)_5Si_3$	$tI32$	Ternary solid solution based on the high temperature form of $Nb_5Si_3(D8m)$
Nb-Ti-Hf-Si			
(Nb)	$(\mathbf{Nb},\mathbf{Hf},\mathbf{Ti},Si)_1(Va)_3$	$cI2$	Quaternary solid solution with the bcc_A2 structure
Hf_2Si	$(Nb,\mathbf{Hf},Ti)_2Si$	$tI12$	Quaternary solid solution based on the Hf_2Si
$(Hf,Ti)_5Si_3$	$(Nb,\mathbf{Hf},Ti)_5Si_3$	$hP16$	Quaternary solid solution based on the Hf_5Si_3 and Ti_5Si_3
$(Nb,Ti)_3Si$	$(\mathbf{Nb},Hf,Ti)_3Si$	$tP32$	Quaternary solid solution based on the Nb_3Si and Ti_3Si
αNb_5Si_3	$(\mathbf{Nb},Hf,Ti)_5Si_3$	$tI32$	Quaternary solid solution based on the low temperature form of $Nb_5Si_3(D8l)$
βNb_5Si_3	$(\mathbf{Nb},Hf,Ti)_5Si_3$	$tI32$	Quaternary solid solution based on the high temperature form of $Nb_5Si_3(D8 m)$

Note: The T element in bold font is the major element in that sublattice

2.1.2   The Nb-Cr-Si system

The Cr is added to Nb-silicide based alloys to improve their oxidation resistance. The beneficial effect of Cr is via its presence in the Nb_{ss} and the formation of the Cr_2Nb oxidation resistant C14 Laves phase. The Cr content does not usually exceed 5 at% to maintain a low DBTT, an addition of 2 at% Cr raises the DBTT from −200 to −100 °C (Chan 2002a). The Cr addition at 5 at% is close to the minimum Cr concentration at which the Laves phase can be stabilised, thus contributing to oxidation resistance, without a strong adverse effect on the fracture toughness. Goldschmidt and Brand published the 1000 °C isothermal section of the Nb-Si-Cr system in 1961 (Goldschmidt & Brand 1961). Since then, phase equilibria in this system has been re-visited, either experimentally, using cast and heat treated alloys (Bewlay et al. 2009; Geng, Shao, et al.

2006) and diffusion multiples (Bewlay et al. 2009), or via the CALPHAD method (Shao 2004; David et al. 2006; Zhao et al. 2003). The calculated 1000 °C and 1150 °C isothermal sections by Zhao et al (Zhao et al. 2003), gave a different three phase equilibria region to that of the Nb_{ss}-Nb_5Si_3-Cr_2Nb region in the calculated isothermal sections by Bewlay et al (Bewlay et al. 2009), Shao (Shao 2004), and David et al (David et al. 2006). Geng et al (Geng, Shao, et al. 2006) confirmed the latter three phase equilibria that were first suggested by Goldschmidt and Brand (Goldschmidt & Brand 1961). Figure 2.2 shows the calculated isothermal section of the Nb-Cr-Si phase diagram by Bewlay et al (Bewlay et al. 2009).
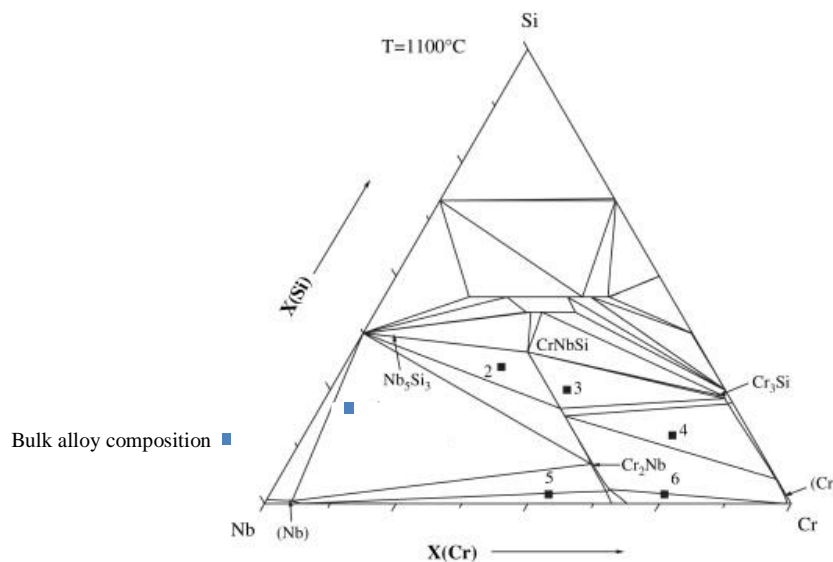
Figure 2.2 Isothermal section of the Nb-Si-Cr ternary phase diagram at 1100 °C (Bewlay et al. 2009)

The bulk alloy composition of an alloy with 18 at% Si and 5 at% Cr is shown in Figure 2.2. The alloy lies in the three phase field Nb_5Si_3, Nb_{ss} and Cr_2Nb Laves phase. Bewlay et al (Bewlay et al. 2009) showed that for alloys in this region there is the possibility of forming the $Nb_9(Cr,Si)_5$ phase during solidification, for example in the Nb-16Si-8Cr alloy. According to Bewlay et al, the formation of $Nb_9(Cr,Si)_5$ could be via the following solidification paths: $L+Nb_5Si_3 \rightarrow (Nb_{ss})+Nb_9(Cr,Si)_5$, $L \rightarrow (Nb_{ss})+Nb_9(Cr,Si)_5$, and $L \rightarrow Nb_9(Cr,Si)_5+(Nb_{ss})+Cr_2Nb$ (Bewlay et al. 2009). There is no chemical analysis available for this phase, the latter eutectic transformation is shown in the microstructure in Figure 2.3 (b).
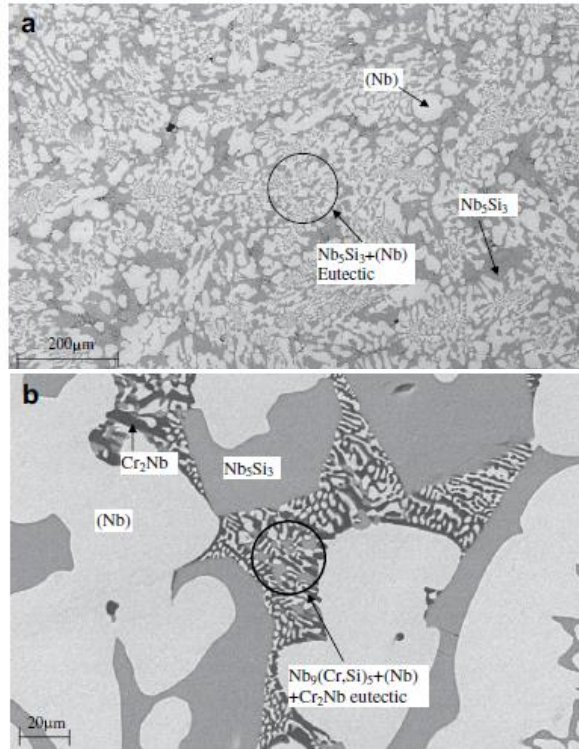
Figure 2.3 BSE images of the as-cast microstructure of the Nb–16Si–8Cr alloy at (a) low magnification and (b) high magnification (Bewlay et al. 2009).

The microstructure shown in Figure 2.3 consists of large-scale (~50 μm) $(Nb)_{ss}$ dendrites, and an inter-dendritic two-phase $(Nb)_{ss}$–Nb_5Si_3 eutectic, and a terminal ternary eutectic of $Nb_5(Cr,Si)_3$ + $(Nb)_{ss}$ + Cr_2Nb (Bewlay et al. 2009). The $Nb_9(Cr,Si)_5$ + Nb_{ss} + Cr_2Nb eutectic was observed in the as-cast structure of the directionally solidified (DS) Nb-18Si-15Cr alloy (located in the three phase Nb_{ss} − Nb_5Si_3 − Cr_2Nb region in Figure 2.2) but not in an alloy of the same composition that was studied by Geng et al (Geng, Shao, et al. 2006). This discrepancy could be attributed to the sensitivity of the aforementioned phases on growth conditions, as the eutectic was formed by the last of the liquid to solidify and it is highly likely that the DS structures studied by Bewlay et al were grown slowly compared with the arc melted alloys of Geng et al.

2.1.3   The Cr-Hf-Si system

Hafnium is an important alloying addition in Nb-silicide based alloys because it provides solid solution strengthening (SSS) in the Nb_{ss} and scavenges oxygen in solution to form HfO_2. Hafnium, like Ti, can substitute for Nb in the lattice of Nb_5Si_3. Figure 2.4 shows an isothermal section at 1200 °C of the Cr-Hf-Si system and the binary Hf-Si phase diagram.
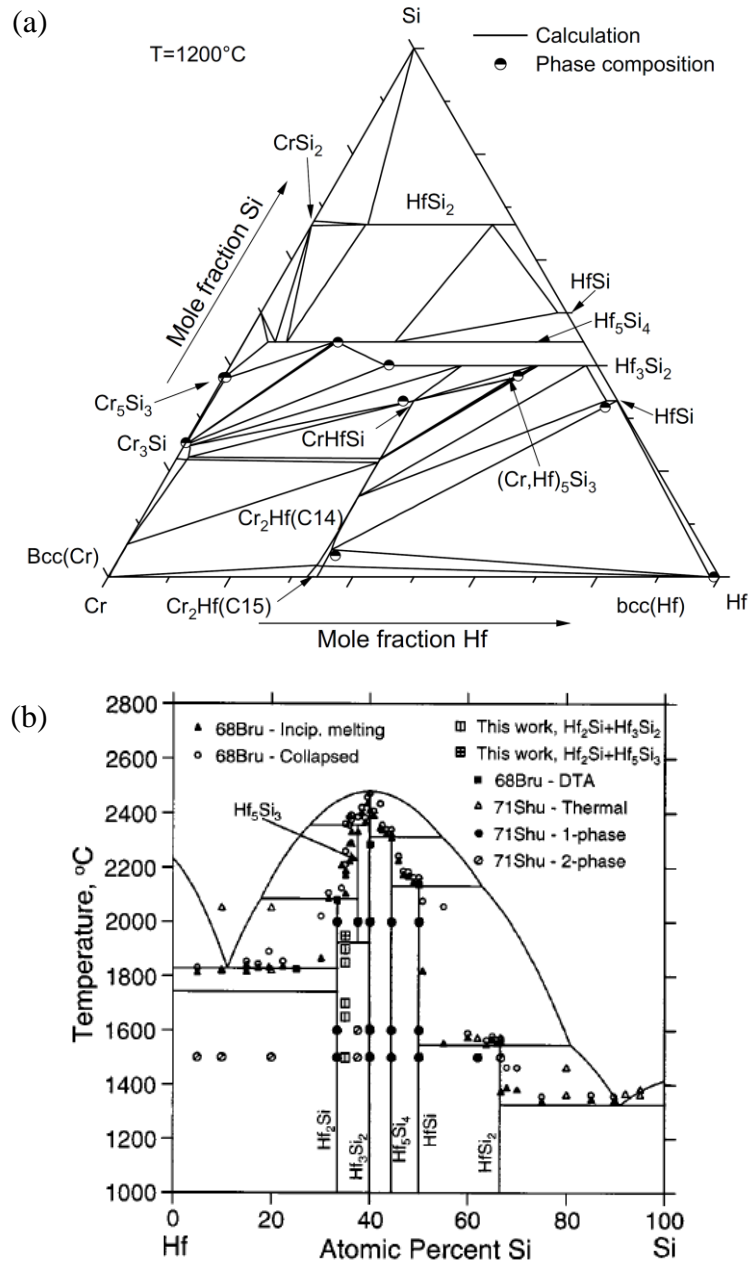
Figure 2.4 (a)isothermal section of the Hf-Cr-Si ternary phase diagram at 1200 °C (Yang et al. 2009) and (b) the Hf-Si binary phase diagram (Zhao et al. 2000).

The isothermal section in Figure 2.4 shows that the $(Cr,Hf)_5Si_3$ is stable at 1200 °C, even though in the binary phase diagram the Hf_5Si_3 phase transforms to $Hf_2Si + Hf_3Si_2$ at ~ 1920 °C. This means that Cr stabilises the Hf_5Si_3 phase to lower temperatures. Table 2.2 gives the crystal structure data for the Hf-Cr-Si system. The $(Cr, Hf)_5Si_3$ has the same crystal structure as Ti_5Si_3 and thus Cr and Hf in synergy would aid the stabilisation of the hexagonal γNb_5Si_3. This must be taken into account when developing alloys as the hexagonal phase is less resistant to creep than the tetragonal phase.

According to Yang et al (Yang et al. 2009) Cr and Hf form the $(Cr,Hf,Si)_5Si_3$ that has the same structure as Cr_5B_3, which is isomorphous with αNb_5Si_3. Thus the synergy of Cr and Hf would also destabilise the βNb_5Si_3.

Table 2.2 Crystal structure data for phases in the Hf-Cr-Si ternary system (Yang et al. 2009).

Phase symbol	Space group	Thermodynamic models	Phase description
L	N/A	(Cr,Hf,Si)	Liquid phase
bcc(Cr) and bcc(Hf)	$Im3m$	(Cr,Hf,Si)	Bcc solid solution in the Cr-rich corner
Cr_2Hf (C15)	$Fd3m$	$(Cr,Hf)_2(Cr,Hf)$	Low temperature polymorph of laves phase Cr_2Hf_C15 with Si dissolved in it
Cr_2Hf(C14)	$P6_3/mmc$	$(Cr,Hf,Si)_2(Cr,Hf)$	High temperature polymorph of laves phase Cr_2Hf with Si dissolved in it
Cr_3Si	$Pm3n$	$(Cr,Hf,Si)_3(Cr,Si)$	Cr_3Si phase with Hf dissolved in it
$Cr_5Si_3\_LT$	$I4/mcm$	$(Cr,Hf,Si)_5(Si)_3$	low temperature polymorph of Cr_5Si_3 phase with Hf dissolved in it
Hf_2Si	$I4/mcm$	$(Cr,Hf)_2Si$	Hf_2Si phase with Cr dissolved in it
Hf_3Si_2	$P4/mbm$	$(Cr,Hf)_3Si_2$	Hf_3Si_2 phase with Cr dissolved in it
$(Cr,Hf)_5Si_3$	$P6_3/mcm$	$(Cr,Hf)_5Si_3$	$(Cr,Hf)_5Si_3$ phase with Cr and Hf dissolved in the metal sublattice
Hf_5Si_4	$P4_12_12$	$(Cr,Hf)_5Si_4$	Hf_5Si_4 phase with Cr dissolved in it
CrHfSi		CrHfSi	Ternary CrHfSi phase
hcp(Hf)	$P6_3/mmc$	(Cr,Hf,Si)	Hcp solid solution in the Hf-rich corner
CrSi	$P2_13$	CrSi	Binary CrSi phase
$CrSi_2$	$P6_222$	$(Cr,Si)(Cr,Si)_2$	Binary $CrSi_2$ phase
HfSi	$Pnma$	HfSi	Binary HfSi phase
$HfSi_2$	$Cmcm$	$HfSi_2$	Binary $HfSi_2$ phase
(Si)	$Fd3m$	(Si)	Unary Si phase

2.1.4   The Hf-Ti-Si System

Hf and Ti are both added to the alloy to improve the oxidation and pest resistance and the toughness of the alloy. These two alloys however have a synergistic effect on the Nb_5Si_3 in which they stabilise the hexagonal γNb_5Si_3 over the β and α Nb_5Si_3. Figure 2.4 (b) shows the binary phase diagram for the Hf-Si system. The Hf_5Si_3 phase has the hP16 hexagonal crystal structure however, unlike the Ti-Si and Nb-Si systems, Hf_5Si_3 is not stable at room temperature as mentioned in section 2.1.3. The Ti-Si binary system (Figure 2.1b) does present a stable hexagonal hP16 Nb_5Si_3 phase at room temperature, as it is isomorphous with the 5-3 silicide formed with Hf, the Ti stabilises the Hf_5Si_3 to room temperature.
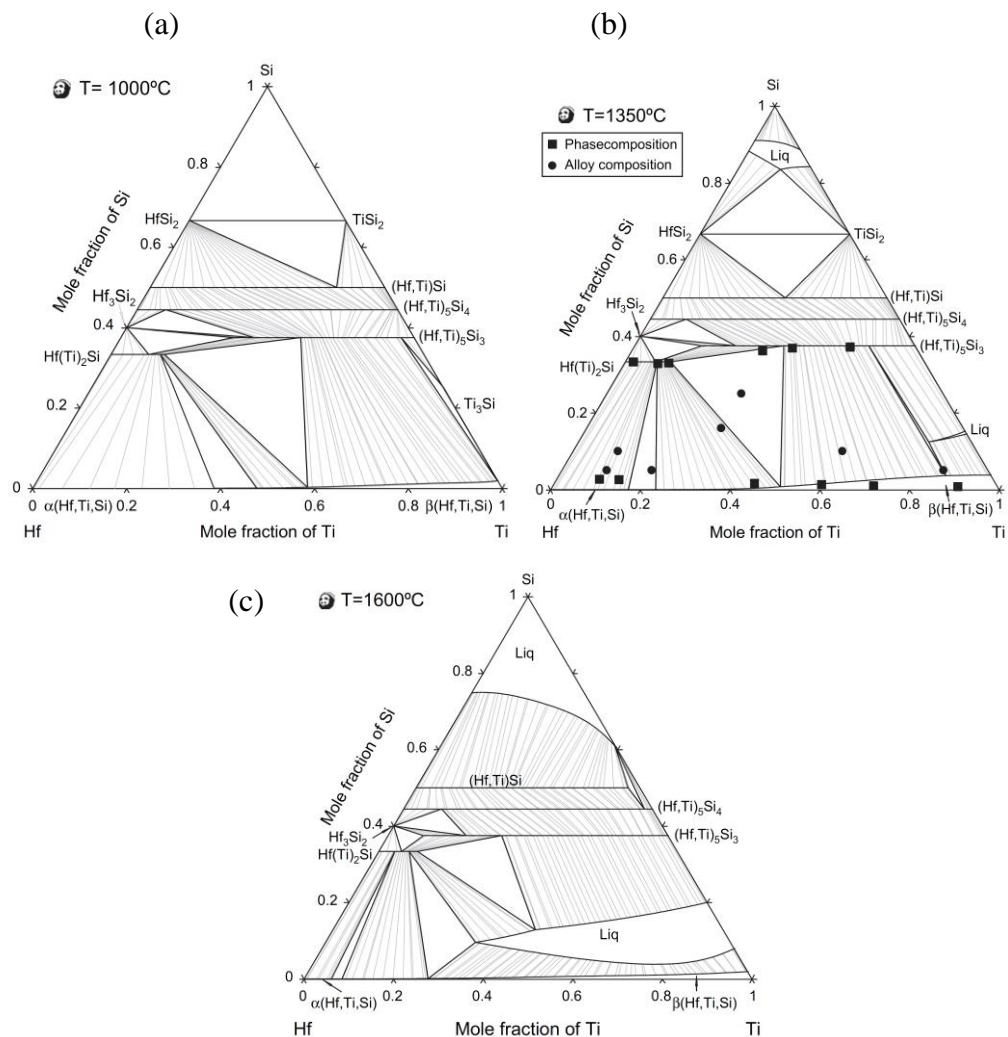
Figure 2.5 isothermal sections of the ternary Ti-Hf-Si system at (a) 1000, (b) 1350 and (c) 1600 °C (Yang, B P Bewlay, et al. 2007)

Figure 2.5 shows the ternary Ti-Hf-Si system at 1000, 1350 and 1600 °C, it shows that the $(Hf,Ti)_5Si_3$ phase is stable at these temperatures. As the temperature is reduced from 1600 to 1000 °C, the Hf solubility in $(Hf,Ti)_5Si_3$ reduces and destabilises the 5-3 silicide phase, instead stabilising the Hf_3Si_2 phase.

2.1.5   The Nb-Si-Hf System

Hafnium is added to Nb-silicide based alloys to improve their oxidation at high temperature, Hf reduces the oxidation rate at ~1200 °C, but has little to no effect at lower temperatures ~800 °C (Geng, Tsakiropoulos, et al. 2006a). Hf is also added to increase the fracture toughness of the alloy as it increases the alloy's ability to deform plastically. Hf forms Hf_5Si_3 but does not form Hf_3Si (Figure 2.4 b), therefore it would be expected to destabilise the Nb_3Si, which is beneficial as the Nb_3Si has inferior creep properties compared to Nb_5Si_3. The Hf_5Si_3 is not isomorphous with tetragonal Nb_5Si_3 but is with Ti_5Si_3, as both phases have a hP16 crystal structure (Zhao et al. 2004; Zhao et al. 2000) this means that Hf stabilises the Ti_5Si_3 silicide and vice versa. An increase in Hf and Ti content in the 5-3 silicide could also stabilise the hexagonal γNb_5Si_3, which is undesired. Due to the undesirable phase stabilisation, the amount of Hf and Ti must be limited to reduce the formation of these unwanted phases. The ratio Nb:(Ti+Hf) has been used to determine the stability of the hexagonal or the desired tetragonal phase. It has been suggested that the optimum ratio for tetragonal phase stabilisation is in the range 1.8-2.2. As the ratio decreases towards 0.8, the chance of stabilising the hexagonal phase increases (Bewlay et al. 2004).

Figure 2.6 shows the ternary Nb-Hf-Si phase diagram and the isothermal section at 1500°C and the phases in the ternary system are shown in Table 2.1.
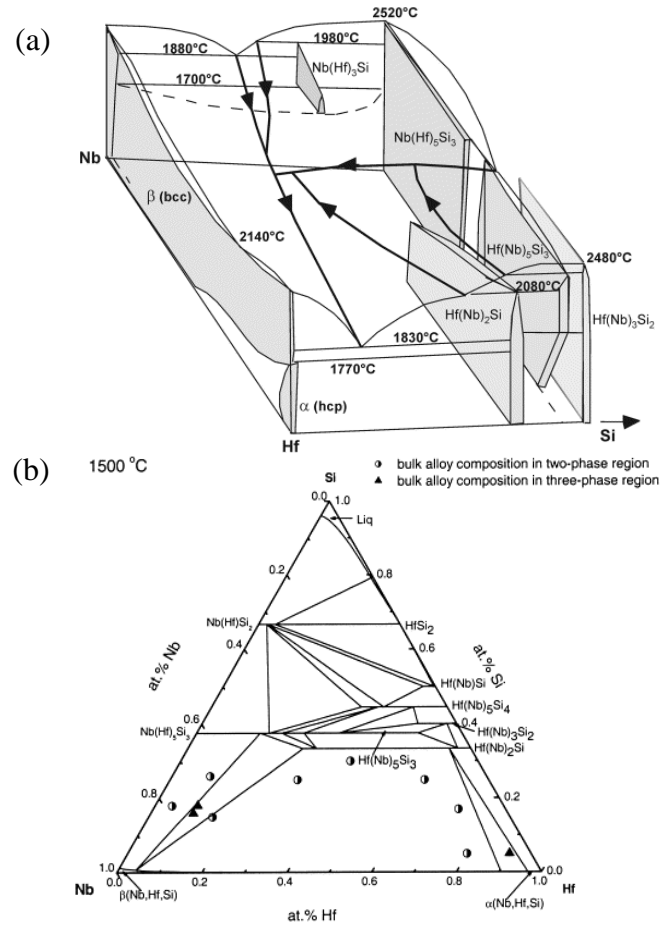
Figure 2.6 (a) the ternary phase diagram of the Nb-Hf-Si system (b) isothermal section of the Nb-Hf-Si system at 1500 °C (Bewlay, Zhao, et al. 1999).

Alloying with Hf does not cause a significant drop in the melting temperature, the latter decreases it from 1880 °C towards 1800 °C with increasing Hf, it does however increase the eutectoid transformation temperature from 1700 °C to 1770 °C. The Nb stabilises the Hf_5Si_3 to lower temperatures (~1500 °C).

2.1.6   The Nb-24Ti-18Si-5Cr-5Al alloy

The Nb-24Ti-18Si-5Cr-5Al (at%) alloy is considered to be the base alloy for the development of Nb-silicide based alloys and thus important for this project. Zelenitsas and Tsakiropoulos (Zelenitsas & Tsakiropoulos 2005) performed a detailed study of this alloy to examine the effects of Cr and Al on its microstructure and oxidation resistance.

The alloy was studied in both the as cast and heat treated condition using SEM/EDS and EPMA. The microstructure of the as cast alloy consisted of two main phases, namely the $(Nb,Ti)_{ss}$ and $\beta(Nb,Ti)_5Si_3$, as well as a small volume fraction of the C14 Laves phase, which formed at the interface between the $(Nb,Ti)_{ss}$ and $\beta(Nb,Ti)_5Si_3$ as can be seen in Figure 2.7 (Zelenitsas & Tsakiropoulos 2005). Both the $(Nb,Ti)_{ss}$ and the $\beta(Nb,Ti)_5Si_3$ contained areas that were rich in Ti, which can be seen in Figure 2.7 as regions exhibiting darker contrast. However, after 100 h heat treatment at 1500 °C the $(Nb,Ti)_{ss}$ was homogenised and no longer contained Ti rich areas, which however were still present in the $(Nb,Ti)_5Si_3$.
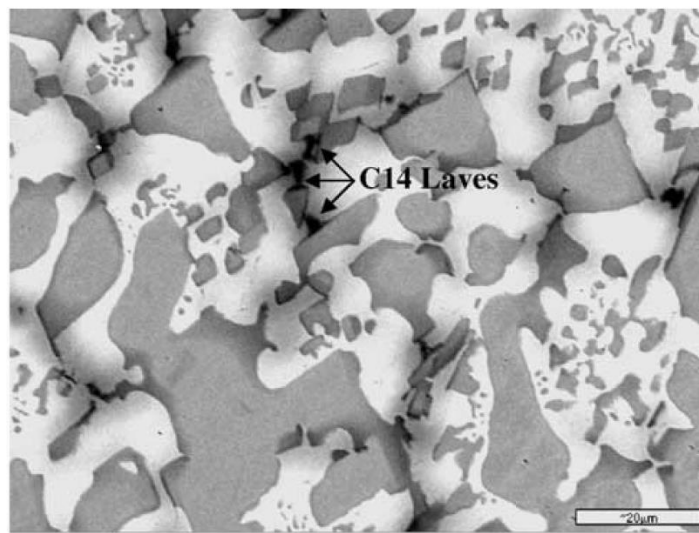
Figure 2.7 SEM image of as-cast microstructure of the Nb-24Ti-18Si-5Cr-5Al alloy showing Laves phase precipitates at 1000X magnification (Zelenitsas & Tsakiropoulos 2005). The bright areas are $(Nb,Ti)_{ss}$ and the grey areas are $(Nb,Ti)_5Si_3$.

The alloy was heat treated twice, once at 1500 °C for 100 h and again at 1500 °C for another 100 h to promote homogenisation of the microstructure. Figure 2.7 shows the microstructure and the precipitation of Laves phase and TiN at grain boundaries after the first heat treatment.
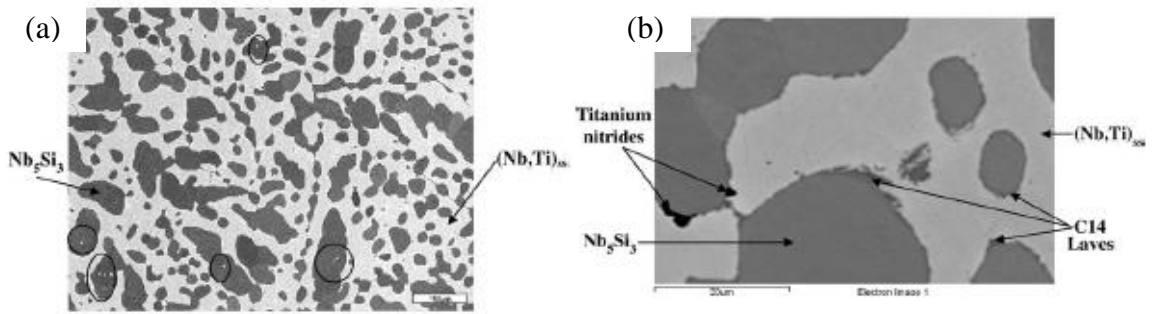
Figure 2.8 SEM images of the heat treated microstructure (1500 °C at 100 h) of the Nb-24Ti-18Si-5Cr-5Al alloy showing formation of Nb_{ss} precipitates in Nb_5Si_3 and Laves phase and TiN at the Nb_{ss}/Nb_5Si_3 interface (a) 300X and (b) 2000X (Zelenitsas & Tsakiropoulos 2005).

In the latter it is thought that the $\beta(Nb,Ti)_5Si_3$ partially transformed into $\alpha(Nb,Ti)_5Si_3$ and $(Nb,Ti)_{ss}$, and small C14 Laves phase precipitates formed between the $(Nb,Ti)_5Si_3$ and $(Nb,Ti)_{ss}$ regions. There was also precipitation of small $(Nb,Ti)_{ss}$ grains within some of the $(Nb,Ti)_5Si_3$ grains. It is believed that the presence of Cr in the alloy caused the formation of the Laves phase and retarded the transformation of $\beta(Nb,Ti)_5Si_3 \rightarrow \alpha (Nb,Ti)_5Si_3 + (Nb,Ti)_{ss}$. Figure 2.9 shows the microstructure of the alloy after the second heat treatment, showing that further homogenisation had occurred.
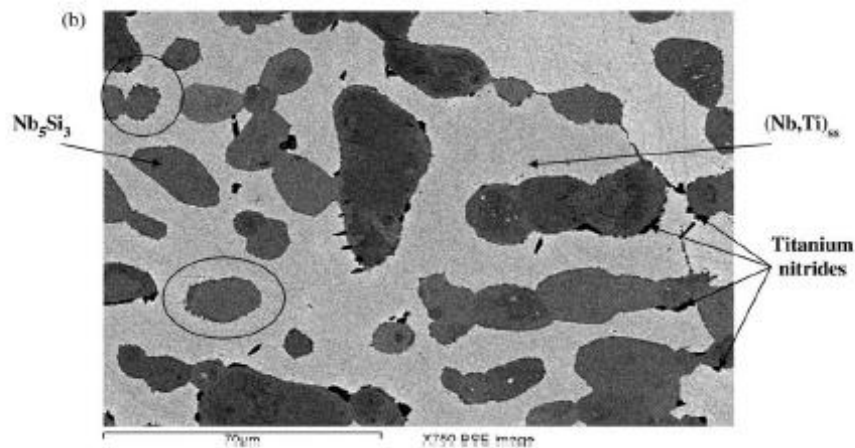
Figure 2.9 SEM image 2000X of the Nb-24Ti-18Si-5Cr-5Al alloy after 200 h at 1500 °C. The circled regions are grains which have Laves phase precipitates on their boundaries (see also figure 2.7 b) (Zelenitsas & Tsakiropoulos 2005).

After the second heat treatment (1500 °C) further refinement to the microstructure and homogenisation had taken place. The transformation of $\beta(Nb,Ti)_5Si_3$ to

16

$\alpha(Nb,Ti)_5Si_3$ and $(Nb,Ti)_{ss}$ had progressed further. There was however still some $\beta(Nb,Ti)_5Si_3$ present so the homogenisation process was not fully completed. This confirmed the sluggish transformation kinetics in this alloy and would indicate that alloying Nb-18Si with Cr and Al did not have a strong effect on the diffusion rate of Ti. There were also some areas of high Ti concentration in $(Nb,Ti)_5Si_3$ where the Cr and Al content was also high. Precipitates of C14 Laves phase had also formed around the $(Nb,Ti)_5Si_3$ particles at the boundary with $(Nb,Ti)_{ss}$ (Zelenitsas & Tsakiropoulos 2005). It has been suggested that the progression of the transformation $\beta(Nb,Ti)_5Si_3 \rightarrow \alpha(Nb,Ti)_5Si_3 + (Nb,Ti)_{ss}$ was accompanied by a reduction of Al and Cr in the $\beta(Nb,Ti)_5Si_3$. It has also been suggested that the Ti, Al and Cr rich areas of $(Nb,Ti)_5Si_3$ corresponded to supersaturated βNb_5Si_3 phase and the Ti, Al and Cr poor areas corresponded to the αNb_5Si_3 phase. During heat treatment the $(Nb,Ti)_{ss}$ came to equilibrium and precipitates of the Laves phase formed on the outside of $(Nb,Ti)_5Si_3$ as the Al and Cr were rejected via the transformation of $\beta(Nb,Ti)_5Si_3$ to $\alpha(Nb,Ti)_5Si_3$. The $(Nb,Ti)_{ss}$ was formed as a product of this transformation and precipitated around and inside the $(Nb,Ti)_5Si_3$ grains.

2.1.7   The Nb-Mo-Si System

Mo is an important alloying addition due to its solid solution strengthening, improvement of the oxidation (at low concentrations), creep and strength of the Nb_{ss} and refinement of the microstructure (Ma et al. 2000). Mo is fully miscible with Nb at all temperatures (Okamoto 2000). Figure 2.10 shows the Mo-Si binary phase diagram (Chen et al. 2009) and 800 °C isothermal section of the Nb-Mo-Si system (Savitskii 1965).

(a)
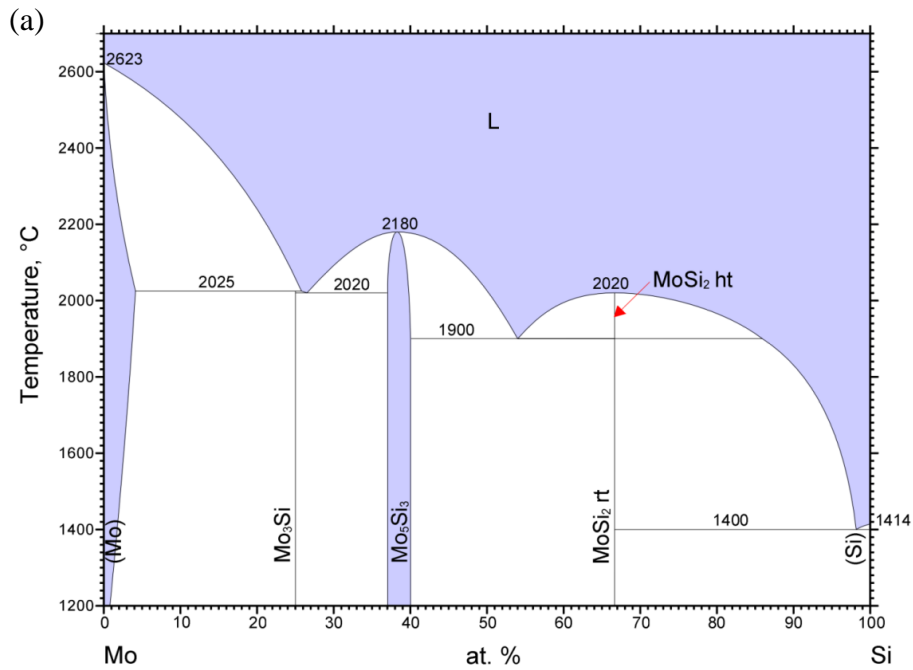
© ASM International 2006.   Diagram No. 901659
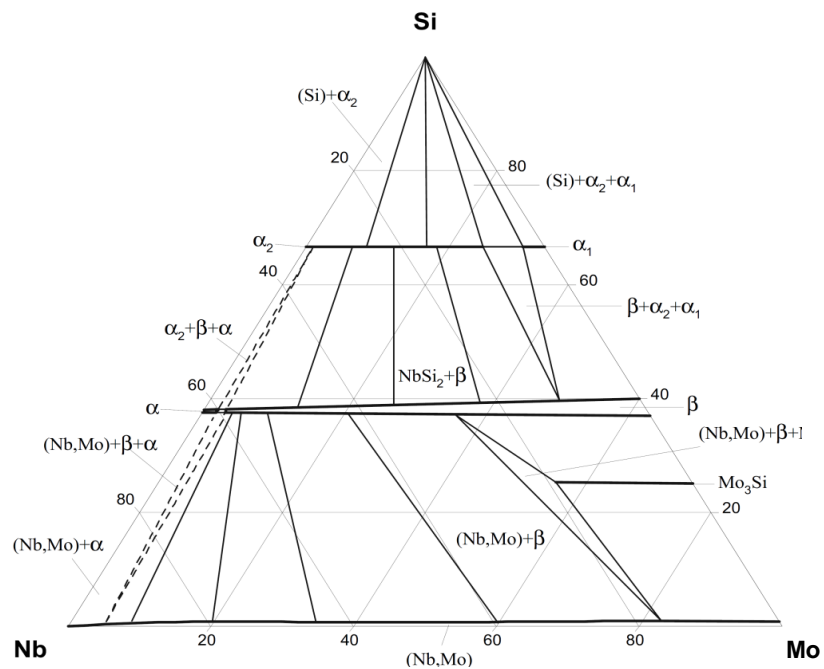
Figure 2.10 (a) Binary Mo-Si phase diagram from 1200-2700 °C (Gokhale & Abbaschian 1990) and (b) 800 °C isothermal section of the Nb-Mo-Si system (Kozlov 2010).

Further work has been done to give finer detail of the Nb-Mo rich region of the ternary diagram as reported by Geng et al (Geng et al. 2010), Ma et al have investigated this Nb-Mo rich region using experimental techniques, quenching alloys of different compositions at 1973 °C to freeze the microstructure (Ma et al. 2000). The partial Ternary system derived from this work can be seen in Figure 2.1. The experimental results from this paper show no evidence of a (Nb(Mo))$_3$Si phase in the Nb rich section of the diagram. This would suggest that Mo has a large effect on the destabilisation of the Nb$_3$Si silicide phase.
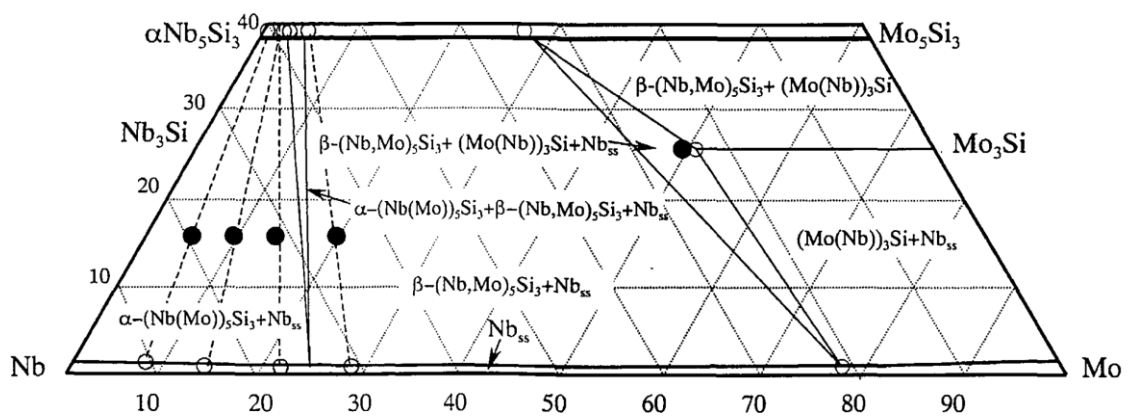
Figure 2.11 Partial isothermal section of the Nb-Mo-Si system at 1973 °C (solid circles are alloy compositions, empty circles are EPMA results) (Ma et al. 2000).

Table 2.3 shows the crystal structure data for the Nb-Mo-Si ternary system. It shows that Mo substitutes for Nb in Nb$_5$Si$_3$, as Mo$_5$Si$_3$ is isomorphous with βNb$_5$Si$_3$ (Savitskii 1965; Bewlay et al. 2003). The βNb$_5$Si$_3$ phase is therefore stabilised in the presence of Mo, except at low Mo concentrations (below ~ 3 at%). Mo forms a 3:1 silicide, the Mo$_3$Si as does Nb, however the Mo$_3$Si is not isomorphous with the Nb$_3$Si thus Mo should be expected to destabilise the latter. The binary phase diagram shows that, although the melting temperature of Mo is higher than that of Nb, the melting temperature of Mo$_5$Si$_3$ is lower than that of Nb$_5$Si$_3$. It is therefore expected that the substitution of Nb by Mo will lower the melting temperature of the Nb$_5$Si$_3$ silicide phase and increase the melting temperature of the (Nb,Mo)$_{ss}$ phase, overall increasing the temperature of the Nb$_5$Si$_3$ eutectic.

Table 2.3 Crystal structure data for the Nb-Mo-Si phase diagram

Phase	Formula	Prototype	Pearson symbol
(Si) Si	Si	C	cF8
(Nb,Mo) (Nb,Mo)	$Nb_{0.48}Mo_{0.52}$	W	cI2
Mo_3Si	Mo_3Si	Cr_3Si	cP8
$MoSi_2$ rt $MoSi_2$	$MoSi_2$	$MoSi_2$	tI6
Nb_5Si_3 rt α-Nb_5Si_3	Nb_5Si_3	Cr_5B_3	tI32
(Nb_5Si_3 ht,Mo_5Si_3) (Mo,Nb)$_5Si_3$	$Nb_{2.6}Mo_{2.4}Si_3$	W_5Si_3	tI32
($NbSi_2$,$MoSi_2$ ht) $NbSi_2$	$Nb_{0.2}Mo_{0.8}Si_2$	$CrSi_2$	hP9

2.1.8   The Nb-W-Si System

The addition of W is used to improve creep, high temperature strength and oxidation at low concentration. The main drawback of alloying with W is the effect on the alloy liquidus temperature and subsequently the problems with solidification, processing and homogenisation. Figure 2.12 shows the binary W-Si phase diagram from 1000-3500 °C.
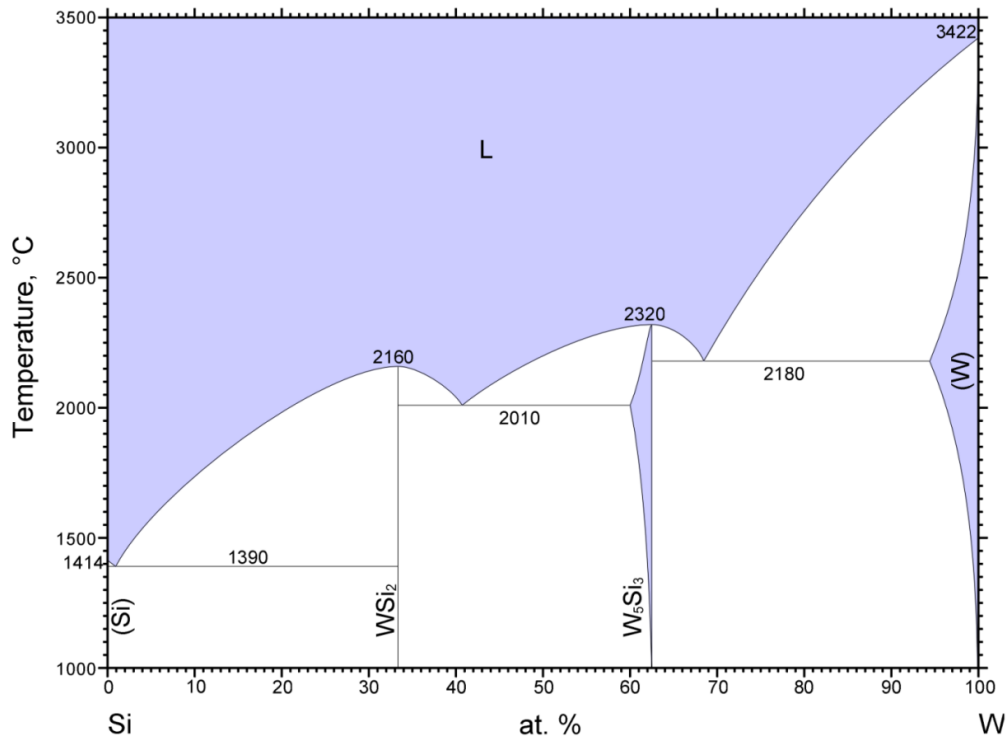
Figure 2.12 The W-Si binary phase diagram from 1000-3500 °C (Naidu Negender et al. 1990)

The W forms a W_5Si_3 silicide that is isomorphous with the βNb_5Si_3 silicide (which has the prototype W_5Si_3). As was the case with Mo, the W_5Si_3 has a lower melting point than the Nb_5Si_3, but the W_{ss}-Nb_5Si_3 eutectic temperature is higher due to the high melting temperature of W. The W does not form a 3-1 silicide and thus will not be expected to contribute to stabilising the Nb_3Si phase. Figure 2.13 shows the 25 °C isothermal section of the Nb-W-Si ternary system. The solubility of W in αNb_5Si_3 is 5 at%, above this concentration the two phase αNb_5Si_3 and $(W,Nb)_5Si_3$ is stabilised to ~15 at% W. The solubility of Nb in W_5Si_3 is up to 50 at%. Experimental work has been done on the Nb-W rich section of the phase diagram with Nb-16Si-xW alloys (x= 5, 10, 15) (Ma et al. 2004). The microstructures of the alloys at 1700 °C consisted of two phases, namely Nb_{ss} and Nb_5Si_3.
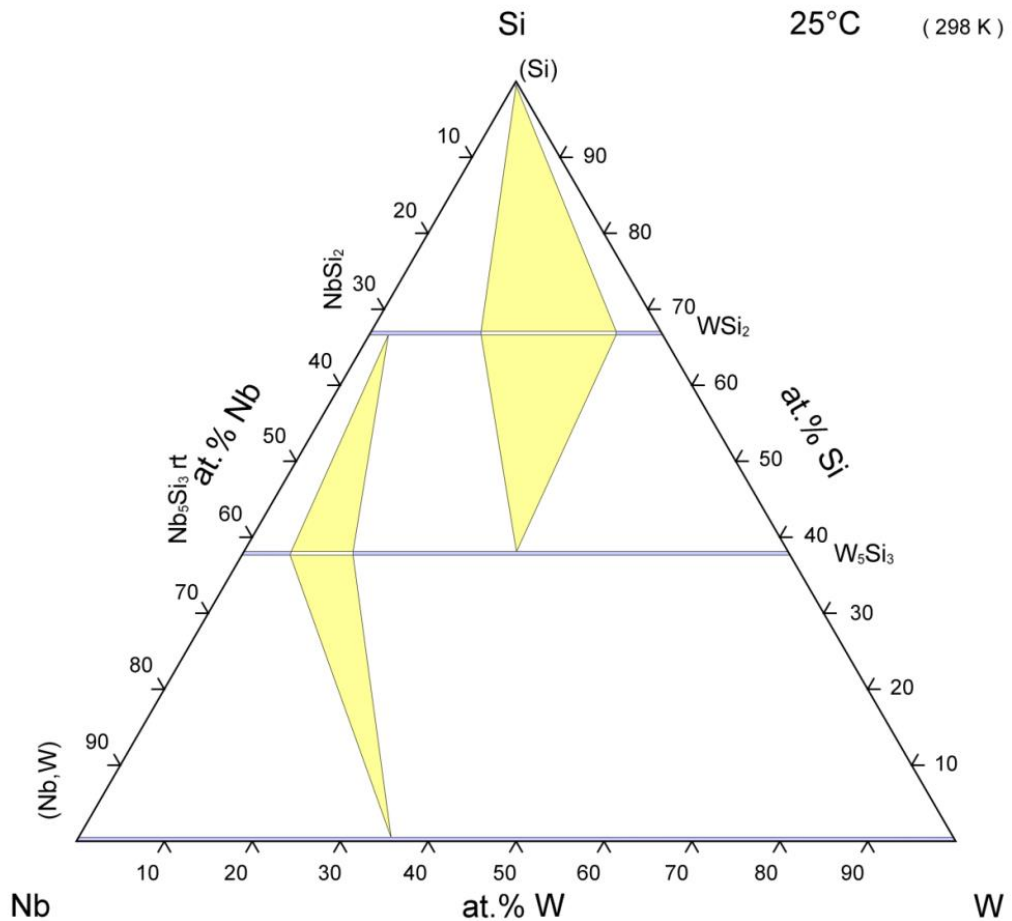
Figure 2.13 Isothermal ternary Nb-W-Si phase diagram at 25 °C (Russ 2007).

Figure 2.14 displays the liquidus projection for the W rich section of the Nb-Si-W ternary phase diagram (a) and the W rich section of the 1700 °C isothermal section of the Nb-Si-W ternary phase diagram. The liquidus projection shows that the β Silicide is stable over a large W concentration range, with the Eutectic ridge shifting towards the Si rich region with increasing W. The isothermal section shows a stable solid solution through all concentrations of W, the stability of the β Silicide increases as both the W and the Si concentration increase, as indicated by the liquidus projection.
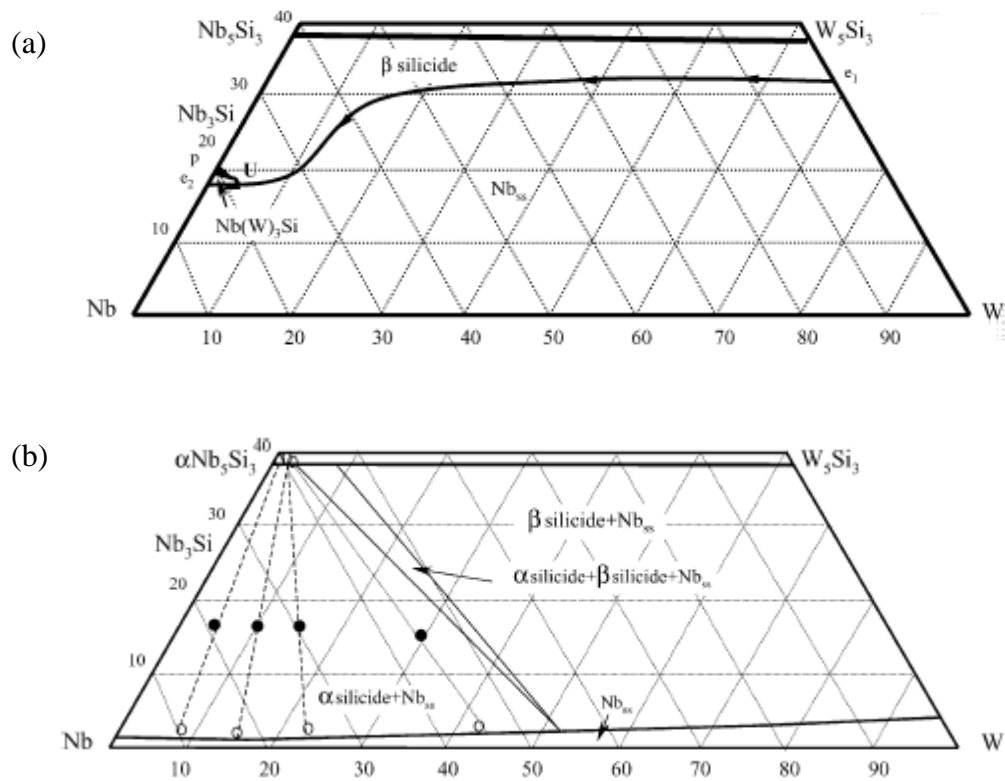
Figure 2.14 Liquidus projection (a) and Isothermal ternary section at 1700 °C (b) of the W rich section of the Nb-Si-W system (Ma et al. 2004)

2.1.9   The Nb-Si-Sn System

The importance of the addition of Sn to Nb silicide based alloys becomes apparent during oxidation studies at intermediate and high temperatures. At low levels ~1.5 at% (Bewlay et al. 2003) Sn has shown to improve oxidation resistance and eliminate pesting and to reduce the overall oxygen ingress into the bulk of the alloy, which is thought to be from the formation of Nb_3Sn (Geng, Tsakiropoulos & G. Shao 2007; Geng & Tsakiropoulos 2007). The binary Si-Sn and Nb-Sn phase diagrams, are shown in Figure 2.15 (a and b). In the Nb-Sn system there are 3 intermetallic phases, Nb_3Sn, Nb_6Sn_5 and $NbSn_2$. In respect to this work the Nb_3Sn is important. In earlier studies the stability of this phase down to room temperature was disputed (Okamoto 1990), more recent work has shown the Nb_3Sn to be stable to room temperature (Toffolon et al. 2002), as shown in the phase diagram in Figure 2.15. The Nb_3Sn phase is isomorphous

with Nb_3Al, the latter phase is considered to be detrimental for the Nb-silicide based alloys.

Figure 2.15 Si-Sn (a) and Nb-Sn (b) binary phase diagrams (Olesinski & Abbaschian 1990) (Okamoto 2003)

The 1600 °C isothermal section of the ternary Nb-Si-Sn system, shown in Figure 2.16, shows that the Nb_3Sn can be in equilibrium with both the Nb_{ss} and Nb_5Si_3. Sn has solid solubility in the Nb_{ss} and Nb_5Si_3 and Si in Nb_3Sn. Furthermore Sn supresses the formation of Nb_3Si (Vellios & Tsakiropoulos 2007b) and its effect on the latter is strong and not affected when it is in synergy with Ti and Si (Vellios & Tsakiropoulos 2007b).

Figure 2.16 Nb-Si-Sn phase diagram at 1600 ºC (Waterstrat & Muller 1977)

2.2   Melting and processing techniques

The following sections will briefly review processing techniques, some of which will be used in this study and others that have been applied by different groups in previous studies.

2.2.1   Vacuum Arc melting

Arc melting has been used in laboratory based studies and pilot studies to produce alloys from 10 g to 1 Kg. Arc melting uses a non-consumable tungsten electrode to produce an arc in an argon atmosphere to melt the elemental charge. The charge is melted in a water cooled copper crucible and forms a skull between the melt and the crucible. The electrode movement and its distance from the surface of the charge control the melt to improve homogeneity in the melt.

There are several advantages and disadvantages with regards to using vacuum arc melting. Large enough samples can be produced for mechanical testing and further processing (Bewlay, Jackson, et al. 1999) such as heat treatment and extrusion. Disadvantages include the possible formation of defects, macro/micro cracking due to the large thermal gradient between the electrode and the cooled crucible (Bewlay, Jackson, et al. 1999) and macrosegregation. The water cooled crucible causes the formation of randomly orientated microstructures with dendrites growing, perpendicular to the crucible walls at a different rate compared with the dendrites growing from the top and in the centre of the solidifying melt, resulting in a microstructure with non-uniform grain size and orientation. The fast cooling rate also hinders solid state transformations during cooling and thus heat treatments are needed to bring the microstructure to equilibrium and complete the transformation of phases (Geng, Tsakiropoulos, et al. 2006a; Vellios & Tsakiropoulos 2007b). If high melting temperature elements such as Mo and W are present in the alloy charge, their melting may be difficult using this technique.

2.2.2   Powder metallurgy

Powder metallurgy (PM) processing has been used to produce Nb-silicide based alloys using elemental Nb, Hf, Al, Cr, Ti and Si powders or pre-alloyed powder particles. In the former case, to achieve the desirable microstructure (owing to the sluggish transformation kinetics of Nb-silicide based alloys), the use of HIPing/extrusion (hot isostatically pressed) is required to refine the microstructure and aid in homogenisation of the alloy and minimise porosity. In the latter case the pre-alloyed powder must be produced by atomisation. Special atomisation techniques however must be used owing to the very high liquidus temperatures of the alloys and the reactivity of their melts. The latter requires container less melting. Elemental powders are first cold-isostatically pressed at 200 MPa and then sintered under vacuum ($\leq 10^{-3}$ Pa) at about 1500 °C to form a bar. The bar is then atomised using an EIGA atomiser. The powder particles are then mixed and hot-isostatically pressed at 1400 °C under 200 MPa for 4 hours to produce a billet that is then pre-heated to 1500 °C before being extruded at a 6:1 ratio. A second step such as forging, or hot extrusion, is mandatory for the enhancement of the mechanical properties of the alloy (Jéhanno et al. 2005). An advantage of the PM method with pre-alloyed powder particles is the directionality caused by the extrusion process, giving an increase in strength and ductility in the required direction. Disadvantages are the formation of pores and Hf oxide inclusions during the PM processing (Jéhanno et al. 2005).

2.2.3   Directional solidification and processing

Directional solidification (DS) has been exploited to produce alloys to be compared with Ni-based superalloys. DS can improve the mechanical properties of the alloys by aligning their grains in a single direction. Two DS processing techniques have been used for Nb-silicide based alloys.

2.2.4   Float zone processing

Float zone processing uses a heat source, for example, a tungsten halogen lamp, electron beam or electromagnetic induction to heat the alloy (Bewlay, Jackson, et al. 1999). The melt zone is formed in a relatively large rod-type charge that was pre-melted using another technique and is held in position by surface tension between two co-linear rods of the same alloy. The melt is then translated along the rod, without the need for a crucible, producing a directionally solidified alloy (Bewlay, Jackson, et al. 1999).

Advantages of this process are the cleanliness of the product and the ability to produce a wide range of materials (Bewlay, Jackson, et al. 1999). Disadvantages are that only induction heating is viable for the melting of Nb-Si based alloys due to the high vapour pressure of some of its constituent elements (i.e. Al). The specimen size is limited due to a compromise between liquid surface tension and hot-zone dimensions. In the case of induction melting, some allowances can be made for the electromagnetic levitation zone, which can contain a larger area of melt. The alloy being melted must have been produced with a high level of homogeneity. Evaporation of volatile species and condensation on the furnace tube can lead to attenuation of the heat input from the optical source, and destabilization of the directional-solidification conditions (Bewlay, Jackson, et al. 1999).

2.2.5   Czochralski Method

The alloy is first induction levitation melted in a segmented, water cooled, copper crucible. A seed of the alloy, which is to be directionally solidified, is then lowered into the melt and then drawn out. A schematic of this can be seen in Figure 2.17. This produces a directionally solidified bar attached to the seed. Samples up to ~15 mm diameter and more than 100 mm long have been prepared using this technique (Bewlay, Jackson, et al. 1999). Nb-Si binary and higher order alloys have been produced using this method with melting temperatures up to 2300 °C. Ingots were machined by grinding and lathe turning to produce small airfoils (Bewlay, Jackson, et al. 1999).
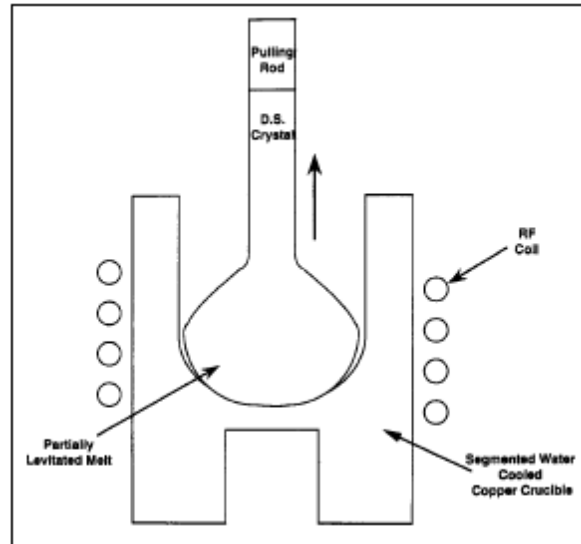
Figure 2.17 A schematic diagram of the Czochralski method (Bewlay, Jackson, et al. 1999)

2.2.6　Extrusion

Large ingots and PM billets have been extruded by first machining them to a cylinder and then placing them in molybdenum cans with a wall thickness of ~6 mm. The alloy is then heated in an induction furnace to 1400 to 1600 °C and extruded through tool-steel dies with extrusion ratios in the range of 3:1 to 10:1 (Bewlay, Jackson, et al. 1999).

2.2.7　Rapid solidification

Rapid solidification (RS) has been used to study the microstructural effects of alloying under non-equilibrium conditions. The RS microstructures exhibit many features such as fine grain structure and metastable phases and transformations, similar to those formed when the ingot is in contact with the water cooled copper crucible. The literature on the effect of high cooling rates on the microstructure of Nb-Silicide based alloys is limited. In binary Nb-Si alloys RS has been shown to suppress the Nb_{ss}-Nb_3Si eutectic which is replaced by the Nb_{ss}-Nb_5Si_3 eutectic.

　　　　Rapid solidification techniques include containerless drop tube solidification in which small droplets are dropped down an Ar filled long tube. The resultant solidified droplets are then bisected and their microstructures are analysed (Yu-ren et al. 2006; Li

& Kuribayashi 2003; Han & Wei 2002; Yao et al. 2006; Li et al. 2006; Abbaschian & Lipschutz 1997; Dai & Wei 2009).

Other rapid solidification techniques include melt spinning in which a stream of molten alloy is ejected from a nozzle or levitated melt onto a spinning wheel. This technique provides a ribbon of material about 50 μm thick and 1 to 2 cm wide which displays a tiered microstructure; as the distance from the cooled surface increases so does the grain size.

2.3   Oxidation

The ability for Nb-silicide based alloys to resist oxidation at low and high temperatures is critical to their application as high temperature alloys in gas turbines. The oxidation resistance of Nb-Si based alloys is inherently poor, with the Nb_{ss} oxidising readily. Alloying additions must therefore be added to improve the oxidation resistance of an alloy but efforts must also be made to achieve a balance of properties. This section will cover the advantages and disadvantages of different additions that have been made through various studies. The most widely studied additions for improving the oxidation of Nb-silicide based alloys are Al, Cr, Ge, Hf, Sn and Ti.

2.3.1   Oxidation resistance of Nb-silicide based alloys

The main issue with regards to the poor oxidation resistance of Nb-silicide based alloys is the high solid solubility of oxygen in Nb (~9 at%) and the tendency for the Nb_{ss} to readily form low and high order oxides such as NbO, NbO_2 and Nb_2O_5 (Hennessey & Morral 1992; Lyutyi et al. 1996). XRD studies of the oxide scale, formed on Nb silicide based alloys, have shown that the main Nb based oxide present is Nb_2O_5 (Geng & Tsakiropoulos 2007; Geng, Tsakiropoulos & G. Shao 2007; Geng, Tsakiropoulos, et al. 2006a). The speed of formation of Nb_2O_5 is too small to be detected by kinetic studies above 500 °C in air and it is therefore thought that the lower oxides play a negligible role in the oxidation of Nb at high temperatures (Geng 2006).

Additions must be made in an attempt to retard the formation of Nb based oxides, and to decrease the diffusion of O_2 into the alloy. Many of the oxides formed allow the diffusion of O_2 through the oxide scale into the substrate. Alloying additions define the phase equilibria and thus the volume fraction of the Nb_5Si_3 and Nb_{ss} thus allowing the alloy developer to achieve a balance between mechanical properties and oxidation. For example an optimum balance between oxidation resistance and creep properties is achieved with Si content between 17-19 % (Bewlay et al. 2003; Zelenitsas & Tsakiropoulos 2006b). The C14 $NbCr_2$ Laves phase can be stable with the appropriate Cr concentration and synergy with other elements. This is said to give improved oxidation resistance, however it can be detrimental to fracture toughness due to the brittle nature of the Laves phase and the decreased volume fraction of Nb_{ss}.

Several elements are known to have a marked effect on the diffusion rate of O_2 within the Nb_{ss}, these are Ti, Zr, V, Hf, Cr, Mo and Si. These elements either interact more strongly with O_2 than Nb or have a smaller atomic radius which traps oxygen and limits diffusivity (Geng 2006). Unfortunately, although having a reducing effect on the diffusion of oxygen, the additions Zr and V have a negative effect on the oxidation resistance of the alloy. Small concentrations ~ 2 at% of Mo increase the oxidation resistance at 800 °C and have a small effect at 1200 °C when compared with a Mo free alloy (Geng, Tsakiropoulos, et al. 2006a). Other studies have shown that the use of Mo at very high concentrations >10 at% had mixed effects. Alloys displayed catastrophic oxidation due to the evaporation of MoO_3 (Mo ≈ 10 at%) (Xiong et al. 2009), whereas other alloys showed improved oxidation resistance with increased Mo content (Mo ≈ 20 at%) (Chattopadhyay et al. 2008; Liu et al. 2005). This implies that the synergy of Mo with other elements is very important as they can have negative (W), or positive (B) effects on oxidation resistance.

2.3.2   Oxidation mechanism

The greatest issue with the oxidation of Nb is the phenomenon known as pest oxidation or 'pesting' (Grabke & Meier 1995; Katsman et al. 1996), which occurs in the temperature range 700 to 1000 °C (Chattopadhyay et al. 2008). Pesting is caused by the

accelerated oxidation of Nb, particularly in pre-existing micro cracks, originally caused by the stresses induced during the high cooling rates found in clean melting with a water cooled copper crucible. This rapid oxidation causes a volume increase which, in turn, causes shear stresses in the Nb_{ss} matrix around the silicide grains resulting in internal tensile stress within the silicide itself. These tensile stresses cause transgranular cracking perpendicular to the applied stress (parallel to the oxygen ingress), ultimately 'pulverising' the oxidised sample (Mathieu et al. 2012).

The oxidation of Nb silicides happens through the formation of a non-cohesive mixed oxide scale. With the addition of Hf, Al and/or Sn the risk of pest oxidation at intermediate temperatures ~800 °C can be avoided (Bewlay et al. 2003). The oxidation occurs in 3 zones; first the base metal, second a diffusion zone that is still coherent with the base metal, lastly an oxide scale which is generally very brittle and has a tendency towards spallation. Figure 2.18 shows an image of the three zones after oxidation at 800 °C. The additions of Al, Cr and Hf stopped catastrophic pest oxidation occurring but there was severe cracking in the diffusion zone.
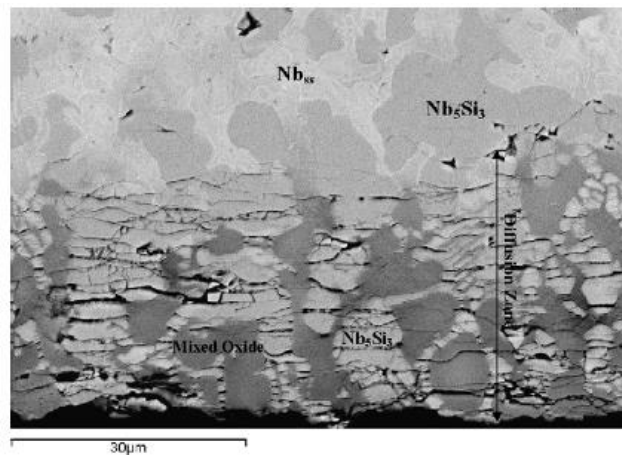
Figure 2.18 BSE image of the as-cast alloy Nb-18Si-24Ti-5Al-5Cr-5Hf-2Mo after oxidation at 800 °C for 100 h (Geng, Tsakiropoulos, et al. 2006a).

In the diffusion zone the Nb_{ss} preferentially oxidised to form Nb_2O_5, mixed oxides and SiO_2 and TiO_2. During the oxidation of the alloy at 800 °C there was no measurable oxygen dissolved in the Nb_5Si_3 phase (Geng, Tsakiropoulos, et al. 2006a). The oxidation occurred primarily via diffusion along the grain boundaries but also through diffusion into the Nb_{ss} grains, oxidising the Nb_{ss} (Sheasby & Smeltzer 1981). It

is thought to be beneficial to form HfO_2, $NbCr_2$ or Nb_3Sn along the grain boundaries to reduce the rate of oxygen diffusion and stop pest oxidation occurring.

2.4   Effect of alloying additions on oxidation

Different alloying additions have been made to Nb-silicide based alloys in order to systematically study their individual and combined effectiveness at improving oxidation resistance. The alloys that will be studied in this project will be a product of extensive research that has been undertaken to optimise the composition to decrease the rate of oxidation. Alloying additions have also been made to specifically target and remove the problem of pest oxidation which is caused by preferential oxidation at microstructural features. The preferential oxidation creates high internal stresses and causes the alloy to self-pulverise (Bewlay et al. 2003). The high residual compressive stresses are brought on by both a difference in anisotropic properties between the Nb_2O_5 and Nb_5Si_3, and an increase in volume. As the alloy cools the residual stresses cause micro-cracking of the Nb_5Si_3 parallel to the surface of the alloy, resulting in spallation (Mitra 2006).

The base composition for the development of Nb-silicide based alloys is Nb-18Si-24Ti-5Al-5Cr (Zelenitsas & Tsakiropoulos 2005). To this base alloy, additions of Mo, Ta, Hf, Ge and Sn (Geng, Tsakiropoulos, et al. 2006a; Geng & Tsakiropoulos 2007; Geng, Tsakiropoulos & G. Shao 2007; Zifu & Tsakiropoulos 2010; Ventura & Varma 2009), have been made in an attempt to improve the oxidation resistance of the base alloy. All additions were made aiming to avoid the formation of undesired phases and reduce any large detrimental impact on mechanical properties. Figure 2.19 shows the effect of Al, Cr and Ta additions to Nb-24Ti-18Si. The compositions of the KZ alloys can be found in Table 2.4.

Table 2.4 Nominal compositions of the KZ series alloys (at%) (Zelenitsas & Tsakiropoulos 2006a).

Alloy	Nominal composition (at%)
KZ3	Nb–24Ti–18Si
KZ4	Nb–24Ti–18Si–5Cr
KZ7	Nb–24Ti–18Si–5Al
KZ5	Nb–24Ti–18Si–5Cr–5Al
KZ6	Nb–24Ti–6Ta–18Si–5Cr–5Al
KZ2	Nb–24Ti–18Si–8Cr–4Al
KZ8	Nb–24Ti–6Ta–18Si–8Cr–4Al

It can be seen from Figure 2.19 that the alloy KZ5 exhibited the second lowest weight gain per unit area of all the alloys in their heat treated condition at 800 °C (Zelenitsas & Tsakiropoulos 2006a).
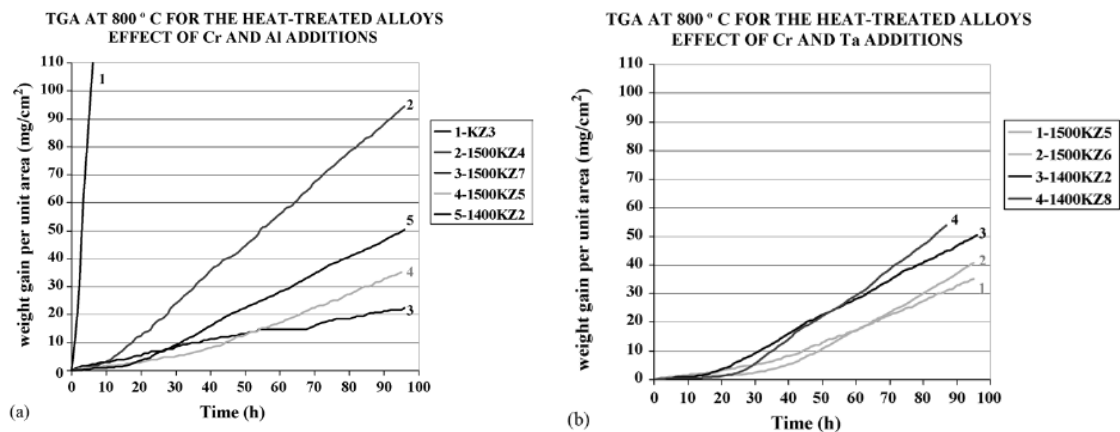
Figure 2.19 Thermogravimetric analysis results of the heat treated KZ series of alloys at 800 °C (Zelenitsas & Tsakiropoulos 2006a). The compositions of the alloys are given in Table 2.4

Figure 2.20 shows the effect that Ti addition of 24 at% has on the oxidation resistance of Nb-18Si-5Cr-5Al-xMo alloys at 800 and 1200 °C.
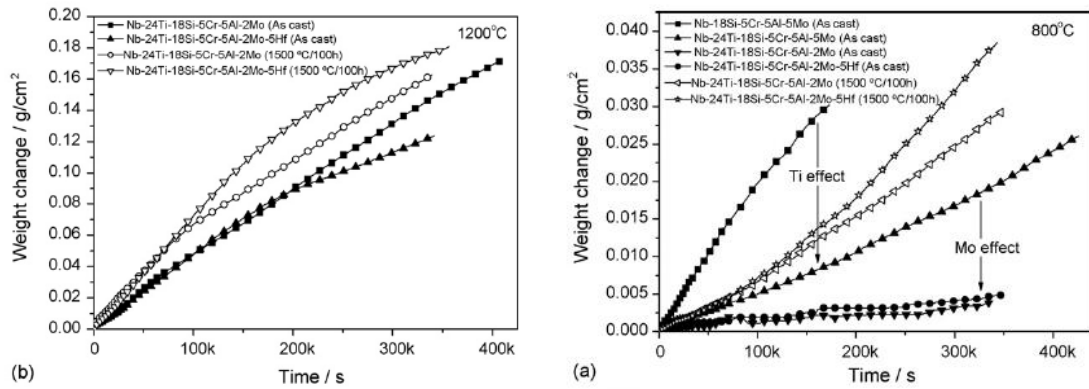
Figure 2.20 Thermogravimetric analysis data of Nb-18Si-5Cr-5Al-xMo alloys with varying Mo, Ti and Hf additions at 800 (a) and 1200 °C (b) for 100 h (Geng, Tsakiropoulos, et al. 2006a).

Figure 2.20 shows that at both intermediate (a) and high (b) temperatures, the addition of Ti significantly increase the oxidation resistance. It can also be seen that at high temperatures the addition of Hf gave a slight decrease in weight change compared with the non Hf containing alloys. It also shows that even a small (3 at%) decrease in Mo content can drastically improve the oxidation resistance, displaying the detrimental effect Mo has on the oxidation resistance at high concentrations.

Three of the alloys studied in this project contained Sn to improve the pest oxidation resistance and the intermediate strength. Figure 2.21 shows the improvement that Sn had on the oxidation resistance of the alloy JG6 (Nb-24Ti-18Si-5Al-5Cr-5Hf-5Sn) compared with the alloy to JG4 (Nb-24Ti-18Si-5Al-5Cr-5Hf) at 800 (a) and 1200 °C (b). The data shows that an addition of 5 at% Sn significantly increased the oxidation resistance of the JG4 as-cast and heat treated alloy at 800 °C. At 1200 °C the Sn still had a positive effect on the oxidation resistance of the alloy which was not as significant as at intermediate temperatures (Geng, Tsakiropoulos & G. Shao 2007).
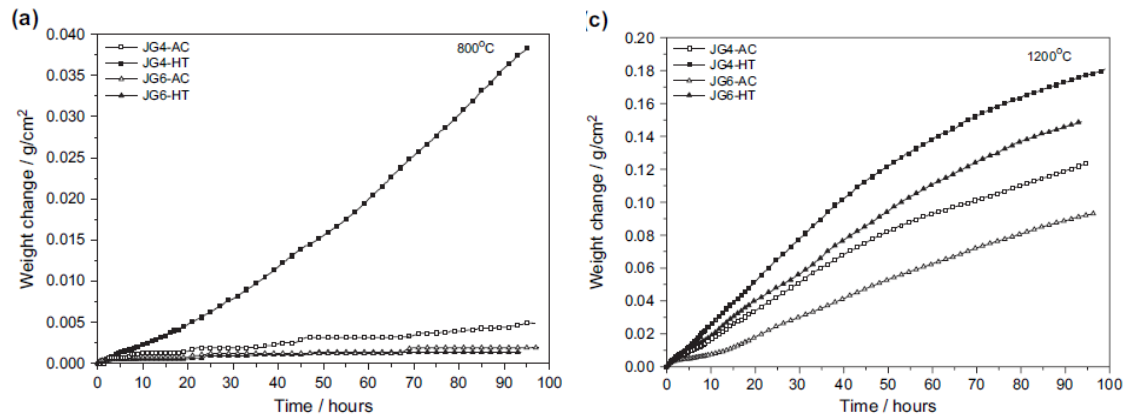
Figure 2.21 Thermogravimetric analysis data of JG4 (Nb-24Ti-18Si-5Al-5Cr-5Hf-2Mo) and JG6 (Nb-24Ti-18Si-5Al-5Cr-5Hf-2Mo-5Sn) as-cast and heat treated after oxidation at 800 and 1200 °C for 100 h (Geng, Tsakiropoulos & G. Shao 2007).

The Sn content was set as 5 at% in (Geng, Tsakiropoulos & G. Shao 2007), however Sn has been reported to have a beneficial effect on the intermediate oxidation resistance with additions as low as 1.5 at% (Bewlay et al. 2003).

Additions of Hf were reported to have an effect on the oxidation resistance of Nb-20Cr-20Si-(5, 10) Hf alloys, where higher Hf containing alloys showed an improvement in oxidation resistance, with a larger effect achieved at higher temperatures (~1400 °C) (Vazquez & Varma 2011). The addition of Ge has also been shown to be beneficial at high temperatures with regards to the adhesion of the oxide scale, with Ge diffusing to the region between the oxide scale and the substrate (Menon n.d.).

2.5   Mechanical properties

The mechanical properties of Nb silicide based alloys depend on the properties of the solid solution and the intermetallic phases. Alloying can have a strong effect on the properties of the solid solution and the intermetallic phases, increasing or decreasing the creep resistance, yield strength and fracture toughness of each phase. A key challenge with alloy development is that to increase the oxidation resistance, many alloying additions must be made that do not necessarily benefit the mechanical properties. This section will discuss the effects of alloying on fracture toughness, intermediate and high temperature strength and creep.

2.5.1   Fracture toughness

Fracture toughness is a critical property for high temperature turbine blades, as the blades must be able to sustain impact during operation without catastrophic failure occurring. The minimum fracture toughness goal for Nb-silicide based alloys has been set as 20 MPa$\sqrt{m}$ (Bewlay et al. 1997) to ensure that components will survive manufacturing and assembly of the engine and resist foreign body damage (Bewlay et al. 1997). This target has been reached in developmental alloys, however, alloying additions must be made to improve oxidation resistance which means that the fracture toughness will change with the Nb_{ss}/Nb_5Si_3 volume fraction ratio, alloy microstructure and solid solution effects.

2.5.2   Effects of microstructure and alloying additions on fracture toughness

By altering the Nb_{ss}/Nb_5Si_3 volume fraction ratio the fracture toughness can be controlled, by increasing the volume fraction of the Nb_{ss} the fracture toughness can be increased while an increase in the vol% of Nb_5Si_3 will cause a decrease in fracture toughness. Figure 2.22 shows the effect of processing on the fracture toughness of the base binary alloy Nb-18Si. It can be seen that at this composition, an alloy manufactured using hot pressing (HP) achieved a fracture toughness of ~12.5 MPa$\sqrt{m}$ (Kimura et al. 2005).
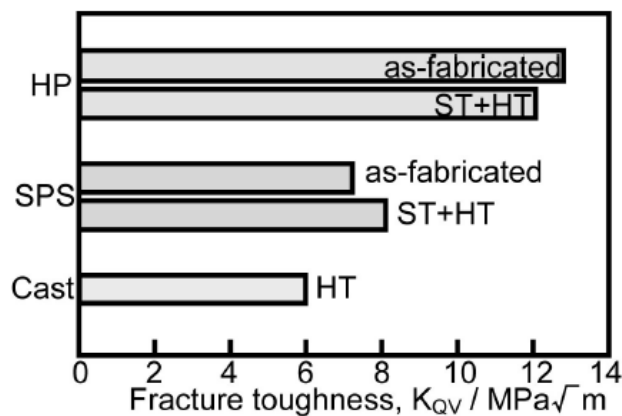
Figure 2.22 A comparison of different processing methods (HP= hot pressed, SPS= spark plasma sintered) on the fracture toughness of Nb-18Si (Kimura et al. 2005).

Figure 2.23 shows the difference in microstructure between the SPS (spark plasma sintering) and HP (hot pressed) as-fabricated and solution treated (ST) + heat treated (HT) alloys. It can be seen that the HP alloy after ST+HT has large co-continuous Nb_{ss} grains and large Nb_5Si_3 and Nb_3Si grains along with lamellar Nb_{ss}/Nb_5Si_3. The SPS ST+HT had a different microstructure consisting mainly of lamellar Nb_{ss}/Nb_5Si_3 and few large Nb_{ss} grains (Kimura et al. 2005). The contrast in microstructures shows how important large grains were on the ability of the alloy to resist crack propagation as can be seen in Figure 2.24. Other HP alloys, e.g. the alloy (Nb-16Si-18Ti) have shown marked improvements when alloyed with Ti, reaching a fracture toughness above 16 MPa$\sqrt{m}$ (Wang et al. 2010).
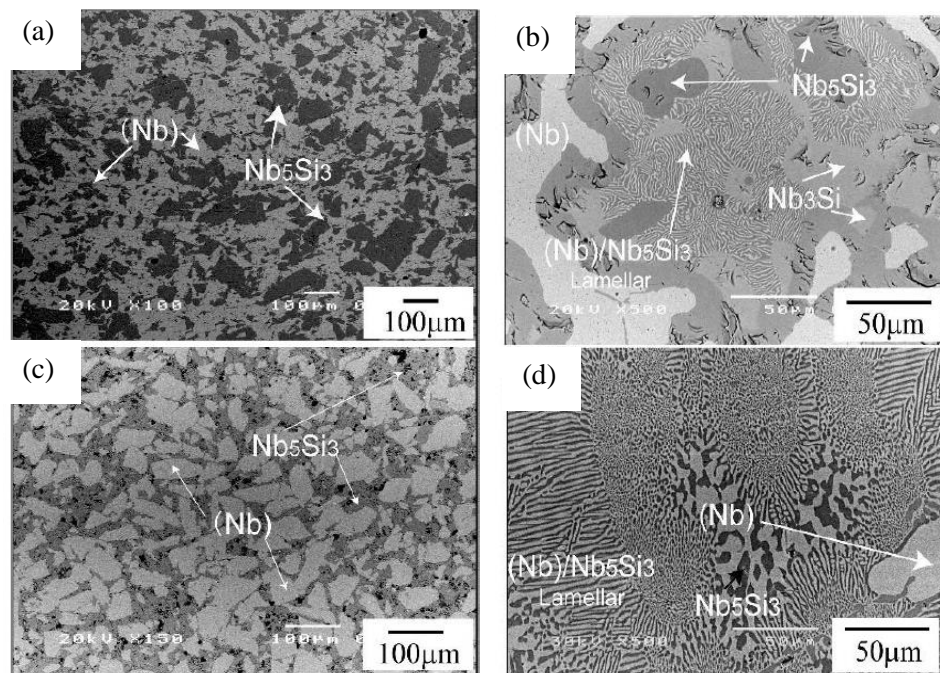
Figure 2.23 Back scattered electron images of Nb-18Si after HP (a) as-fabricated (b) ST+HT and after SPS (c) as-fabricated and (d) ST+HT (Kimura et al. 2005).
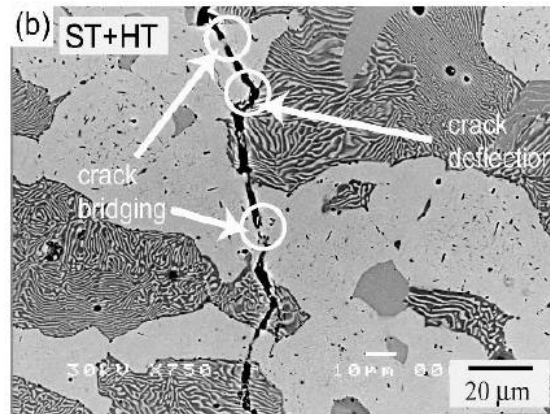
Figure 2.24 Back scattered electron image showing crack propagation through HP, ST+HT Nb-18Si (Kimura et al. 2005).

Controlling the fracture toughness by altering the Nb_{ss}/Nb_5Si_3 volume fraction ratio, can be deleterious to both the creep and the oxidation resistance of the alloy as the Nb_{ss} volume fraction increases. It was thought that the addition of alloying elements could be used to increase the fracture toughness of the silicide phase, thus increasing the fracture toughness of the alloy as a whole. It has been shown that the Nb_{ss} phase is largely responsible for the fracture resistance of Nb silicide based alloys (Liu et al. 2010). The total fracture toughness of the alloy depends on the volume fraction and fracture toughness of the Nb_{ss}, and the plastic constraint of the silicide on the Nb_{ss} phase (Chan & Davidson 2001).

Figure 2.25 shows the effect of vol% of silicide on fracture toughness. An increase in the vol% causes in general a decrease in the fracture toughness with the exception to those alloys that contain Ti, which maintain reasonable fracture toughness. The data in Figure 2.25 is for alloys that were either pressed powder-metallurgy (PM) materials, directionally solidified (DS) materials, or arc-cast (AC) and extruded (EX) materials that had been heat treated (HT) at 1500 °C for 100 h (Chan & Davidson 2001). It can be seen that even at high vol% silicide the alloys that contain Ti had better fracture toughness compared with the PM, AC, EX and HT binary Nb-Si alloys at the same vol% silicide.
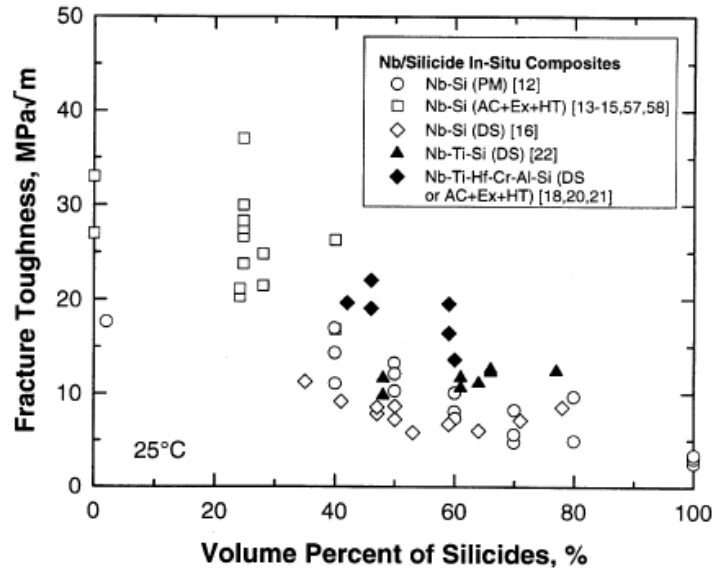
Figure 2.25 Fracture toughness of Nb-silicide based alloys without and with Ti additions as a function of vol% silicides (Chan & Davidson 2001).

Figure 2.26 shows the effect of the addition of Ti on the fracture toughness of the un-alloyed and alloyed Nb$_5$Si$_3$. As the Ti content increases towards 30 at% the fracture toughness of the tetragonal D8$_1$ Nb$_5$Si$_3$ based silicide increases, however for more than 30 at% Ti the tetragonal Nb$_5$Si$_3$ transforms into the undesired hexagonal D8$_8$ structure. K$_Q$ values up to 18.7 MPa$\sqrt{m}$ have been obtained in annealed DS ternary alloys Nb-17.5Si-10Ti, compared with   14.5 MPa$\sqrt{m}$ obtained in DS binary Nb-17.5Si alloys (Sekido et al. 2006).
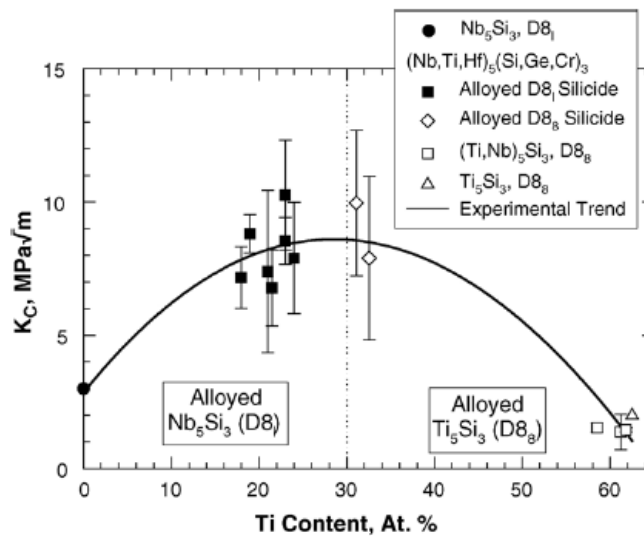
Figure 2.26 Plot of fracture toughness against Ti content of D8$_1$ and D8$_8$ Nb$_5$Si$_3$ silicides with other D8$_8$ silicides (Chan 2005).

The addition of Hf has also been shown to have a positive effect on the fracture toughness of Nb silicide based alloys. Like Ti, Hf also gives beneficial oxidation resistance and has no effect on the DBTT of the alloy (Chan 2002a). Figure 2.27shows the effect of increasing Hf on the fracture toughness of a binary Nb-16Si alloy.
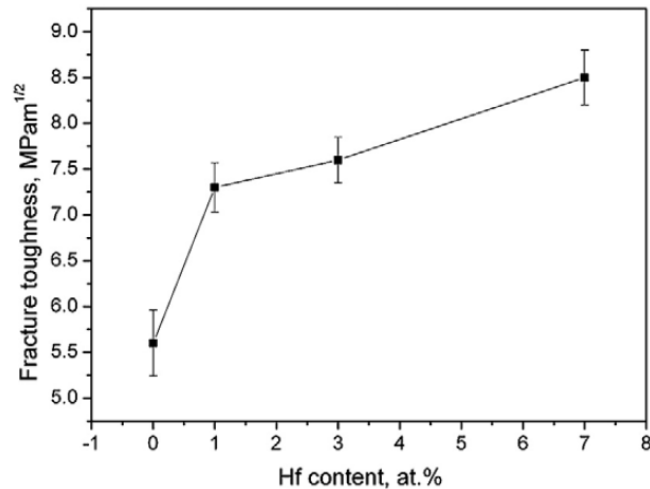
Figure 2.27 Effect of increasing Hf content on the fracture toughness (Tian et al. 2008).

As can be seen in Figure 2.27 there was an initial jump in fracture toughness with the first 1 at% addition of Hf and then a steady increase in fracture toughness with increasing Hf content. The increased Hf content changed the fracture manner of the Nb_{ss} from brittle cleavage to plastic behaviour (Tian et al. 2008). Hf also refined the eutectic structure of the alloy until at 7 at% Hf the Nb_3Si/Nb_{ss} eutectic had almost disappeared and only primary Nb_{ss} particles were left with Nb_3Si.

Although it has been proven that Ti has a significant effect on improving the fracture toughness, many other alloying additions used to improve the oxidation resistance also affect the fracture toughness. It has been established that Al has a negative effect on the fracture resistance due to it preventing dislocation nucleation at the crack tip. This limits the formation of a plastic zone at the crack tip thus reducing the alloys' ability to crack arrest, therefore promoting cleavage cracking (Davidson & Chan 1999). Cr also inhibits the nucleation of dislocations at the crack tip but to a lesser extent than Al, decreasing the ductility of these alloys (Kim et al. 2002).

2.5.3   Fracture mechanisms

The Nb-silicide based alloys or Nb in situ composites have either brittle phases in a ductile matrix or a ductile phase in a brittle matrix. In both cases it is the ductile Nb_{ss} phase that gives the composite its fracture resistance. The different mechanisms that define the crack type can be determined by whether the cracks enter a ductile or a brittle phase. When a crack tip hits a brittle phase it will tend to travel through the grain, breaking atomic bonds along a crystal plane, causing cleavage fracture. The crack may divert around the brittle/ductile phase instead, moving along the grain boundary, causing intergranular cracking. If the crack encounters a ductile phase, crack tip blunting through dislocation pile-up, crack deflection and the formation of ligaments can occur, these give resistance to crack propagation (Chan & Davidson 2001; Chan & Davidson 2003; Bloyer et al. 1998). Figure 2.28 shows typical crack propagation through several different Nb silicide based alloys.
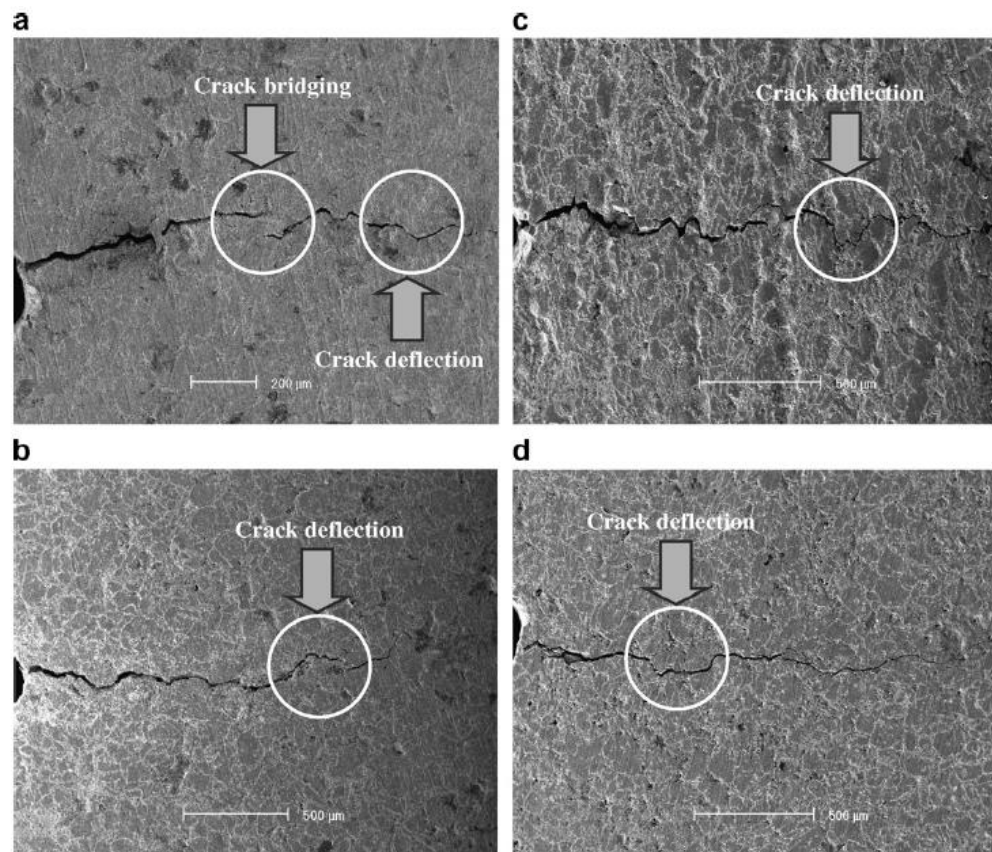
Figure 2.28 Images showing crack paths in the alloys (a) Nb-11Si-6Ti, (b) Nb-16Si-6Ti, (c) Nb-18Si-6Ti and (d) Nb-18Si (Li & Peng 2007).

The alloys in Figure 2.28 either had Ti additions (a-c) or were binary alloys (d) and were produced using hot pressing and had the following fracture toughness values; (a) 13, (b) 10.4, (c) 8.5, (d) 8.3 (MPa√m) (Li & Peng 2007). The alloys with lower Si content exhibited more ductile features, for example they showed, crack bridging/ligament formation and crack deflection.

Figure 2.29 shows a crack propagating through an as cast Nb-16Si-1Hf alloy, where the light grey phase is the Nb_{ss} and the dark phase is the Nb_3Si.
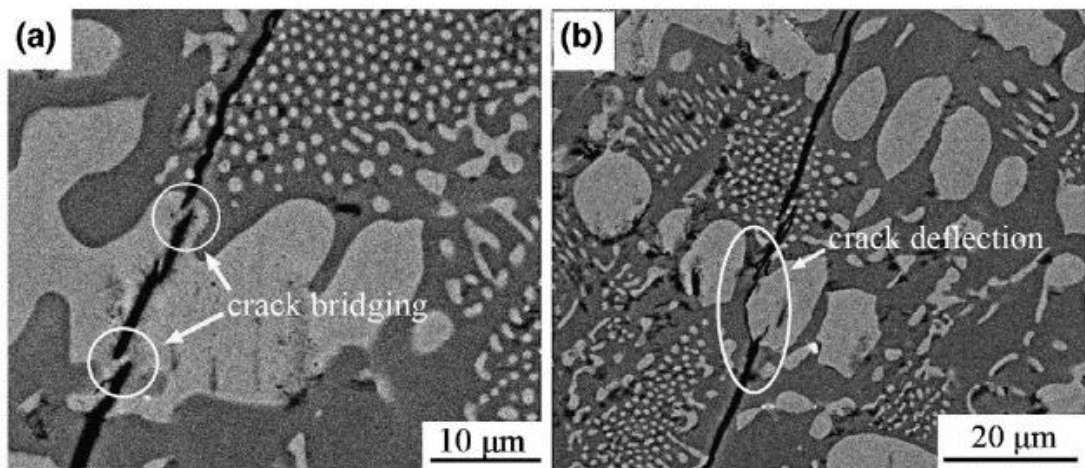
Figure 2.29 Back scattered electron images of crack propagation through as-cast Nb-16Si-1Hf (Tian et al. 2008).

It can be seen that as the crack enters the light grey Nb_{ss} phase there are signs of both crack deflection and crack bridging. The addition of Hf leads to microstructural refinement, promoting the formation of primary Nb_{ss} particles, and reducing the fine eutectic phase. The presence of primary Nb_{ss} and silicide phases and a reduction in vol% of lamellar Nb_{ss}/Nb_3Si or Nb_{ss}/Nb_5Si_3 have been shown to be beneficial to the fracture toughness of the alloy (Tian et al. 2008; Kimura et al. 2005). The images shown in Figure 2.30 are of the Nb-16Si-1Hf alloy, which had a fracture toughness of ~7.25 MPa√m (Tian et al. 2008). The fracture toughness of this alloy could be greatly increased with the addition of Ti to increase the toughness of the Nb_5Si_3 phase (Chan 2003).

The shape of the grains in the alloy microstructure is important as it can determine what path the crack will take through the alloy. A study has shown that the crack will choose to travel around spherical ductile particles rather than through them. This

bypasses the fundamental toughening of the alloy, as the ductile particles are unable to cause crack bridging or other toughening mechanisms. Figure 2.30 shows R-curve data for spherical particles and acicular particles. Under monotonic loading the spherical particles failed to give any increase in fracture toughness, but the acicular particles had a large effect on the fracture toughness (Dimiduk 1995).
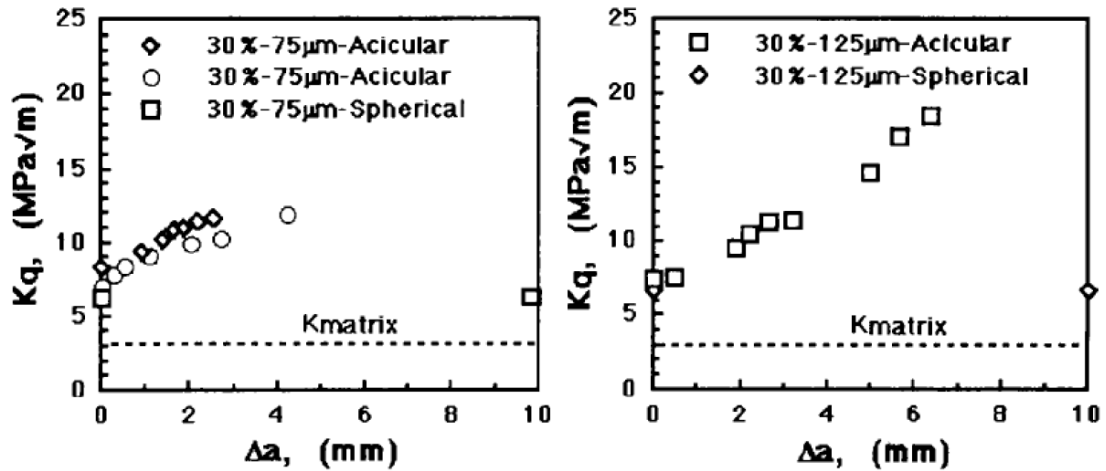
Figure 2.30 R-curve data for Nb-silicide based alloys containing either spherical or acicular ductile particles of different sizes (Dimiduk 1995).

Figure 2.30 also shows how an increase in the ductile phase particle size has a positive effect on the fracture toughness. Therefore to achieve balance between creep, high temperature strength and fracture toughness the ductility of the Nb_{ss} must be controlled via alloying additions. These Nb_{ss} particles can themselves be optimised by increasing their size as to increase the area of interaction with cracks, and ensuring they have an acicular geometry opposed to spherical. It is also effective to increase the volume fraction of the Nb_{ss} phase so long as the creep, high temperature strength and oxidation resistance are not diminished.

2.6 Intermediate and high temperature strength

A problem with regards to Nb silicide based alloys meeting the requirements for high temperature strength and low temperature fracture toughness is the conflicting demand on their microstructure and alloying. To achieve a high strength, the volume fraction of

Nb_5Si_3 must be increased, this in turn has a detrimental effect on the fracture resistance of the alloy. The increase in the vol% of Nb_5Si_3 does however increase the creep and oxidation resistance of the alloy, therefore the optimisation of mechanical and environmental properties relies on finding a balance with fracture toughness.

The high temperature yield strength depends on grain size and solid solution strengthening. The grain size of the alloys can be controlled with heat treatments, alloying additions, which have microstructural refining properties, and solidification rate. Figure 2.31 shows the proof stresses of the Nb-18Si binary alloy at various temperatures after solution treatment (ST), heat treatment (HT), hot pressing (HP) and as-cast (Kimura et al. 2005).
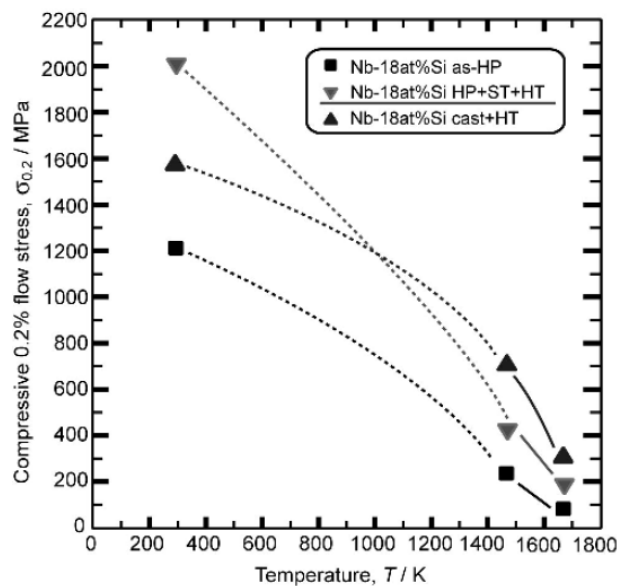
Figure 2.31 0.2% compressive flow stress of binary Nb-18Si in as-hot-pressed, (ST + HT) heat-treated and cast conditions+HT (Kimura et al. 2005).

Figure 2.31 shows that the low temperature strength can be improved by processing (HP, ST, HT) and that the as cast alloy had better high temperature strength. The microstructures of (a) as-HP and (b) HP+ST+HT are shown in Figure 2.29 (a) and (b) (Kimura et al. 2005). The highest room temperature strength was achieved with the microstructure which shows a semi-continuous Nb_{ss} phase, large Nb_5Si_3 and Nb_3Si particles and a transformed fine Nb_{ss}/Nb_5Si_3 lamellar structure (Kimura et al. 2005). The lowest room temperature strength was obtained with the microstructure shown in Figure

2.29 (a) which has Nb_5Si_3 particles in a Nb_{ss} matrix. Growth speed affects the grain size and morphology, increasing the growth rate whilst maintaining continuous silicide growth brings the optimum yield strength (Tian et al. 2009).

Solid solution hardening also has a large effect on the high temperature strength. Figure 2.32 shows a plot of proof stress against temperature for several three phase (Nb_3Al, Nb_{ss}, Nb_5Si_3) Nb- silicide based alloys under compression with compositions Nb-5Si-9Al, Nb-7Si-9Al, Nb-8Si-9Al-10Ti, Nb-10Si-9Al-10Ti, Nb-6Si-11Al-15Ti, Nb-8Si-11Al-15Ti. These alloys had Nb_{ss} volume fractions 50, 40, 62, 36, 65 and 58, respectively.
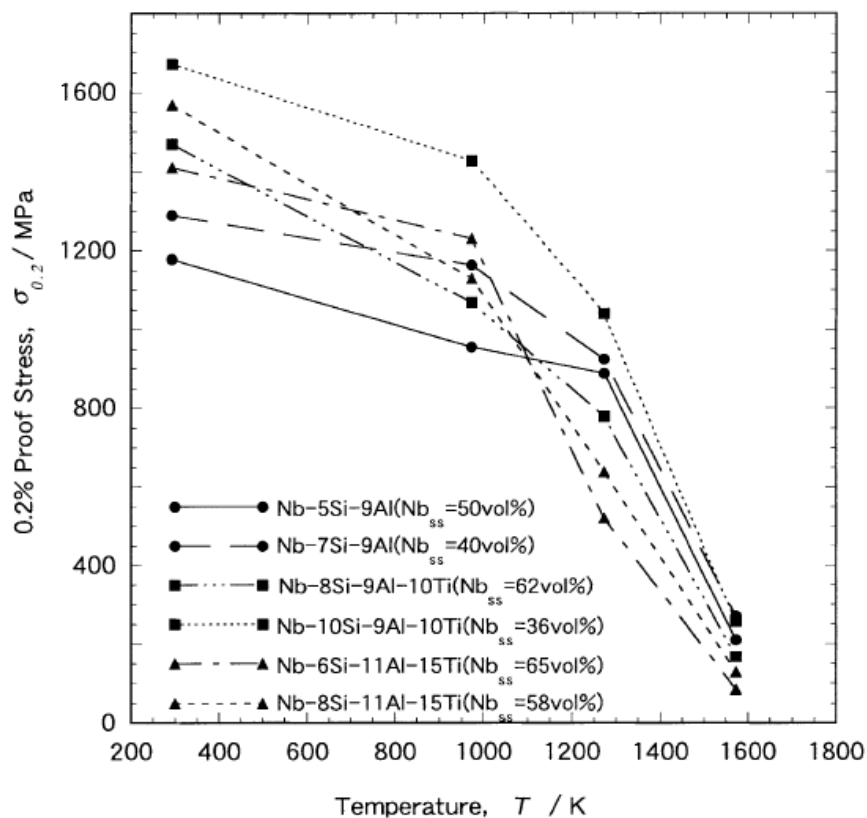
Figure 2.321 Proof stress against temperature for a range of as-cast Nb-silicide based alloys (Murayama & Hanada 2002).

The Nb-10Si-9Al-10Ti alloy had the highest proof stress at 250 K due to the solid solution hardening effect on the Nb_{ss} and the reduced vol% of the Nb_{ss}. All the Ti containing alloys maintained a high proof stress at the lower temperatures. Above 1100 K the alloys with highest Ti content (15Ti) suffered a reduction in proof stress

(Murayama & Hanada 2002). The Nb-10Si-9Al-10Ti retained a high proof stress at ~1600 K. Figure 2.33 shows plots of fracture toughness and proof stress against temperature for alloys with different vol% of Nb_{ss} (Murayama & Hanada 2002).
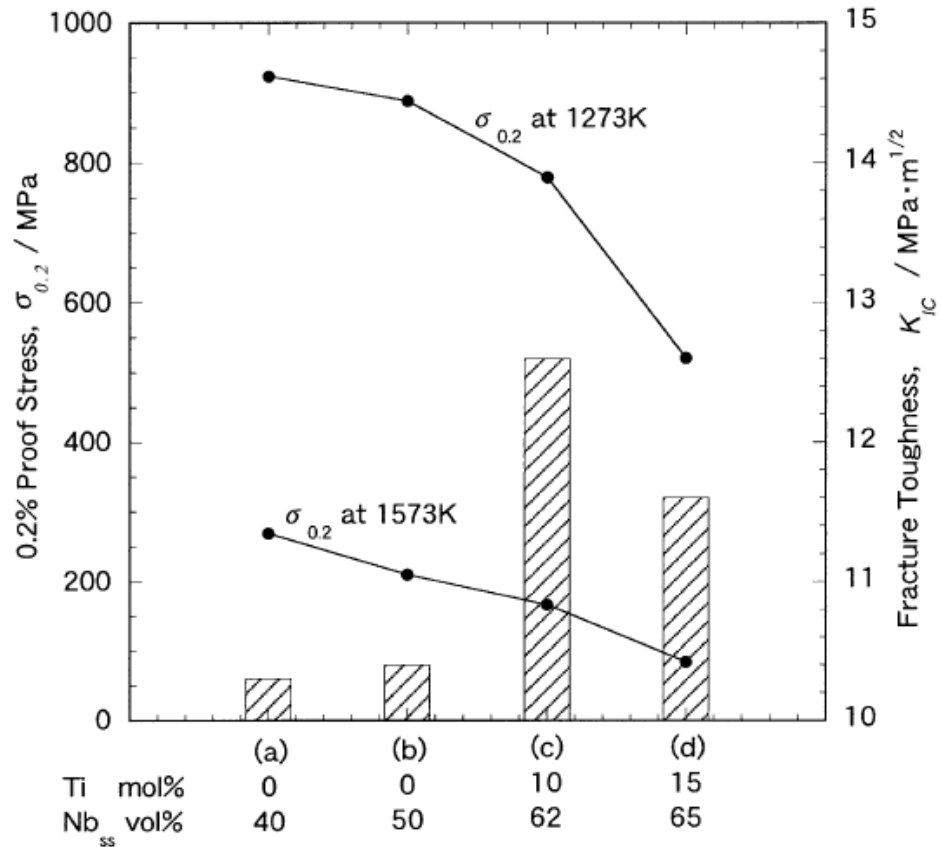
Figure 2.33 Plots of proof stress and fracture toughness against Ti mol% and Nb_{ss} vol% (Murayama & Hanada 2002).

It can be seen that a good balance between proof stress and fracture toughness was achieved with 10Ti (mol%) with Nb_{ss} vol% 62, with a fracture toughness of ~12.5 MPa√m and a 0.2% proof stress of ~180 MPa. This shows that although the addition of Ti has a positive effect on the fracture toughness, it has a deleterious effect on the high temperature strength.

The addition of refractory metals can be used to impart solid solution hardening in the ductile Nb_{ss} phase to improve the high temperature strength. Figure 2.34 shows the effect of increasing the Mo and W content on high temperature strength.

(a)   (b)
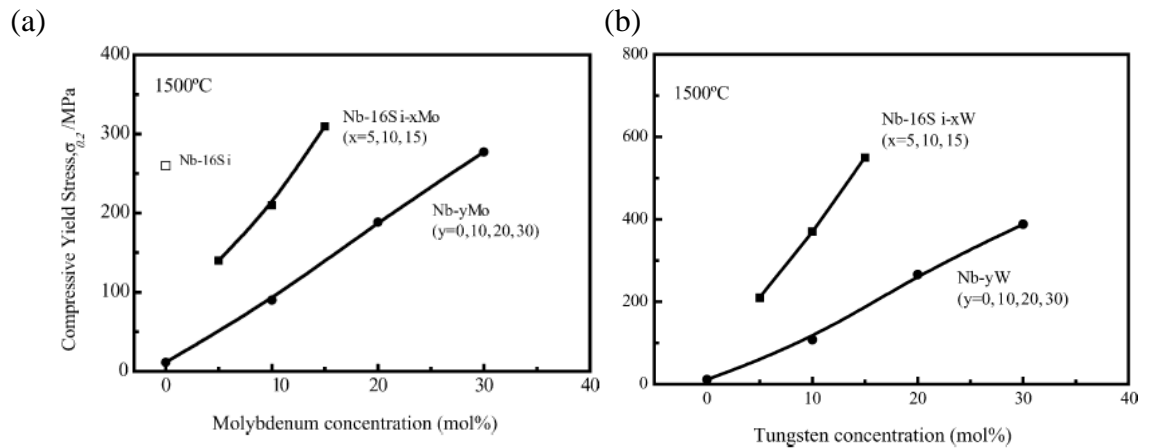
Figure 2.34 Effect of increasing (a) mol% Mo and, (b) mol% W on compressive yield stress at 1500 °C for Nb-16Si based ternary alloys (Ma et al. 2004).

Both Mo and W had a positive effect on increasing the high temperature compressive yield stress of the binary Nb-16Si, and W had a stronger effect on the yield stress, showing an increased compressive yield stress with additions above 5 mol%, while Mo showed a comparative increase in the yield stress at 10 mol%. Figure 2.35 shows the microstructures of the Nb-16Si-5W and Nb-16Si-15W alloys. It can be seen that with increasing W content there was a coarsening of the eutectic region (Ma et al. 2004).
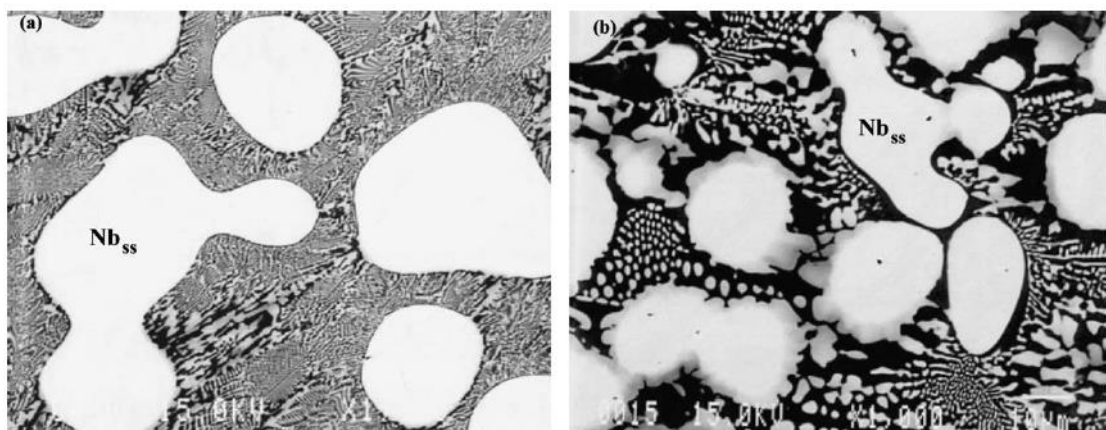
Figure 2.35 Back scatter electron images of (a) Nb-16Si-5W and (b) Nb-16Si-10W (Ma et al. 2004).

The Nb-16Si-10Mo alloy also had a very fine eutectic microstructure similar to that of the Nb16Si-5W alloy, as can be seen in Figure 2.36 (Ma et al. 2004).
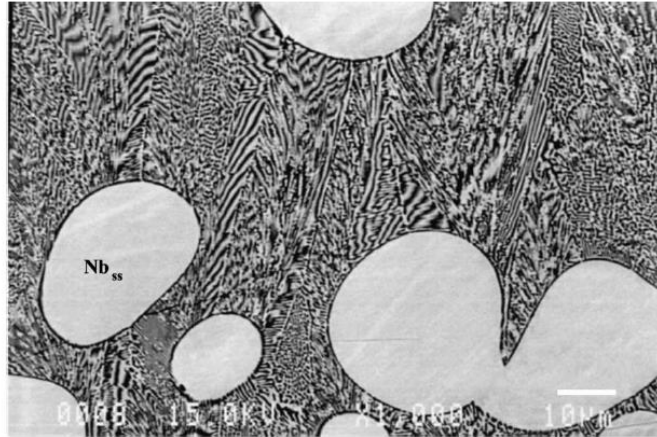
Figure 2.36 Back scatter electron image of Nb-16Si-10Mo (Ma et al. 2004).

Higher order alloys with Nb-18Si-10Ti-(10, 20)Mo-(0, 5, 10, 15)W have also been studied and show improved results to those in Figure 2.34 Mo and W both increase the yield strength of all alloys above a 0.2% proof stress of 700 MPa at 1500 °C even in the presence of Ti (Sha, H. Hirai, et al. 2003).

Hf has been added to alloys containing Mo. The alloys were tested under tensile conditions. Figure 2.37 shows the proof and ultimate tensile stresses (UTS) of Nb-18Si-5Mo-5Hf (mol%) (Kim et al. 2004), in which the Si content was higher by 2 mol% compared with the Nb-16Si-5Mo alloy (Ma et al. 2004) with the addition of 5 mol% Hf.
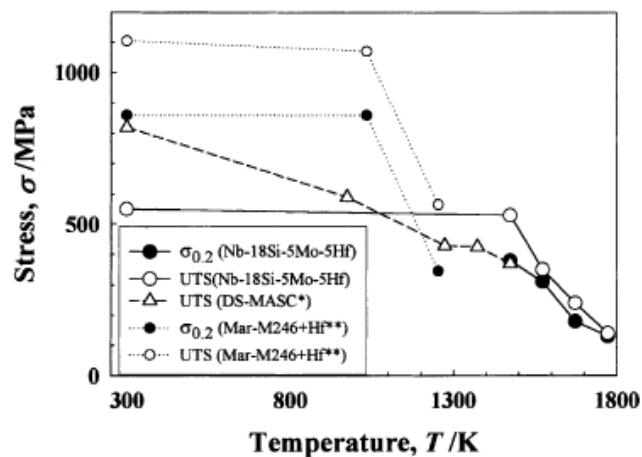
Figure 2.37 Tensile strengths of Nb–18Si–5Mo–5Hf, compared with a cast Ni-base superalloy, Mar–M246 + Hf and directionally solidified Nb–24.7Ti–8.2Hf–2.0Cr–1.9Al–16.0Si (DS-MASC) as cited in (Kim et al. 2004).

Figure 2.37 shows that the 0.2% proof stress increased from 200 MPa to 400 MPa at 1500 °C. Figure 2.37 also shows data for a Ni-based superalloy and the DS-MASC alloy. Comparison with the data for Nb-18Si-5Mo-5Hf shows superior high temperature UTS at 1300 °C compared with both the DS-MASC and the Ni based superalloy.

2.7   Creep resistance

Creep resistance is an important property for gas turbine blades as they spend a large portion of their lifetime under high temperatures and centrifugal loads. It is therefore important to make sure there is a minimum amount of creep during the product's use as the engine has tight dimensional tolerances and any change in part dimension can cause catastrophic failure. Due to the high operating temperature the creep mechanism of the alloy is thought to rely on diffusional creep (Ashby & Jones 2005), this type of creep is dominated by Nabarro- Herring, and Coble creep (Cadek 1988). Nabarro-Herring creep relies on the diffusion of vacancies from the bulk of the material to the edge perpendicular to the applied stress, thus causing elongation of the grain. Coble creep occurs through diffusion of vacancies along the grain boundaries to the edge perpendicular to the applied stress. Both creep mechanisms rely on diffusion which is largely affected by the grain size within the alloy. Nabarro-Herring creep has a $\frac{1}{d^2}$ relationship and Coble creep has a $\frac{1}{d^3}$ relationship, where d is the diameter of the grain (Cadek 1988). To reduce diffusion creep a large grain size is beneficial due to its effect on reducing the creep rate, a high melting temperature compared with the operating temperature as the rate of diffusion is increased by T, and precipitates at grain boundaries to impede grain boundary sliding (Ashby & Jones 2005).

Figure 2.38 shows the goal for creep resistance for Nb-silicide based alloys which is less than 1 % creep in 125 h at 1200 °C and stresses above 170 MPa. This goal assumes alloy density of 7 g/cm^3. This goal has been achieved by Nb-silicides up to stresses of 200 MPa (Bewlay et al. 2003).
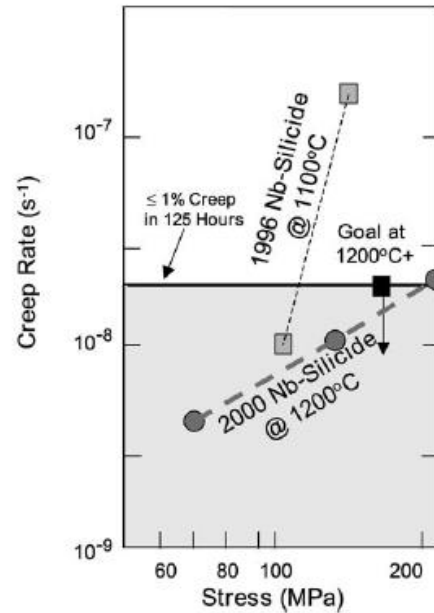
Figure 2.38 Creep rate against applied stress and the creep goal for Nb-silicide based alloys (Bewlay et al. 2003).

The creep mechanism in Nb-silicide based alloys (or Nb in situ composites) is dependent on the matrix phase. These materials can be formed with either Nb_5Si_3 particles in an Nb_{ss} matrix or Nb_{ss} particles in an Nb_5Si_3 matrix. Typically, binary Nb-Si composites have large Nb_{ss} particles distributed within an Nb_5Si_3 matrix. With increased alloying however the microstructure changes and tends towards brittle intermetallic phases such as Nb_5Si_3 and Laves forming within an Nb_{ss} matrix (Chan 2002b). The alloys to be studied in this project will likely consist of an Nb_5Si_3 phase with/without Laves phase distributed within a Nb_{ss} matrix, as this has been the case in previous work with a high number of alloying additions (Geng, Tsakiropoulos, et al. 2006b; Zelenitsas & Tsakiropoulos 2006b; Zelenitsas & Tsakiropoulos 2005; Geng, Tsakiropoulos, et al. 2006a; Zelenitsas & Tsakiropoulos 2006a; Geng & Tsakiropoulos 2007).

Figure 2.39 shows data for secondary creep rates reported by different groups referenced in (Chan 2002b). The data is compared with a solid solution alloy, pure Nb, Nb_5Si_3 and Nb-1.25Si, with Nb_5Si_3 having the lowest secondary creep rate and Nb and Nb-1.25Si having the highest. It can be seen that increased Nb_{ss} volume fraction gives an increase in creep rate. This was shown to be true in other creep studies (Bewlay et al. 2001). The wide variation in creep response is thought to be related to alloy composition, microstructure, or both (Chan 2002b).
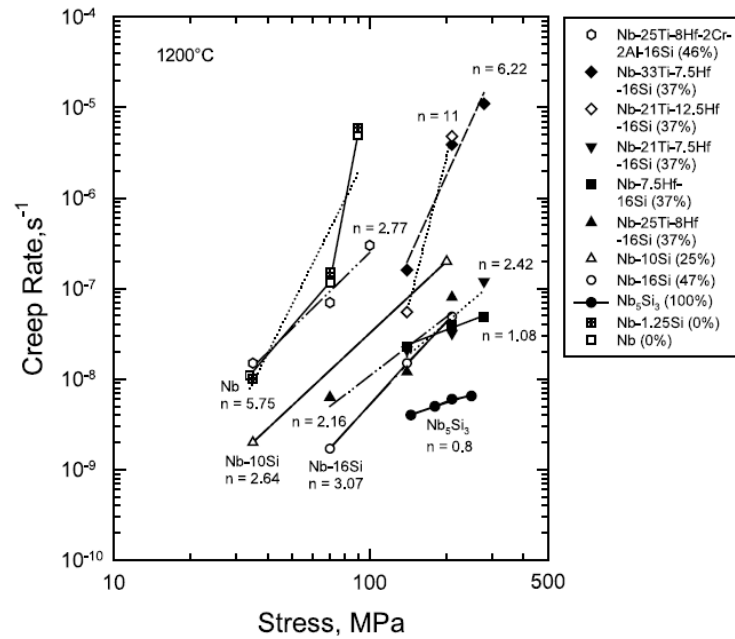
Figure 2.39 Plot of secondary creep rates at increasing stress for different Nb-silicide based alloys. (Chan 2002b).

Chan (Chan 2002b) suggested that the ability of Nb-silicide based alloys to resist creep can be tailored by changing the volume fraction of the silicide, where an increase in vol% silicide promotes a decrease in creep rate. He also suggested that the type of silicide present in the matrix affects the resistance to creep, with the silicide being either creeping or rigid. Nb_5Si_3 is a creeping silicide. The effect of a rigid silicide in a creeping matrix causes the alloy to take the creep exponent of the matrix. Creeping silicides in a creeping matrix however take on the creep exponent of the silicide and are therefore desirable (Chan 2002b).

Additions such as W and Mo give solid solution hardening to the Nb_{ss} phase, decrease the creep rate and increase the length of the secondary creep regime. Figure 2.40 shows a plot of minimum creep rate for directionally solidified Nb-18Si with varying content of Ti, Mo and W (mol%). With increased W and decreased Ti content the secondary creep rate was $<10^{-6} s^{-1}$ at 300 MPa and 1670 K. A decrease in W content was followed by an increase in creep rate. An increase in Mo content also had a positive effect on creep rate, however it was not as effective as W. This is due to Mo not being as strong a solid solution hardener as W (Sha, H. Hirai, et al. 2003).
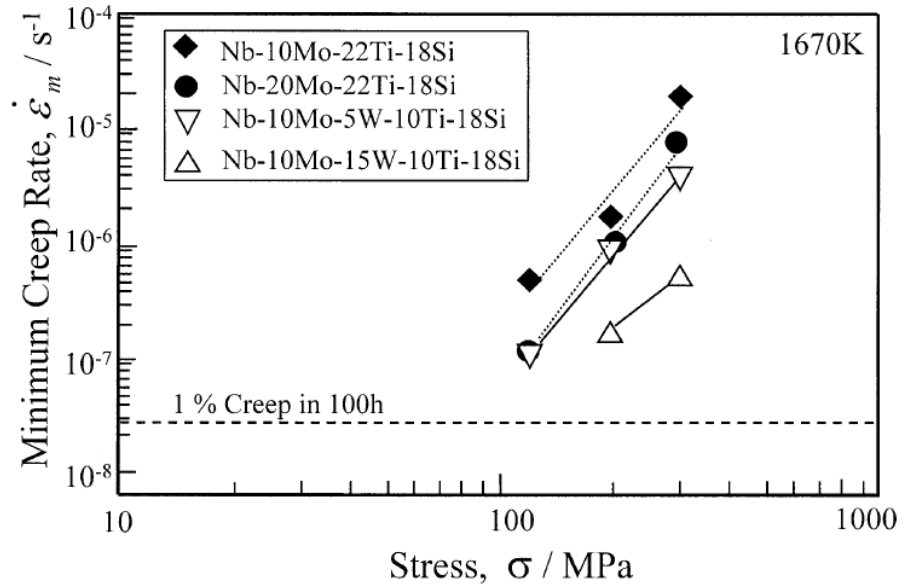
Figure 2.40 creep rate against Stress at 1670 K for Nb-18Si based alloys with varying Ti, Mo and W contents (Sha, H. Hirai, et al. 2003).

The creep rate can therefore be controlled in three main ways; controlling the microstructure, altering the silicide volume fraction and solid solution hardening of the Nb_{ss} phase.

Experimental

3.1   Introduction

Research has shown that alloying with Hf and Sn benefits oxidation resistance with (Geng, Tsakiropoulos & G. Shao 2007) or without (Zacharis 2013) RM (refractory metal) addition. A balance of properties was reported for the MASC alloy (Nb-23Ti-16Si-8Hf-2Al-2Cr-xSn (+ sp elements), however, references to this alloy seem to ignore the additions of Sn and other sp elements, for example Ge (Bewlay et al. 2003), which would suggest that the synergy of Hf and Sn with Al, Cr and Ti and other sp elements is beneficial. Data about the microstructure of MASC has been scarce, for example it is not clear whether the Nb_3Si is stable in its microstructure or what is/are the structure(s) of the Nb_5Si_3 (tetragonal and/or hexagonal given the high Hf concentration). Furthermore, to the author's knowledge there has been no study where the effect of Hf in synergy with Al, Cr, Si and Ti simultaneously but in the absence of other sp elements has been studied. The study of the latter via alloy JN1 (see below) became one of the focal points of the early stages of the research described in this thesis. Previous research on Nb silicide based alloys without Sn has shown that:

i.   Alloying with refractory metals (with/out Hf) (a) affects phase selection (i.e., the stability of Nb_3Si and Nb_5Si_3 and of the eutectics formed by these intermetallics with the Nb_{ss}) (Grammenos & Tsakiropoulos 2010b; Grammenos & Tsakiropoulos 2011), (b) affects the chemistry of the Nb_{ss} (solid solubility of Si, concentration of RM) (Grammenos & Tsakiropoulos 2010b; Grammenos & Tsakiropoulos 2011) and (c) improves significantly the creep of the alloys compared with MASC type alloys, (i.e. alloys with the same elements as in MASC but with different Al, Hf and Si contents and no Sn and sp elements) (Tsakiropoulos & Grammenos 2008).

ii.   The oxidation behaviour of such alloys is inferior compared with MASC (Tsakiropoulos & Vellios 2009).

iii.   The solid solubility of Si in the Nb_{ss} depends on the type of RM (= Mo, Ta, W) (Zelenitsas & Tsakiropoulos 2006a; Grammenos & Tsakiropoulos 2010b).

Furthermore, research on Nb silicide based alloys with Sn addition would suggest that the stability of the Nb_3Sn is important regarding the beneficial effects of Sn on oxidation and that Nb_3Sn formation depends on the concentration of Sn in the alloy. However, there has been no previous study about the stability of Nb_3Sn when Sn is in synergy with RM(s).

In the research described in this thesis, in addition to the alloy JN1, three alloys were designed to study the effects of the synergy of Hf and Sn on the microstructure of Nb silicide based alloys with refractory metal(s). This chapter describes the selection of the alloys and the experimental techniques used for the research. It should be noted that parallel to this work other projects in the research group studied the effects of the synergy of Hf with Sn and Ge and RMs (= Mo, Ta, W) on processability, phase stability and properties of alloys with $10 < Ti < 20$ at% and $18 < Si < 22$ at%.

3.2   Alloy selection

In the research described in this thesis four alloys were studied. The nominal compositions of these alloys are given in Table 3.1. The alloy JN1 was selected in order to understand how the addition of Hf to the base composition Nb-24Ti-18Si-5Al-5Cr affects phase selection and stability (see above). The composition of the base alloy was chosen by reviewing the effects of alloying additions on the properties of Nb alloys with/without Si. The Si was set at 18% to give optimum creep properties and ~60 vol% Nb_5Si_3 in binary Nb-18Si with good oxidation resistance.

The Al concentration was chosen as 5 at% as Al has a positive effect on the oxidation of the alloy, by destabilising the undesired Nb_3Si and stabilising the C14 $NbCr_2$ Laves phase (Zelenitsas & Tsakiropoulos 2005). The Al composition was limited to ≤5 at% to reduce the detrimental effect on the DBTT as 5 at% addition can change the DBTT from −200 to 100 °C (Chan 2002a), and to avoid the formation of the Nb_3Al phase.

The addition of Cr at 5 at% was made to allow the formation of the C14 Laves phase which is said to have a beneficial effect on oxidation resistance of the alloy (Zelenitsas & Tsakiropoulos 2005; D. Yao et al. 2009). The Cr addition was limited at 5

at% to reduce the effect on the DBTT and to limit the volume fraction of Laves phase formed to achieve a balance of creep and fracture properties.

Ti was set at 24 at% to keep the melting point above 1700 °C and avoid the formation of Ti_5Si_3 and the hexagonal γNb_5Si_3. Ti has beneficial effects on Nb silicide alloys by decreasing their density and increasing the fracture toughness of the Nb_{ss} phase. It also has a beneficial effect on the oxidation resistance of the $(Nb,Ti)_{ss}$ (Shyrokov & Rats'ka 2009) and the Nb_5Si_3 phases (Zelenitsas & Tsakiropoulos 2006b) due to the formation of TiO_2 and mixed Ti-Nb oxides. The Hf content was set at 5 at% to avoid the formation of Hf_5Si_3 and to avoid promoting the formation of the hexagonal γNb_5Si_3 phase.

There are no phase equilibria available for Nb-Si based systems with Sn (other than for the Nb-Si-Sn system, as was discussed briefly in chapter 2). The alloys JN2, JN3 and JN4 contained Sn and were designed on the basis on current knowledge about phase equilibria in ternary systems. The concentration of Sn was changed from 2 at% in the alloys JN2 and JN3 to 5 at% in the alloy JN4 in order to study the stability of the Nb_3Sn in their microstructures. The Nb_3Sn is isomorphous with Nb_3Al (A15 compounds) and the latter is undesirable in the microstructure of Nb silicide based alloys owing to its creep (inferior to Nb_5Si_3) and oxidation properties (pest oxidation). Thus, to avoid stabilisation of Nb_3Al in the presence of Sn it was decided to exclude Al in the alloys JN2, JN3 and JN4. This was expected to create a problem for oxidation which had to be counterbalanced by the other alloying additions.

The addition of Cr is known to benefit oxidation. The latter effect is attributed to the formation of the C14 $NbCr_2$ Laves phase, the effectiveness of which depends on its vol% in the microstructure that depends on the Cr concentration in the alloy and the other elements with which it is in synergy. However, increasing the Cr concentration has an adverse effect on alloy liquidus and toughness. It was anticipated that the adverse effect on the liquidus will be "balanced" by the additions of Mo and W. Thus, alloys JN2 and JN3 were designed to study the dependence of the stability of the microstructure and alloy properties on the synergy of Cr and Sn when the Cr/Sn ratio changes from 5 (in JN2) to 1 (in JN3) with Sn at the lowest end of the concentration range where it is expected to benefit oxidation. In these two alloys the concentrations of Si, Ti, Hf, Mo and W were not changed.

The addition of Ti is known to benefit oxidation and toughness and to reduce the alloy density. Increasing however the Ti concentration has an adverse effect on alloy liquidus, high temperature strength and creep. Previous research (Tsakiropoulos & Vellios 2009) had shown that the creep behaviour of MASC type alloys (without Sn and sp elements) falls well below the creep goal when Ti > 20 at% and acceptable oxidation was exhibited by simple alloys with 15 < Ti < 20 at%. Thus, in the alloys JN2 and JN3 the Ti content was kept at 15 at% and the effect of Ti on the alloy liquidus was expected to be counterbalanced by the addition of Mo and W. Mo and W benefit creep (Tsakiropoulos & Vellios 2009) but can be detrimental to oxidation even when Ti is present in the alloy at ~ 25 at% and without sp element additions (Tsakiropoulos & Vellios 2009). The design of the fourth alloy was influenced by the results for the alloys JN2 and JN3. It was decided to remove W (owing to processing difficulties and oxidation behaviour), to increase the Ti concentration to 20 at% and the Mo content to 6 at% and to increase the Si to 20 at% and the Sn to 5 at%. Hafnium was added to the alloys to scavenge oxygen in solution. Owing to the effect of the synergy of Hf with Cr and Sn on the stability of Nb_{ss} (Zacharis 2013) the concentration of Hf was kept at 2 at% in the alloys JN2 to JN4.

Table 3.1 Nominal compositions of JN1, JN2, JN3 and JN4 (at%)

Alloy	Nb	Si	Ti	Cr	Al	Hf	Mo	W	Sn
JN1	43	18	24	5	5	5	-	-	-
JN2	43	18	15	10	-	2	5	5	2
JN3	51	18	15	2	-	2	5	5	2
JN4	45	20	20	2	-	2	6	-	5

3.3   Ingot production

Button ingots of each alloy were produced using elemental charges of 10g weights. The elemental charges were placed in a water cooled copper crucible and the arc melter was pumped down to $1X10^{-5}$ torr. Pure Ar was then introduced to the system (20 torr) and a

high electrical current was used to form an arc between a moveable non-consumable tungsten electrode and the crucible which is then moved over the charge in order to melt it. The sample was allowed to cool and was then flipped and re-melted at least 4 times to achieve homogenisation. The melting of the charge was difficult when using solid W. The nature of this melting technique led to the ingot having a fast cooled bottom section, in contact with the water cooled copper hearth, while the top and bulk of the ingot cooled slower.

3.4   Sample preparation

In order to characterise each alloy the ingots were sectioned and specimens were prepared for heat treatment, microstructural characterisation, oxidation and mechanical testing.

3.4.1   Heat treatment

Each alloy was heat treated in a tube furnace, the specimens were wrapped in Ta foil and heat treated for 100 hours at 1500 °C under flowing argon after which they were furnace cooled. The argon is gettered by Ti sponge that was placed in an alumina crucible at the entrance of the furnace. It should be noted that owing to the sluggish kinetics in Nb silicide based alloys, heat treatments are usually done at 1500 °C for at least 100 h or at 1600 °C for 20 or 40 h. The latter option was not available to this author because of the range of heat treatment facilities available in the Department. The purpose of these heat treatments was to homogenise the microstructures as there was partitioning of solutes in the Nb_{ss} and intermetallic phases and encourage phase transformations of the Nb_3Si if present in the cast alloy. The heat treatment temperature is below the eutectoid transformation of Nb_3Si in the Nb-Si binary, see section 2.1.1 and βNb_5Si_3 and precipitation of other phases (Zelenitsas & Tsakiropoulos 2005).

3.4.2   Sample Polishing (EDS/WDS/Nano indentation/XRD/oxidation)

Samples for EDS, WDS and nano indentation are prepared in the same fashion, Cross sections of the ingot, either as-cast (AC) or heat-treated (HT), were hot mounted in sizes of 32 mm or 25 mm using conductive Bakelite (depending on the size of the specimen holder). They are then ground using increasing grit SiC papers (120, 240, 400, 800, 1200, 4000 grit) on a circular grinding wheel using running water for cooling, lubrication and debris removal. Once a 4000 grit finish had been achieved, the samples were then polished to a 1 μm finish using a water based diamond suspension on a woven cotton cloth.

Sample preparation for nano indentation was slightly different owing to the need to image the sample using atomic force microscopy (AFM) without etching. For this to be possible the sample had to be relief polished so that the soft phase will wear away more than the hard phase, leaving a discernible height difference between the two phases. This was achieved by polishing the sample with 6 μm diamond suspension (after following the grinding procedure described above) for an extended period of time, before finishing with the 1 μm diamond suspension.

For XRD no more than a 1200 grit finish was required for the sample and it wasn't necessary to mount the sample in Bakelite. Oxidation samples prepared for TGA are first cut into cubes slightly larger than the required size $\approx$ 4 mm^3 and then ground down to approximately 3 mm^3 to a 1200 grit finish, the side lengths are then measured using a Polyvar light microscope to calculate the surface area.

3.4.3   Powder preparation for X-ray diffraction

Powder XRD allows, the texture effect caused by directionality in the AC ingot to be eliminated. For the as-cast and heat treated samples the STOE STADI P (Cu, PSD) was used and data was collected using Win XPOW, analysis was done using Sieve +.

To prepare a sample for Powder XRD, a solid sample was crushed and then ground to a fine powder. Firstly a small section taken from the bulk of the ingot was crushed using an impact mortar until it was small enough to be ground by hand. Once it

had been crushed the ingot was then ground into a fine powder using a marble pestle and mortar until the latter reaches the consistency of icing sugar. This method unavoidably introduced small amounts of mechanical strain in the powder.

The powder was then mounted according to the XRD equipment specifications; in this case it was adhered to an acetate disk using Elmer's glue and then dried using a hot air gun. The acetate disk is then placed in a circular sample holder and loaded into the equipment sample holder. The correct amount of powder that is applied to the disk can only be calculated through trial and error. Firstly the specimen is prepared and then a quick diffraction pattern was collected at lower Kv and mA (30 Kv, 10mA), with and without the sample. If the ratio between the two was between 1.2 and 1.6 the specimen is prepared adequately and can be run for a full length test at 40Kv and 35 mA. If the specimen is too thin or too thick the diffraction patterns will be low as there will be either too little material for diffraction or not enough X-Rays will be able to pass through. Before running the final test a Silicon standard was used to check the accuracy of the equipment.

For the Oxide scale from the 1200 °C samples, the STOE STADI P (Cu, IP) was used to collect the diffractogram. The method is the same as described above however the detector collects data from 8 different ranges and these are combined to give a final peak file.

3.4.4   Sample preparation for fracture toughness evaluation

For fracture toughness, large 600 g ingots were prepared in an arc melter so that samples big enough for fracture toughness could be cut. Bars 6 X 3 X 45 mm^3 were cut from the centre of each respective ingot perpendicular to the cooling direction using electro discharge machining (EDM) (Ideally the bars would be parallel to the cooling direction so that the fracture would occur perpendicularly rather than, in this case, parallel to the direction of the grain). A notch was then cut into the width of the bar to 0.5 X the width i.e. ≈3 mm with a root tip radius of 0.2 mm. The samples were not fatigue cracked as the specimens were of limited number, there was therefore no room for trial and error. Thus a K_Q value was obtained for the alloys as a true K_{Ic} value could

not be obtained. A representative sample was mounted in conductive Bakelite and prepared as described previously for SEM and images of the longitudinal cracks were taken in an SEM.

3.5   Scanning Electron Microscopy (SEM)

SEM is one of the most useful analytical techniques to be used in this project as it can give secondary electron (SEI) and backscattered electron (BSI) images of the alloys, the equipment used to obtain images during this study can be found in section 3.6. Secondary electron imaging SEI was used to get topographical information about the sample surface and works based on the amount of sample "surface" within the interaction volume of the electron beam. Raised areas have a greater volume within the interaction volume and as such produce a higher number of emitted secondary electrons thus causing a bright contrast. Recessed areas such as pores have the opposite effect and produce a dark contrast as less secondary electrons are emitted.

BSE imaging gives an image of the sample surface with regards to the atomic number of the atoms being imaged. Heavier atoms have a higher contrast as they produce a higher density of backscattered electrons whereas lighter atoms appear darker. This technique was used to produce an image of the sample surface which varies in contrast depending on the atomic weight of the phases present. This atomic weight dependant contrast allowed an image of the alloy microstructure to be produced, where different phases with different atomic weights appear as different shades of grey, thus showing the microstructure.

3.6   Energy dispersive X-ray spectroscopy (EDS) and wavelength dispersive analysis (WDS)

EDS and WDS are both useful microanalysis techniques for the characterisation of phases within an alloy determining the composition of the alloy in a given condition. Both of these quantitative techniques use the characteristic X-rays given off by atoms as high energy electrons drop into the space left by low energy electrons that are excited out of the atom by the incident electron beam.

EDS uses the energy of the characteristic X-rays given off by different atoms to determine the element from which it emanated. This technique gathers X-ray energies across the entire range produced by the elements within the sample and therefore, if elements have peaks at similar energy levels, then they cannot be resolved. Light elements are also a cause of problems (Z<Na) as the characteristic energy peaks given off are too small to analyse. It is possible to analyse for O_2 by stoichiometry, but due to the large array of oxides present in the oxidised alloys it is not possible to know the exact stoichiometry of the phases formed.

WDS works on the same principle as EDS using the characteristic X-rays produced during electron bombardment. Rather that determining the composition using the energy levels, the specific wavelength of the X-ray is used to determine the generating atom. This is done using analytical crystals which can be used to allow only the specified wavelengths through to the X-ray detector. The benefit of this is the high resolution and the ability to pick up trace elements and allow for the analysis of oxygen.

For The EDS large area analysis a Phillips PSEM 500 SEM was used to analyse the specimen, with an accelerating voltage of 25 Kv, the spot size was adjusted to alter the dead-time of the microscope and the data was collected at a magnification of 320x.

For WDS analysis a JEOL JXA-8230 SUPERPROBE was used with a working distance of 11.1 mm, an accelerating voltage of 20 Kv and a probe current of 30 nA, this was used to gather both point analysis and X-ray maps (EDS).

Maps were also taken using the Phillips XL30 FEG/SEM, at a working distance of 11 mm and an accelerating voltage of 20 Kv and a spot size of 5, the analysis was done using a Bruker EDX system.

3.7   Bulk and powder XRD analysis

XRD was used for the analysis of bulk alloys in the AC and HT conditions to give a peak profile so that different phases could be matched with the XRD data in PDF cards of the relevant crystal structures. XRD using glancing angle and normal (Bragg–Brentano) scanning is based on Bragg's law, $n\lambda = 2d \sin\theta$, where n is an integer, λ is the X-ray wavelength, d is the lattice spacing and θ is the incident angle of the X-ray

and the scattering planes. The intensity of the peaks produced is proportional to the amount of X-rays diffracted into the detector. The position of these peaks on the 2θ axis is related to the lattice d spacing of the crystals being analysed. Complications arise when changes in the lattice parameters and texture effects cause changes to peak shape (width and height) and position. In respect to the alloys of this study the microsegregation in both Nb_5Si_3 and Nb_{ss} causes peak broadening as varying compositions increase or decrease the lattice parameters slightly creating a broadened peak rather than it being sharp and well defined. The substitution of different elements in a crystal also has the effect of shifting the characteristic peaks to higher (lattice expansion) or lower (lattice contraction) 2θ values than that of the pure crystal.

Texture effects i.e. directionality caused by cooling have an effect on the peak intensities. Each characteristic peak corresponds to a certain crystal orientation and the preferential growth direction of a crystal means some peaks have a greater intensity, as more lattice planes are scattering at this angle than others. The addition of heavier elements to the crystal lattice also has an effect on the peak intensity as they cause more scattering.

To avoid the effect of texture in the characterisation of the microstructure of the bulk samples, powder samples were prepared so that they can be analysed using transmission XRD. The advantage of this technique is that the resulting peak profiles can be processed and matched using Rietveld analysis which compensates for changes in 2θ shifts and peak broadening due to lattice substitution. This technique, unlike the Le Bail method, does rely on the peak height ratios being maintained which is why the removal of texture effects is important.

3.8   Rietveld analysis

Rietveld analysis is a least squares refinement which uses the profile intensities to extract data from a peak profile (Rietveld 1969)(Rietveld 1967). The technique was originally developed to extract data from neutron diffraction experiments however, it can also be applied for use in XRD. The refinement alters the Gaussian (peak width, asymmetry) and the Lorentzian (peak tails) shape of the profile parameters which have been chosen to match the unknown peak profile. In the case of our alloys the refinement

alters the peak width and 2θ position, along with the peak height (moving all peak heights the same amount) of the Nb_{ss} and Nb_5Si_3 profile parameters. To complete the Rietveld analysis GSAS was used along with the graphical interface EXPGUI to analyse powder profiles. Profile parameter files (.CIF) were obtained for Nb_{ss}, and α, β and γ Nb_5Si_3 from the ICSD website. By altering the peak parameters for the chosen peak files it is possible to align these files with the peaks achieved with powder XRD.

3.9   Thermogravimetric analysis (TGA)

Thermogravimetric analysis is the use of accurate scales to measure the weight loss (or gain) due to the oxidation of an alloy under controlled conditions. Before a sample was oxidised, its dimensions were first measured (in this research a Polyvar light microscope was used) to calculate its surface area. The sample was placed in an alumina crucible and heated to 800 or 1200 °C at 3 °C/min in air. The sample was then held at temperature for 100 h before cooling back to room temperature at 3 °C /min. The slow cooling rate was used to avoid the rapid contraction of the sample and the resulting spallation of any oxide layer formed. The equipment used in these experiments was a Netzsch STA 449 F3 JUPITER and the data was analysed using Pyris software. After oxidation an image of the oxidised sample was taken before further analysis was performed.

The weight change data was normalised, it was then divided by the surface area to give a value of g/cm^2, and the weight change with respect to area was plotted against time in seconds. From this plot the oxidation rate constant was calculated for linear or parabolic oxidation. The K_p or K_l value that had the best R^2 value was deemed the best fit and determined whether the oxidation was linear (K_L) or parabolic (K_P).

3.10 Nano indentation

Due to the fine microstructure present in the alloys of this study, nano indentation was used to get the hardness of individual phases in the HT samples. A Hysitron Triboscope

nanomechanical test instrument attached to a vico dimension 3100 atomic force microscope was used for the analysis. Serpentine runs, typically 8X8 were run in areas of the bulk of the alloy with the least porosity using a 4000 μN load the nature of the serpentine runs meant data could be collected fast and efficiently. However some indentions were on the edge of phases, or in pores which gave erroneous results. The values were sorted to remove erroneous data, firstly they were matched with the respective phases and set into two groups, namely data for Nb_{ss} and Nb_5Si_3. The two columns of data were then refined and data points which lay on the edge of phases were removed. The modulus of the two phases was estimated using the nano-indentation data and Equation 1:

Equation 1

$$E_s = \frac{E_r \times E_i \left(1 - v_s^2\right)}{E_i - E_r \left(1 - v_i^2\right)}$$

Where E_r is the reduced modulus (data from indenter), E_s is the elastic modulus, E_i and v_i are indenter parameters and v_s is the Poisons ratio of the respective phase being analysed, as described in the seminal paper by Oliver and Pharr (Oliver & Pharr 1992). The values $E_i = 1140$ GPa and $vi = 0.07$ were used for the Berkovitch indenter and $v_s = 0.38$ and 0.27 for Nb_{ss} and Nb_5Si_3 respectively. As described in the seminal paper by Oliver and Pharr (Oliver & Pharr 1992). In alloys with more than two phases it is impossible to differentiate between the Nb_5Si_3 and the Laves phase. The Laves phase was typically found in small volumes at the edge of silicide grains. The data points in these areas were not considered in order to reduce the error caused by analysing the wrong phase.

3.11 Fracture toughness

The fracture toughness of the alloys was measured using a Zwick Roell model: BT2-FR050TH machine with a 5KN load cell and a 3 point bend rig. Specimens were prepared to conform with U.S. (ASTM 2013) and British standards (Anon 2010), to get K_Q values, see section 3.4.4. Specimen dimensions were based on previous work done in the field, in agreement with the afore mentioned standards, as was the decision not to

pre crack the samples (Subramanian 1997; Kimura et al. 2005; Kim et al. 2004; Soboyejo et al. 1999; Kim & Tanaka 2002; Sha, H. Hirai, et al. 2003). Specimens with dimensions $\approx$ 6 x 3 x 45 mm^3 were cut using electro discharge machining (EDM) and these samples were notched at the centre to half the width (3mm) also using EDM to a notch root diameter of 0.2mm. These samples were then placed in the 3 point bend rig with a span 0f 40 mm and load was applied until failure. The F_Q data gained from the test was then applied to Equation 2 and Equation 3, to get the K_Q value.

Equation 2
$$K_Q = F_Q \frac{S}{BW^{3/2}} f(a/W)$$

Equation 3

$$f(a/W) = 3(a/W)^{1/2} \times \frac{1.99 - (a/W)(1 - a/W)[2.15 - 3.93(a/W) + 2.7(a/W)^2]}{2(1 + 2\,a/W)(1 - a/W)^{3/2}}$$

Where:

- K_Q= provisional fracture toughness (MPa·m^2)
- F_Q= Force (kN)
- S= Span between outer loading points (mm)
- B= Specimen thickness (mm)
- W= Width of specimen (mm)
- a = crack length (mm)

After the test was completed the samples were mounted and polished, BSE images were then taken to show the crack propagation path.

3.12 Density Measurements

Density measurements were completed using a Mettler Toledo NewClassic MF set of density scales. This method is based on the Archimedes principle, which states an object immersed in water is buoyed up by a force equal to the weight of the water it displaces. With the density of the water known through a range of temperatures (buoyancy varies

with water temperature) the density of the object can be found. Equation 4 was used for the density calculation where ρ is the density of the sample, $W_{(a)}$ is the weight of the sample in air, $\rho_{(L)}$ is the density of the water and $W_{(L)}$ is the weight of the sample in water.

Equation 4

$$\rho = \frac{W_{(a)} \cdot \rho_{(L)}}{W_{(a)} - W_{(L)}}$$

This equation does not include the errors caused by several factors, most notably:

1) The formation of bubbles on the surface of the sample that is being analysed
2) Air buoyancy during weighing in air
3) A change in depth of immersion of the pan hanger assembly
4) The dependency of the buoyancy of water on temperature
5) Adhesion of water to the suspension wire of the pan hanger assembly

Smooth pieces of the alloy were weighed to avoid the formation of bubbles on the outside of the sample. A correction factor was also added automatically within the equipment's built in software to counter the effect of air buoyancy.

3.13 Volume fraction measurements

Volume fractions were calculated using image j software and BSE images. The contrast of the images was first altered to make the difference between the dark (Nb_5Si_3) and light (Nb_{ss}) phases more distinguished. The image was then made into a binary and a threshold was set so that all the Nb_5Si_3 was marked, the area being analysed was then selected with a box. After the area for analysis had been selected it could be measured, this provided the area fraction of the phases in that area. This method was repeated for a minimum of 5 images to calculate an average value.

As-cast Microstructures: Results and Discussion

Understanding the microstructure of alloys is a crucial step in the identification of phases present in the alloys, the alloying effects on the stabilities of these phases, the solidification paths and for tracking the changes caused by different alloying additions. The following chapter will be a comparative study of the alloys of this research; giving a detailed progression through the changes that were influenced by varying alloying additions, and the resulting microstructural effects that followed.

Table 4.1 shows the volume fractions and densities of the phases present in this study. Laves phase containing alloys show a notable decrease in Nb_{ss} volume fraction and the densities are comparable to the amount of RM added to the respective alloy.

Table 4.1 Volume fraction and densities of alloys

Alloy	Fraction of phase (%)			Density (g/cm^3)
	Nb_{ss}	Nb_5Si_3	$NbCr_2$	
JN1-AC	42	58	-	6.9
JN1-HT	42	58	-	
JN2-AC	40	55	5	7.6
JN2-HT	39	61	-	
JN3-AC	51	49	-	7.5
JN3-HT	50	50	-	
JN4-AC	44	56	-	7.1
JN4-HT	47	53	-	
AC:As-Cast, HT: Heat Treated				

4.1   Alloy Nb-18Si-24Ti-5Cr-5Al-5Hf (JN1-AC)

The alloy JN1 was developed to bridge the knowledge gap between the alloys KZ5 of nominal composition Nb-18Si-24Ti-5Cr-5Al (Zelenitsas & Tsakiropoulos 2005; Zelenitsas & Tsakiropoulos 2006b; Zelenitsas & Tsakiropoulos 2006a) and JG4 of nominal composition Nb-18Si-24Ti-5Cr-5Al-5Hf-2Mo (Geng, Tsakiropoulos & G Shao 2007; Geng, Tsakiropoulos, et al. 2006a) as an alloy (with Hf, without Mo or another 5d

of sp element addition) had not been investigated. The bulk microstructures of the alloy KZ5 and JG4 can be seen in Figure 4.1, both alloys had complex microstructures with the presence of Nb_{ss}, Nb_5Si_3 and $NbCr_2$ Laves phase. The most notable difference between them was the presence of Hf rich Nb_5Si_3 in the Hf containing alloy JG4, The segregation of Nb_{ss} is clear in KZ5.
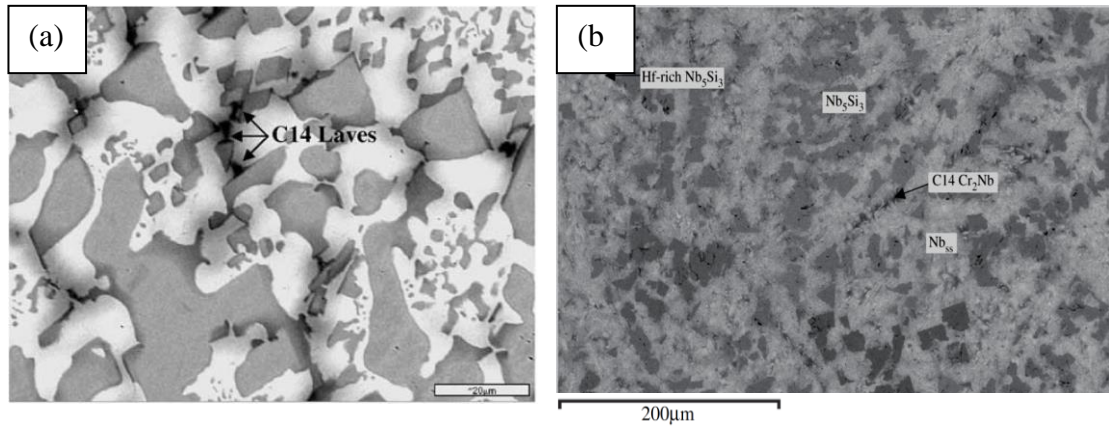
Figure 4.1 images from the bulk of KZ5(a) (Zelenitsas & Tsakiropoulos 2005) and JG4 (b) (Geng, Tsakiropoulos & G Shao 2007) AC

Table 4.2 gives the large area EDS analysis results. The EDS analysis was obtained at 320X magnification from the top, bulk and bottom. An average was calculated using at least 5 analyses, taken from these areas. All analyses showed the composition to be within 0.5 at% of the nominal composition except for Si and through balance Nb. This would be attributed to the EDS analysis used for Si, as a difference of roughly 2 at% has been observed by other students in this group when using both EDS and WDS analyses for similar Nb-Si based alloys. There were however notable differences between the Si concentration in the top and the bottom of the button ingot locations to Si macrosegregation with $C_{max}^{Si} - C_{min}^{Si} \approx 4.1\ at\%$.

Table 4.2 EDS large area analysis of JN1-AC (at%)

Area in ingot	Nb	Si	Ti	Cr	Al	Hf
Top	40.7±0.2	20.9±0.6	23.5±0.5	4.5±0.2	5.3±0.2	5.1±0.1
	40.4-40.8	20.1-21.7	22.6-24	4.2-4.7	5.0-5.6	5.0-5.3
Bulk	40.9±0.4	20.3±1.0	23.7±0.5	4.6±0.3	5.4±0.2	5.1±0.1
	40.4-41.4	19-21.7	23-24.1	4.2-5.0	5.2-5.7	5.0-5.3
Bottom	41.4±0.5	19.6±1.0	23.5±0.6	4.4±0.3	5.7±0.1	5.4±0.2
	40.8-42.4	17.7-21	22.7-24.5	4.0-4.9	5.5-5.9	5.2-5.6
Average composition	41.2±0.6	20.1±1.0	23.5±0.5	4.5±0.3	5.5±0.2	5.2±0.2
	40.4-42.4	17.7-21.7	22.6-24.5	4.0-5.0	5.0-5.9	5.0-5.6

Figure 4.2 shows the microstructures at 250X and 1200X magnification of the top, bulk and bottom of the alloy JN1 AC. There was a difference in the scale of the microstructure, which was finer at the bottom and in the directionality, which was more defined at the top, furthermore there was no eutectic in the bottom. In all three areas the partitioning of Hf made the identification of phases extremely difficult, in particular the Nb_{ss}.

In the bottom of the button ingot the microstructure was fine and consisted of mostly closely spaced Nb_5Si_3 grains, surrounded by Hf rich Nb_5Si_3 and Nb_{ss}. Some boundaries of Nb_5Si_3 exhibited dark contrast areas that were attributed to the segregation of Ti.

In the bulk of the alloy the bulkier Nb_5Si_3 seemed to be randomly oriented in the microstructure and the interdendritic regions between the silicide grains were larger when compared with the top. In the interdendritic regions the formation of eutectic was observed; the constituent phases also appeared to have an acceptable degree of microsegregation. This was attributed to the slower cooling rate that allowed more time for the partitioning of Hf to occur, leading to microsegregation. The overall architecture of the microstructure in this part was similar to that of JG4, see Figure 4.1.

The top of the ingot displayed more directionality of the Nb_5Si_3 than the bulk. There was visibly less microsegregation in the Nb_{ss}, and the Nb_5Si_3 grains were smaller and more closely spaced than the bulk. There was less eutectic in the interdendritic regions.
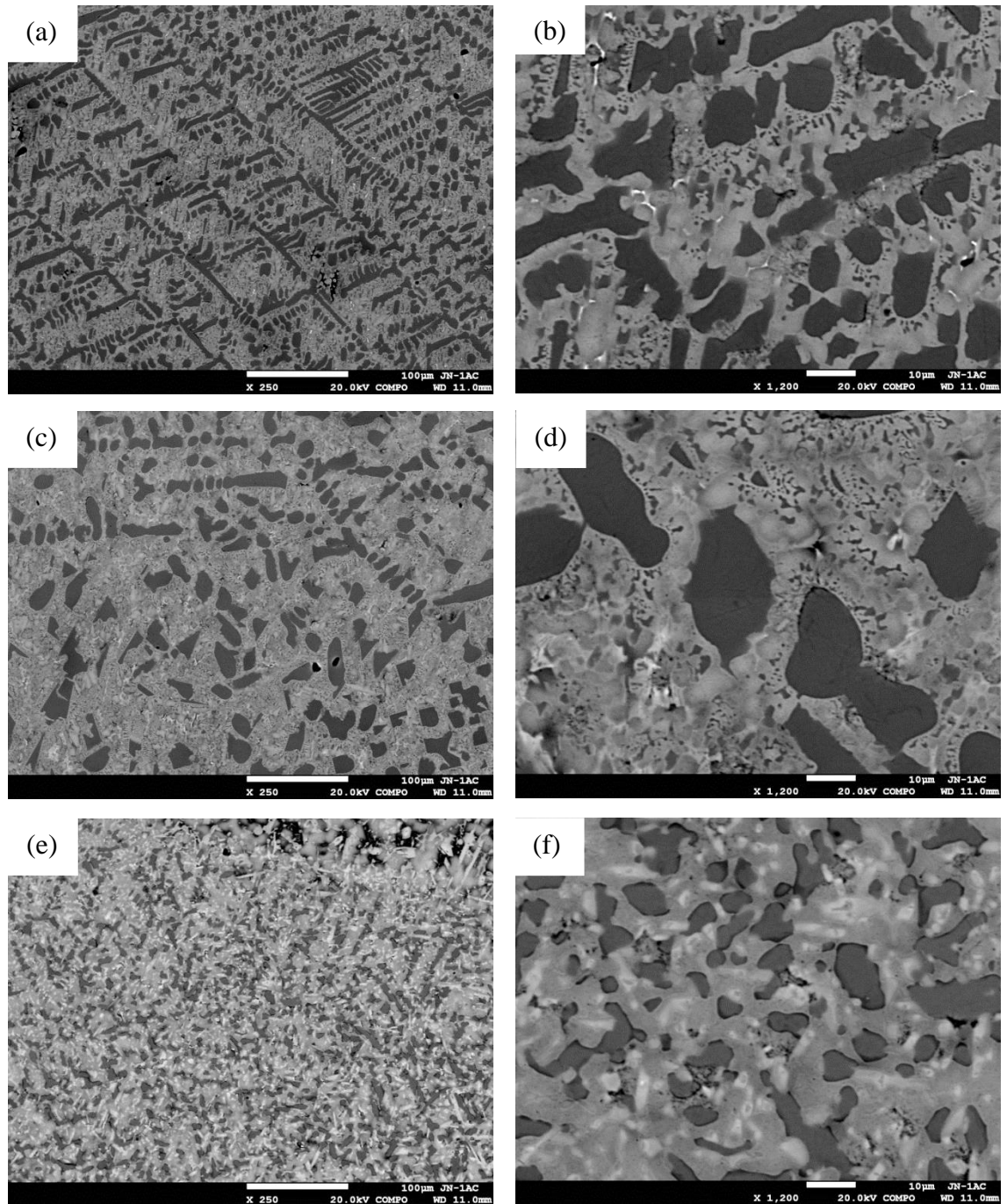
Figure 4.2 BSE at 250 X and 1200 X magnification of the top (a, b), bulk (c, d) and bottom (e, f) of JN1 AC

Figure 4.3 shows X-ray maps of the Bulk of JN1-AC. This qualitative method is one of the only methods to distinguish between the Hf –rich Nb_5Si_3 and Nb_{ss}. The red areas have a higher concentration of the analysed element, and in the blue areas there is little or none of the analysed element. Elemental maps were used to assist with the

characterisation of the microstructure, owing to the complication of the contrast of the phases due to the partitioning of Hf. The technique is very useful to determine the different areas of microsegregation of elements (Si) which is not easy to identify in a simple BSE image e.g. when an element of high Z number, such as Hf, partitions between all the phases present.

The Si and Nb maps clearly show the silicide grains and the Hf rich regions align with the low Nb, high Si regions indicating the Hf rich Nb_5Si_3. The Hf rich Nb_5Si_3 regions were found in the interdendritic spaces between the Nb_5Si_3 grains and the Nb_{ss}. The Ti and Cr rich regions corresponded with the Hf rich regions as both elements partition to regions which are rich in Hf. Al does appear to have a higher solubility in the Nb_{ss} as opposed to the Nb_5Si_3. The Cr map shows no convincing evidence of the presence of the C14 Laves phase. With the exception of one area which was also rich in Ti. Thus it was not possible to confirm the presence of Laves phase in JN1-AC on the basis of the X-ray maps.
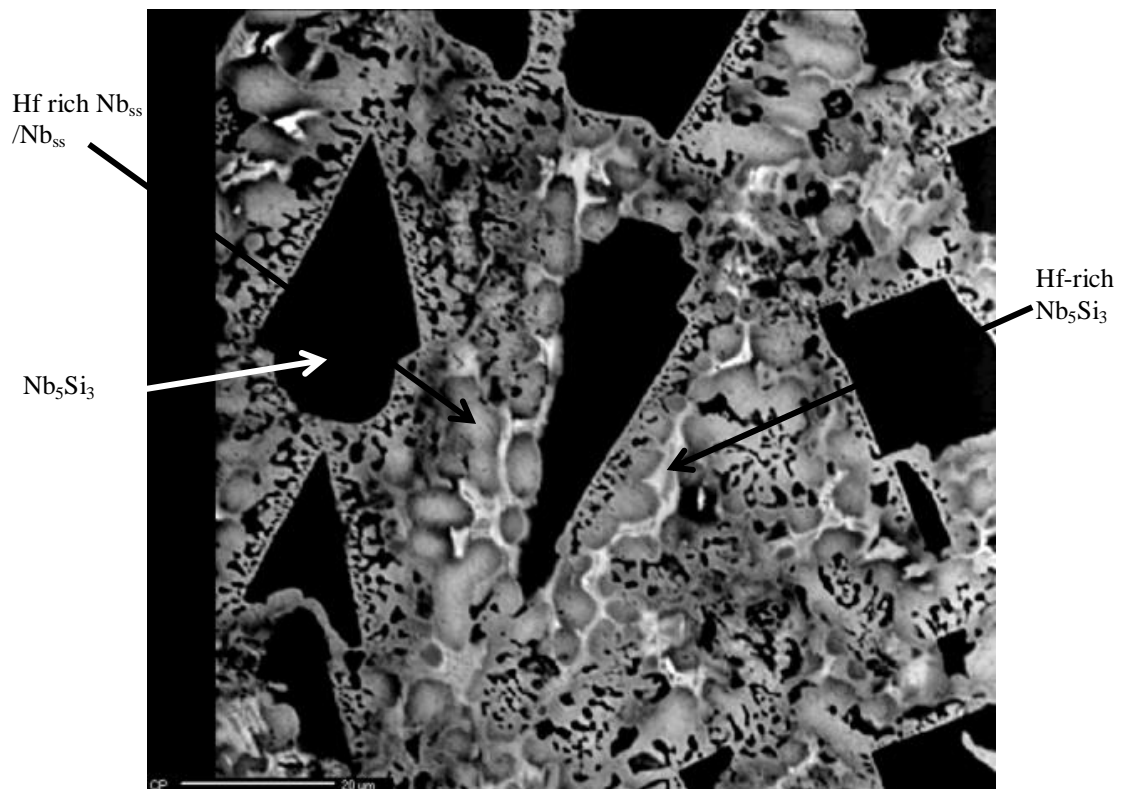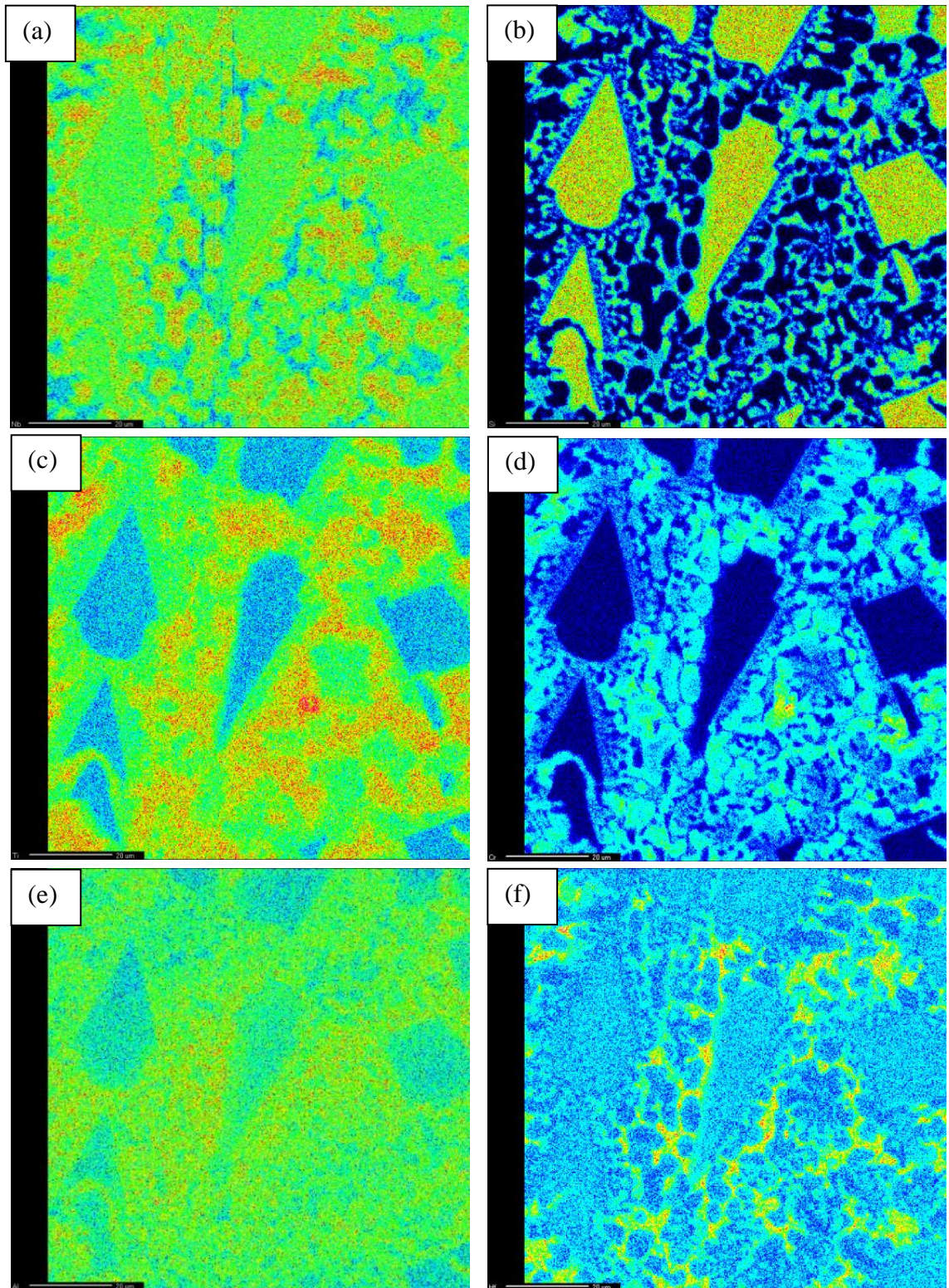
Figure 4.3 BSE image of JN1 AC bulk and X-ray maps for Nb (a), Si (b), Ti (c), Cr (d), Al (e) and Hf (f)

The microstructure of the alloy JN1-AC was characterised using both XRD and Rietveld analysis. Figure 4.4 shows the X-ray diffractogram produced by Rietveld analysis; the red and black markers under the graph represent the βNb_5Si_3, which has the W_3Si_3-type $D8_m$ structure (Geng, Shao, et al. 2006; Bewlay et al. 2004) and the Nb_{ss} respectively. The purple line represents the goodness of fit with peaks representing deviations between the fitted standard profile and the sample profile, with bigger peaks representing a larger mismatch. The majority of the mismatch lies in the first $\approx 25\%$ of the data meaning the largest portion of the data is fitted with a large degree of accuracy, the overall peak profile has a chi^2 value of 1.73.
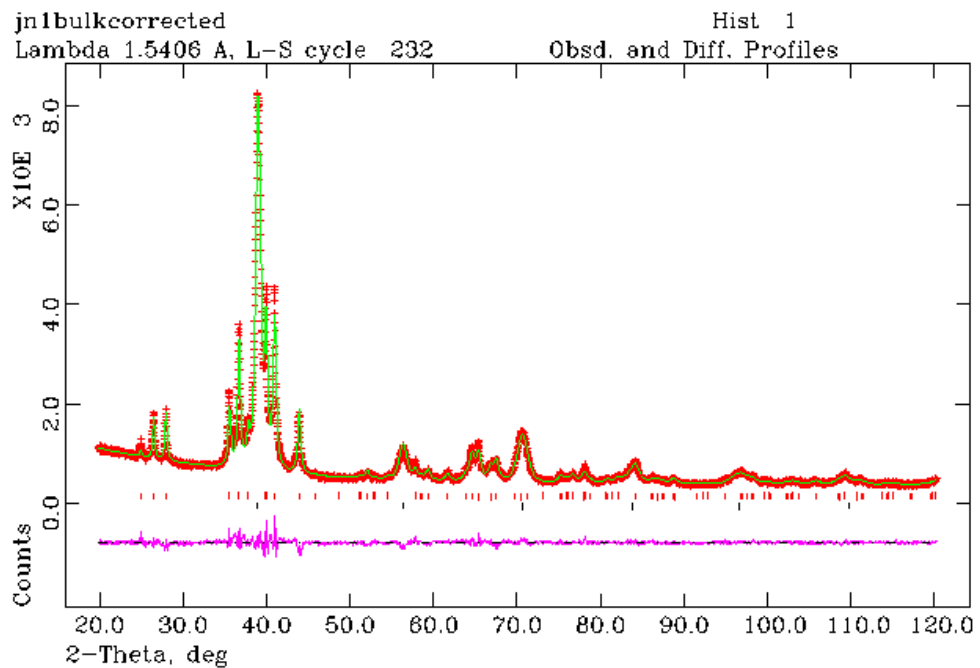
Figure 4.4 Rietveld analysis of JN1-AC The green line is the original pattern, the red markers are the fitted pattern and the purple line is the goodness of fit. The tick marks under the graph represent the Nb_{ss} and the Nb_5Si_3 phases in black and red respectively.

For comparative reasons the powder pattern was also fitted using the Sieve+ software to ensure similar results were achieved. This is important as none of the other alloys were characterised using Rietveld analysis as they were too complex and the chi^2 values were very large. Figure 4.5 shows the same powder pattern as Figure 4.4 however the pattern was indexed using the Sieve+ software. It can be seen by comparison that a good match between the two patterns was achieved, with the main phases being indexed as Nb_{ss} and

βNb$_5$Si$_3$; this gave good confidence for the use of sieve+ software to analyse the diffractograms of the other alloys.
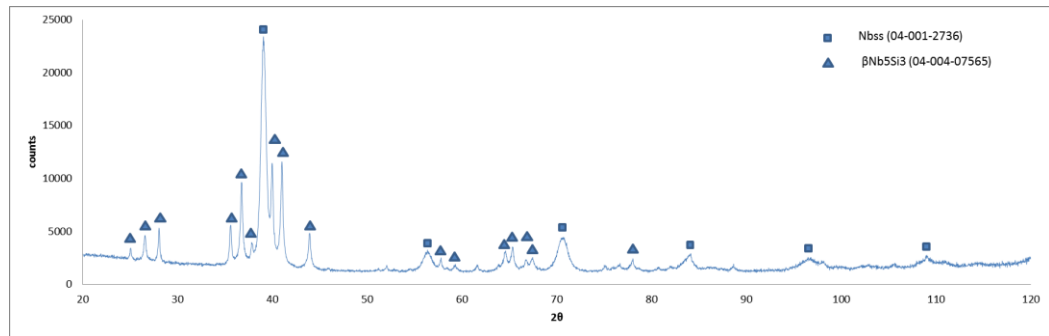
Figure 4.5 JN1-AC powder X-ray diffractogram analysis using Sieve+

Using the peak data obtained from the powdered sample it was also possible to calculate the lattice parameter of the Nb$_{ss}$ phase using a Nelson Riley plot.

The value for "a" was calculated from Equation 5, where H, K and L are miller indices and d is the d spacing of the peak.

The value of d was calculated from Equation 6 where n is an integer, λ is the wavelength of the incident wave and θ is the angle between the incident ray and the scattering planes.

The value for f(θ) was calculated using Equation 7 where f(θ) is the error function, and θ is the angle between the incident ray and the scattering planes.

The calculated lattice parameter values for JN1-AC can be seen in Table 4.3 These were used to create the Nelson-Riley plot. The Nelson Riley plot can be seen in Figure 4.6

Table 4.3 The calculated lattice parameter of the BCC Nb$_{ss}$ in JN1-AC

	d (Å)	2 θ	theta	a (Å)	f (θ)	hkl	Corrected a (Å)
JN1 ac	2.305	39.04	19.52	3.260	2.704168	110	
	1.633	56.28	28.14	3.266	1.676321	200	
	1.333	70.62	35.31	3.264	1.170963	211	3.270
	1.151	84	42	3.256	0.838495	220	
	1.032	96.54	48.27	3.264	0.602851	310	
	0.947	108.94	54.47	3.279	0.421175	222	
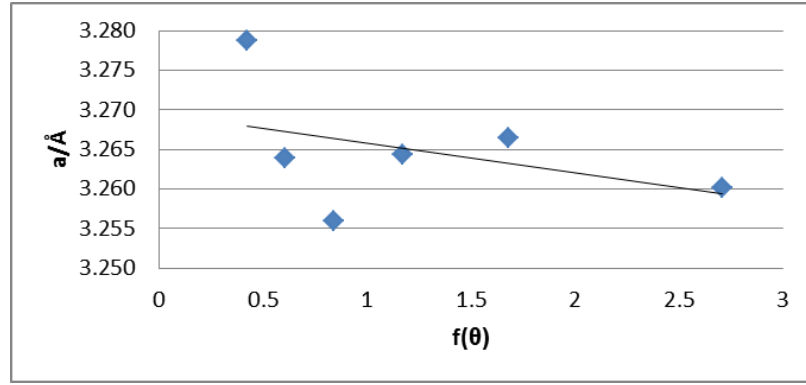
Figure 4.6 Nelson-Riley plot for the lattice parameter of the bcc Nb_{ss} in JN1-AC

The value for "a" was extrapolated from the Nelson Riley plot; the lattice parameter of Nb_{ss} in JN1 AC "a" is 3.27 Å. The lattice parameter of pure Nb_{ss} is 3.303 Å; indicating a contraction of the lattice parameter by 0.033 Å. This contraction is due to the presence of elements with small atomic radii within the Nb_{ss}; in this case Ti, Si, Cr, Al and Hf have atomic radii of 1.47, 1.17, 1.30, 1.43and 1.59 Å (Gale & Totemeier 2003) respectively. The effect of covalent bonding also has a large effect on reducing the lattice parameter (Kim et al. 2004).

Equation 5

$$a = d\sqrt{H^2 + K^2 + L^2}$$

Equation 6

$$n\lambda = 2d \sin\theta$$

Equation 7

$$f(\theta) = \frac{\cos\theta \cos\theta}{\sin\theta} + \frac{\cos\theta \cos\theta}{\theta}$$

Phase analysis of the phases present in JN1 AC was performed using WDS in EPMA to determine the chemical composition and the effects of alloying on solute partitioning. The XRD had suggested the presence of Nb_{ss} and βNb_5Si_3 in the alloy. Table 4.4 shows the phase analysis data that confirmed the presence of Nb_{ss} and Nb_5Si_3, and the partitioning of Hf in both phases. The Nb_{ss} phase was thus formed as Hf rich Nb_{ss} and normal Nb_{ss}. This was supported by the X-ray maps in Figure 4.3 where it was noticed that the Hf rich regions were closer to the Nb_5Si_3 grains than the normal Nb_{ss}.

The Hf rich and poor regions in Table 4.4 were determined by grouping all relatively high and low regions together, with a cut-off point of 4.7 at% between the two. The average Hf composition of the normal Nb_{ss} was 3.6 and the Hf rich was 5.6 at% displaying a significant compositional difference. The partitioning of Hf has a direct effect on the partitioning of the other elements, areas that were rich in Hf were also rich in Ti and Cr, however the concentration of Al was not affected by Hf and remained consistent throughout the Nb_{ss}.

The composition of the Nb_5Si_3 was also affected by the partitioning of Hf with two distinct silicides forming, the Hf rich one having an average concentration of 9.3 at% and the normal Nb_5Si_3 4.6 at%. As with the Nb_{ss}, the Hf also affected the partitioning of elements, notably Ti in the silicide, the concentration of which increased with Hf.

In JN1-AC some eutectic areas were large enough to be analysed. The analyses showed that the average Si content was 13.3 at% and the Si+Al was 18.9 at%, the latter being very close to the eutectic components of 18.75 at% in the Mo-Si binary. The eutectic was formed from the last to solidify melt.

Table 4.4 EPMA phase analysis of JN1-AC (at %)

Phase	Nb	Si	Ti	Cr	Al	Hf
Nb_{ss}	53.7±3.2	1.7±0.4	26.5±1.9	8.0±1.1	6.2±0.2	3.6±0.7
	48.7-57.0	1.3-2.5	24.7-29.5	6.7-9.3	6.2-6.8	3.0-4.5
Nb_{ss} Hf rich	45.9±4	2.0±0.7	30.7±1.7	9.4±1.0	6.5±0.2	5.5±0.7
	40.6-51.8	1.3-3.5	28.1-33.4	7.5-11.1	6.2-6.8	4.7-6.4
Nb_5Si_3	41.0±1.4	30.4±1.2	19.2±1.4	1.3±0.5	3.5±0.5	4.6±0.1
	38.8-42.6	28.2-31.5	17.8-20.8	0.9-2.3	3.0-4.2	4.4-4.7
Nb_5Si_3 Hf rich	30.4±0.6	32.6±0.9	23.7±0.1	1.1±0.4	2.9±0.1	9.3±0.3
	30.1-31.3	31.2-33.3	23.5-23.7	0.9-1.8	2.8-3.0	8.9-9.5
Eutectic	46.8±2.2	13.3±1.5	24.2±1.1	5.3±0.6	5.6±0.2	4.8±0.5

The $NbCr_2$ Laves phase was formed in both the alloys KZ5 and JG4, any regions in JN1-AC where there could be Laves phase (see Figure 4.2) were much too small to analyse using EDS/WDS. The X-ray maps were also non-conclusive regarding the presence of the Laves phase. The existence of the Laves phase in JN1-AC, whilst possible, is not likely to be at a high volume fraction.

The formation of $NbCr_2$ in Nb-silicide alloys has been limited with the partitioning of Cr to the melt which becomes rich in Cr and the Laves forms from the last to solidify Cr-rich melt. In JN1-AC the strong partitioning of Hf in the Nb_{ss}, which was not observed in JG4, and the corresponding increase in the concentration of Cr (and Ti) in the Hf rich Nb_{ss} would be the reason for the interdendritic melt not becoming rich enough in Cr to allow the formation of $NbCr_2$.

Another reason for the stabilisation of the C14 $NbCr_2$ Laves phase in KZ5 and not in JN1 would be the higher actual Cr content in KZ5, being 6.8-7.6 at%, resulting in the alloy sitting deep in the Nb_{ss}-Nb_5Si_3-$NbCr_2$ ternary phase field (Bewlay et al. 2009). The Nb_5Si_3 grains and the eutectic were much coarser in KZ5, compared with JN1; this would suggest a refining effect of Hf on the microstructure (Tian et al. 2008).

The Scheil solidification path of JN1-AC was calculated using the Pandat database and software and gave the following result, see Figure 4.7. Solidification starts at $\sim$ 1958 °C, then L$\rightarrow$ L + Nb_5Si_3 $\rightarrow$ L + Nb_5Si_3 + Nb_{ss} $\rightarrow$ L + Nb_5Si_3 + Nb_{ss} + Ti_5Si_3 $\rightarrow$ L + Nb_{ss} + Ti_5Si_3 $\rightarrow$ L + Nb_{ss} + Ti_5Si_3 + C14 $NbCr_2$ $\rightarrow$ Nb_{ss} + Ti_5Si_3 + C14 $NbCr_2$ with the last liquid solidifying at $\sim$ 1223 °C and vol% Nb_{ss} of 44.6% and vol% Nb_5Si_3 of 44.2% and Ti_5Si_3 of 11.2%. In other words the calculations gave Nb_5Si_3 as the primary phase, in agreement with the experimental results, the formation of hexagonal 5-3 silicide, the formation of C14 Laves phase, which was not confirmed conclusively by the experimental results and a final microstructure consisting of Nb_{ss}, hexagonal 5-3 silicide and Laves that is not in agreement with the experimental results. Regarding the structure of Nb_5Si_3 the XRD data for JN1-AC confirmed the presence of tetragonal β Nb_5Si_3 and there were no peaks corresponding to the hexagonal γNb_5Si_3. The Nb/(Ti+Hf) ratio for the Hf rich Nb_5Si_3 was less than one ($\approx$0.9) but the Nb/(Ti+Hf) ratio in the alloy was above one ($\approx$ 1.44). The so called "strict" "Bewlay rule" suggests formation of hexagonal Nb_5Si_3 when the above ratio is below one ($\leq$0.7) in both the

alloy and the 5-3 silicide. The calculated volume fractions were close to the experimentally measured ones, see Table 4.1.
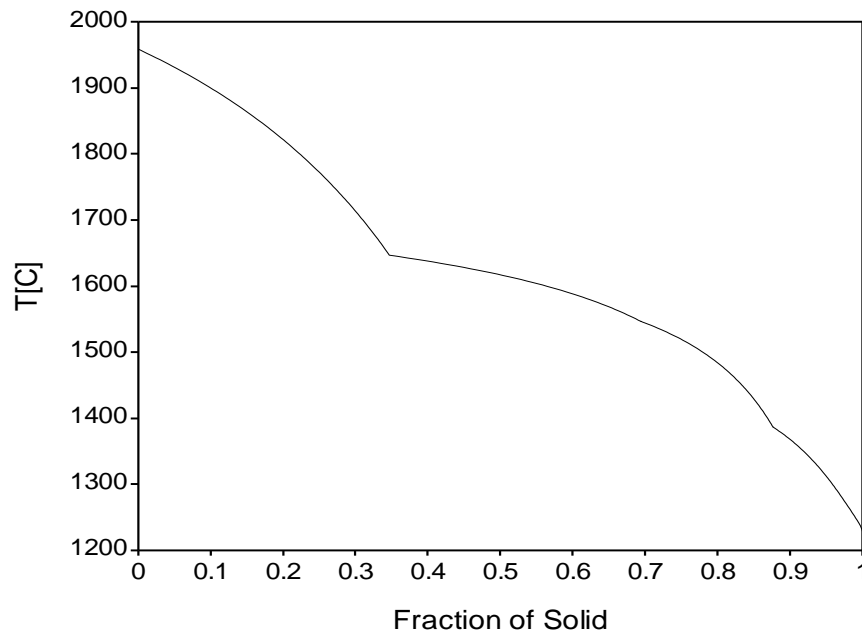
Figure 4.7 Scheil solidification path for JN1 calculated using the Pandat software

4.2 Alloys Nb-18Si-15Ti-10Cr-2Hf-5Mo-5W-2Sn (JN2-AC) and Nb-18Si-15Ti-2Cr-2Hf-5Mo-5W-2Sn (JN3-AC)

The alloys JN2 and JN3 were studied to understand how Cr affects the microstructure evolution, phase stability, oxidation and mechanical properties of high order alloys with RM additions and Sn. Mo and W were added, and the concentration of Ti and Hf were reduced to balance the properties of the alloy. The increased Cr content and addition of Sn were expected to balance the negative effect on oxidation resistance anticipated from the reductions in Ti and Hf concentrations.

4.2.1 JN2-AC

The large area analysis for JN2 is given in Table 4.5. The data shows that the average composition for most elements was close to the nominal composition, with the

exception of W which was far from the nominal. Their difference was attributed to the difficulty of fully melting the W pellets. The W concentration was stable throughout the top, bulk and bottom of the alloy with an average of 2 at%. There was macrosegregation of Si with $C_{max}^{Si} - C_{min}^{Si} \approx 3.2\ at\%$ and no segregation for the other elements.

Table 4.5 EDS large area analysis of JN2-AC (at%)

Area in ingot	Nb	Si	Ti	Cr	Hf	Mo	W	Sn
Top	42.6±0.3	20.6±0.4	15.9±0.2	9.5±0.2	1.6±0.0	5.6±0.1	2.1±0.2	2.0±0.2
	42.3-42.9	20.2-21.1	15.6-16.2	9.3-9.8	1.6-1.7	5.5-5.7	2-2.4	1.8-2.3
Bulk	42.6±0.5	20.3±1.3	16.0±0.2	9.4±0.3	1.6±0.2	5.8±0.3	2.2±0.4	2.0±0.2
	42-43.1	19.5-22.6	15.9-16.2	8.9-9.7	1.3-1.9	5.5-6.2	1.5-2.5	1.8-2.3
Bottom	42.5±0.2	20.3±0.6	16.0±0.2	9.7±0.4	1.7±0.1	5.9±0.2	2.0±0.3	1.9±0.1
	42.3-42.8	19.4-20.9	15.7-16.2	9.4-10.4	1.5-1.9	5.6-6.2	1.7-2.3	1.7-2
Average composition	42.6±0.1	20.4±0.2	16.0±0.1	9.5±0.2	1.7±0.1	5.8±0.2	2.1±0.1	2.0±0.1
	42.0-43.1	19.4-22.6	15.6-16.2	8.9-10.4	1.3-1.9	5.5-6.2	1.5-2.5	1.7-2.3

Figure 4.8 shows the microstructure at low and high magnification for the top, bulk and bottom of the alloy JN2. The dark grey grains are Nb$_5$Si$_3$, the bright grains are Nb$_{ss}$ and the black areas are the NbCr$_2$ Laves phase. There was a noticeable variability in contrast in the Nb$_{ss}$ which suggests microsegregation but not in the Nb$_5$Si$_3$.

In the bottom of the ingot where the melt had been in contact with the water cooled copper hearth the microstructure consisted of three distinct phases normally the Nb$_{ss}$, Nb$_5$Si$_3$ and the NbCr$_2$ Laves phase. The low magnification images would suggest almost equal volume fraction for the Nb$_{ss}$ and the Nb$_5$Si$_3$. The spatial distribution of the Laves was not uniform and the Nb$_{ss}$ did not exhibit a dendritic morphology.

In the top and bulk of the ingot the dendritic structure of the Nb$_{ss}$ was apparent and finer in the former. The NbCr$_2$ Laves phase was formed at the Nb$_5$Si$_3$-Nb$_{ss}$ interface as was the case in the bottom of the ingot.

None of the phases within JN2-AC appeared to have any micro cracks, however there was noticeable porosity throughout the ingot, mostly in the bulk and top.
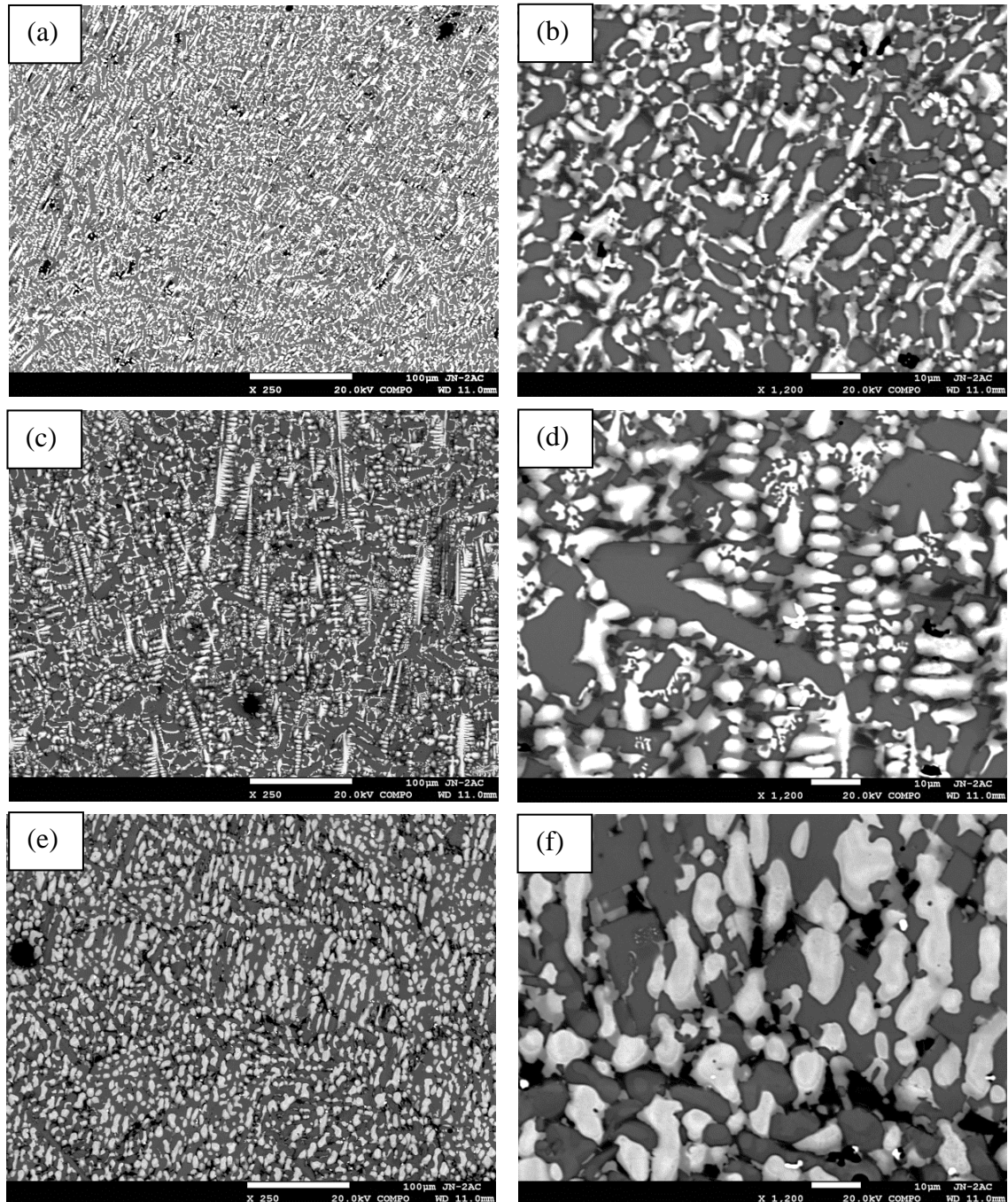
Figure 4.8 BSE at 250 X and 1200 X magnification of the top (a, b), bulk (c, d) and bottom (e, f) of JN2 AC.

Given the partitioning of solutes in the Nb$_{ss}$, elemental maps were used to aid further characterisation of the microstructure. Figure 4.9 shows the X-ray maps from the bulk of JN2-AC. The maps clearly show the high degree of solute partitioning, i.e. microsegregation in the alloy. The Nb, Si and Cr maps show where the Nb$_{ss}$, βNb$_5$Si$_3$ and NbCr$_2$ Laves phase were formed. The other elemental maps help to distinguish

between areas of segregation within the alloy. The Ti map indicates regions within the Nb_{ss} which also correspond with areas of high Sn and Cr. The Mo and W maps show the partitioning of these elements to the Nb_{ss} phase and the Hf map shows partitioning of these elements to Ti rich regions of Nb_{ss}. Small regions of Hf rich areas exist in the map; these were attributed to HfO_2 formed as the Hf scavenges O_2 from the Nb_{ss}. There is no evidence of partitioning in the silicide phase which indicated that the decrease in Hf content in the alloy had an effect of partitioning of solute. Thus the increased Cr content in the alloy appears to have instigated the micro segregation in the Nb_{ss} rather than the Nb_5Si_3.
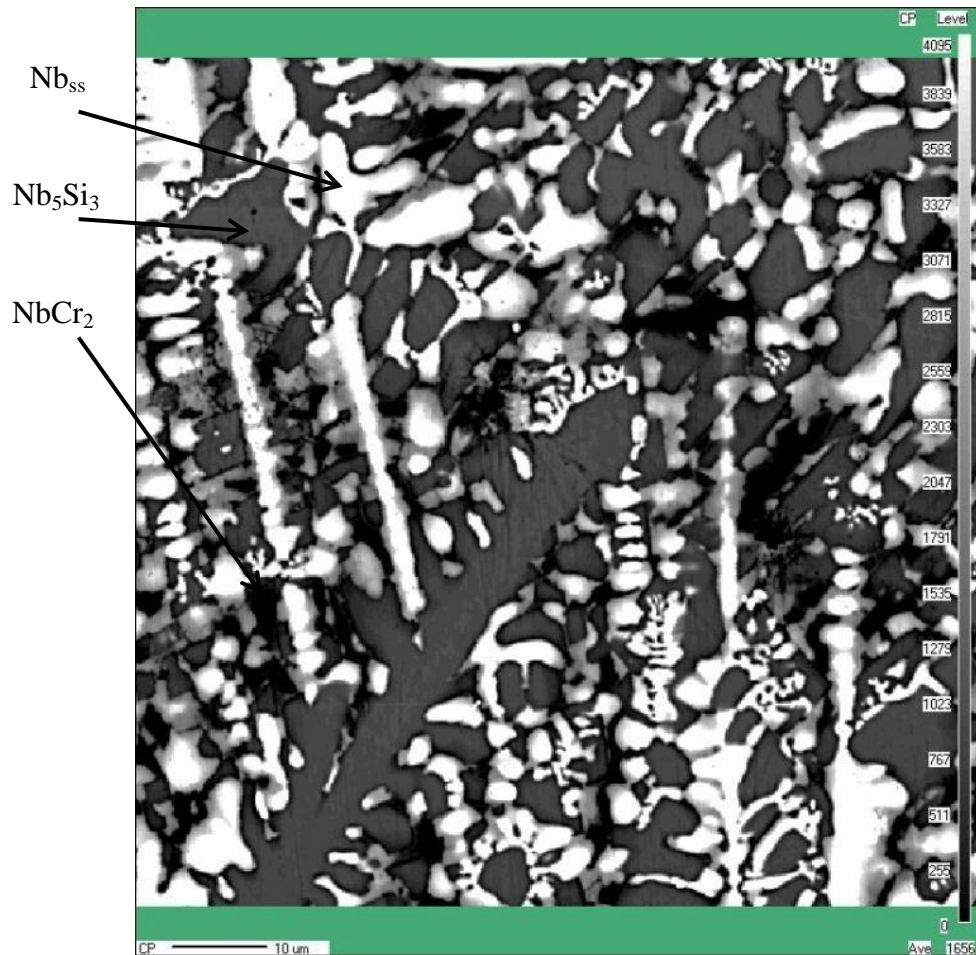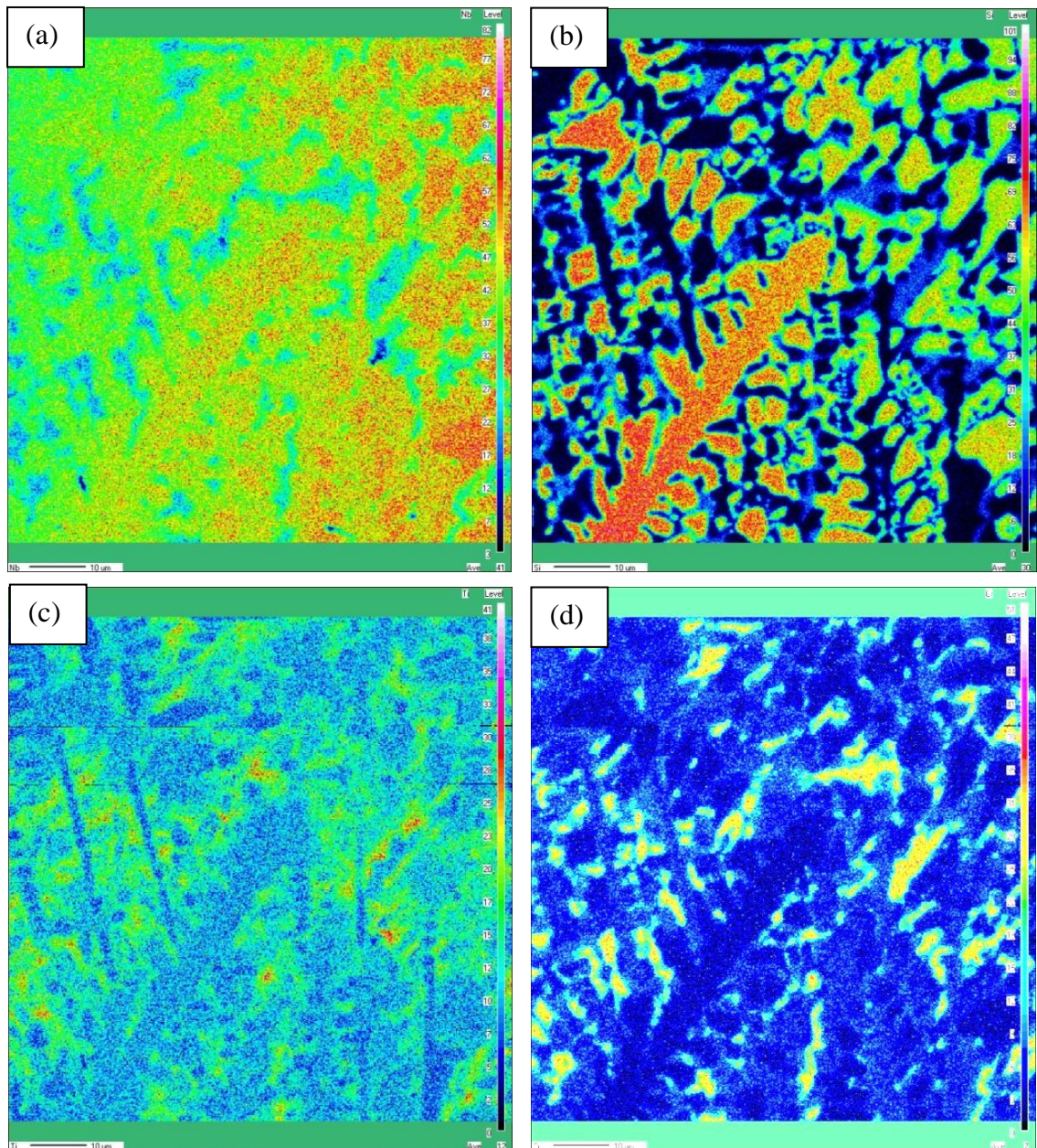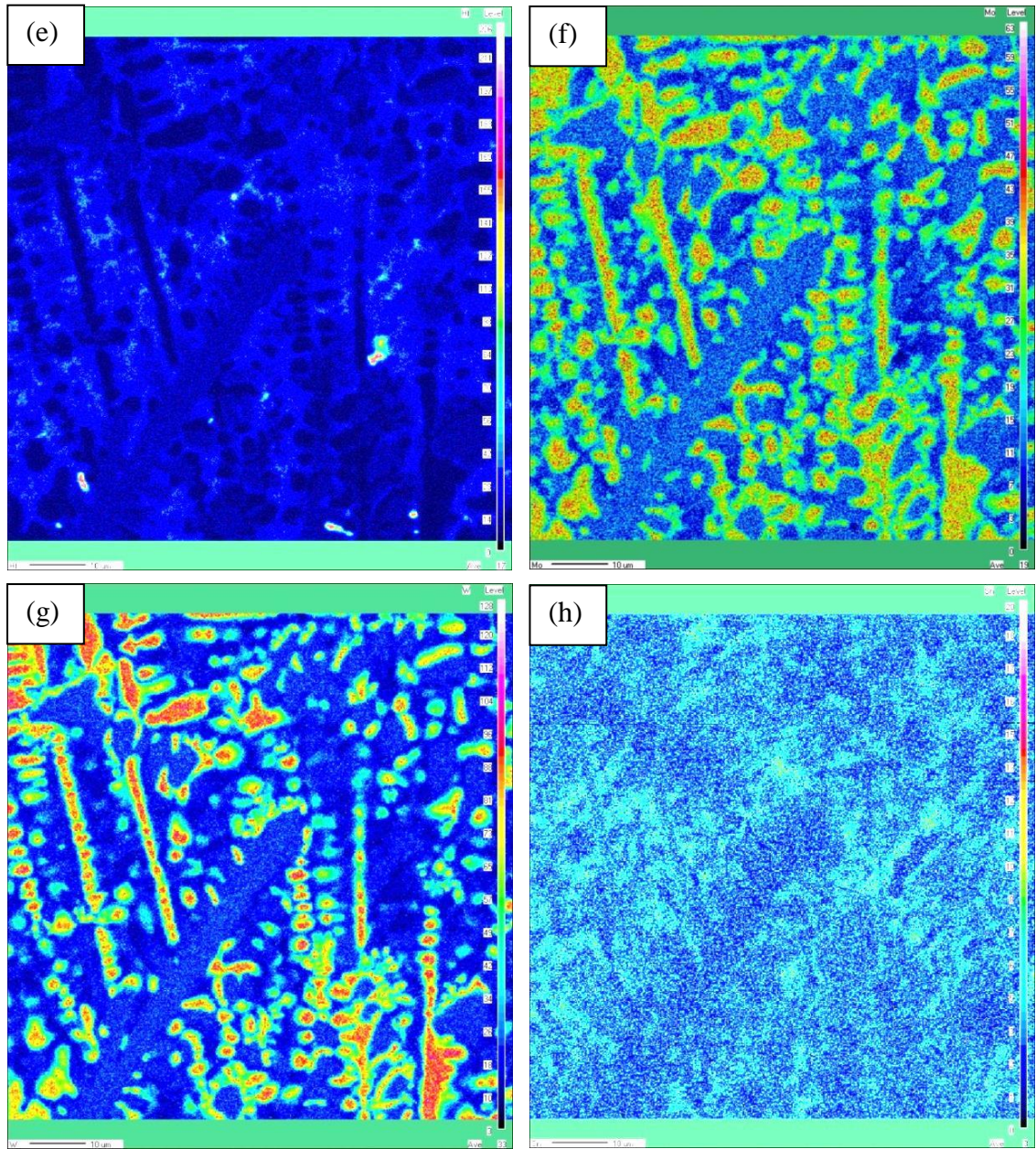
Figure 4.9 X-ray maps of the bulk of JN2 for Nb (a), Si (b), Ti (c), Cr (d), Hf (e), Mo (f), W (g) and Sn (h).

Figure 4.10 shows the powder X-ray diffraction pattern for JN2 AC. The data informed the presence of Nb_{ss} and βNb_5Si_3, but there are no characteristic peaks for the $NbCr_2$ Laves phase. The lack of $NbCr_2$ peaks is most likely due to the small volume fraction ($\approx$5 at%) of this phase.
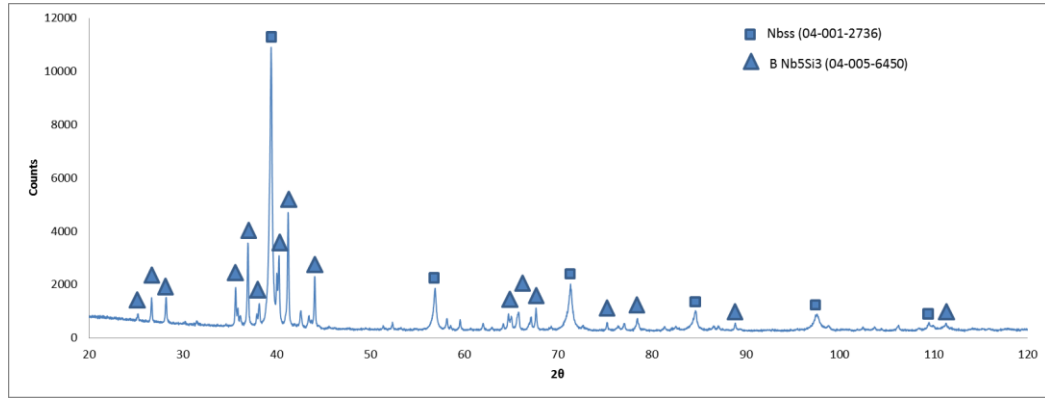
Figure 4.10 JN2 AC powder XRD pattern fitted with Sieve+

Equation 5, Equation 6 and Equation 7 were used to calculate the lattice parameter of JN2 AC as with JN1 AC these can be seen in Table 4.6. The Nelson-Riley plot from which the corrected Lattice parameter is calculated can be seen in Figure 4.11.

Table 4.6 The calculated lattice parameters of the bcc Nb_{ss} in JN2-AC

	d (Å)	2 θ	theta	a (Å)	f (θ)	hkl	Corrected a (Å)
JN2 AC	2.286	39.38	19.69	3.233	2.676058	110	
	1.618	56.84	28.42	3.237	1.652429	200	
	1.322	71.28	35.64	3.238	1.152018	211	
	1.145	84.58	42.29	3.238	0.826198	220	3.254
	1.024	97.54	48.77	3.239	0.586501	310	
	0.944	109.44	54.72	3.269	0.414738	222	
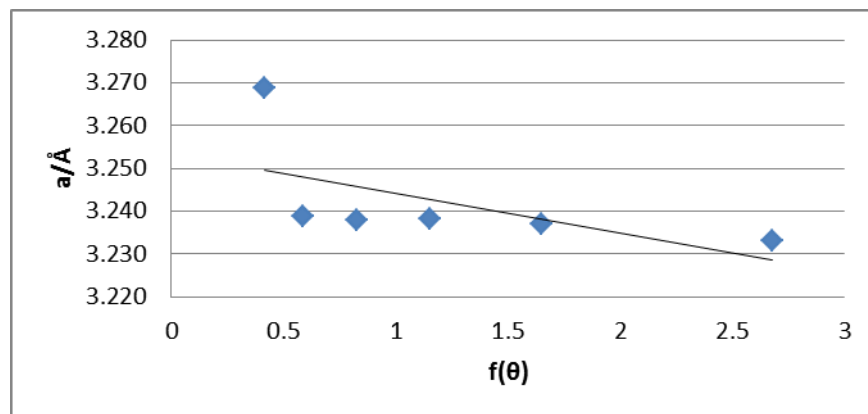
Figure 4.11 Nelson-Riley plot for the lattice parameter of the bcc Nb_{ss} in JN2-AC

The lattice parameter for pure Nb is 3.303 Å and the value for (a) obtained for Nb_{ss} in JN2 AC is 3.254 Å causing a total reduction of 0.049 Å. The atomic radius of pure Nb

1.47 Å, the presence of Ti, Si, Cr, Mo, Sn and Hf within the Nb_{ss}, with atomic radii of 1.47, 1.17, 1.30, 1.40, 1.58 and 1.59 Å (Gale & Totemeier 2003) respectively, leads to an overall contraction of the crystal lattice. This contraction in the lattice is particularly effected by the covalent bonding between Nb and Si (Kim et al. 2004).

Table 4.7 shows the WDS phase analysis data for JN2-AC. The analysis confirmed that are 3 phases were present, namely the Nb_{ss}, Nb_5Si_3 and C14 $NbCr_2$ Laves phase. As suggested by the elemental maps there was strong partitioning of solutes in the Nb_{ss}, resulting in three different chemistries for the Nb_{ss}; normal, Sn and Ti rich, and Ti and Cr rich. There was no evidence for the formation of Nb_3Si. The high Cr content in the Cr and Ti rich Nb_{ss} was close to the maximum solid solubility of Cr in Nb_{ss}, which is 24 at% at 1625 °C. It is possible that neighbouring regions (Nb_5Si_3, Laves phase) were inside the interaction zone during WDS analysis, and therefore contributed to the results for the Nb_{ss}. Whilst this effect is a possibility, the concentrations of the element were too high compared with neighbouring grains, there were also too many data points to simply dismiss the data as erroneous, and similar results have been seen in previous work (Grammenos & Tsakiropoulos 2010a; Geng, Tsakiropoulos & G Shao 2007).

The Sn and Ti rich Nb_{ss} had 7.3 and 33 at% of each element in solution respectively and the Ti and Cr rich Nb_{ss} contained equal concentrations of the two elements (22.5 and 22.9 at% Ti and Cr respectively). In the normal Nb_{ss} the Si concentration was as in the Nb_{ss} in other Nb-silicide alloys without Sn (Vellios & Tsakiropoulos 2007b) and the Sn content was also low. In all three where the Si+Sn concentration in the Nb_{ss} did not approach the 17 at% or higher concentrations that is typical for Nb_3Si. The Si + Sn content of the solid solution changed from 3.8 at% in the normal Nb_{ss} to 8 at% in the Cr + Ti rich Nb_{ss} to 9.4 at% in the Sn + Ti rich Nb_{ss} but the ratio (Ti + Cr)/(Si + Sn) was remarkably "constant" and in the range 5 to 5.7. This suggested that Cr and Ti played a key role in the partitioning of solutes to the solid solution. Given the strong effects of Ti (positive) and Cr (negative) on the toughness of the solid solution (Chan & Davidson 2003; Chan & Davidson 2001), and the solid solution strengthening effect of both elements, it is important to find out how these elements affect the solubilities of RMs as the latter also have a strong solid solution strengthening effect (Begley 1994). The data for the compositions of the solid solution makes this task possible.

There was variation in the Mo + W content (different partitioning behaviour) of the solid solution that was highest (18.2 at%) in the normal Nb_{ss} and decreased in the Cr + Ti and Sn + Ti rich Nb_{ss} respectively to 6.6 and 5.4 at%. In other words as the Cr, Sn and Ti segregated in the solid solution the Mo and W were "pushed out" i.e. there was no synergy with Mo and W in the Nb_{ss}. However, as the Si + Sn content of the solid solution increased there was also an increase in the Cr + Ti content of the solid solution from 21.5 at% in the normal Nb_{ss} to 46.6 at% in the Sn + Ti rich areas (resulting to the (Ti + Cr)/(Si + Sn) ratio values discussed above). The latter content (i.e., the 46.6 at%) was essentially the same as in the Cr + Ti rich Nb_{ss}, where however the two elements were present at almost equal concentrations (i.e. Cr/Ti $\approx$ 1). Furthermore, the total sd element content of the solid solution excluding Nb increased from $\sim$ 41 at% in the normal Nb_{ss} to $\approx$ 54 at% in the Sn + Ti rich and Cr + Ti rich Nb_{ss} resulting in the latter two having to the same ratio (Cr + Hf + Mo + Ti + W)/(Cr + Ti) of $\approx$ 1.2, lower than in the normal Nb_{ss} ($\approx$ 1.9).

Sn rich Nb_{ss} was reported by Geng et al for their JG6 alloy (Nb-24Ti-18Si-5Al-5Cr-5Hf-2Mo-5Sn). In this alloy the Al + Si + Sn content was about 21 at%. The Nb_3Sn is formed with Si + Sn in the range 17 to 19 at% and Al can substitute for Sn as Nb_3Al and Nb_3Sn are both A15 compounds. Subsequent research in the group on Sn containing alloys and the aforementioned compounds has confirmed that the Sn rich Nb_{ss} reported by Geng et al was indeed the Nb_3Sn intermetallic phase. As mentioned above, in the alloy JN2 this intermetallic was not formed.

Contrary to the strong partitioning of elements (microsegregation) in the Nb_{ss}, there was little microsegregation in the Nb_5Si_3, which has the D8m βNb_5Si_3 crystal structure, as confirmed by the XRD data. Unlike the JN1-AC and JG6 AC, the Nb_5Si_3 did not exhibit Hf microsegregation which was attributed to the reduced Hf content in JN2-AC (2 at%) compared with the alloy JG6 (5 at%). The Laves phase formed in the interdendritic regions between the Nb_{ss} and the Nb_5Si_3 as the Cr was rejected into the melt. It forms from the last to solidify melt. The Laves phase grew much larger in the bottom of the alloy with grains up to $\sim$6-8 μm in diameter, whilst in the rest of the alloy the Laves phase is much smaller, only $\sim$2 μm across. This was attributed to the reduced time for solute partitioning (because of the high cooling rates) and the enrichment in Cr of the melt. As with the Nb_5Si_3 there was little microsegregation in the Laves phase.

Considering that in the Laves phase Cr can be substituted by Si and Sn, the Cr+Si+Sn content was ≈56.4 at%, lower than the Cr content of unalloyed $NbCr_2$ but in agreement with data in the literature (Geng & Tsakiropoulos 2007). However error in the analysis of this phase cannot be observed owing to its small grain size.

Table 4.7 EPMA phase analysis of JN2-AC (at%)

Phase	Nb	Si	Ti	Cr	Hf	Mo	W	Sn
Nb_{ss}	55.3±2.1	1.8±0.4	12.7±1.5	8.8±1.9	1.1±0.1	10.7±0.6	7.5±1.2	2.0±0.3
	52.4-57.6	1.4-3.0	10.9-15.3	6.6-12.3	0.9-1.2	9.8-11.6	5.0-9.0	1.6-2.7
Nb_{ss} **Sn+Ti rich**	36.3±1.7	2.1±1.0	33.0±2.1	13.6±1.5	2.2±0.2	4.5±0.5	0.9±0.2	7.3±0.7
	33.7-38.3	1.3-4.1	31.0-36.9	12.0-16.0	1.8-2.5	3.8-5.0	0.7-1.1	6.7-8.5
Nb_{ss} **Ti+Cr rich**	37.4±1.9	4.2±0.5	22.5±2.1	22.9±1.7	2.4±0.4	5.1±0.3	1.5±0.4	3.8±0.7
	35.2-39.6	3.6-4.7	20.7-25.5	21.4-24.8	1.9-2.9	4.9-5.6	1.2-2.1	3.2-4.6
Nb_5Si_3	46.3±1.8	32.7±1.1	13.1±1.3	2.2±0.6	2.2±0.7	1.7±0.5	0.9±0.3	0.9±0.2
	42.3-47.9	31.7-35.8	12.0-16.1	0.9-3.4	1.7.-4.2	0.5-2.1	0.2-1.2	0.8-1.4
Laves	25.5±0.7	11.6±1.3	11.3±1.4	44.9±2.9	3.5±0.3	2.1±0.1	0.9±0.1	0.2±0.1
	25.0-26.5	10.7-13.6	10.1-13.2	40.6-47.1	3.1-3.9	1.9-2.2	0.8-1.1	0.1-0.3

The solidification path of JN2-AC was calculated using the Pandat database and gave the following result, see Figure 4.12. Solidification starts at ~ 1969 °C, then $L \rightarrow L + Nb_5Si_3 \rightarrow L + Nb_5Si_3 + Nb_{ss} \rightarrow L + Nb_5Si_3 + Nb_{ss} + C14\ NbCr_2 \rightarrow L + Nb_5Si_3 + Nb_{ss} + C14\ NbCr_2 + Ti_5Si_3 \rightarrow L + Nb_{ss} + C14\ NbCr_2 + Ti_5Si_3 \rightarrow Nb_{ss} + C14\ NbCr_2 + Ti_5Si_3$ with the last liquid solidifying at ~ 1225 °C and vol% Nb_{ss} of 41% and vol% Nb_5Si_3 of 52.5% and C14 $NbCr_2$ of 6.5%. The calculations gave Nb_5Si_3 as the primary phase, in agreement with the experimental results, the formation of hexagonal 5-3 silicide, which was not confirmed by the XRD, the formation of C14 Laves phase, which was confirmed by the experimental results and a final microstructure consisting of Nb_{ss}, hexagonal 5-3 silicide and Laves that is not in agreement with the experimental results. The calculated volume fractions for the solid solution, 5-3 silicide and Laves phase were remarkably close to the experimentally measured ones, see Table 4.1.
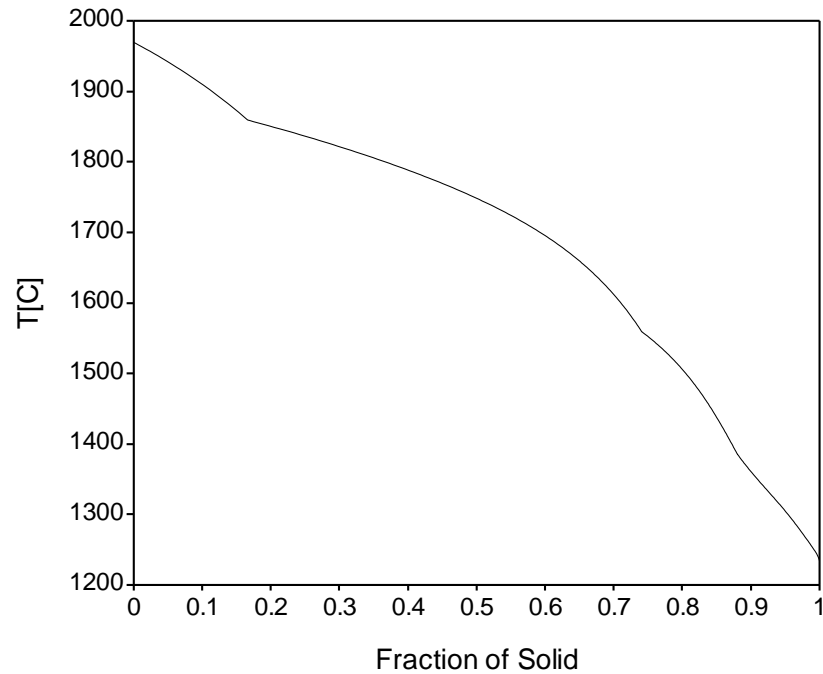
Figure 4.12 Scheil solidification path for JN2 calculated using the Pandat software

4.2.2 JN3-AC

The large area analysis data is given in Table 4.8

Table 4.8. As was the case in JN2, the W content was well below the nominal value owing to difficulty in fully melting the W charge, compared with JN2, the average W concentration was 50 % lower. There was weak Si macrosegregation in this alloy ($C_{max}^{Si} - C_{min}^{Si} = 1.4\ at\%$)

Table 4.8 EDS large area analysis of JN3-AC (at%)

Area in ingot	Nb	Si	Ti	Cr	Hf	Mo	W	Sn
Top	50.38±0.2	20.98±0.4	16±0.6	1.8±0.2	1.46±0.1	5.9±0.2	1.6±0.2	1.86±0..2
	50.1-50.6	20.7-21.6	15.3-16.7	1.5-2	1.4-1.6	5.6-6.1	1.3-1.8	1.6-2
Bulk	50.32±0.3	20.8±0.6	16.1±0.1	1.82±0.1	1.62±0.1	6.04±0.4	1.4±0.2	1.9±0.1
	49.9-50.2	20.2-21.6	15.9-16	1.7-1.9	1.4-1.7	5.5-6.4	1.1-1.7	1.8-2.1
Bottom	49.64±0.3	20.9±0.4	16.48±0.4	2.06±0.2	1.68±0.1	6.02±0.3	1.0±0.1	2.2±0.2
	49.2-50	20.3-21.3	16-17	1.8-2.2	1.6-1.8	5.8-6.5	0.9-1.1	2-2.4
Average	50.1±0.4	20.9±0.1	16.2±0.3	1.9±0.1	1.6±0.1	6.0±0.1	1.3±0.3	2.0±0.2
	49.2-50.6	20.2-21.6	15.3-17	1.5-2.2	1.4-1.8	5.5-6.5	0.9-1.8	1.6-2.4

composition

Figure 4.13 shows low and high magnification BSE images of the microstructure of JN3 AC. The bottom of the button ingot, as with JN2, contained two phases, namely Nb_{ss} and Nb_5Si_3 and no eutectic. There was evidence of microsegregation in the Nb_{ss} and possibly in the Nb_5Si_3 as some darker regions were observed at the centre of some grains.

The microstructures at the top and bulk of the ingot were almost identical, consisting of Nb_{ss} and Nb_5Si_3 showing lower directionality than in JN2, and significant volume fraction of Nb_{ss}/Nb_5Si_3 eutectic. The microsegregation in the Nb_{ss} was apparent as regions of darker contrast but there was no strong evidence for microsegregation in the Nb_5Si_3.
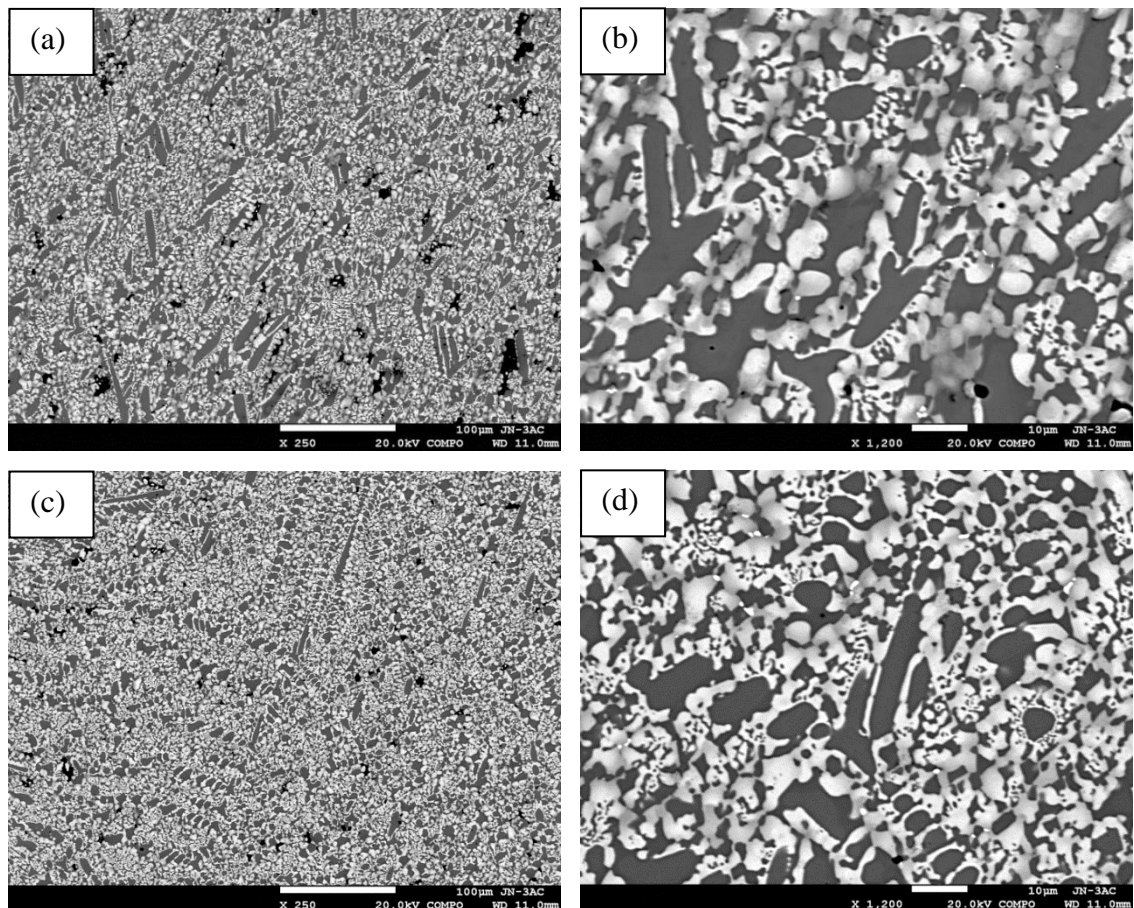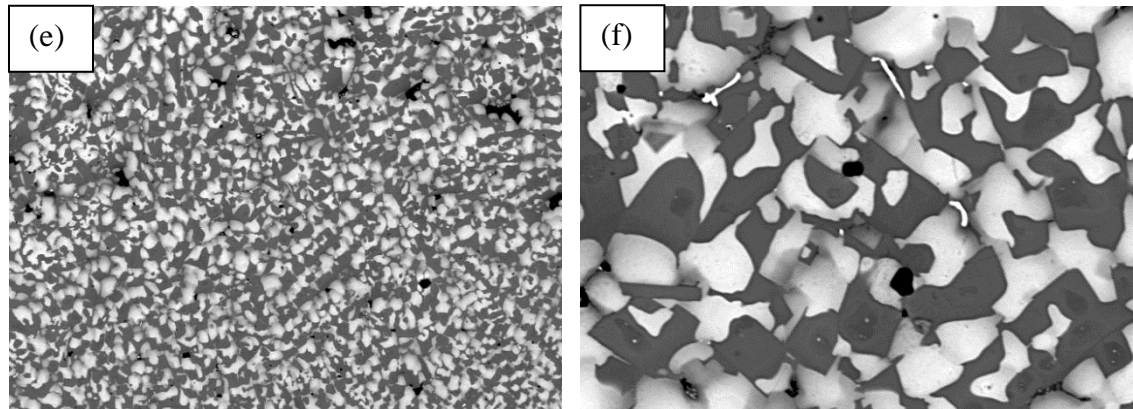
Figure 4.13 BSE images at 250X and 1200X magnification of the top (a, b), bulk (c, d) and bottom (e, f) of JN3 AC.

Figure 4.14 shows X-ray maps from the bulk section of the ingot. The W, Mo and Si maps clearly display the phases, Nb_{ss} and Nb_5Si_3. The Cr, Ti, Hf and Sn maps show the microsegregation in the Nb_{ss}. Within the Nb_{ss} grains, the W and Mo maps show coring, with a higher concentration of the aforementioned elements in the centre compared with the outside. The Hf map also shows hafnia grains formed by scavenging oxygen from the Nb_{ss}. Artefacts in the maps which were caused by problems with the detector; where the concentration gradient in the Nb map and horizontal lines in the Ti, Cr and Sn maps.
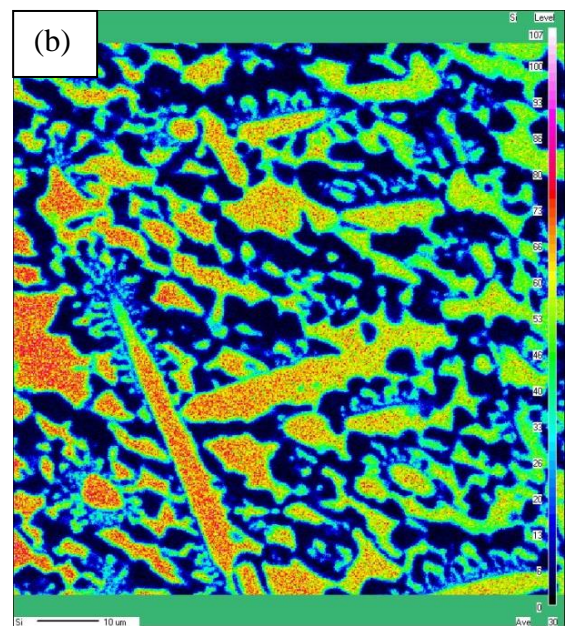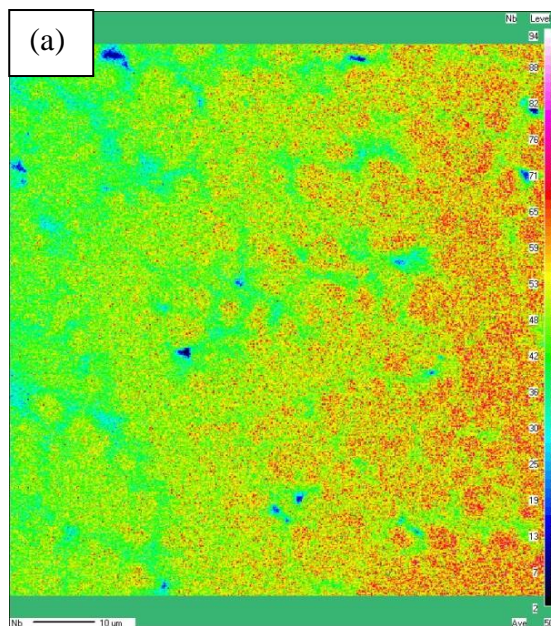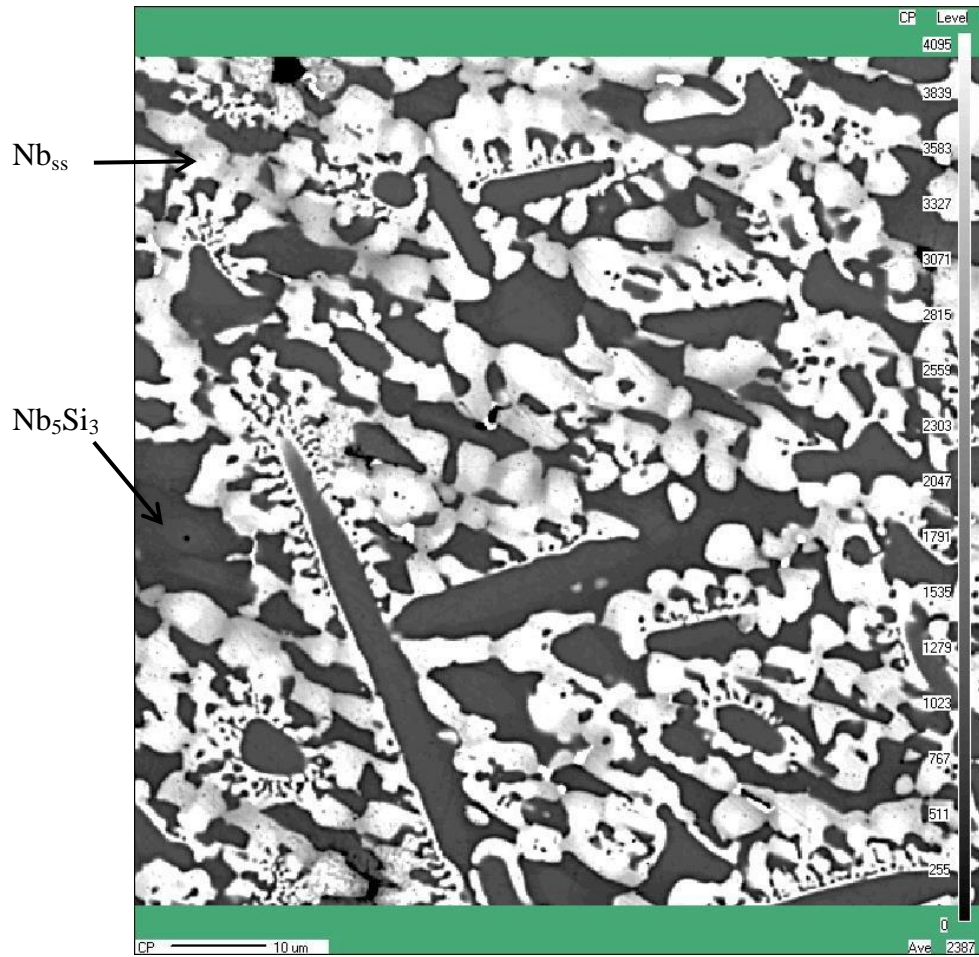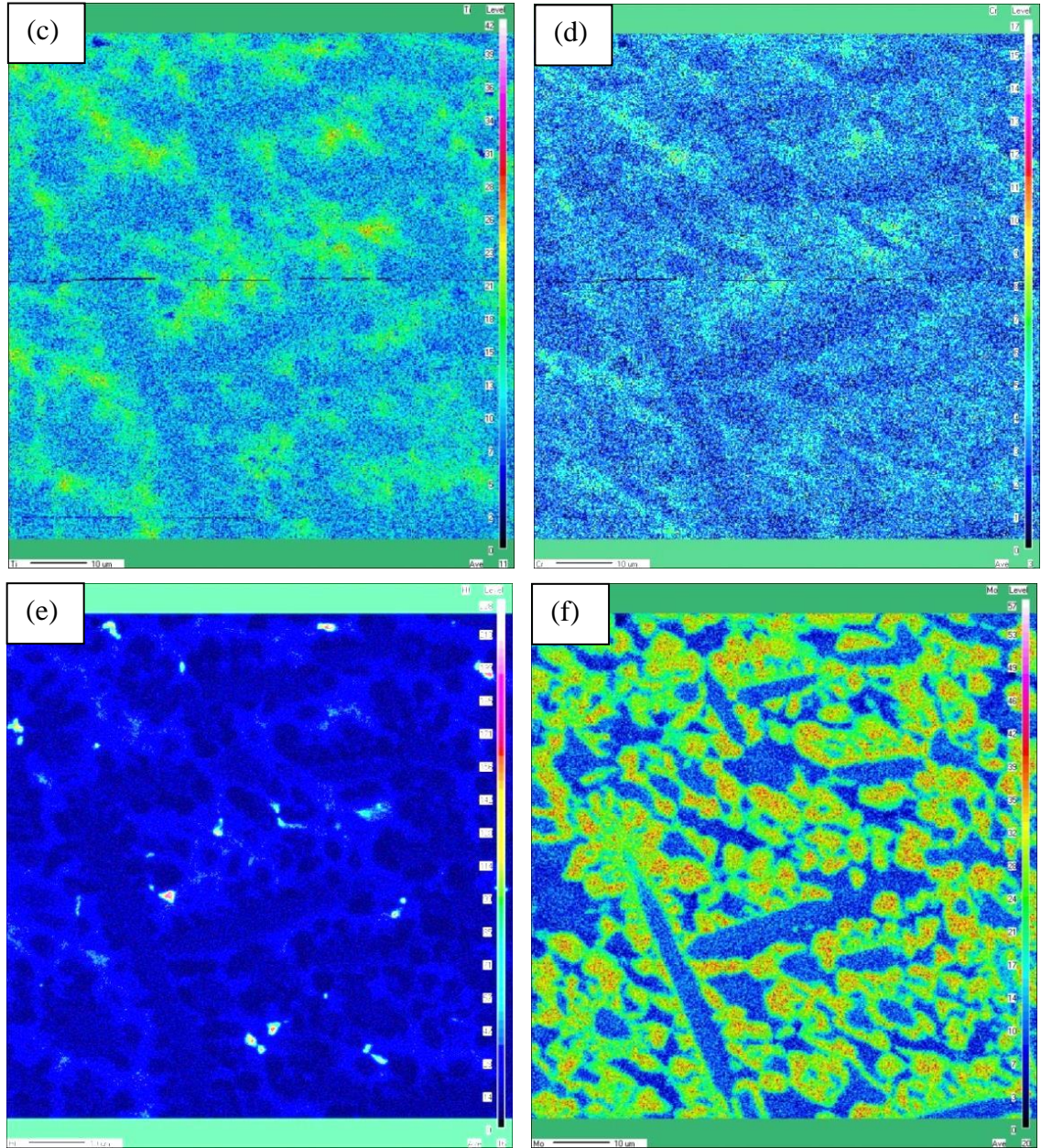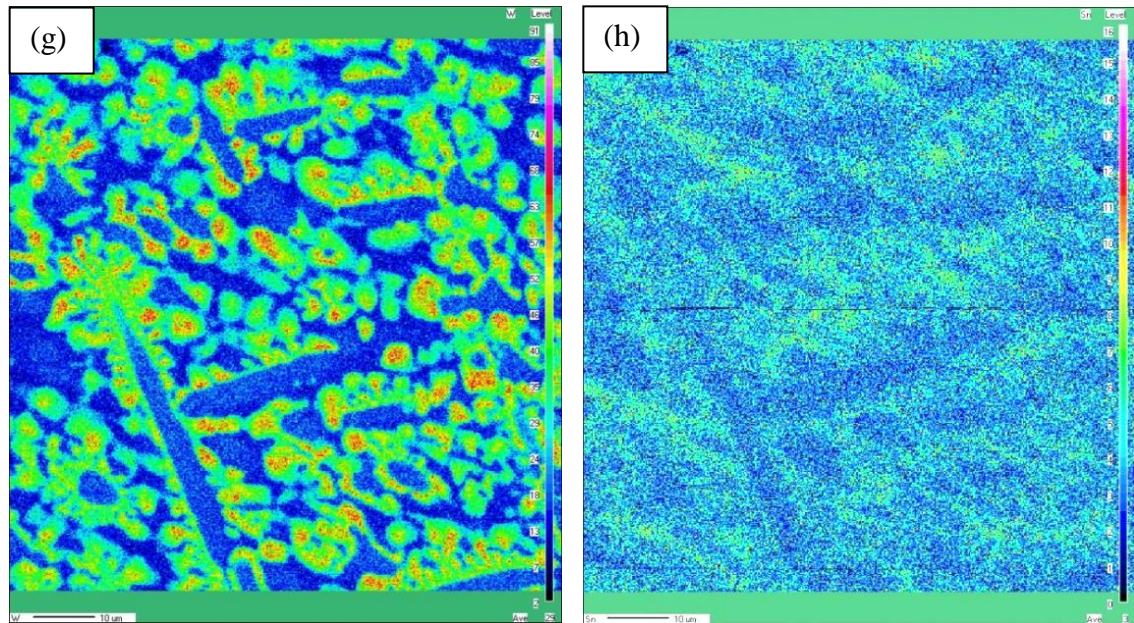
Figure 4.14 X-ray maps of the bulk of JN3 for Nb (a), Si (b), Ti (c), Cr (d), Hf (e), Mo (f), W (g) and Sn (h)

The XRD data obtained through powder diffraction was used to classify the phases in JN3 AC. Figure 4.15 shows the powder-ray diffractogram for JN3-AC; the XRD data suggests that the Nb_{ss} and βNb_5Si_3 phases were present. This was expected as the Mo and W stabilise the βNb_5Si_3 (Geng et al. 2010; Kim & Tanaka 2002; Li et al. 2013).
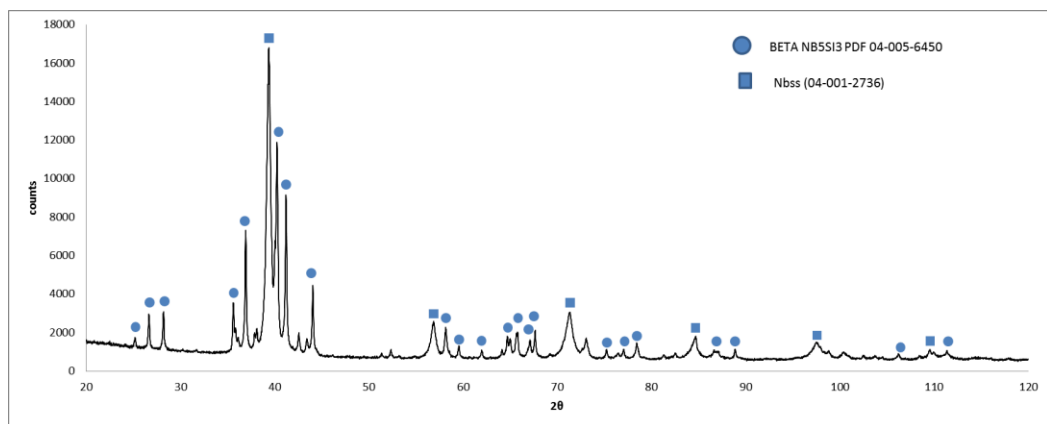
Figure 4.15 JN3 AC powder X-ray diffractogram fitted with sieve+

The lattice parameter calculated for Nb_{ss} in JN3 AC was 3.253 Å, the lattice parameter values can be seen in Table 4.9 and the Nelson-Riley plot can be seen in Figure 4.16. The calculated lattice parameter is almost the same as that calculated for JN2 AC, and

this similarity in lattice parameters is expected, as both contain elements with larger atomic radii when compared to JN1.

Table 4.9 the calculated lattice parameters of the bcc Nb$_{ss}$ in JN3-AC

	d (Å)	2 θ	theta	a (Å)	f (θ)	hkl	Corrected a (Å)
JN3 ac	2.286	39.38	19.69	3.233	2.676058	110	
	1.618	56.84	28.42	3.237	1.652429	200	
	1.322	71.28	35.64	3.238	1.152018	211	
	1.144	84.68	42.34	3.235	0.824093	220	3.253
	1.025	97.46	48.73	3.241	0.587797	310	
	0.943	109.52	54.76	3.267	0.413714	222	
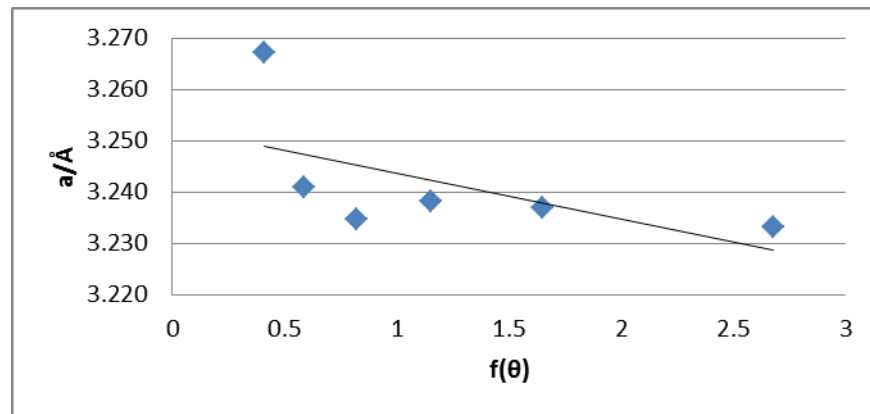
Figure 4.16 Nelson-Riley plot for the lattice parameter of the bcc Nb$_{ss}$ in JN3-AC

Porosity was observed in all areas of the ingot. Furthermore the volume fraction of the Nb$_{ss}$ was higher compared with the alloy JN2, with a significant fraction of the Nb$_{ss}$ being in the eutectic.

Table 4.10 gives the EPMA data for the Nb$_{ss}$ and Nb$_5$Si$_3$. Unlike JN2 AC there was no Laves phase due to the decreased Cr content. There was partitioning of elements in both the Nb$_{ss}$ and Nb$_5$Si$_3$ phases that contained Ti rich regions.

Table 4.10 EPMA phase analysis of JN3-AC (at%)

Phase	Nb	Si	Ti	Cr	Hf	Mo	W	Sn
Nb_{ss}	66.0±1.6	2.1±0.5	12.9±2.0	1.7±0.5	1.3±0.3	9.2±0.7	4.7±1.1	2.2±0.3
	62.4-68.0	1.7-3.4	10.2-16.2	1.0-2.4	1.0-1.8	7.7-10.0	3.5-6.2	1.8-2.5
Nb_{ss} Ti rich	57.5±4.0	1.7±0.3	21.3±3.3	4.1±1.1	2.3±0.6	7.2±0.8	2.3±0.7	3.5±0.5
	52.5-62.8	1.3-2.2	16.9-25.3	2.7-5.5	1.6-3.2	6.2-8.3	1.5-3.5	2.9-4.1
Nb_5Si_3	50.3±0.6	33.0±0.7	11.9±0.7	0.4±0.1	2.1±0.5	1.0±0.5	0.6±0.2	0.8±0.1
	49.4-51.1	31.9-33.7	11.2-13.2	0.2-0.6	1.7-3.0	0.2-1.5	0.2-0.8	0.6-0.9
Nb_5Si_3 Ti rich	45.8±3.2	30.4±3.0	16.8±3.1	1.0±0.8	3.3±0.9	1.0±0.7	0.4±0.2	1.3±0.5
	40.1-49.1	27.1-33.5	14.1-22.0	0.2-2.1	2.4-4.8	0.1-1.7	0.1-0.7	0.9-2.0

The Si + Sn content of the solid solution changed from 4.3 at% in the normal Nb_{ss} to 5.2 at% in the Ti rich Nb_{ss} and the ratio (Ti + Cr)/(Si + Sn) was 4.9, just in the lower part of the range 5 to 5.7 for JN2. This provided further support that the synergy of Cr and Ti played a key role in the partitioning of solutes to the solid solution in the presence of RMs.

The Mo + W content changed in the solid solution, it was highest (13.9 at%) in the normal Nb_{ss} and decreased in the Ti rich Nb_{ss} to 9.5 at%. The latter solution was also richer in Cr compared with the normal one and in agreement with previous research that has shown the solid solubility of Cr in Nb_{ss} to increase with its Ti content (Bewlay et al. 1997). This provided further support that as the Cr, Sn and Ti segregate in the solid solution the Mo and W are rejected as Cr, Sn and Ti do not have synergy with Mo and W in the Nb_{ss}. Compared with JN2, the percentage decrease of the Mo + W content in the Nb_{ss} was smaller in JN3 than in JN2, which would suggest a stronger role for Cr in the synergy of Cr, Sn and Ti.

The total sd element content of the solid solution excluding Nb increased from ~ 30 at% in the normal Nb_{ss} to ≈ 37 at% in the Ti rich Nb_{ss} resulting in the latter having to the ratio (Cr + Hf + Mo + Ti + W)/(Cr + Ti) of ≈ 1.46, lower than in the normal Nb_{ss} (≈ 2). However, the latter was essentially the same as for the normal Nb_{ss} in the alloy JN2.

As was the case in JN2, the Si + Sn content of the Nb_5Si_3 was below the Si content of un-alloyed Nb_5Si_3 (36.5 to 40.5 at% Si compared with 33.6 at% and 33.8 at% (Si + Sn) in JN2 and JN3 respectively). The data for the Ti-rich Nb_5Si_3 in JN3, which

shows Si + Sn = 31.7 at%, would suggest that alloying the 5-3 silicide with RMs, Hf and Sn shifts its composition to the Nb rich side of the phase diagram. In the alloys JG4 (Nb-24Ti-18Si-5Al-5Cr-5Hf-2Mo) and JG6 (Nb-24Ti-18Si-5Al-5Cr-5Hf-2Mo-5Sn), a similar effect was observed regarding the Si content of the Nb_5Si_3 (32.8 at% in the former and 32.3 at% Si or Si + Sn = 34.4 at% in the latter), but in these alloys (i.e., JG4 and JG6) the presence of Al compensated for the difference bringing the total sp element content of Nb_5Si_3 to 36.3 at% and 37.7 respectively.

     The solidification path of JN3-AC was calculated using the Pandat database and gave the following result, see Figure 4.17. Solidification starts at ~ 1969 °C, then L → L + Nb_5Si_3 → L + Nb_5Si_3 + Nb_{ss} → L + Nb_5Si_3 + Nb_{ss} + Ti_5Si_3 → L + Nb_{ss} + Ti_5Si_3 → L + Nb_{ss} + Ti_5Si_3 + C14 $NbCr_2$ → Nb_{ss} + Ti_5Si_3 + C14 $NbCr_2$ with the last liquid solidifying at ~ 1236 °C and vol% Nb_{ss} of 41.5% and vol% Nb_5Si_3 of 58.5%. The calculations gave Nb_5Si_3 as the primary phase, in agreement with the experimental results, the formation of hexagonal 5-3 silicide, which was not confirmed by the XRD, the formation of C14 Laves phase, which was not confirmed by the experimental results and a final microstructure consisting of Nb_{ss}, hexagonal 5-3 silicide and Laves that is not in agreement with the experimental results. The calculated volume fractions for the solid solution and 5-3 silicide differed significantly from the experimentally measured ones, see Table 4.1.
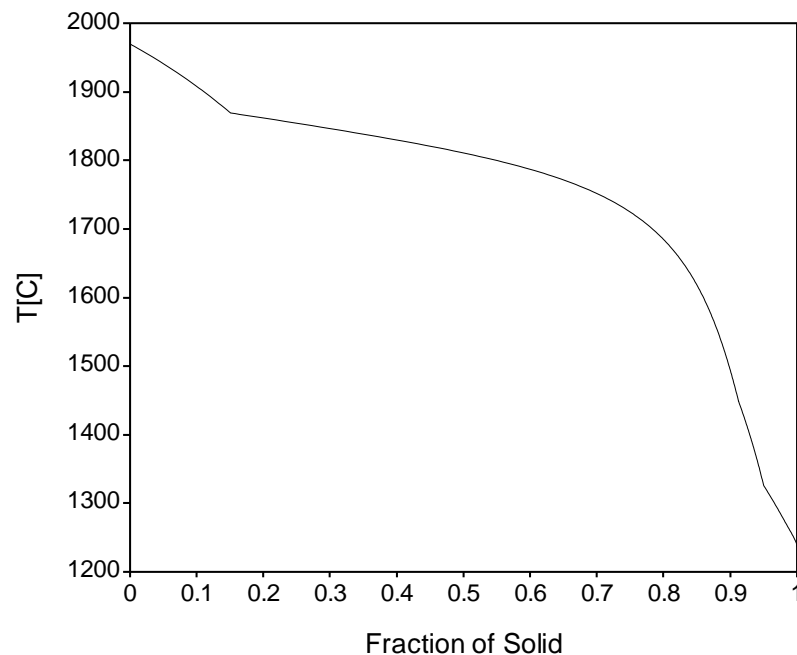
Figure 4.17 Scheil solidification path for JN3 calculated using the Pandat software

4.3   Alloy Nb-20Si-20Ti-2Cr-2Hf-6Mo-5Sn (JN4-AC)

The composition of the alloy JN4 was selected on the basis of the knowledge gained for the alloys JN2 and JN3 in this research (see sections 4.2.1 and 0) and JG6 from previous research in the group(Geng, Tsakiropoulos & G. Shao 2007), see also section on alloy design 2.1. The nominal composition of the alloy JN4 is closer to that of JN3 but with no W (to improve processability, as melting elemental W charge proved to be challenging using the facilities available in the Department), slightly higher Si content (for improved oxidation), higher Ti content (for improved oxidation and toughness of the Nb_{ss} (taking into account the Cr content of the alloy)), slightly higher Mo content (to compensate for the absence of W and not have an adverse effect on oxidation) and higher Sn content (for improved oxidation). The latter addition however aimed to study whether the Nb_3Sn would be stable in JN4 given the high Sn content of the alloy and the results of previous work in the group, which has shown that this intermetallic is stable in Nb silicide based alloys with ~ 5 at% Sn but in the absence of refractory metals.

The large area analyses of different parts (i.e. bottom, bulk and top) of the button ingot and the actual average composition of JN4-AC, all of which were determined by EDS, are given in Table 4.11. The actual composition of JN4 shows that it was leaner in Sn and slightly leaner in Cr and richer in Si and Mo compared with the nominal composition. Previous research on Nb silicide based alloys with Sn addition has shown that control of the concentration of the latter in the alloy becomes more difficult as the Sn content in the alloy increases above 2 at%; this was confirmed by the results for JN4. The latter was also richer in Si than the nominal alloy composition, a trend that was observed also with the alloys JN2 and JN3 and could be attributed to the accuracy of Si analysis by EDS.

The data in Table 4.11 shows that there was weak macrosegregation of Si and Ti, as the difference between the maximum and minimum analyses values was 2.8 at% and 2.4 at%, respectively. Compared with the alloy JN3-AC, where there was no macrosegregation of these elements (the difference between the maximum and minimum analyses values of these elements were less than 2 at%). This is consistent with other research in the group which shows that increasing the Sn content in alloys where Sn is in synergy with Ti, Si, Cr, Hf with/out Al leads to increased macrosegregation of Si (Tsakiropoulos & Singh sethi 2012).

Table 4.11 EDS large area analysis of JN4-AC (at%)

Phase	Nb	Si	Ti	Cr	Hf	Mo	Sn
Top	41.9±0.2	22.4±0.6	20.4±0.2	1.6±0.2	2.0±0.1	7.9±0.4	3.8±0.2
	41.6-42.2	21.8-23.3	20.2-20.6	1.5-1.8	2.0-2.1	7.4-8.5	3.6-4.0
Bulk	41.6±0.2	22.1±0.4	20.6±0.2	1.7±0.1	2.1±0.0	8.0±0.4	3.9±0.1
	41.4-41.8	22.0-22.7	20.4-20.9	1.65-1.78	2.1-2.1	7.6-8.7	3.7-4.0
Bottom	40.8±0.3	21.6±0.9	21.6±0.6	1.7±0.1	2.2±0.1	7.8±0.4	4.3±0.3
	40.5-41.2	20.5-22.4	21.0-22.6	1.6-1.8	2.1-2.4	7.1-8.1	4.0-4.9
Average composition	41.4±0.5	22.1±0.7	20.9±0.6	1.7±0.1	2.1±0.1	7.9±0.4	4.0±0.3
	40.5-42.2	20.5-22.8	20.2-22.6	1.4-1.8	2.0-2.4	7.1-8.7	3.6-4.9

The microstructures of JN4-AC in the top, bulk and bottom of the button ingot are shown in Figure 4.18. In the former two areas the microstructure consisted of dendrites of Nb_5Si_3 (confirmed by the WDS analyses, see below) and inter-dendritic eutectic of Nb_{ss} + Nb_5Si_3, with the vol% of the former (i.e., Nb_5Si_3) apparently being slightly higher in the bulk of the ingot, and in the latter area (i.e., in the bottom) the microstructure consisted of almost equal vol% of the two phases (i.e., the Nb_{ss} and Nb_5Si_3). Figure 4.18 shows the bright contrast phase is hafnia (HfO_2). Compared with JN3-AC, the eutectic was finer and with significantly less vol% of Nb_{ss} dendrites in JN4-AC. The microstructures in the bottom parts of JN3-AC and JN4-AC were essentially the same.
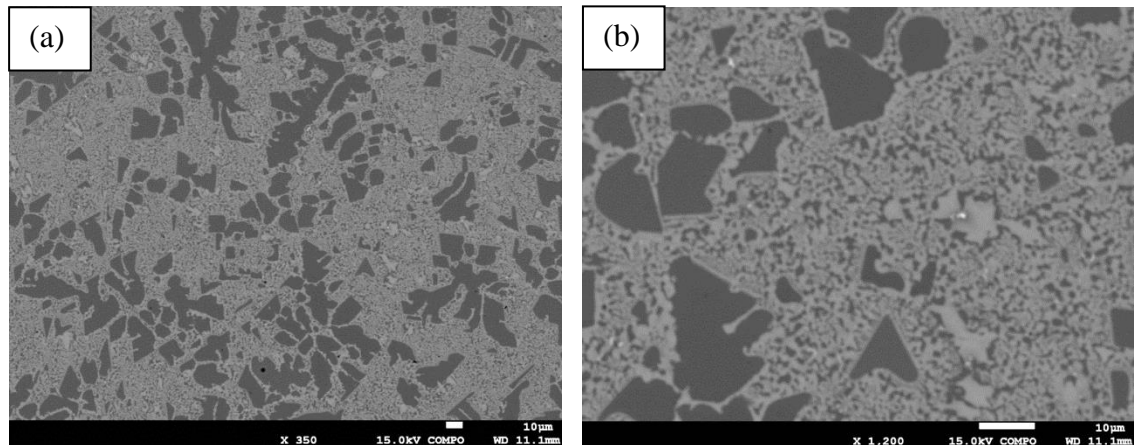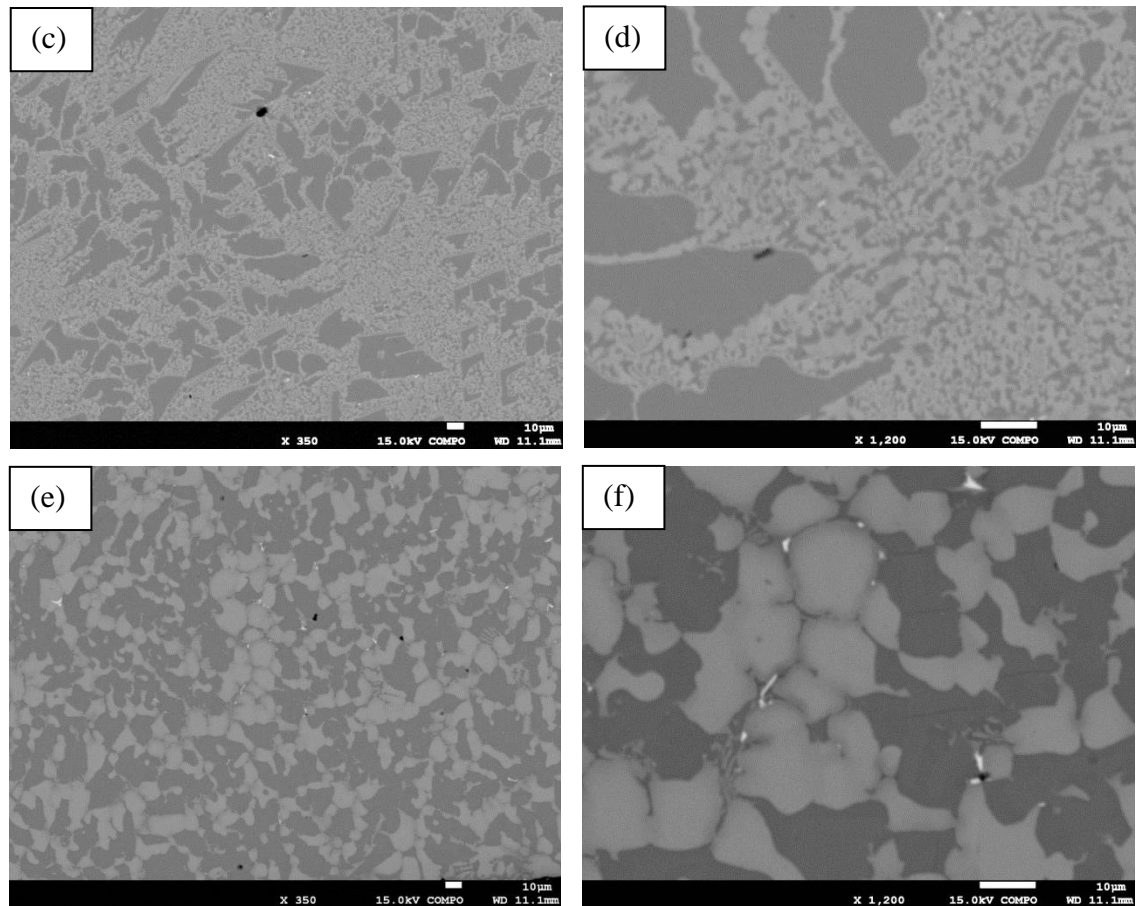
Figure 4.18 BSE at 250 X and 1200 X magnification of the top (a, b), bulk (c, d) and bottom (e, f) of JN4-AC

The XRD diffractogram for JN4-AC is shown in Figure 4.19. The data would suggest the presence of Nb_{ss} and βNb_5Si_3, in other words the XRD did not confirm the presence of Nb_3Sn in the cast microstructure. It should be remembered that the XRD for JN3-AC confirmed the same phases, namely the Nb_{ss} and βNb_5Si_3, see Figure 4.15.
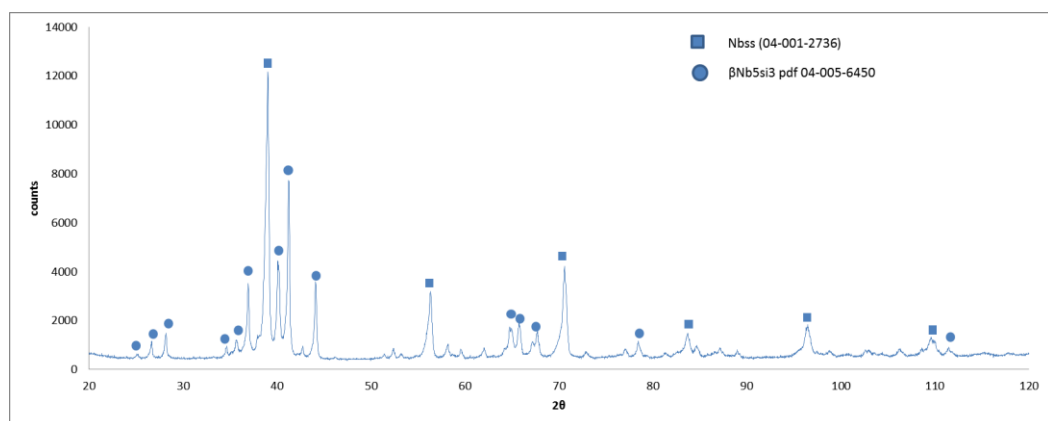
Figure 4.19 JN4 AC powder XRD pattern fitted with Sieve+

The lattice parameter of the Nb_{ss} was 3.266 Å, which is 0.37 Å smaller than the parameter of unalloyed Nb. The latter is smaller than that observed for the alloys, JN2 and JN3 though marginally greater than that for JN1-AC. The lattice parameters and the Nelson Riley plot can be seen in Table 4.12 and Figure 4.20.

Table 4.12 The calculated lattice parameters of the bcc Nb_{ss} in JN4-AC

	d (Å)	2 θ	theta	a (Å)	f (θ)	hkl	Corrected a (Å)
JN4 ac	2.306	39.02	19.51	3.262	2.705836	110	
	1.632	56.34	28.17	3.263	1.673741	200	
	1.333	70.6	35.3	3.265	1.171542	211	3.266
	1.154	83.74	41.87	3.264	0.844057	220	
	1.033	96.48	48.24	3.265	0.603842	310	
	0.943	109.6	54.8	3.265	0.412692	222	
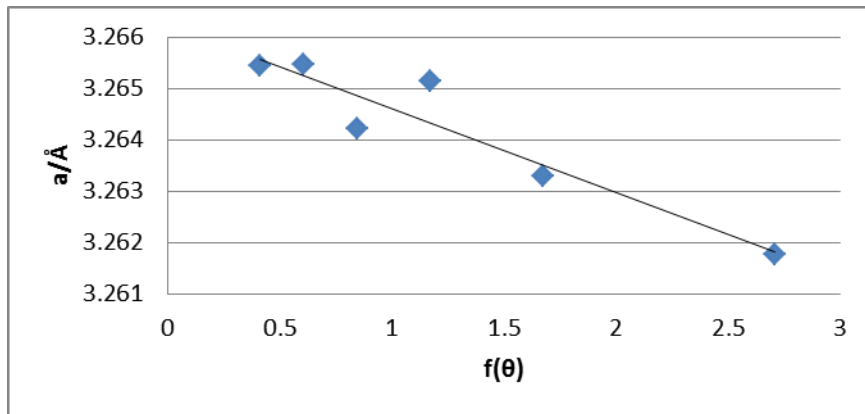
Figure 4.20 Nelson-Riley plot for the lattice parameter of the bcc Nb_{ss} in JN4-AC

X-ray elemental maps for the typical microstructure in the top of JN4-AC are shown in Figure 4.21. The Sn is observed in the areas where the Nb_{ss} was present. The BSE images in Figure 4.18 and Figure 4.21 did not show microsegregation in the two phases, in other words there were no Ti-rich areas in the Nb_{ss} and Nb_5Si_3.
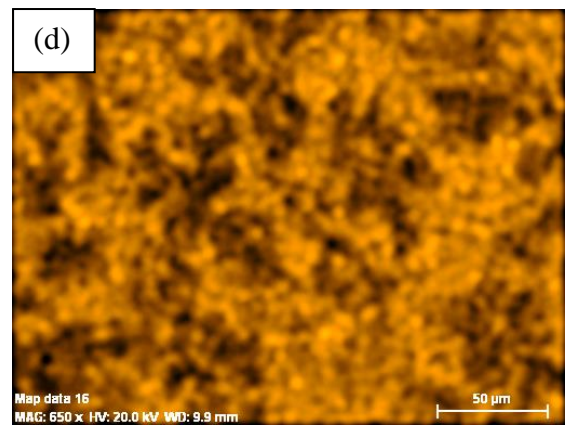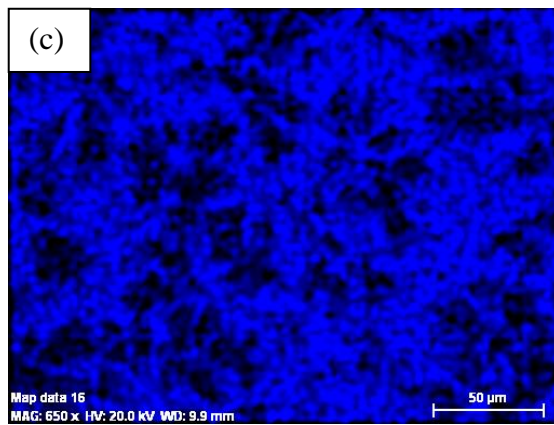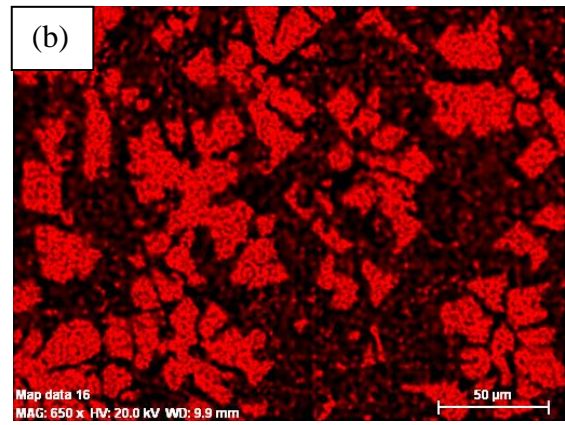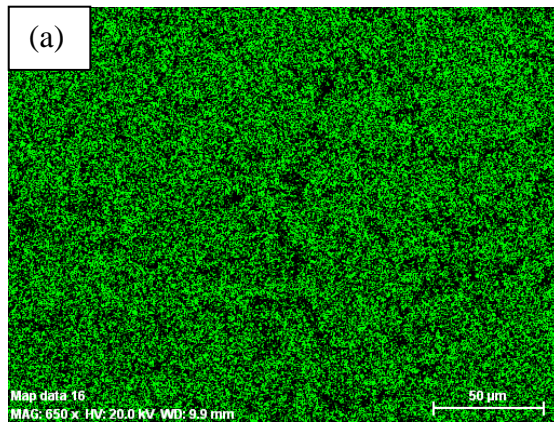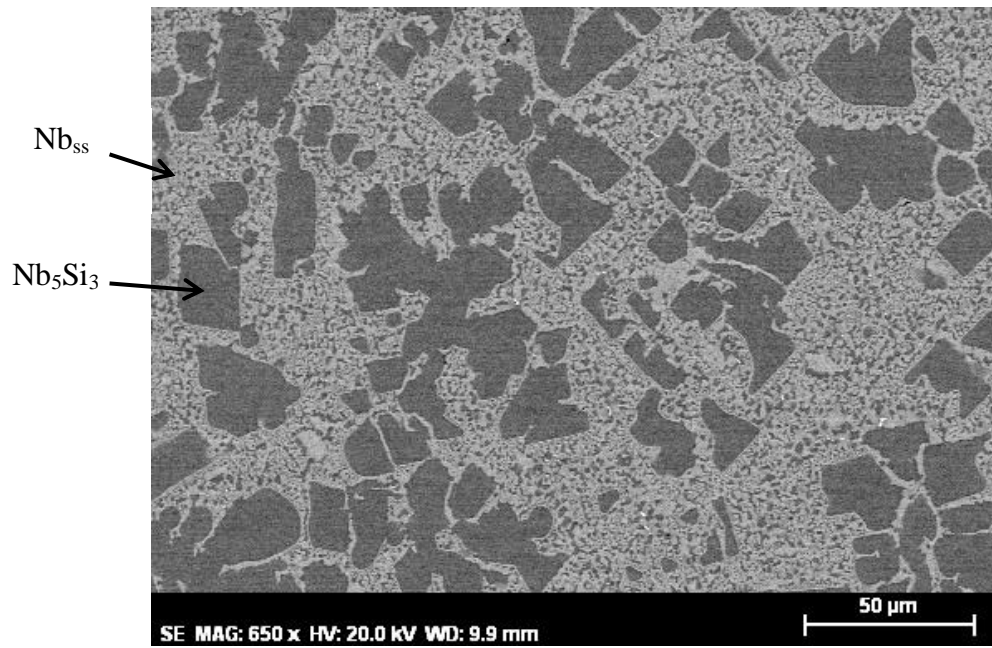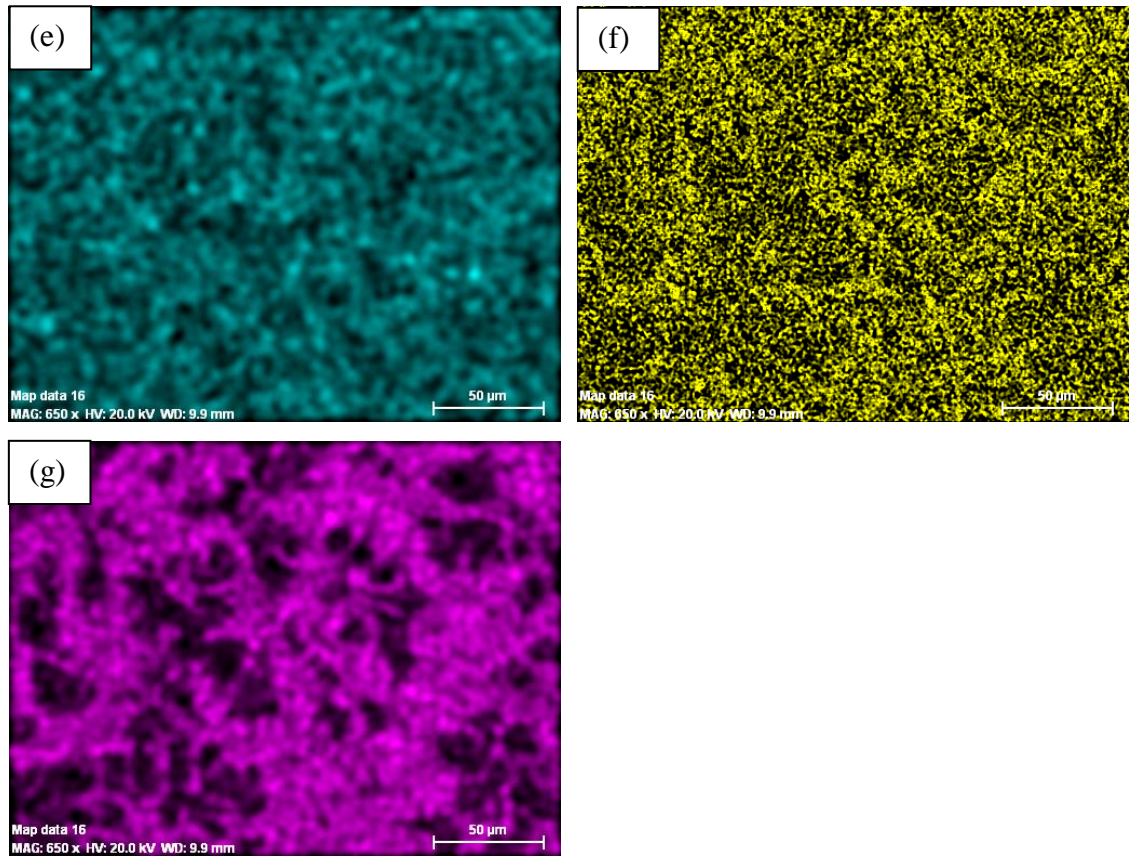
Figure 4.21 X-ray maps of the top of JN4 AC for Nb (a), Si (b), Ti (c), Cr (d), Hf (e), Mo (f) and Sn (g)

The WDS analysis data for the phases in JN4-AC is given in Table 4.13. The data confirmed the presence of Nb_{ss} and Nb_5Si_3 in the microstructure, which was suggested by the XRD. Detailed study of the JN4-AC by WDS did not find any evidence for the presence of Nb_3Sn. Thus, it was concluded that the synergy of 4 at% Sn with ~ 2 at% Cr, 2 at% Hf, 8 at% Mo, 22 at% Si and 21 at% Ti did not stabilize the Nb_3Sn.

Table 4.13 EPMA phase analysis of JN4-AC (at%)

Phase	Nb	Si	Ti	Cr	Hf	Mo	Sn
Nb_{ss}	55.0±1.9	2.3±1.2	22.0±1.3	2.2±0.5	1.7±0.2	11.5±0.6	5.3±0.3
	50.6-56.7	1.5-2.7	20.4-24.8	1.7-3.0	1.4-2.1	10.1-12.4	4.9-5.9
βNb_5Si_3	43.4±1.0	36.5±0.6	14.5±0.4	0.4±0.1	1.5±0.1	2.4±0.1	1.2±0.2
	41.6-45.1	35.2-37.1	14.2-15.8	0.3-0.6	1.4-1.7	2.2-2.5	1.0-1.5

In the Nb_{ss} the Si+Sn was 7.6 at%, and the (Ti+Cr)/(Si+Sn) was 3.2, respectively higher and lower compared with the normal Nb_{ss} in JN2 and JN3, owing to the higher Sn content of JN4. The Mo content in the Nb_{ss} was in-between the values observed for the normal and Ti rich Nb_{ss} in JN3-AC. The Cr content and the Ti + Cr in the Nb_{ss} was higher than that in the normal Nb_{ss} in JN3 owing to the higher Ti content of the alloy JN4. However, in the latter the total content of sd elements excluding Nb was higher (37.4 at%) compared with JN3 (29.8 at%), which is attributed to the higher Ti content of the alloy, and the (Cr+Hf+Mo+Ti)/(Cr+Ti) ratio was 1.54 in JN4-AC compared with (Cr+Hf+Mo+Ti+W)/(Cr+Ti)=1.46 in JN3-AC, which would suggest that essentially the same ratio can be achieved by "balancing" the absence of W with the increased content of Ti and Mo. In the Nb_5Si_3 the Si+Sn content was ~ 37 at%, higher than in JN3-AC. The concentration of Mo and Ti in Nb_5Si_3 in JN4 were also higher (which would suggest that the solubilities of these elements in Nb_5Si_3 depend on their actual concentrations in the alloy) but not the concentration of Sn, which was essentially the same in JN3 and JN4.

The solidification path of JN4-AC was calculated using the Pandat database and gave the following result, see Figure 4.22. Solidification starts at ~ 1964 °C, then L → L + Nb_5Si_3 → L + Nb_5Si_3 + Nb_{ss} → L + Nb_5Si_3 + Nb_{ss} + Ti_5Si_3 → L + Nb_{ss} + Ti_5Si_3 → L + Nb_{ss} + Ti_5Si_3 + C14 $NbCr_2$ → Nb_{ss} + Ti_5Si_3 + C14 $NbCr_2$ with the last liquid solidifying at ~ 1229 °C and vol% Nb_{ss} of 41.5% and vol% Nb_5Si_3 of 58.5%. The calculations gave Nb_5Si_3 as the primary phase, in agreement with the experimental results, the formation of hexagonal 5-3 silicide, which was not confirmed by the experimental results, the formation of C14 Laves phase, which was not confirmed by the experimental results and a final microstructure consisting of Nb_{ss}, hexagonal 5-3 silicide and Laves that is not in agreement with the experimental results. The calculated volume fractions for the solid solution and 5-3 silicide were close to the experimentally measured ones, see Table 4.1. It is proposed that the solidification path of JN4-AC was L → L + Nb_5Si_3 → L + Nb_5Si_3 + Nb_{ss} → Nb_5Si_3 + Nb_{ss} + (Nb_5Si_3 + Nb_{ss})$_{eutectic}$.
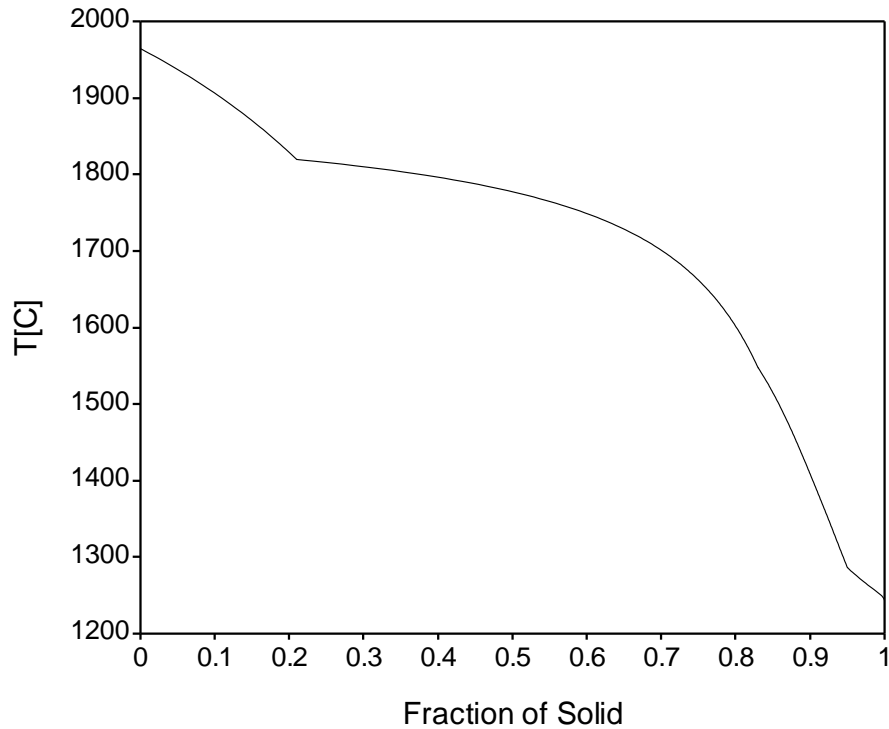
Figure 4.22 Scheil solidification path for JN4 calculated using the Pandat software

4.4   Conclusions

The JN1(Nb-20.9Si-23.5Ti-4.5Cr-5.3Al-5.1Hf), JN2 (Nb-20.4Si-16.0Ti-9.5Cr-1.7Hf-5.8Mo-2.1W-2.0Sn), JN3 (Nb-20.9Si-16.2Ti-1.9Cr-1.6Hf-6.0Mo-1.3W-2.0Sn) and JN4 (Nb-22.1Si-20.9Ti-1.7Cr-2.1Hf-7.9Mo-4.0Sn) were studied in the as cast condition. The conclusions of this research were as follows:

- The addition of Hf in JN1 increased the macrosegregation of Si. Alloying with Cr affected the macrosegregation of Si, which increased with Cr concentration in the alloy JN2 compared with the alloy JN3. Alloying with Sn affected the macrosegregation of Si, which increased with the concentration of Sn in the alloy JN4.

- The partitioning of Hf was dependant on the Hf concentration in the alloy. The Hf partitioned to the Nb_{ss} and Nb_5Si_3 where it formed Hf rich areas. This effect was strong in JN1.

- Molybdenum and W partitioned to the Nb_{ss}, Sn partitioned to the Nb_{ss}. The partitioning of Mo and W in the Nb_{ss} was opposite to that of Sn and Ti and Cr and Ti in the solid solution. The Mo and W additions probably "controlled" the partitioning of Hf in the Nb_{ss} and Nb_5Si_3 in the alloys JN2 and JN3. Titanium partitioned to the Nb_{ss} and Nb_5Si_3 and enhanced the partitioning of Cr and Hf in the former and of Hf in the latter phase.

- The βNb_5Si_3 was the primary phase in the four alloys. The hexagonal γNb_5Si_3 was not formed during solidification in any of the four alloys. $Nb_{ss} + Nb_5Si_3$ eutectic was formed in-between Nb_5Si_3 grains in all four alloys. The Nb_3Sn was not formed in the cast alloys JN2, JN3 and JN4.

Heat Treated Microstructures: Results and Discussion

The alloys were heat treated to homogenise the microstructure and determine the stability of the phases present in each alloy respectively. The alloys JN1, JN2, JN3 and JN4 were heat treated at 1500 °C for 100 h, as described in the experimental chapter, see section 3. The temperature of 1500 °C was selected as it is below the eutectoid transformation temperature in the Nb-Si binary system (see section 2.1.1). The simpler heat treated alloy microstructures allowed study using nano-hardness testing to be achieved, which was not possible for the AC alloys.

The choice of heat treatment conditions allowed comparisons to be made with the microstructures of other Nb silicide based alloys studied in our group and elsewhere. In this chapter the heat treated microstructures of JN1, JN2 and JN3 and JN4 are presented and discussed separately.

5.1   Alloy Nb-19.1Si-24.1Ti-4.1Cr-3.8Al-5.7Hf (JN1-HT)

The actual composition of the heat treated specimen (JN1-HT), which was taken from the bulk of the alloy, is given in Table 5.1. Compared with the average composition of the cast alloy and the composition of the bulk JN1-AC (Table 4.2) and considering the accuracy of analysis, the average concentrations of the solutes in JN1-HT were essentially the same with the exception of Al, the concentration of which was lower in JN1-HT compared with JN1-AC. The data in Table 5.1 however shows significant difference between the minimum and maximum analyses values for Si and Ti, which is attributed to the macrosegregation of these elements in JN1-AC. Furthermore, there is more than 2 at% difference between the minimum and maximum analyses values for Al, which was not observed in JN1-AC.

Table 5.1 Large area analysis of JN1 HT bulk (at%)

Area of alloy	Nb	Si	Ti	Cr	Al	Hf
Bulk analysis	43.1±1.0 42.2-44.7	19.3±1.8 15.3-21.2	24.1±0.8 22.9-25.1	4.1±0.5 3.5-5.0	3.8±0.9 2.5-4.9	5.7±0.3 5.3-6.0

Figure 5.1 shows the bulk microstructure for JN1 HT; it is comprised of two phases, Nb_5Si_3 and Nb_{ss} that the $NbCr_2$ was not stable after the heat treatment. There was also HfO_2, which formed during the heat treatment as the environment was not completely free of O_2, although every precaution was taken to minimise it. Homogeneity was achieved in the Nb_{ss} as there was no Hf-rich Nb_{ss}, however the Nb_5Si_3 still displayed strong Hf partitioning. The eutectic regions observed in JN1-AC were not observed in JN1-HT, thus the microstructure of JN1-HT consisted of large Nb_5Si_3 grains in an Nb_{ss} matrix. The Nb_5Si_3 silicide exhibited three distinct contrasts that were classified as Nb_5Si_3, Hf-rich Nb_5Si_3 and Hf-poor Nb_5Si_3.
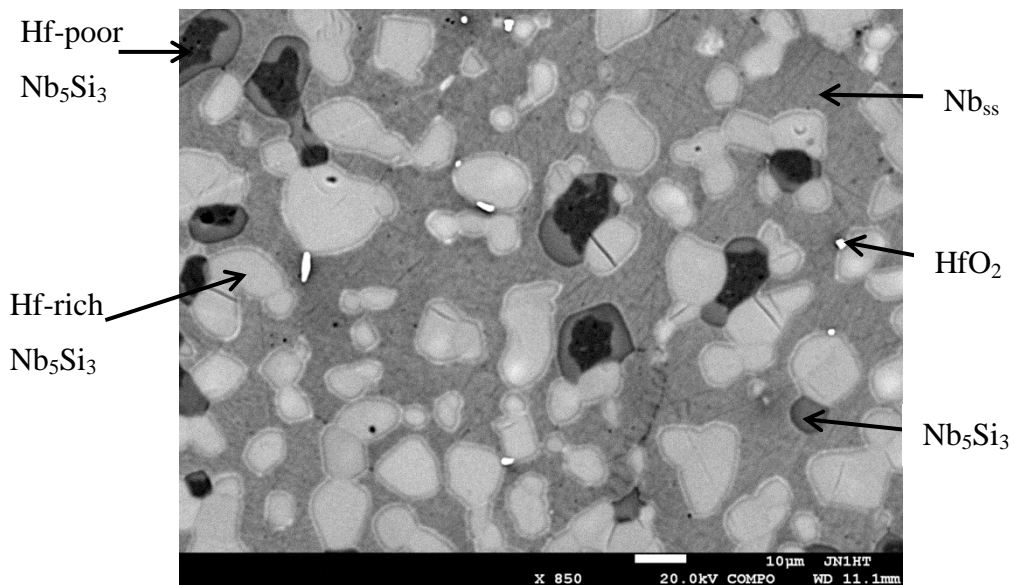
Figure 5.1 BSE image of JN1 HT at 850X magnification (phases are labeled on the diagram)

It is useful to compare the microstructure of the alloy JN1-HT with those of the heat treated alloys KZ5 (48Nb-24.3Ti-15.8Si-7.6Cr-4.9Al at%) and JG4 (41.4Nb-

24.2Ti-18.2Si-4.6Cr-4.8Al-1.7Mo-5.1Hf-5Sn at%). Figure 5.2 shows the microstructure of KZ5-HT after 100h at 1500 °C; the circled regions on the Nb_5Si_3 were thought to be areas of Nb_{ss} which precipitated at the centre of the Nb_5Si_3 grains during the transformation of β to αNb_5Si_3 (Zelenitsas & Tsakiropoulos 2005; Geng, Tsakiropoulos, et al. 2006b). Around the edge of the Nb_5Si_3 there are dark halos which were thought to be the C14 $NbCr_2$ Laves phase precipitating on the Nb_5Si_3 grain boundary; there was however no EDS or XRD data provided in (Zelenitsas & Tsakiropoulos 2005) to support their claims.
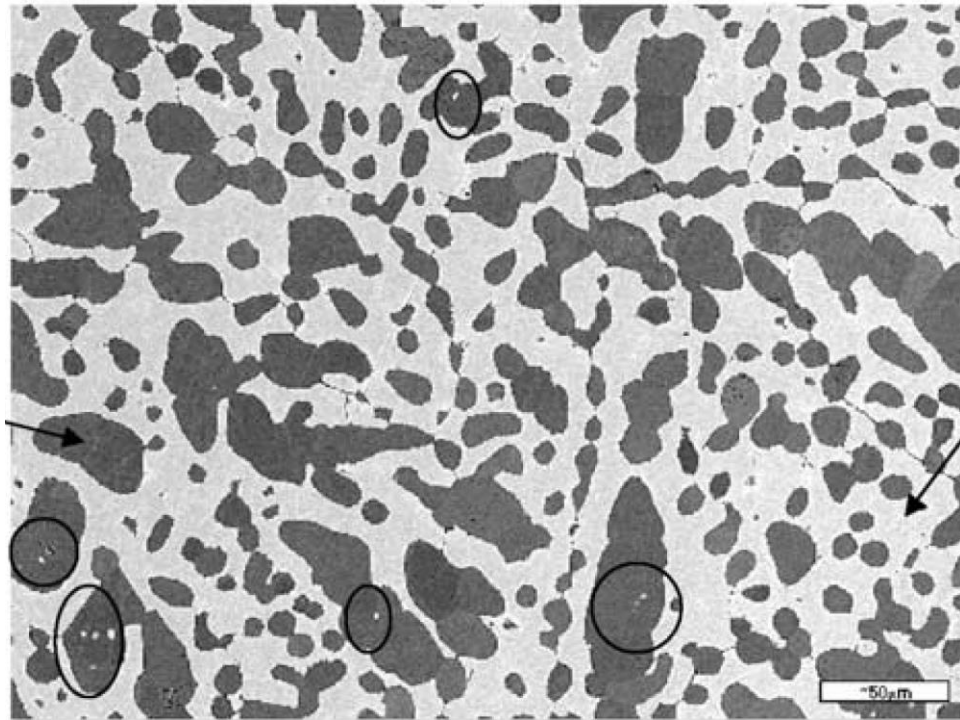
Figure 5.2 BSE image of KZ5-HT 300X magnification (dark regions are Nb_5Si_3, light regions are Nb_{ss}) (Zelenitsas & Tsakiropoulos 2005)

Figure 5.3 shows a typical BSE image of JG4 HT; like KZ5-HT there also seems to be Nb_{ss} precipitates within the Nb_5Si_3 grains (though they were too small to be analysed). Unlike KZ5-HT there was no $NbCr_2$ Laves phase after the heat treatment but in the Nb_5Si_3 silicide there was partitioning of Hf leading to the formation of Hf-rich regions.
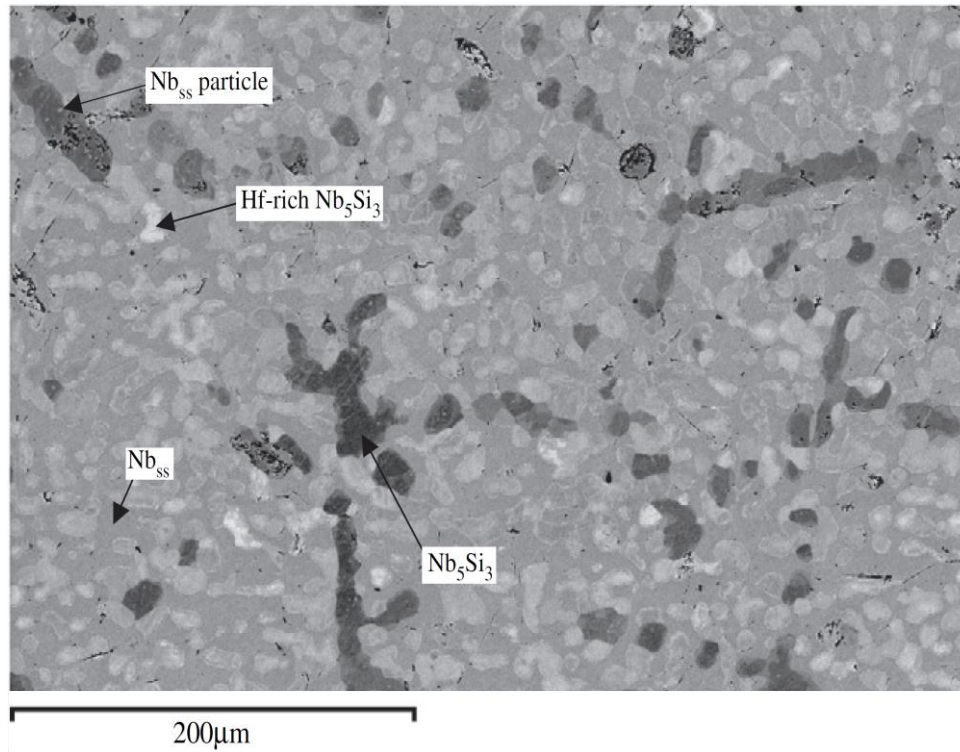
Figure 5.3 BSE image of JG4 HT; with individual phases labled

The microstructure of JN1-HT was therefore very similar to that seen in JG4-HT; with Hf partitioning to form discreet Hf-rich Nb_5Si_3 grains within the Nb_{ss} matrix. Unlike both KZ5-HT and JG4-HT, in JN1-HT the Nb_{ss} precipitates were not clearly observed within the Nb_5Si_3 phase using BSE images. There were holes in some Nb_5Si_3 grains, therefore pull-out of Nb_{ss} may have occurred during polishing. Another possible reason for the lack of Nb_{ss} precipitation in the Nb_5Si_3 may be the sluggish transformation kinetics of Nb_5Si_3, as the centre of the Nb_5Si_3 grains was still inhomogeneous.

The partitioning of Hf to the Hf rich regions, was accompanied by sluggish Hf within the Nb_5Si_3 grains themselves. The Hf-rich Nb_5Si_3 grains were therefore formed due to the relatively high diffusion rates within the Nb_{ss} which lead to a drop in overall Hf content within the Nb_{ss} after HT (see Table 5.3). The addition of 5 at% Hf in JN1 destabilised the $NbCr_2$ phase and stabilised the hexagonal γNb_5Si_3 phase that is detrimental for creep (see below). Compared with JG4, which contained the βNb_5Si_3 stabilising Mo, the synergy of Hf with the other solutes in JN1 had a strong enough

effect on partitioning to the Nb_5Si_3 grains that lead to the formation of discreet Hf-rich γNb_5Si_3.

In order to understand the dispersion and partitioning of elements within JN1-HT, X-ray maps were taken. Figure 5.4 shows the X-ray maps for all the elements in JN1-HT; the maps clearly show the partitioning preference of each element. The Nb map in conjunction with the Hf map shows that in areas of low Nb, Hf levels are higher. This relationship between Nb and Hf, when compared with the Si map, is due to the partitioning effect of Hf within the Nb_5Si_3, as mentioned earlier. Titanium can be seen to be partitioning primarily to the phases that are rich in Hf (brighter = higher Hf content), which is to be expected. The chromium content is predominantly higher in the Nb_{ss} and its concentration is very low in the Nb_5Si_3 and Hf-poor Nb_5Si_3 grains. As would be expected, the Cr content in the Hf-rich Nb_5Si_3 is slightly higher due to its affinity with Ti and Hf. The aluminium content is fairly constant throughout the alloy with a slightly higher concentration in the Nb_{ss} and Hf-rich Nb_5Si_3. The Cr and Ti maps might provide evidence of precipitation in the Nb_{ss}. Compared with KZ5-HT where the precipitation in the Nb_{ss} had grown to a size that made them visible in BS imaging; this would not seem to be the case in JN1-HT owing to the sluggish diffusion.
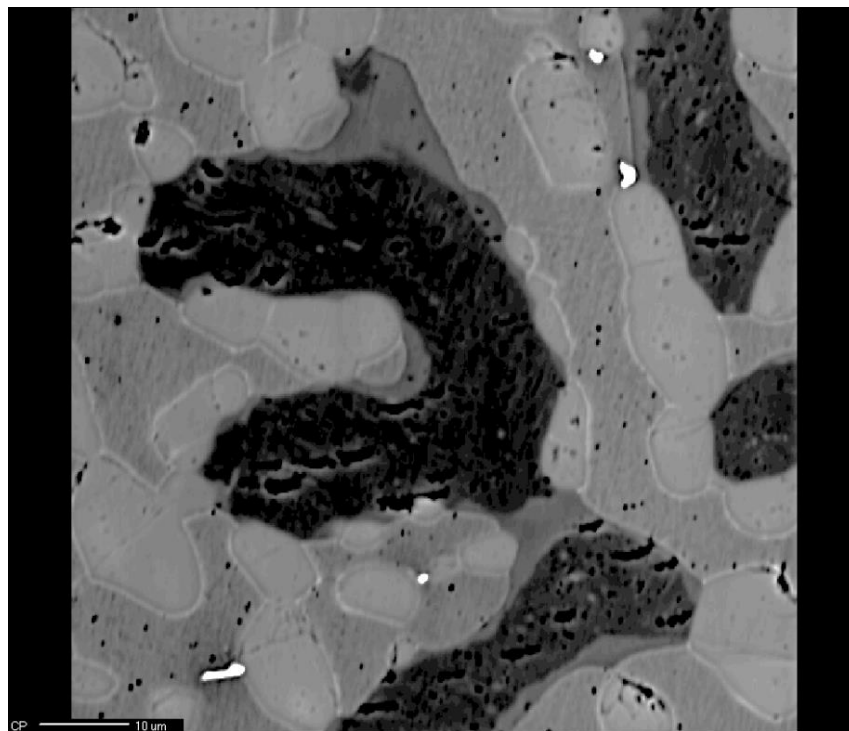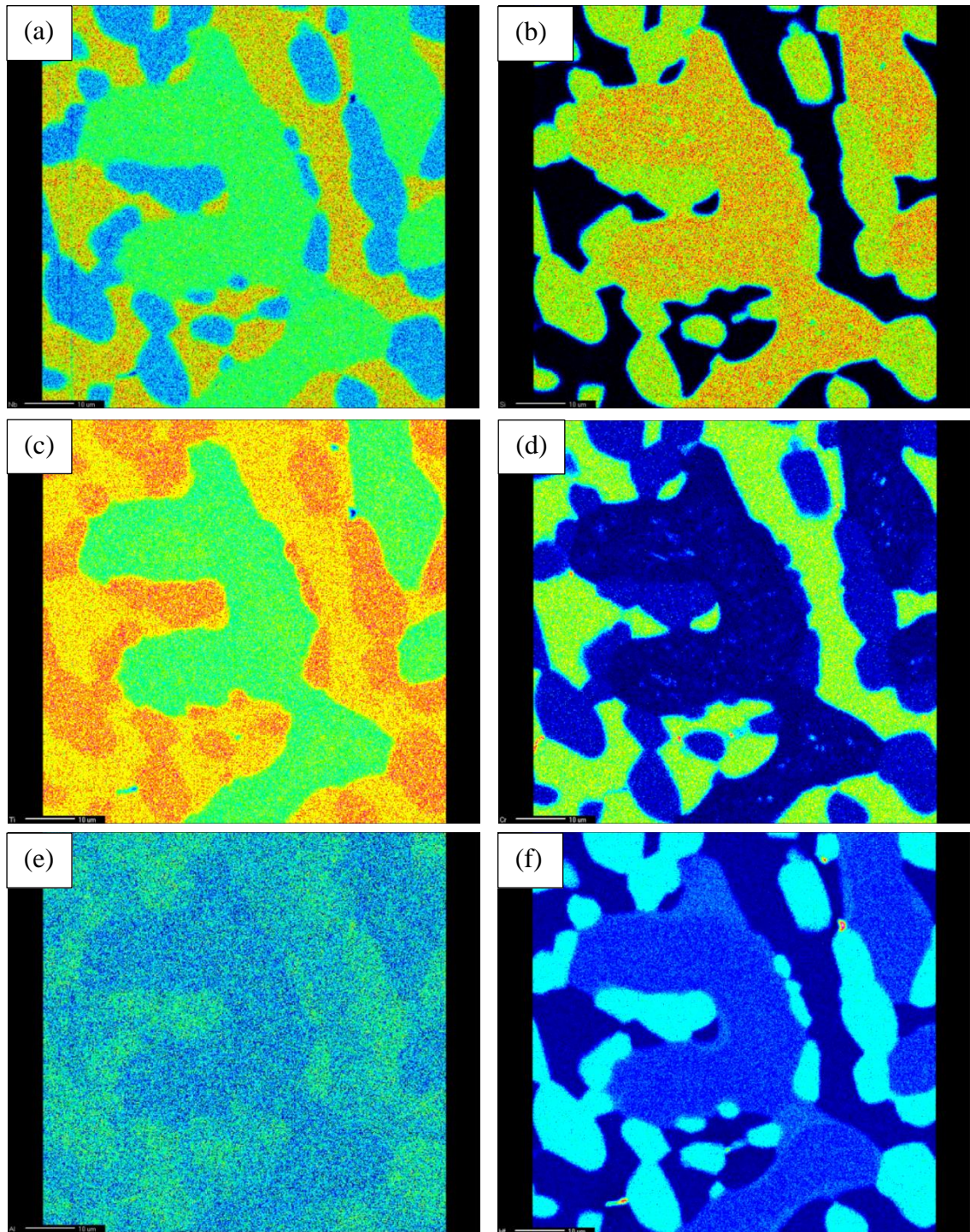
Figure 5.4 X-ray maps of (a)Nb, (b)Si, (c)Ti, (d)Cr, (e)Al and (f)Hf from the bulk of JN1 HT

The halo effect around the outside of the Hf rich Nb_5Si_3 is visible in the Nb and Si maps as areas of lower Nb and higher Si. This increase in Si and decrease in Nb may suggest that the Hf-rich Nb_5Si_3 is still growing and these boundary areas are representative of an

intermediate growth stage which heralds the progression of the silicide interface and the consumption of Nb_{ss}.

Figure 5.5 shows the XRD diffractogram of JN1-HT. In JN1-AC the presence of βNb_5Si_3 and Nb_{ss} was clearly indicated by numerous peaks. The diffractogram of JN1-HT is similar to that of JN1-AC alloy as it also displays Nb_{ss} and βNb_5Si_3 as the main phases in Figure 5.1 there are also small peaks which correspond to both α and γ Nb_5Si_3, though these contribute very little to the pattern. This is consistent with the WDS data (see below) that shows the presence of γNb_5Si_3 and Nb_5Si_3. It should be noted that the microstructure images would suggest a high vol% of γNb_5Si_3, however the diffraction pattern does not reflect this observation.
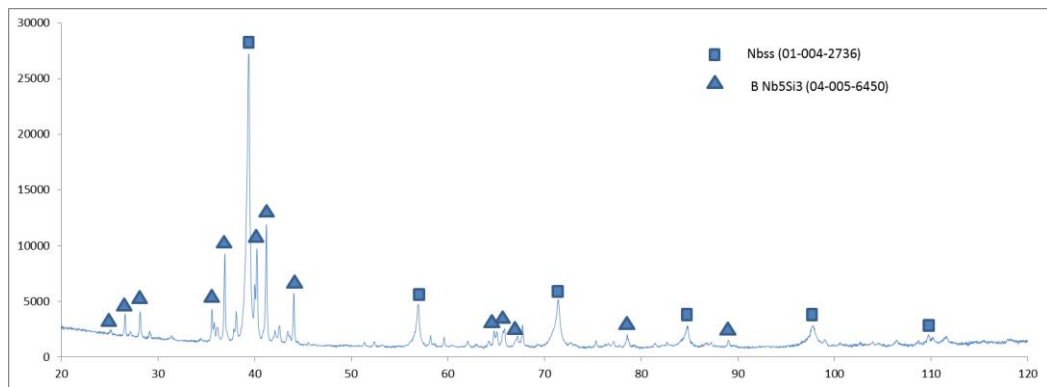
Figure 5.5 JN1-HT powder X-ray diffractogram fitted with Sieve+ software

The lattice parameter of the Nb_{ss} in JN1-HT is 3.246 Å; this was a decrease in lattice parameter compared with that for JN1-AC (3.270 Å). The lattice parameter for pure Nb_{ss} is 3.303 Å. This decrease in the lattice of Nb_{ss} was attributed to the changes in the solute concentration in Nb_{ss} of Si, Hf, Ti and Al after the heat treatment and the homogenisation of the solid solution to a single Nb_{ss} phase chemistry. The lattice parameters and the Nelson-Riley plot can be seen in Table 5.2 and Figure 5.6.

Table 5.2 The calculated lattice parameters of the bcc Nb_{ss} in JN1-HT

	d (Å)	2 θ	theta	a (Å)	f (θ)	hkl	Corrected a (Å)
JN1 HT	2.288	39.355	19.6775	3.235	2.67811	110	
	1.617	56.915	28.4575	3.233	1.649261	200	
	1.320	71.375	35.6875	3.234	1.149317	211	3.246
	1.143	84.735	42.3675	3.233	0.822937	220	
	1.023	97.755	48.8775	3.234	0.583027	310	
	0.942	109.735	54.8675	3.263	0.41097	222	
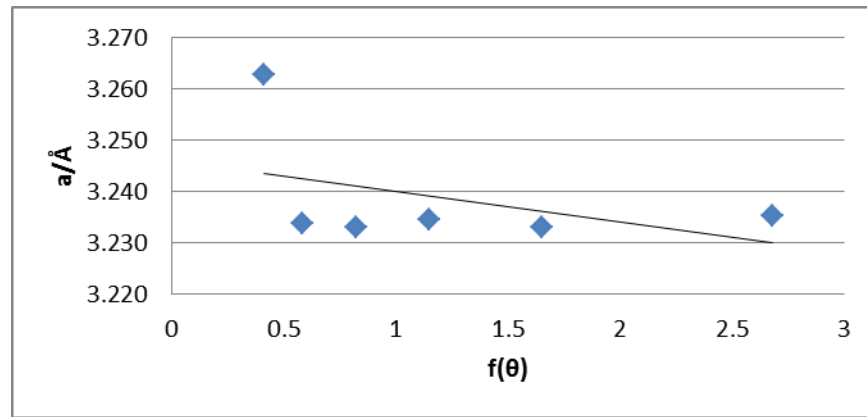
Figure 5.6 Nelson-Riley plot for the lattice parameter of the bcc Nb_{ss} in JN1-HT

Table 5.3 shows the WDS point analysis data for the phases present in JN1-HT; the phases in this table correspond with the four phases that can be seen in Figure 5.1 and Figure 5.4. The largest change compared with the microstructure of JN1-AC is the homogenisation of Nb_{ss} and the partitioning of Hf in the Nb_5Si_3. After the heat treatment the Hf content of the Nb_{ss} dropped to 2.2 at%. In the homogenised Nb_{ss} the Si content was as in the normal solid solution reported for other heat treated Nb silicide based alloys and the Cr content had increased (Grammenos & Tsakiropoulos 2010a; Geng, Tsakiropoulos & G Shao 2007; Zelenitsas & Tsakiropoulos 2005).

Table 5.3 WDS analysis of JN1-HT (at%)

Phase	Nb	Si	Ti	Cr	Al	Hf
Nb_{ss}	53.7±0.8	0.5±0.1	27.0±0.1	9.4±0.3	7.1±0.7	2.2±0.0
	53.1-54.9	0.5-0.8	26.9-27.2	9.0-9.8	6.1-7.7	2.1-2.2
Hf rich	27.3±0.3	32.5±0.1	26.6±0.1	1.2±0.0	3.1±0.2	9.3±0.1
Nb_5Si_3	27.1-27.9	32.3-32.7	26.3-26.7	1.2-1.3	2.7-3.3	9.0-9.5
Nb_5Si_3	40.9±0.3	33.3±0.2	18.2±0.2	0.5±0.0	1.7±0.1	5.4±0.2
	40.6-41.2	33.1-33.6	17.9-18.5	0.4-0.5	1.6-1.8	5.2-5.7
Hf poor	41.3±0.1	32.0±0.3	18.8±0.1	0.6±0.1	2.7±0.3	4.6±0.1
Nb_5Si_3	41.2-41.5	31.4-32.4	18.7-18.8	0.5-0.7	2.4-3.2	4.5-4.7

The Nb_5Si_3 was observed as Hf rich Nb_5Si_3, Hf poor Nb_5Si_3 and Nb_5Si_3; each of these has different compositions and locations within the microstructure. The Hf rich phase,

as can be seen in Figure 5.1, forms as discreet grains which are often found adjacent to the other Nb_5Si_3 phases. The Hf poor Nb_5Si_3 is found at the centre of the Nb_5Si_3 phase owing to incomplete homogenisation and inward diffusion of Hf from the surrounding Nb_{ss}.

The Ti + Hf content of the Nb_5Si_3 silicide can be used to deduce its structure. According to Bewlay, if the ratio Nb/(Ti+Hf) is less than one the Nb_5Si_3 has the hexagonal crystal structure. The data in Table 3.2 for the Hf rich Nb_5Si_3 would thus suggest that this is the γNb_5Si_3, which has also been suggested by the XRD data. The above ratio for the Hf poor Nb_5Si_3 and "normal" Nb_5Si_3 is greater than one and thus the aforementioned would have the tetragonal structure of βNb_5Si_3 or αNb_5Si_3, which has been also suggested by the XRD data. Compared with JN1-AC, the Hf content of the γNb_5Si_3 was the same in JN1-HT but the Ti concentration had increased. In the "normal" Nb_5Si_3 the Si content had increased and the concentrations of Ti, Cr and Al had decreased. In the three 5-3 silicides the sp element content was about 35 at%, in agreement with previous research on Nb silicide based alloys. All the aforementioned changes in concentration of solutes in the 5-3 silicides concern elements with smaller atomic radius than Nb. Thus, the changes in the microstructure of JN1-HT are attributed to the diffusion of the smaller elements while Hf, being the largest element, had sluggish diffusion kinetics and is therefore regarded as the solute determining the rate of homogenisation. The Nb_5Si_3 phase which surrounded the Hf poor Nb_5Si_3 had a composition similar to that of the Nb_5Si_3 in KZ5-HT (Zelenitsas & Tsakiropoulos 2005) and JG4-HT (Geng, Tsakiropoulos & G Shao 2007).

5.2   Alloy Nb-20.5Si-15.3Ti-10Cr-1.6Hf-5.6Mo-2W-1.6Sn (JN2-HT)

The actual composition of the heat treated specimen of alloy JN2 (JN2-HT), which was taken from the bulk of the alloy, is given in Table 5.4. Compared with the average composition of the cast alloy and the composition of the bulk JN2-AC (see Table 4.5) and considering the accuracy of analysis, the average concentrations of the solutes in JN2-HT were essentially the same. The data in Table 5.4 however shows significant

difference between the minimum and maximum analyses values for Si, which is attributed to the macrosegregation of this element in JN2-AC, see Table 4.5.

Table 5.4 EDS Large area analysis of JN2-HT (at%)

Area of alloy	Nb	Si	Ti	Cr	Hf	Mo	W	Sn
Bulk	43.0±0.8	20.5±0.7	15.3±0.8	10.0±1.1	1.6±0.1	5.6±0.2	2.0±0.3	1.9±0.2
	41-43.8	18.7-21.5	14.3-16.7	9.2-13	1.3-1.8	5.3-6.1	1.6-2.4	1.6-2.1

Figure 5.7 displays the microstructures of JN2 HT After the heat treatment at 1500°C for 100h all eutectic regions had disappeared and the Nb_{ss} was homogenised. The $NbCr_2$ Laves phase was still present and continued to grow at the Nb_5Si_3 grain boundaries forming larger grains. The Nb_5Si_3 continued to have Ti-rich areas and, much like the alloys KZ5 and JG4, Nb_{ss} precipitates were formed within the Nb_5Si_3 grains. HfO_2 had precipitated on the edge of Nb_5Si_3 as the Hf scavenged Oxygen from the Nb_{ss}.
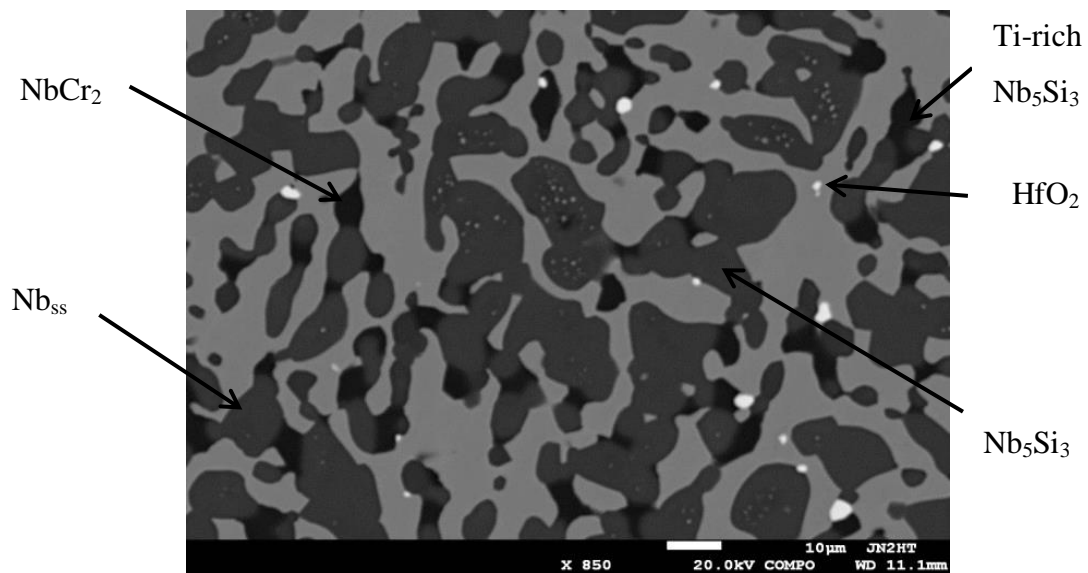
Figure 5.7 BSE image of JN2 HT (1500 °C/100 h)

Figure 5.8 shows X-ray maps for Nb, Si, Ti, Cr, Hf, Mo, W and Sn, taken from an area in the bulk of JN2-HT. The Nb, Si, Ti, Cr, Hf, Mo, W and Sn maps display the positioning of the three phases: Nb_{ss}, Nb_5Si_3 and $NbCr_2$. The $NbCr_2$ phase has notably lower Nb content than the surrounding Nb_{ss} and Nb_5Si_3 but contains more Si than the

Nb_{ss} phase. The precipitates within the Nb_5Si_3 grains are not easily distinguished on the Ti, Hf or Nb maps; the Mo and Cr maps however show the same intensity as the surrounding Nb_{ss} which advocates the presence of Nb_{ss} precipitates. The Ti map shows areas of Ti rich Nb_5Si_3, located adjacent to the Laves phase. The Hf map shows Hf rich regions which correspond to HfO_2. The W, Mo and Sn maps each display a propensity for partitioning to the Nb_{ss} phase rather than the Nb_5Si_3. Compared with JN1-HT and JG4-HT there was little or no damage to the silicide grains in the form of visible micro cracks or sample preparation damage.
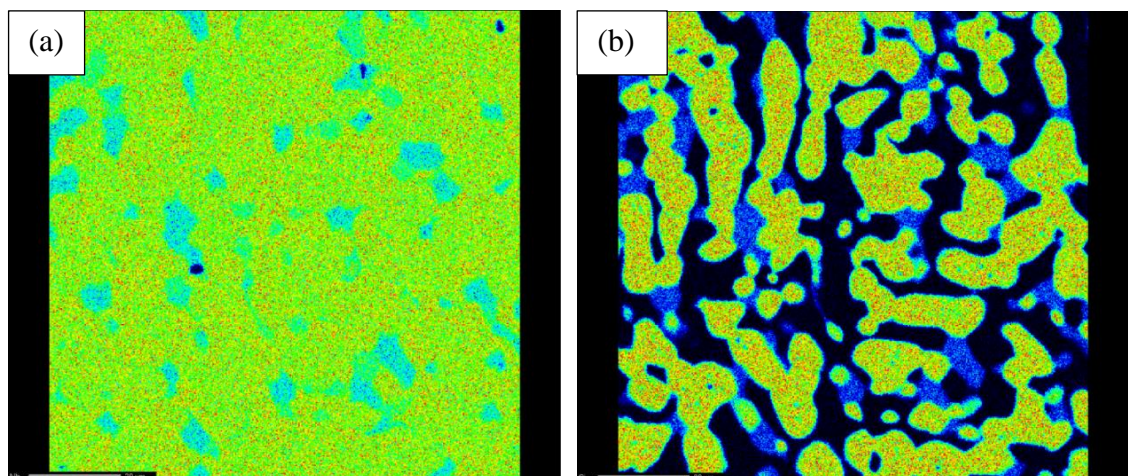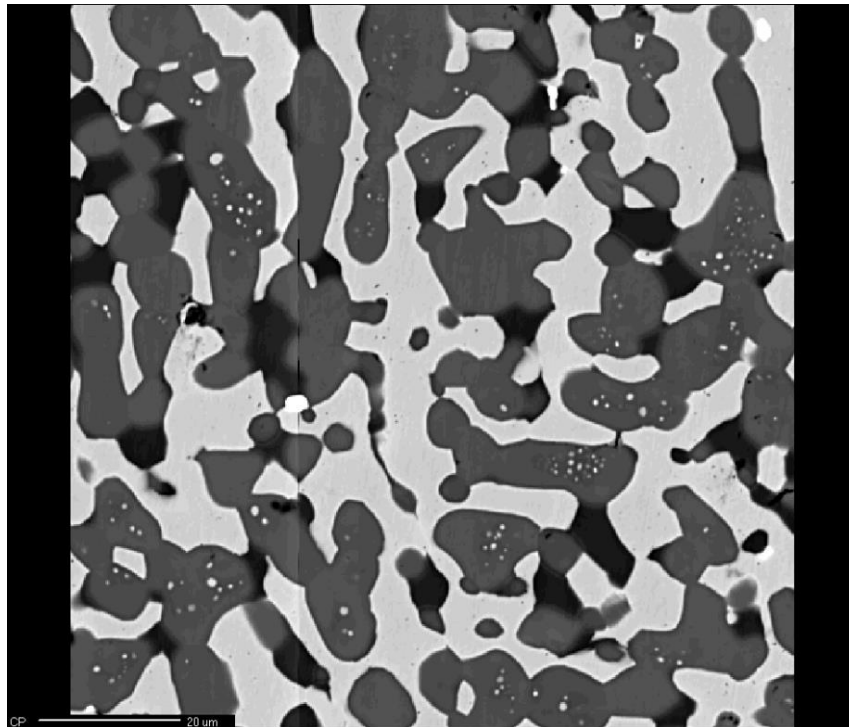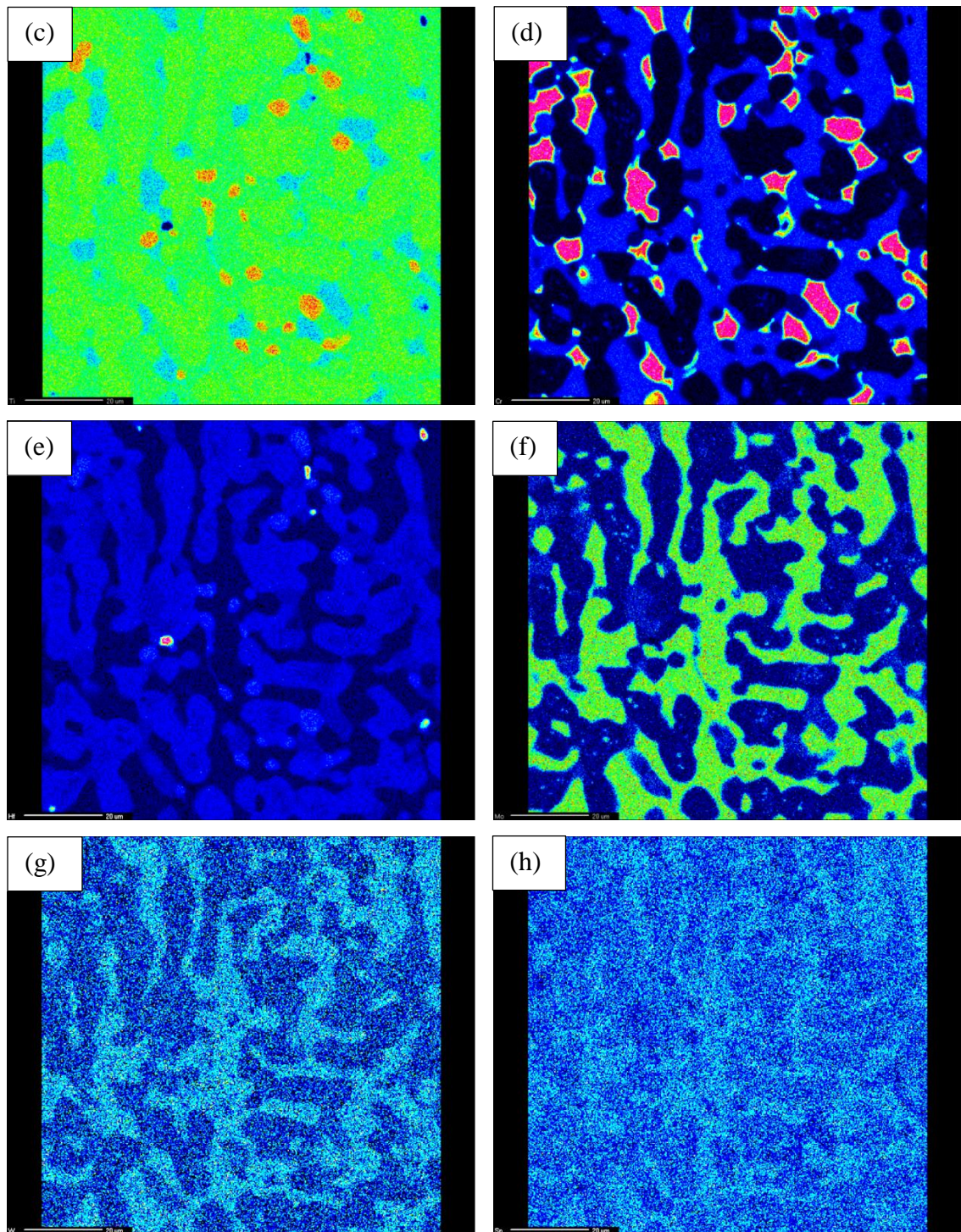
Figure 5.8 X-ray maps of JN2 HT bulk showing elements: Nb (a), Si (b), Ti (c), Cr (d), Hf (e), Mo (f), W (g), Sn (h)

The composition of alloy JN2 is close to that of the alloy JG6 (Nb-18.8Si-24.6Ti-4.8Cr-4.6Al-5.2Hf-1.8Mo-5.1Sn) (Geng & Tsakiropoulos 2007). As we can see, both alloys have Sn in synergy with TM, RM and simple metals; in the case of JN2 there is no Al

present and TM=Cr, Hf, Ti and RM=Mo,W. However, the alloy JG6 was richer in Hf and Ti and leaner in Cr, Mo and Sn compared with JN2. The microstructure of JG6-HT (1300 °C/100 h) is shown in Figure 5.9, which is reproduced from (Geng & Tsakiropoulos 2007). Figure 5.9 shows a phase labelled Sn rich Nb_{ss}, which subsequent research in the group has confirmed it to be the Nb_3Sn intermetallic (Si+Sn+Al=19.7 at%), which is formed in Nb silicide based alloys with Sn $\geq$ 5 at% (Vellios & Tsakiropoulos 2007b). The latter intermetallic was not observed in JN2-HT owing to its low Sn content, which is agreement with other work in the group (Tsakiropoulos & Singh sethi 2012). The presence of Hf rich Nb_5Si_3 was not confirmed in JN2-HT. In both alloys (i.e., JG6 and JN2) the $NbCr_2$ Laves phase was stable.
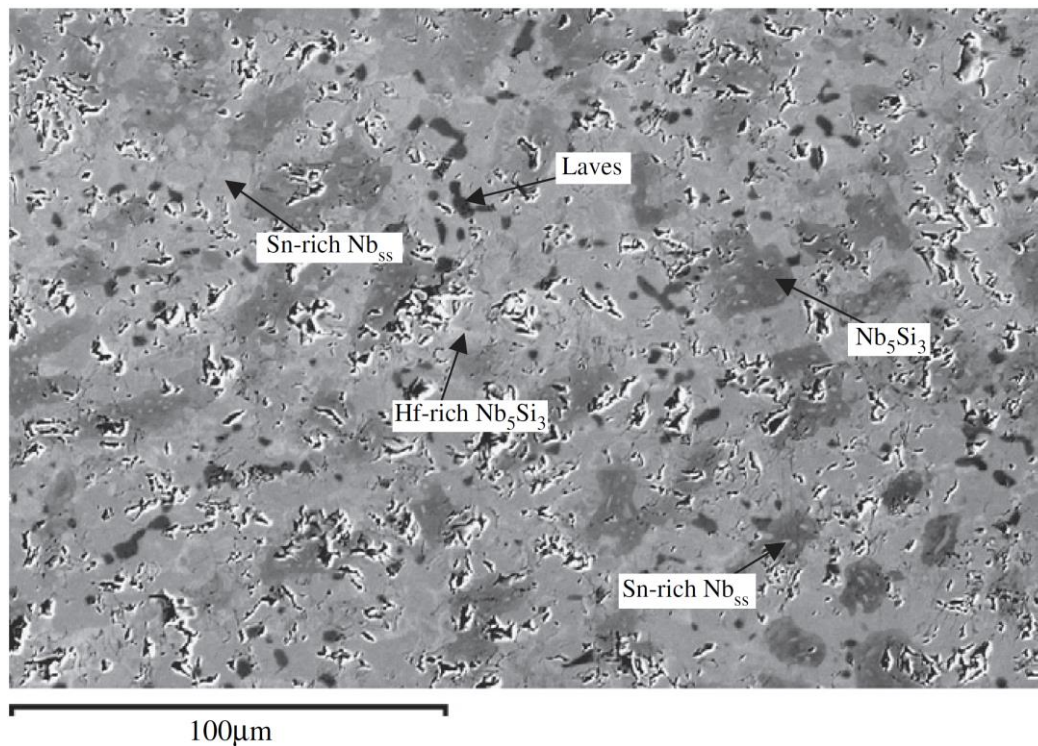
Figure 5.9 Bulk BSE image of JG6 HT: Nb-18Si-24Ti-5Al-5Cr-5Hf-2Mo-5Sn (100h at 1300°C)

Figure 5.9 shows severe micro-cracking in the microstructure, which was not observed in JN2-HT. If the latter were to be attributed to anisotropy of properties, then comparison of the microstructures of KZ5-HT (see Figure 5.2), JG4-HT (Figure 5.3), JN1-HT (where the Nb_5Si_3 exhibited micro-cracking, see Figure 5.1 and Figure 5.4) and JG6-HT would suggest:

(i)   that when the alloying of Nb silicide based alloys with Hf leads to formation
        of Hf rich areas in Nb_5Si_3 the latter becomes anisotropic (KZ5 vs JN1),

(ii)   that when alloying with Sn and Hf leads to the formation of Nb_3Sn and Hf
        rich areas in Nb_5Si_3 the anisotropy in the microstructure is enhanced (KZ5 vs
        JG6), and

(iii)   That when alloying with Hf and Sn avoids the formation of Nb_3Sn and Hf
        rich Nb_5Si_3 anisotropy in the microstructure is less likely (JG6 vs JN2).

Figure 5.10 shows the XRD diffractogram for JN2-HT; it shows the existence of Nb_{ss}
and αNb_5Si_3. Like the XRD data for JN2-AC, peaks for the $NbCr_2$ Laves phase were not
present in the diffractogram this was attributed to the low vol% of this phase. There
were no peaks for βNb_5Si_3 the transformation $\beta Nb_5Si_3 \rightarrow \alpha Nb_5Si_3$ after the heat
treatment.
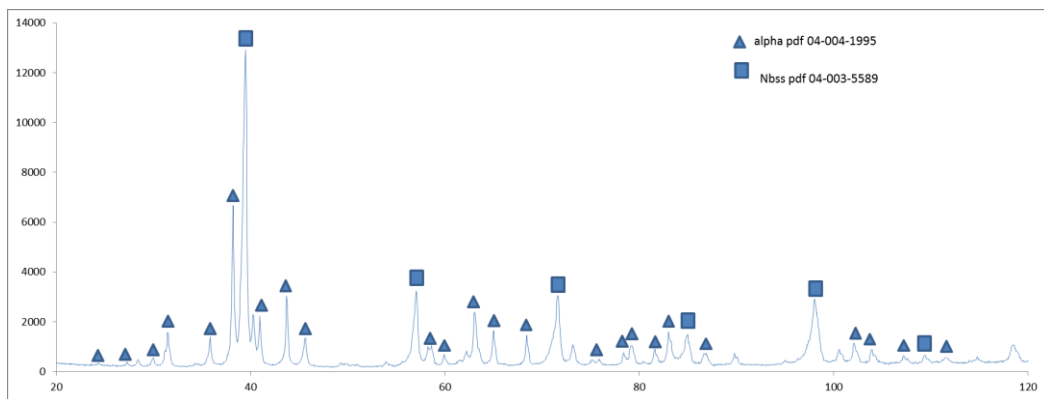
Figure 5.10 JN2 HT powder XRD pattern fitted with Sieve+

The d spacing calculated for each of the Nb_{ss} characteristic peaks of JN2-HT were used
to calculate an average lattice parameter. The calculated lattice parameter of Nb_{ss} in
JN2-HT was 3.246 Å, slightly lower than that in JN2-AC (3.254 Å) and the same as that
of JN1-HT. The calculated lattice parameters and Nelson Riley plot can be seen in
Table 5.5 and Figure 5.11.

Table 5.5 The calculated lattice parameters of the bcc Nb$_{ss}$ in JN2-HT

	d (Å)	2 θ	theta	a (Å)	f (θ)	hkl	Corrected a (Å)
JN2 HT	2.282	39.45	19.725	3.228	2.670326	110	
	1.613	57.05	28.525	3.226	1.643576	200	
	1.318	71.55	35.775	3.227	1.144356	211	
	1.141	84.95	42.475	3.226	0.818432	220	3.246
	1.020	98.05	49.025	3.226	0.578286	310	
	0.944	109.3	54.65	3.271	0.416534	222	
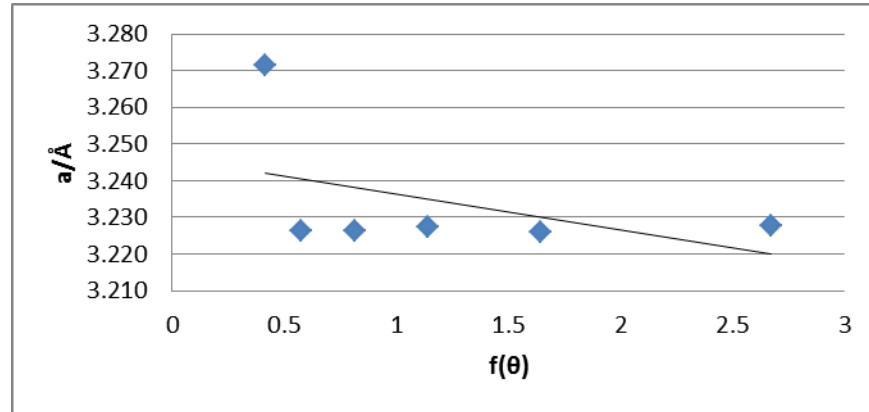
Figure 5.11 Nelson-Riley plot for the lattice parameter of the bcc Nb$_{ss}$ in JN2-HT

Table 5.6 shows the WDS analysis for the phases in JN2 HT. As shown in Figure 5.7, homogeneity was achieved in the Nb$_{ss}$ and the eutectic was not present. This indicates that the Sn and Ti-rich and the Cr and Ti-rich Nb$_{ss}$ compositions observed in JN1-AC were not stable and formed owing to the partitioning of the Cr, Sn and Ti during solidification. The composition of the Nb$_{ss}$ in JN2-HT was close to that of the normal Nb$_{ss}$ in JN2-AC and richer in Ti, Cr and Sn and leaner in W.

Table 5.6 WDS analysis of JN2 HT (at%)

Phase	Nb	Si	Ti	Cr	Hf	Mo	W	Sn
Nb_{ss}	49.5±0.4	0.5±0.1	18.5±0.4	12.1±0.6	0.9±0.0	10.3±0.3	5.3±0.3	3.1±0.1
	49.4-49.8	0.3-0.6	18.1-19.0	11.4-13.0	0.8-0.9	9.6-10.7	4.8-5.5	3.0-3.3
Nb_5Si_3	45.1±1.3	34.0±0.5	15.1±1.3	0.8±0.1	2.9±0.4	0.6±0.1	0.3±0.1	1.2±0.2
	43.6-46.4	33.3-34.7	13.4-16.5	0.7-0.9	2.0-3.1	0.5-0.8	0.2-0.4	0.9-1.4
Ti rich Nb_5Si_3	36.4±1.0	34.8±0.1	21.3±0.0	2.3±0.1	3.9±0.9	0.7±0.0	0.2±0.0	0.3±0.0
	35.3-37.0	34.9-34.7	21.3-21.3	2.3-2.4	3.3-5.0	0.7-0.7	0.2-0.3	0.3-0.3
Laves Phase	24.7±1.9	10.0±0.5	8.2±0.6	51.6±2.0	2.0±0.5	1.8±0.2	1.6±0.1	0.1±0.1
	23.4-28.5	9.3-11.2	6.8-8.8	46.1-52.8	1.0-2.5	1.6-2.1	1.5-1.7	0-0.3

In the Nb_{ss}, the Si content was at the level reported for normal Nb_{ss} in Nb silicide based alloys. The Si+Sn was 3.6 at% and the Cr/Ti ratio was 0.65, both essentially the same as in the Nb_{ss} in JN2-AC (3.8 at% and 0.69, respectively), but the ratio (Ti+Cr)/(Si+Sn)=8.5 was higher owing to the higher Ti+Cr=30.6 at% in JN2-HT, the sd element content excluding Nb was 47.1 at% and the Mo+W=15.6 at%, respectively higher and lower than in JN2-AC and the ratio (Ti+Cr+Hf+Mo+W)/(Ti+Cr) was 1.54, which is a value between 1.2 and 1.9 observed for the solid solutions in JN2-AC, which is consistent with the homogenisation of the solid solution after the heat treatment. The suggestion that Cr and Ti played a key role in the partitioning of solutes to the solid solution in JN2-AC (see 4.2.1) is supported by the above data.

Unlike the Nb_{ss}, there was still partitioning of Ti in the silicide phase forming normal Nb_5Si_3 and Ti rich Nb_5Si_3. Unlike JN1-HT the compositions of Nb_5Si_3 in JN2-HT was not related to the composition of the Nb_5Si_3 in JN2-AC. This implies that the compositions of Nb_5Si_3 in JN2-AC were the product of the homogenisation of the alloy, rather than a lack of homogenisation as in JN1-HT. As would be expected, from previous studies the Ti rich Nb_5Si_3 was richer in both Cr and Hf, compared to the normal Nb_5Si_3. In the silicide the Si+Sn ≈ 36 at% and Mo+W ≈ 0.9 at%. In the 5-3 silicide the Nb/(Ti+Hf) ratio was higher than one, which would indicate a tetragonal structure for this phase, as suggested by XRD.

The NbCr$_2$ Laves phase formed in JN2-AC is still present in JN2-HT, this is attributed to the high Cr content of the alloy causing the stabilisation of the Laves phase. The Laves phase was leaner in Si, Ti, Hf and W and richer in Cr. The Cr + Si + Ti content had increased to ≈ 62 at%, closer to the solubility value of Cr in NbCr$_2$.

5.3   Alloy Nb-22.1Si-15.8Ti-1.6Cr-1.7Hf-5.4Mo-1.2W-1.8Sn (JN3-HT)

The actual composition of the heat treated specimen of alloy JN3 (JN3-HT), which was taken from the bulk of the alloy, is given in Table 5.7. Compared with the average composition of the cast alloy and the composition of the bulk JN3-AC (see Table 4.8) and considering the accuracy of EDS analysis of elements, the average concentrations of the solutes in JN3-HT were essentially the same as in JN3-AC with the exception of Si, which was higher than the average Si content of the bulk and overall alloy values of the cast alloy. The data for Si in Table 5.7 also shows wider difference between the minimum and maximum analyses values for Si compared with JN3-AC, which is attributed to the accuracy of Si analysis by EDS.

Table 5.7 EDS Large area analysis of JN3 HT (at%)

Area in alloy	Nb	Si	Ti	Cr	Hf	Mo	W	Sn
bulk	50.4±0.6	22.1±0.9	15.8±0.5	1.6±0.2	1.7±0.3	5.4±0.3	1.2±0.3	1.8±0.3
	49.5-51.2	21.1-23.6	14.8-16.4	1.3-2.0	1.3-2.1	4.9-5.9	0.6-1.5	1.4-2.2

Figure 5.12 shows the BSE image of JN3-HT. After 100 h at 1500 °C, the microstructure had been almost fully homogenised and the eutectic regions observed in JN3-AC were not present. Furthermore in agreement with previous work, HfO$_2$ had formed at the Nb$_5$Si$_3$ grain boundaries. Like JN2-HT, there appeared to be Nb$_{ss}$ precipitates within some of the Nb$_5$Si$_3$ grains, but not to the same extent. In some Nb$_5$Si$_3$ grains there was some evidence of micro cracking, this damage was possibly caused during sample preparation.
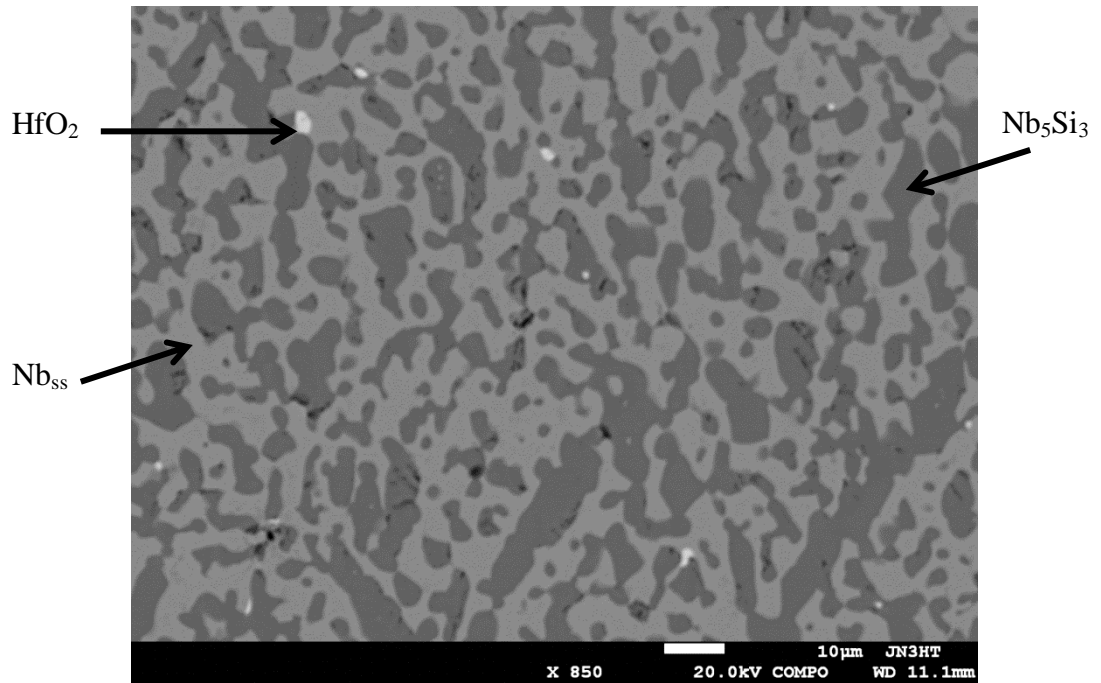
Figure 5.12 BSE image of JN3 HT (1500 °C/100 h)

Figure 5.13 shows the X-ray maps for Nb, Si, Ti, Cr, Hf, Mo, W and Sn; the Ti map shows that the Ti-rich regions were still present in the Nb_5Si_3. HfO_2 particles are indicated in the Hf map.
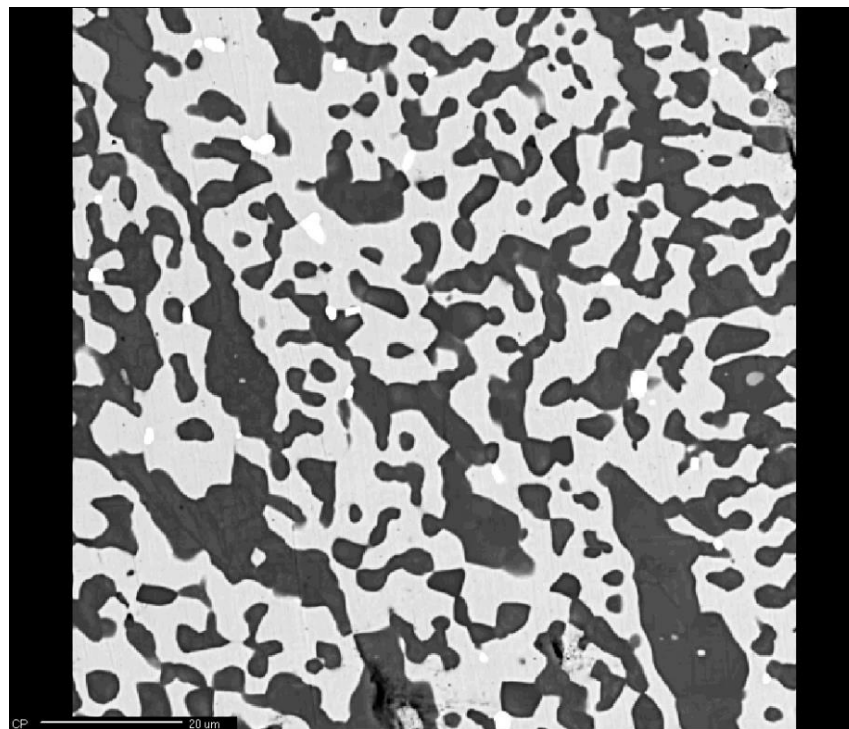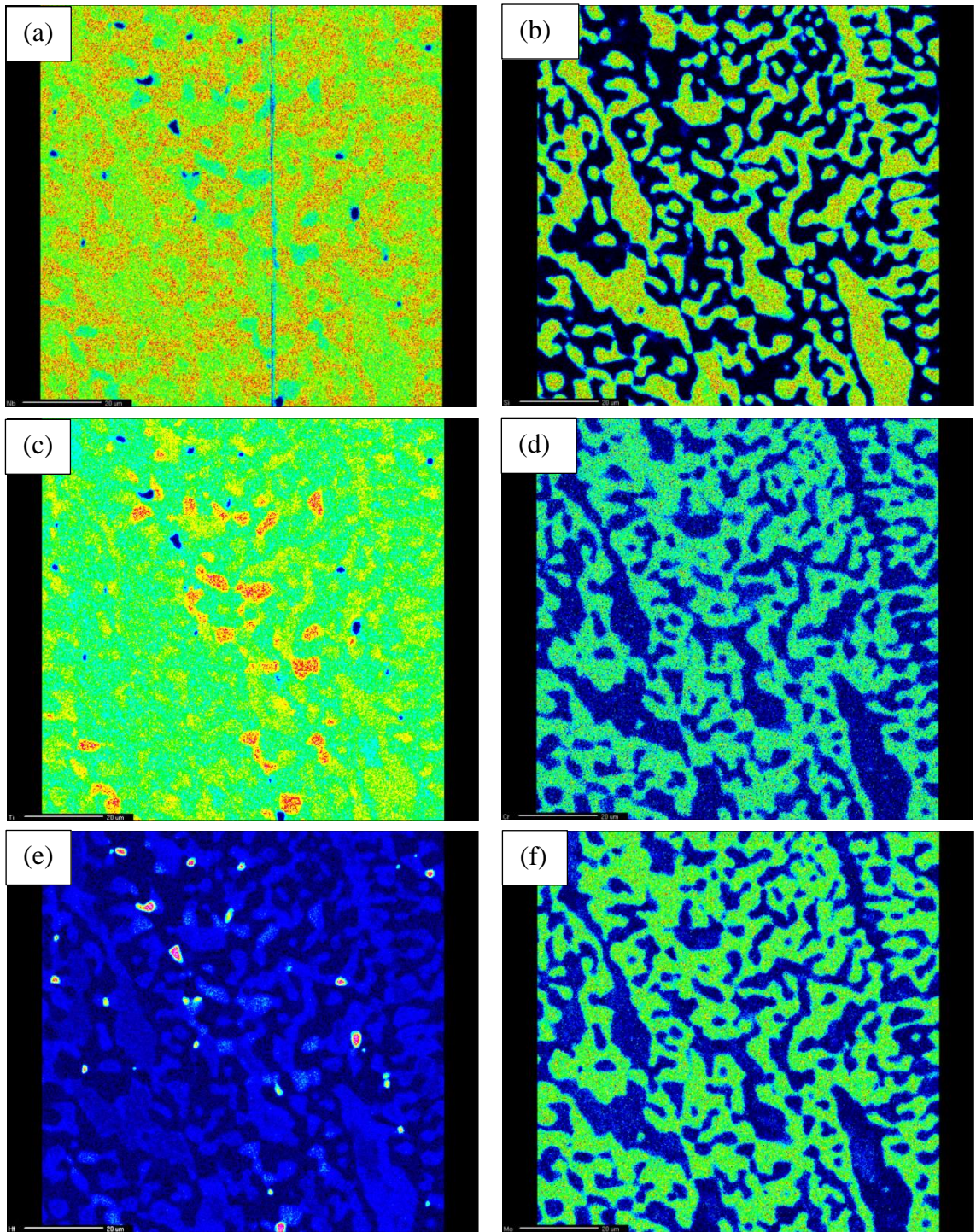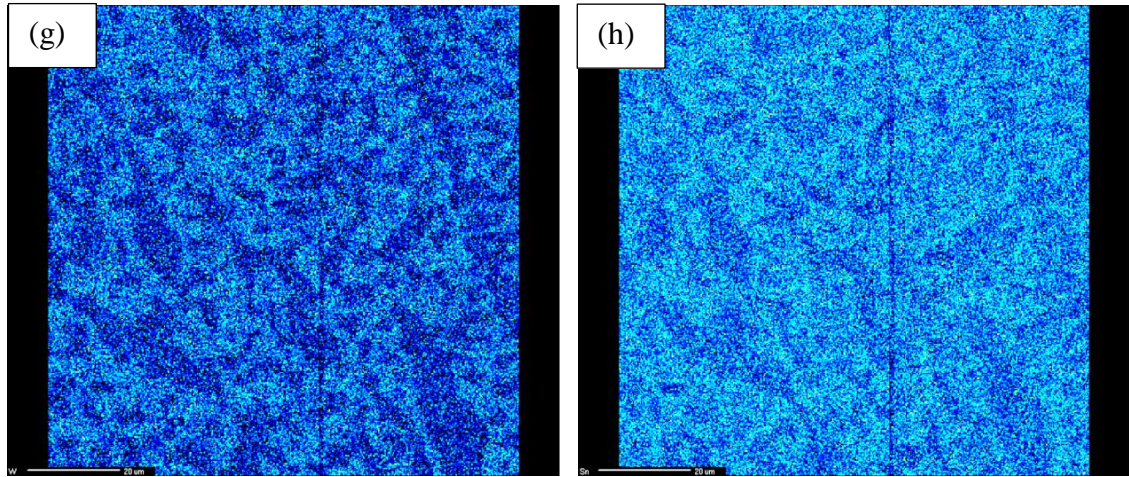
Figure 5.13 X-ray maps of JN3 HT bulk showing elements: Nb (a), Si (b), Ti (c), Cr (d), Hf (e), Mo (f), W (g), Sn (h). (The verical line present in some of the scans is an artifact left by the detector).

Figure 5.14 shows the diffractogram for JN3-HT. The peaks correspond to Nb_{ss} and αNb_5Si_3, indicating that the βNb_5Si_3 present in JN3-AC had fully transformed to αNb_5Si_3.
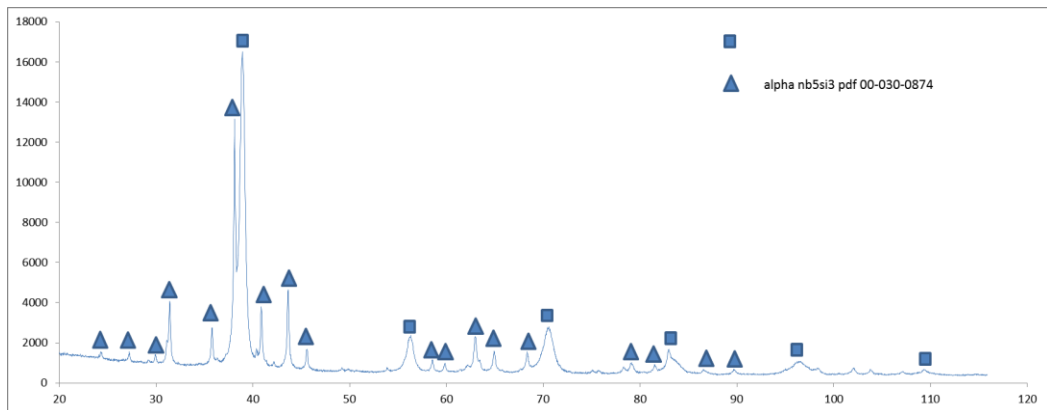
Figure 5.14 JN3 HT powder X-ray diffraction pattern fitted with Sieve+

The lattice parameter was calculated for Nb_{ss} in JN3 HT from a Nelson-Riley plot which can be seen in Table 5.8, this was 3.277 Å; compared with the 3.253 Å in JN3-AC and the 3.303 Å for pure Nb. This change in the lattice parameter of the Nb_{ss} was attributed to the decreased and increased concentrations of Si and Ti, and Cr respectively, compared with the cast alloy.

Table 5.8 The calculated lattice parameters of the bcc Nb_{ss} in JN3-AC

	d (Å)	2 θ	theta	a (Å)	f (θ)	hkl	Corrected a (Å)
JN3 HT	2.313	38.906	19.453	3.271	2.715372	110	
	1.633	56.306	28.153	3.265	1.675203	200	
	1.336	70.426	35.213	3.272	1.17659	211	3.277
	1.163	82.966	41.483	3.289	0.860798	220	
	1.035	96.226	48.113	3.272	0.608052	310	
	0.944	109.286	54.643	3.272	0.416714	222	
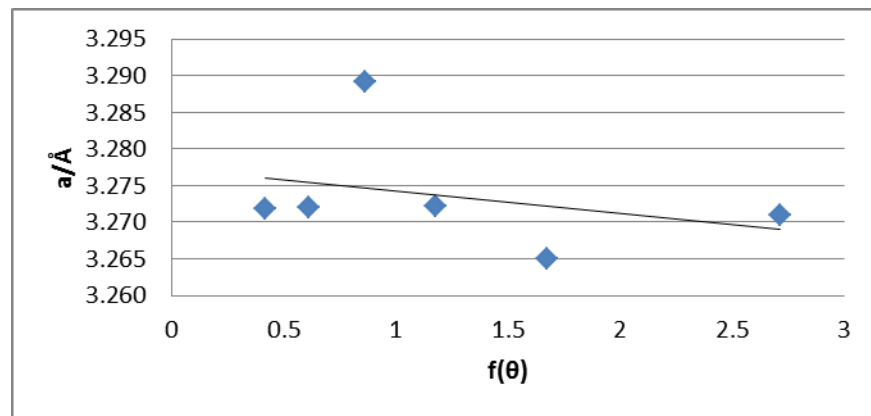
Figure 5.15 Nelson-Riley plot for the lattice parameter of the bcc Nb_{ss} in JN3-HT

Table 5.9 shows the WDS analysis data for the phases in JN3-HT. As seen in Figure 5.12, the microstructure was comprised of only two phases, Nb_{ss} and Nb_5Si_3 and there was no remaining eutectic. In the Nb_{ss} the Si content was at the level reported for normal Nb_{ss} in Nb silicide based alloys. The Si+Sn was 3.4 at% and the Cr/Ti ratio was 0.22, both different from those in the Nb_{ss} in JN3-AC, the former being lower and the latter higher, and resulting in (Ti+Cr)/(Si+Sn)=6.3, which was also higher than in the cast alloy owing to the higher Ti+Cr=21.3 at% and lower Si+Sn in JN3-HT. Furthermore, in the Nb_{ss} the sd element content excluding Nb was 35.4 at% and the Mo+W=13.1 at%, respectively higher and essentially the same compared with JN3-AC and the ratio (Ti+Cr+Hf+Mo+W)/(Ti+Cr) was 1.66, which is a higher than the values 1.4 and 1.46 observed for the solid solutions in JN3-AC. The data for the alloys JN2 and JN3 would provide further support for the importance of Ti and Cr in solute partitioning in these alloys.

Table 5.9 WDS analysis of JN3-HT (at%)

Phase	Nb	Si	Ti	Cr	Hf	Mo	W	Sn
Nb$_{ss}$	61.2±0.7	0.5±0.1	17.5±0.8	3.8±0.1	1.0±0.1	9.4±0.2	3.7±0.4	2.9±0.1
	60.5-62.3	0.4-0.6	16.5-18.5	3.7-3.9	0.9-1.1	9.2-9.6	3.1-4.0	2.8-3.2
Nb$_5$Si$_3$	45.9±1.2	33.5±0.3	15.7±1.4	0.2±0.0	3.0±0.2	0.4±0.2	0.2±0.0	1.0±0.1
	44.7-48.1	33.1-34.1	13.3-16.6	0.2-0.3	2.7-3.4	0.3-0.7	0.2-0.3	0.8-1.1

The Nb$_5$Si$_3$ stabilised at a composition in between the Ti rich and the normal Nb$_5$Si$_3$ found in JN3-HT. The Si+Sn content was ≈34.5 at%, essentially the same as in JN2-HT and the ratio Nb/Ti+Hf was higher than 1, which would suggest a tetragonal structure and is supported by XRD data. Even though the X-Ray maps confirmed the presence of Ti-rich Nb$_5$Si$_3$ in JN3-HT, the WDS failed to find these areas in the microstructures. The latter is considered as further strong evidence to support the conclusion that the microstructure of JN3-HT was almost fully homogenised after 100h at 1500 °C.

Compared with the alloy JN2, in the alloy JN3 an almost fully homogenised microstructure was achieved after 100 h at 1500 °C. This could be attributed to the reduction in the concentrations of Cr in JN3. However, there is more than the role played by Cr, as the results for JN1, JN2 and JN3 suggest.

The results for the alloy JN1 confirmed that the synergy of 5 at% Hf with 5 at% Al and 5 at% Cr leads to strong partitioning of Hf in the microstructure which causes the formation of Hf rich areas in Nb$_5$Si$_3$ and stabilisation of γ Nb$_5$Si$_3$ that forms its own discrete grains. In other words the partitioning of Hf has a strong effect on the stability of (and can stabilize) Hf rich Nb$_5$Si$_3$. The NbCr$_2$ Laves phase was formed in the cast alloy Nb-24Ti-18Si-5Cr (alloy KZ4 in (Zelenitsas & Tsakiropoulos 2005)) but was not stable (absent after heat treatment at 1500 °C for 100 h). Aluminium stabilises the NbCr$_2$ Laves phase in the Nb-Al-Cr system. The NbC$_2$ was formed in a cast alloy of the same composition as JN1 but without Hf, i.e., the alloy KZ5 (can be considered as the alloy KZ4 + Al) (Zelenitsas & Tsakiropoulos 2005), but was not stable (absent after

heat treatment at 1500 °C for 100 h). The absence of $NbCr_2$ in JN1-AC (can be considered as the alloy KZ5 + Hf) would thus suggest that Hf, which can form the $HfCr_2$ Laves phase and thus is expected to have a strong effect on the stability of Laves in Nb silicide based alloys, can also suppress the formation of the Laves phase.

The Laves is formed by the rejection (partitioning) of Cr to the inter-dendritic melt during solidification (Zelenitsas & Tsakiropoulos 2005), which becomes very rich in Cr thus making the formation of the $NbCr_2$ possible. Therefore the absence of $NbCr_2$ in JN1-AC would suggest that Hf has an effect on the partitioning of Cr (can reduce the rejection of Cr from the Nb_{ss} dendrites) in Nb-Si based melts.

In JN2 the Hf content was reduced, no Al was present, the concentration of Cr was increased and Mo, W and Sn were added. The latter three elements are known to partition to the Nb_{ss} rather than the Nb_5Si_3 (Vellios & Tsakiropoulos 2007b; Grammenos & Tsakiropoulos 2010a; Grammenos & Tsakiropoulos 2011; Geng, Tsakiropoulos, et al. 2006b). The high Cr content was expected to stabilize the $NbCr_2$ in JN2 which, even in the absence of Al, was the case, and the synergy of Hf, Cr, Mo and Sn was expected to lead to partitioning of Hf in Nb_5Si_3 (in other words lead to the formation of Hf rich Nb_5Si_3) based on the results for the alloy JG6 (Nb-18i-24Ti-5Cr-5Al-5Hf-2Mo-5Sn). In the alloy JN2 the $NbCr_2$ was stabilised in the microstructure, as expected, there was partitioning of the Mo and W and Sn in the Nb_{ss}, but the synergy of high Cr with high Mo and W and low Hf and Sn did not lead to segregation (partitioning of solutes) in the Nb_5Si_3 but instead there was segregation of solutes in the Nb_{ss}, which formed three types of solid solution (normal Nb_{ss}, Sn+Ti rich Nb_{ss} and Ti+Cr rich Nb_{ss}) in the cast alloy owing to opposite partitioning behaviours of Sn, Ti and Cr and Mo and W (Cr, Sn and Ti did not like to be together with Mo and W in the Nb_{ss}, see section 1.2.1). The Sn+Ti rich Nb_{ss} and the Ti+Cr rich Nb_{ss} were not stable after heat treatment, thus as the microstructure of the Nb_{ss} homogenised the Ti that was in the two unstable solid solution became available and partitioned between the normal Nb_{ss} (increasing its Ti content) and the Nb_5Si_3 leading to the formation of Ti rich areas in the latter (i.e., introduced chemical inhomogeneity with the formation of Ti rich areas in the Nb_5Si_3).

In JN3 the reduction in Cr content lead to the usual partitioning behaviour of solutes between the Nb_{ss} and Nb_5Si_3 and Ti rich areas were formed in both phases in the cast microstructure, with the RMs (Mo, W) and TMs (Ti, Cr, Hf) and Sn partitioning in

the Nb_{ss} as expected from previous work (Vellios & Tsakiropoulos 2007b; Grammenos & Tsakiropoulos 2010a; Grammenos & Tsakiropoulos 2011; Geng, Tsakiropoulos, et al. 2006b; Geng, Tsakiropoulos & G Shao 2007; Grammenos & Tsakiropoulos 2010b). It is thus concluded that in Nb silicide based alloys with Mo and W (required for solid solution strengthening, high temperature strength and creep resistance) and Sn (added for oxidation behaviour) whether or not a chemically homogeneous microstructure forms after heat treatment depends on the Cr and Hf contents in the alloy. Chemical inhomogeneity increases as the concentrations of these two solutes increase above 5 and 2 at% respectively.

5.4   Alloy Nb-21.9Si-20.9Ti-1.6Cr-2.0Hf-8.2Mo-3.9Sn (JN4-HT)

The actual composition of the heat treated specimen of alloy JN4 (JN4-HT), which was taken from the bulk of the alloy, is given in Table 5.10. Compared with the average composition of the cast alloy and the composition of the bulk JN4-AC (see Table 4.11) and considering the accuracy of analysis, the average concentrations of the solutes in JN4-HT were essentially the same. The data in Table 5.10 however shows difference between the minimum and maximum analyses values for Si, which is attributed to the macrosegregation of this element in JN4-AC, see Table 4.11.

Table 5.10 EDS Large area analysis of JN4-HT (at%)

Area in ingot	Nb	Si	Ti	Cr	Hf	Mo	Sn
Bulk	41.6±0.3	21.9±0.9	20.9±0.3	1.6±0.1	2.0±0.1	8.2±0.2	3.9±0.1
	40.9-41.8	20.6-23.5	20.4-21.3	1.5-1.7	1.9-2.2	8.0-8.5	3.7-4.0

The microstructure of JN4-HT is shown in Figure 5.16 and the XRD diffractogram is shown in Figure 5.18. The latter has peaks that correspond to Nb_{ss}, Nb_3Sn and αNb_5Si_3. In the BSE image in Figure 5.16 the bright phase is hafnia. There are no peaks for this oxide in the diffractogram, which means that its volume fraction was low (< 5 %). The presence of Nb_3Sn, as suggested by the XRD, is consistent with previous work that

shows that Nb_3Sn is stable in Nb silicide based alloys when $Sn \geq 5$ at% (Vellios & Tsakiropoulos 2007a; Vellios & Tsakiropoulos 2010; Vellios & Tsakiropoulos 2007b; Geng, Tsakiropoulos & G. Shao 2007). However, in the latter alloys the Nb_3Sn can form in the cast microstructure. This was not the case in JN4, as the XRD for JN4-AC did not suggest its presence, which however cannot be dismissed as XRD would not detect it if present at very low volume fraction.
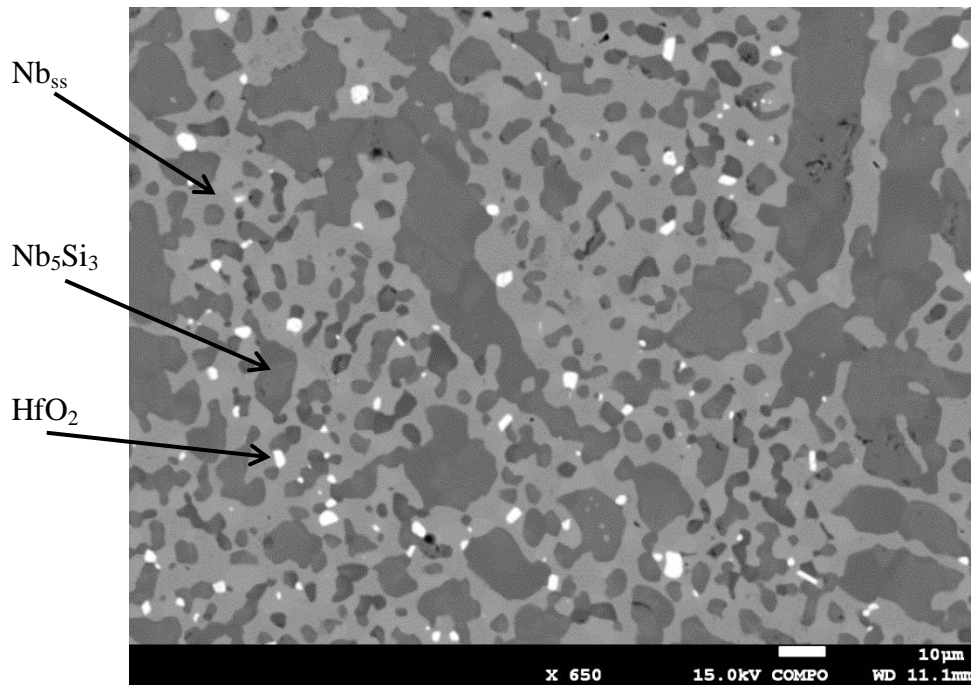
Figure 5.16 BSE image of JN4 HT (1500 °C/100 h)

The contrast of phases is Figure 5.16 would suggest the presence of two phases that, on the basis of the research presented in this thesis, are the Nb_5Si_3 dark (contrast phase) and the Nb_{ss} (lighter contrast phase). It was not possible to distinguish the Nb_3Sn in the microstructure of JN4-HT using BSE in the SEM, as for example in Figure 5.16. The Nb_3Sn is known to form next to the Nb_{ss} (Vellios & Tsakiropoulos 2007a; Vellios & Tsakiropoulos 2010; Vellios & Tsakiropoulos 2007b) and to be very difficult to image under BSE imaging conditions as a separate phase from the Nb_{ss}.

Data from previous research shows that in Nb silicide based alloys with 24 at% Ti and 18 at% Si the solid solubility of Ti is higher in the Nb_{ss} than in the Nb_3Sn and the opposite is the case for Si and Sn (Vellios & Tsakiropoulos 2007a; Vellios & Tsakiropoulos 2010; Vellios & Tsakiropoulos 2007b). This difference in solid

solubilities allows Nb_{ss} and Nb_3Sn to be differentiated, admittedly with some difficulty, as the Nb_{ss} exhibits slightly darker contrast than the Nb_3Sn under BSE imaging conditions (owing to its higher Ti content). However, in alloys with Ti, Mo, Hf and Sn contents that are comparable with those in JN4, the solid solubility (SS) of Ti in the Nb_{ss} is slightly lower than in Nb_3Sn, the SS of Si and Cr in the Nb_{ss} is lower than in Nb_3Sn while the SS of Mo and Sn is significantly higher respectively in the Nb_{ss} and Nb_3Sn and the SS of Hf is essentially the same in both the Nb_{ss} and Nb_3Sn (Tsakiropoulos & Anazodo 2015). Considering the atomic number of the above elements (Sn-50, Nb-41, Mo-42, Hf-72, Ti-22, Si-14, Cr-24), it is no surprise that imaging the Nb_{ss} and the nearby Nb_3Sn in JN4-HT was an impossible task under BSE imaging conditions in the SEM.

The X-ray maps of elements in the microstructure of the JN4-HT are shown in Figure 5.17. The maps for Si and Mo help one to distinguish the Nb_5Si_3 and Nb_{ss} in the microstructure. The Sn map shows that there are Sn rich areas in the areas where the Nb_{ss} is (see the X-Ray maps of Nb, Cr and Mo), which is the location where the Nb_3Sn is expected to have formed.
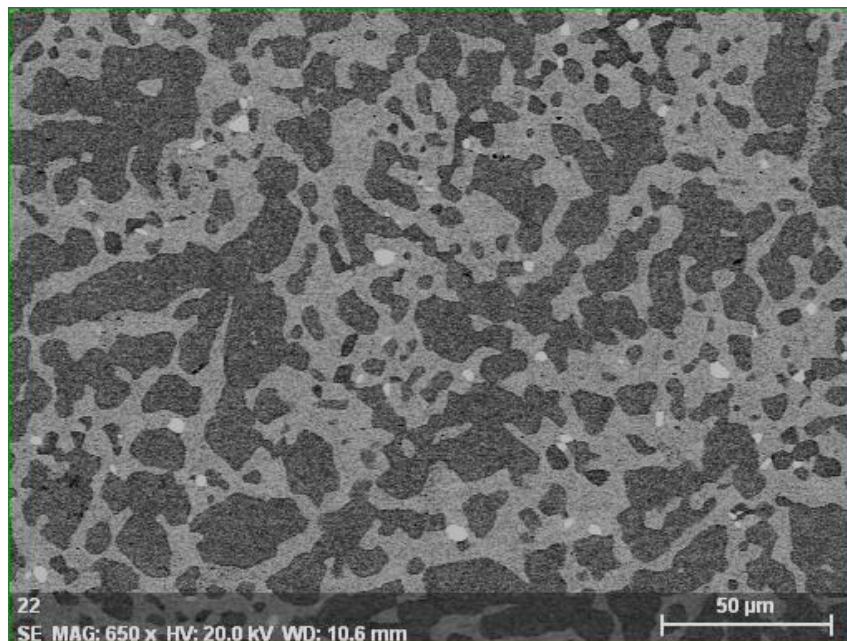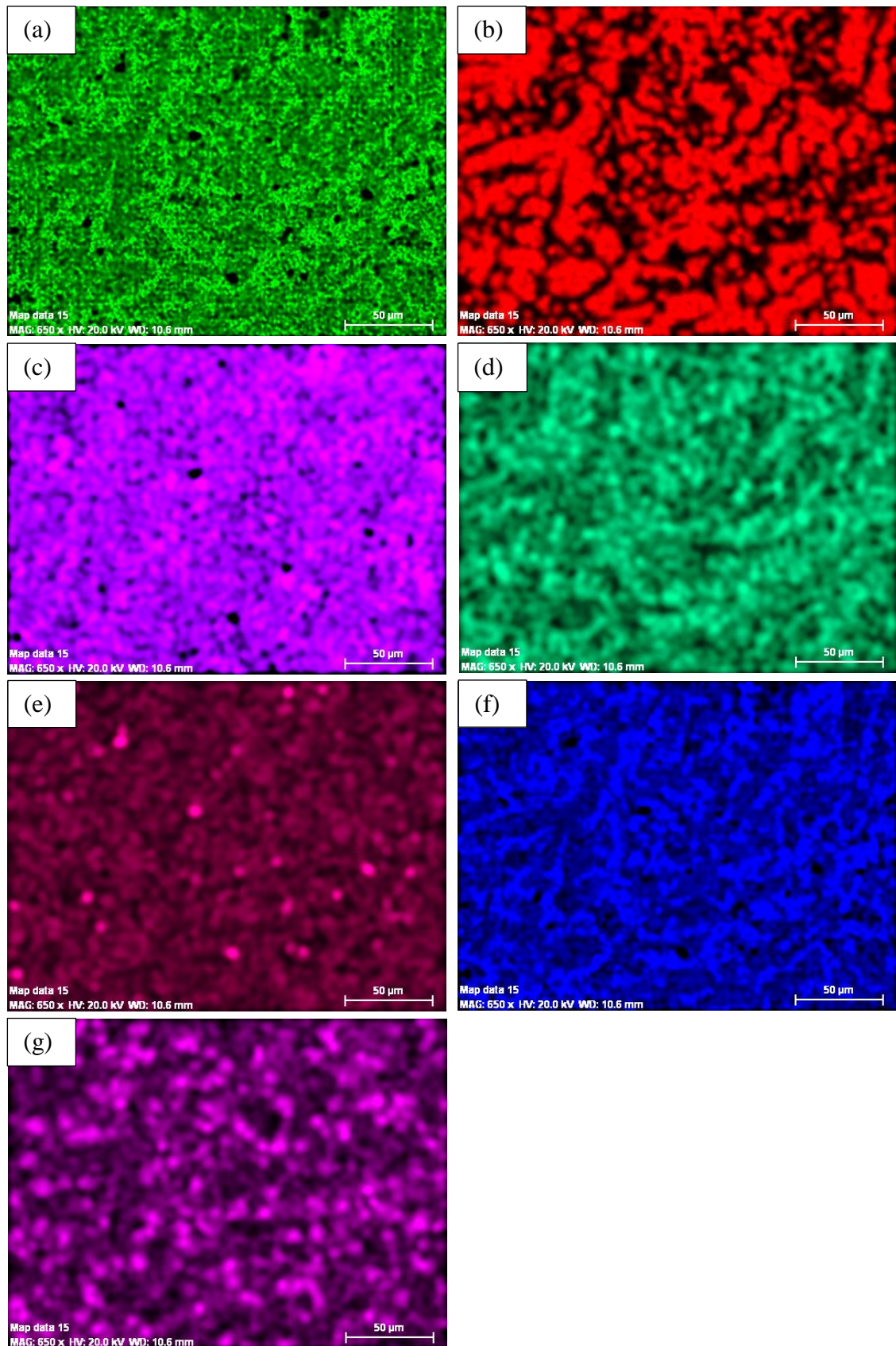
Figure 5.17 BSE image and X-ray maps of JN4 HT bulk showing elements: Nb (a), Si (b), Ti (c), Cr (d), Hf (e), Mo (f), Sn (g)

The lattice parameter of the Nb_{ss} was calculated using the peaks corresponding to niobium and was found to be 3.261 Å, a slight reduction compared to 2.266 Å in JN4-AC.
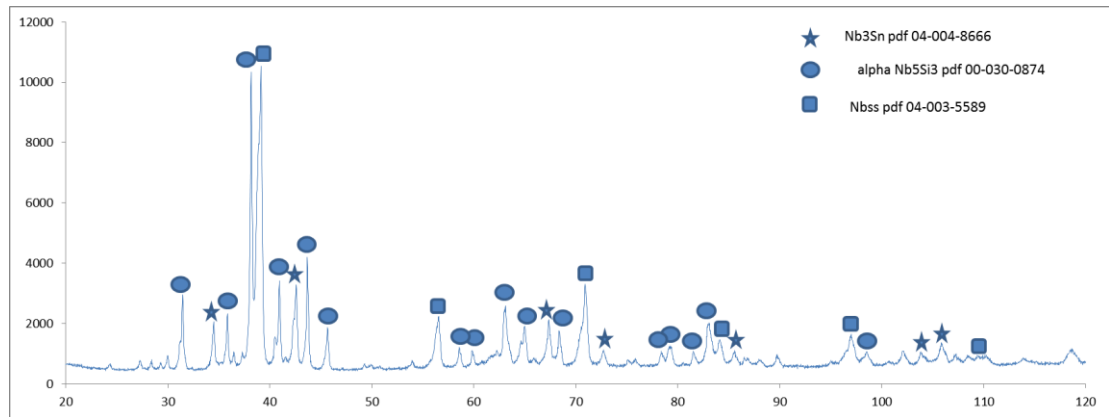
Figure 5.18 JN4 HT powder XRD pattern fitted with Sieve+

The calculated lattice parameters and the Nelson-Riley plot can be seen in Table 5.11 and Figure 5.19.

Table 5.11 The calculated lattice parameters of the bcc Nb_{ss} in JN4-HT

	d (Å)	2 θ	theta	a (Å)	f (θ)	hkl	Corrected a (Å)
JN4 HT	2.299	39.16	19.58	3.251	2.694196	110	
	1.626	56.56	28.28	3.252	1.664323	200	
	1.328	70.9	35.45	3.253	1.162888	211	3.261
	1.150	84.08	42.04	3.253	0.83679	220	
	1.028	97.02	48.51	3.252	0.594962	310	
	0.944	109.36	54.68	3.270	0.415764	222	
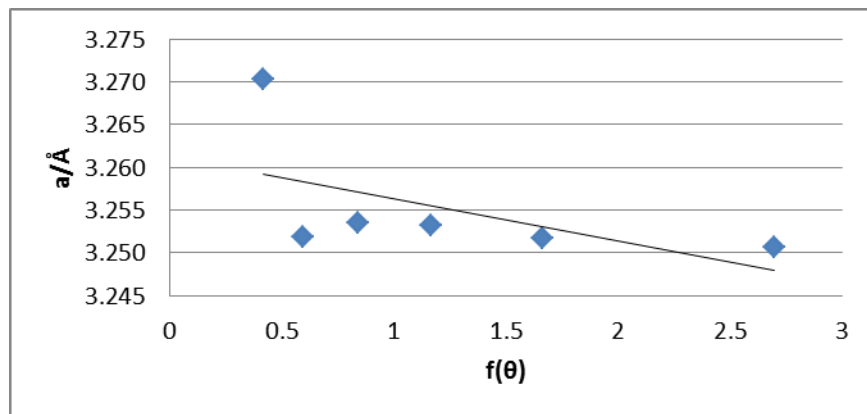
Figure 5.19 Nelson-Riley plot for the lattice parameter of the bcc Nb_{ss} in JN4-HT

The compositions of the Nb_{ss} and Nb_5Si_3 determined by WDS are given in Table 5.12. Compared with JN4-AC, see also Table 4.13 the Si, Hf and Sn contents decreased and the concentrations of Cr and Mo increased. The Si concentration was in agreement with that in the other heat treated alloys of this research and previously published work for Nb silicide based alloys. The unchanged lattice parameter of the Nbss compared with the cast alloy is attributed to the redistribution of solutes of smaller and larger atomic radii than Nb between the Nb_{ss} and the other phases in the microstructure of JN4-HT. In the Nb_5Si_3 the concentration of Ti increased and those of Hf and Mo decreased compared with JN4-AC, see also Table 4.11. The Nb/(Ti+Hf) ratio was greater than one, which would suggest tetragonal structure, consistent with the XRD data, which had peaks corresponding to αNb_5Si_3.

Table 5.12 WDS analysis of JN4-HT (at%)

Phase	Nb	Si	Ti	Cr	Hf	Mo	Sn
Nb_{ss}	53.4±0.1	0.3±0.0	23.6±0.2	4.7±0.1	0.6±0.0	13.7±0.2	3.7±0.2
	53.2-53.5	0.3-0.4	23.4-23.8	4.6-4.8	0.6-0.7	13.5-13.9	3.4-4.0
Nb_5Si_3	40.9±1.0	36.8±0.3	17.7±0.8	0.3±0.0	2.1±0.5	0.9±0.4	1.4±0.1
	39.8-42.6	36.1-37.1	16.2-18.3	0.2-0.3	1.7-2.8	0.6-1.5	1.3-1.5

If we were to consider JN4-HT as 53Nb-22Si-21Ti-4Sn (at%), in other words consider Nb, Cr, Hf and Mo together, the Pandat database gives at 1500 °C a microstructure consisting of the Nb_{ss}, αNb_5Si_3, Nb_3Sn and tetragonal Nb_3Si phases. The former three phases were confirmed by the experimental results for JN4-HT, which however provided no evidence for the Nb_3Si.

5.5   Conclusions

The alloys JN1 (Nb-19.3Si-24.1Ti-4.1Cr-3.8Al-5.7Hf), JN2 (Nb-20.5Si-15.3Ti-10.0Cr-1.6Hf-5.6Mo-2.0W-1.9Sn), JN3 (Nb-22.1Si-15.8Ti-1.6Cr-1.7Hf-5.4Mo-1.2W-1.8Sn) and JN4 (Nb-21.9Si-20.9Ti-1.6Cr-2.0Hf-8.2Mo-3.9Sn) were studied in the heat treated (1500 °C for 100 h) condition. The conclusions of this research were as follows.

- There was chemical inhomogeneity of Si in JN1-HT, JN2-HT, JN3-HT and JN4-HT. In JN1-HT there was also chemical inhomogeneity of Al and Ti that was attributed to the strong partitioning of Hf. The chemical homogeneity of the microstructures alloyed with Mo, W and Sn depended on the Cr and Hf content of the alloy. Chemical inhomogeneity increased as Cr > 5 at% and Hf > 2 at%.

- In the alloy JN1, where the Hf concentration was the highest, the partitioning of Hf was enhanced by the heat treatment, the Nb_{ss} was homogenised and there was formation of Hf rich and Hf poor Nb_5Si_3. Titanium rich areas in Nb_5Si_3 could persist after heat treatment. This was dependant on the concentration of Cr in the alloy.

- The synergy of Hf with Al, Cr and Ti stabilised the βNb_5Si_3 in JN1-HT, where the Hf rich Nb_5Si_3 was probably the hexagonal γNb_5Si_3. The synergy of Hf with Mo, W and Sn enhanced the transformation of βNb_5Si_3 to αNb_5Si_3.

- The Laves phase was confirmed by XRD and WDS only in the cast and heat treated alloy JN2. The Nb_3Sn was stabilised in the JN4-HT. The $Nb_{ss} + Nb_5Si_3$ eutectic microstructure was not stable after the heat treatment.

- The addition of Hf most likely suppressed the precipitation of Nb_{ss} in the Nb_5Si_3 in JN1-HT. The latter was observed in JN2-HT and JN3-HT but the extent of Nbss precipitation was stronger in the former, which would suggest that the concentration of Cr in the alloy is important for this phase transformation.

Oxidation at 800 °C: Results and Discussion

Thermogravimetric analysis was used to determine the oxidation behaviour at 800 °C of the alloys studied in this work. The alloys were oxidised isothermally as opposed to cyclically, to give a benchmark mass gain. This allowed all alloys to be quantitatively compared with previous alloys studied in the group and literature. In this research the alloys were oxidised at 800 °C (within the pest regime (Menon n.d.; Behrani et al. 2006; Grabke & Meier 1995)) for 100 h, allowing them to be directly compared with other work in this group.

In this research particular emphasis was on comparing the compositions of phases in the bulk and below the scale to establish the depth of contamination by interstitials and whether any of the phases present were immune to this contamination. Due to the nature of the oxidised sample (e.g. cracks forming below the scale and parallel to the specimen surface below) and the method of preparation (3.4), there was a degree of error related to the oxygen analysis of the oxidised specimens. External causes of error, regarding the depth of contamination, were the surface roughness of the samples, porosity (when present), and bevelling at the edge of samples due to polishing. The oxygen content of the phases was analysed by difference, as any variations from 100 wt% achieved during EPMA analysis were compensated for by the addition of oxygen to reach a total of 100 wt%. This rounding of the wt% total eliminated the normal process of vetting analysis points which have wt% totals which deviate too far from 100. Due to the oxidation of these alloys in air it should be noted that other elements such as N could also contaminate the alloy, forming nitrates and dissolving within the constituent phases (this would have an effect on the mechanism of oxidation and growth of the scale as has been the case in the oxidation of γ-TiAl based alloys) however only one element can be analysed by difference at a time. As N and O have similar atomic weights, compounds such as TiN and TiO must be determined by XRD, if this is not possible then a common sense approach must be taken. The aforementioned variables affect the accuracy of results gained from the EPMA; aside from the standard deviation given in the tables, each reading must be treated with caution as the related error varies from point to point during analysis.

6.1   Alloy JN1 (Nb-18Si-24Ti-5Cr-5Al-5Hf) after oxidation at 800 °C

Specimens were taken from JN1 AC were oxidised for 100 h in dry air (as described in 3.9). The weight of the specimen was measured at the start and end of the experiment allowing the mass gain to be determined. Prior to oxidation the specimen was polished and its surface area was calculated. A light microscope was used to measure the lengths of the edges of the specimen.

Figure 6.1 shows the mass gain in g/cm^2 against the oxidation time in hours. In total there was a mass gain of 0.005 g/cm^2 after 100 h heating at 800 °C in air. The mass gains of the alloys; KZ5-HT and JG4-AC were ~0.035 and 0.0047 g/cm^2 respectively (Zelenitsas & Tsakiropoulos 2006a; Geng & Tsakiropoulos 2007). The data for JN1-AC thus shows that the addition of Hf had a dramatic effect on the oxidation resistance as far as weight gain is concerned. The slightly lower weight gain of JG4 AC is within the experimental error but could also be due to the addition of Mo in the alloy as it does not have an entirely negative effect on the oxidation resistance of Nb silicide based alloys at 800 °C, particularly when added in low concentrations. The data in Figure 6.1 gave a linear oxidation rate constant of $1x10^{-8}$ $gcm^{-2}s^{-1}$ indicating no arrest of the oxidation by the scale that was formed on JN1 at 800 °C. Analysis of the oxidation data for KZ5 using $ln\Delta w=lnk+\eta lnt$ (where Δw is weight gain per unit area, k is the oxidation rate constant and t is the time) gave the kinetic constant $\eta>0.5$(Zelenitsas & Tsakiropoulos 2006a), this indicated faster than parabolic oxidation kinetics. The data for JN1 would thus suggest that the addition of Hf did not change the oxidation kinetics. Compared with the alloy KZ5, where there was also evidence for adherence of the scale, the data would suggest that the addition of Hf did not improve the adherence of the scale. The oxidation rate constant of JG4 was parabolic with a value of $4.7x10^{-11}$ $g^2cm^{-4}s^{-1}$, which would suggests that due to the synergy of Hf and Mo in JG4, the oxide formed better protection during oxidation at 800 °C.

However the linear oxidation rate constant of JN1—AC was better than that of JG4-HT after oxidation at 800 °C ($K_l=1.10^{-7}gcm^{-2}s^{-1}$). Both alloys (i.e. JN1-AC and JG4-HT) had the same phases present in their microstructures, namely Nb_{ss}, Nb_5Si_3, Hf-rich Nb_5Si_3 and Hf-rich Nb_{ss} were also present in JN1-AC, but the vol% of the solid solution was higher in JG4-HT (Geng, Tsakiropoulos & G Shao 2007) compared with

JN1-AC ($\approx$55 % vs 42%). This confirms the strong dependence of the oxidation of Nb-silicide based alloys on the vol% of the Nb_{ss}.

The vol% of Nb_{ss} in KZ5-HT was higher than that in JN1-AC (Zelenitsas & Tsakiropoulos 2006a) which provides further support from the role of Nb_{ss} on oxidation. It is also comparable with JG4-HT which has the same oxidation behaviour at 800 °C as KZ5-HT. However, in JG4-AC the $NbCr_2$ Laves phase was present but it is not in JG4-HT (it should be noted that the $NbCr_2$ Laves phase was formed in KZ5-AC but was not stable in KZ5-HT, as was the case in JG4. Thus the superior oxidation behaviour of JG4-AC compared to JN1-AC at 800 °C is attributed to the synergy of Hf, Mo, Al and Cr forming the $NbCr_2$ Laves phase and a lower vol% of Nb_{ss} which was $\approx$39% in JG4-AC (Geng, Tsakiropoulos & G Shao 2007). The data for the alloys KZ5, JN1 and JG4 would therefore suggest:

i.   That Hf benefits oxidation (in the form of weight gain) by reducing the vol% of Nb_{ss}.

ii.   That Hf brings parabolic oxidation kinetics at 800 °C when in synergy with other elements, such as Mo, promotes the formation of the $NbCr_2$ Laves phase

iii. That the Laves phase is key to improving oxidation resistance at 800 °C in the absence of alloying additions that supress pest oxidation such as Sn.

Figure 6.2 shows the specimen JN1-AC after 100 h oxidation at 800 °C. The scale that was formed was very brittle and easily crumbled into a powder; there was also powdered oxide around the sample after testing, representative of pesting. It can be seen that the sample was generally intact; however some pesting had occurred along the edges and at the corners. The smooth nature of the TGA curve indicated, along with the morphology of the oxidised specimen, that there was no catastrophic failure, sudden spallation or sudden cracking of the oxide.
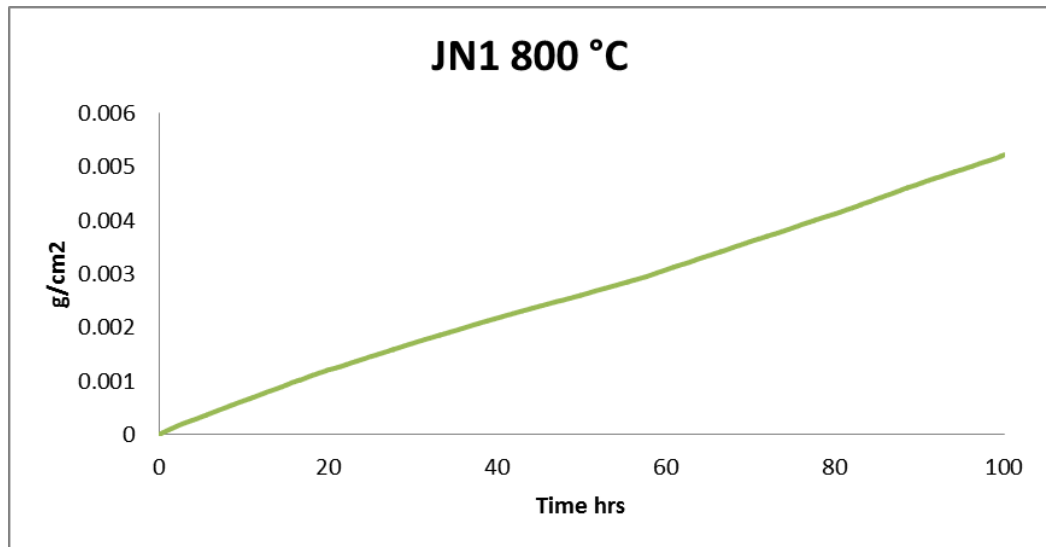
Figure 6.1 TGA data of JN1-AC at 800 °C

Figure 6.2 a specimen of JN1-AC after 100 h oxidation at 800 °C

Figure 6.3 shows images of the surface of JN1-AC after oxidation at 800 °C. In the image the phases below the scale are indicated. The silicide phase can be clearly seen surrounded by oxidised Nb_{ss} (Figure 6.3 a); the silicide phase itself was covered with fine needle oxide precipitates (Figure 6.3 c). It can also be observed that the Nb_5Si_3 displayed trans-granular and intergranular cracking (Figure 6.3 b) attributed to the strain induced by oxide growth (Mathieu et al. 2012) and the subsequent propagation of the cracks along the embrittled Nb_{ss} adjacent to the grain boundary.
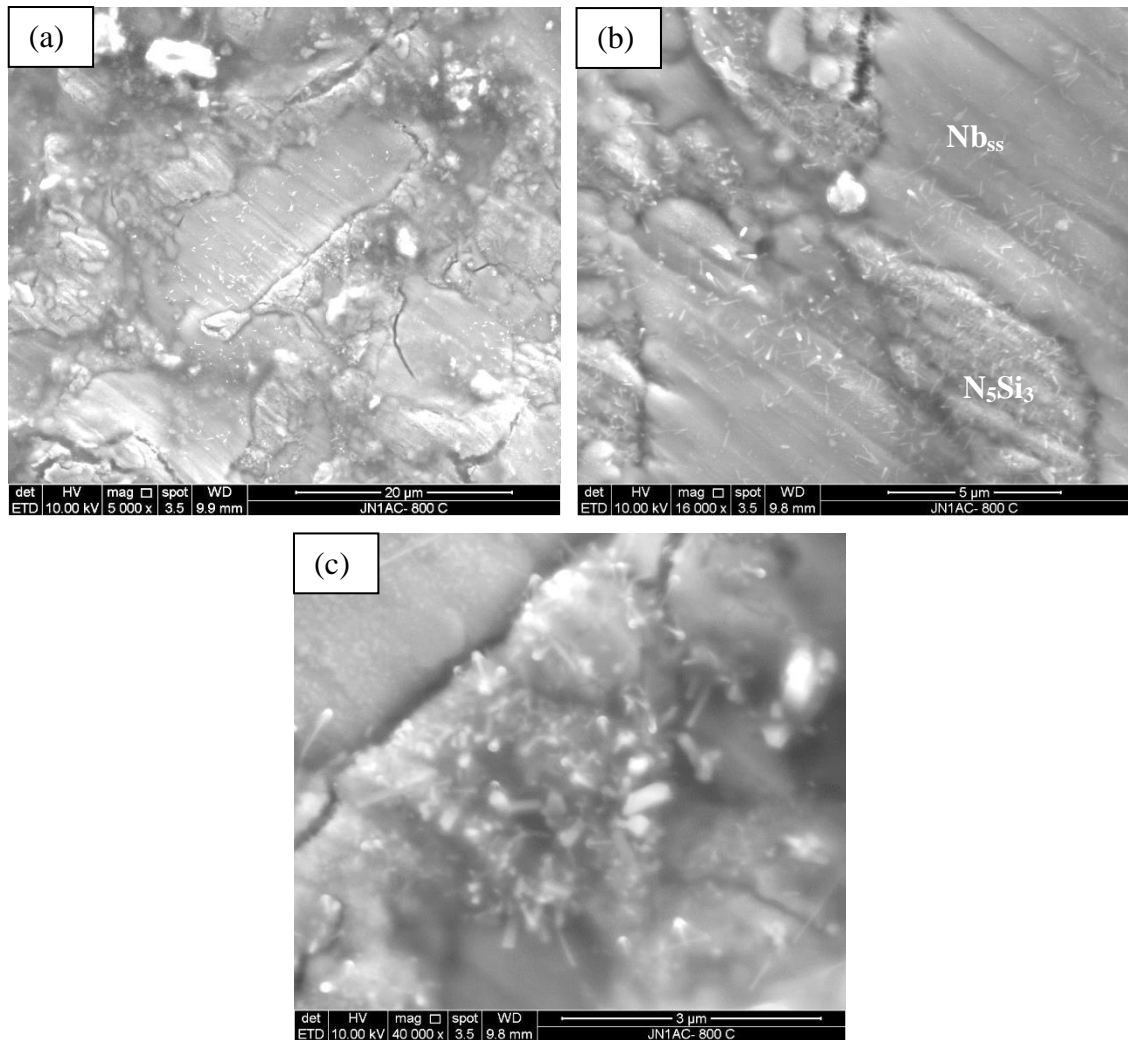
Figure 6.3 BSE images of oxide surfaces on JN1 AC 800 °C at (a) 5000X, (b) 16,000X and (c) 40,000X magnification. The oxidised phases below the scale are indicated.

Cross sections of the oxidised specimen were also studied, see Figure 6.4 below. The diffusion zone extended roughly 75 μm below the surface of the alloy and there was cracking throughout the diffusion zone parallel to the oxide surface. The cracks had travelled predominantly through the silicide grains rather than the embrittled Nb_{ss} and oxide phases. The details of the microstructure shown in Figure 6.4 are essentially the same as those reported in (Geng & Tsakiropoulos 2007) for JG4-AC after oxidation at 800 °C. The toughness of Nb_5Si_3 is ~3 MPa√m and increases to ~10 MPa√m with 30 at% Ti (Chan 2005). The Figure 6.4 would suggest that after 100h at 800°C the toughness of the Nb_5Si_3 in the diffusion zone was lower than that of the Nb_{ss}. The diffusion zone which exhibited the silicide cracking comprised of Nb_5Si_3, heavily contaminated Nb_{ss} and a mixed oxide. The alloy below the diffusion zone is comprised

of the same phases as JN1-AC before oxidation, however with an increased O_2 content. The chemical compositions of these phases can be seen in Table 6.1.
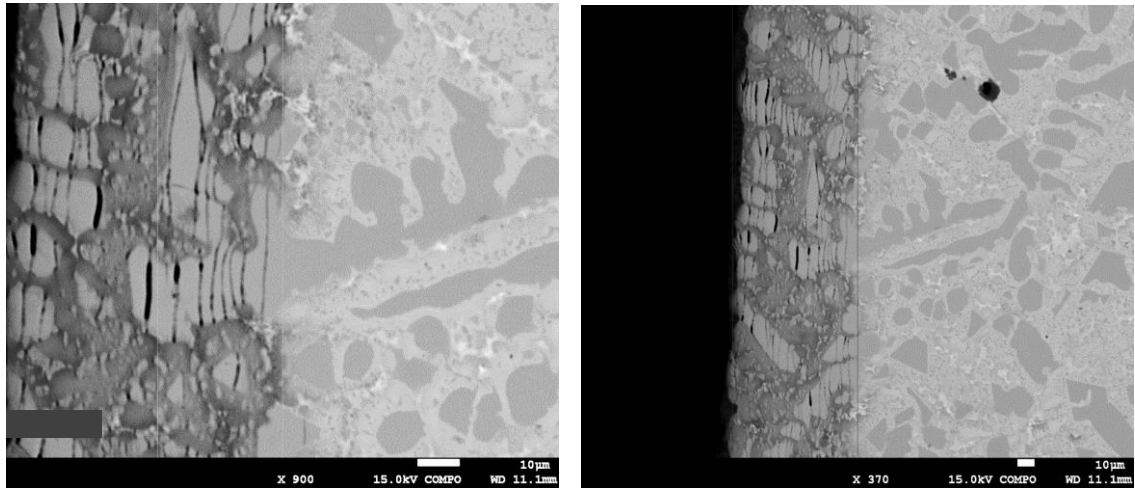
Figure 6.4 BSE image of cross sections of JN1-AC 800°C showing cracks in the diffusion zone.

Figure 6.5 shows X-ray maps for an area of JN1-AC after oxidation at 800 °C. The Hf map shows the formation of HfO_2 in the bulk of the alloy. All the maps show the distribution of elements within the oxidised sample and are identical to those of the cast alloy. There is no visible banding towards the surface where element depletion may have occurred due to diffusion towards the surface (Dengzun Yao et al. 2009). The oxygen map shows the highest oxygen concentration near the edge of the specimen (RHS on image).
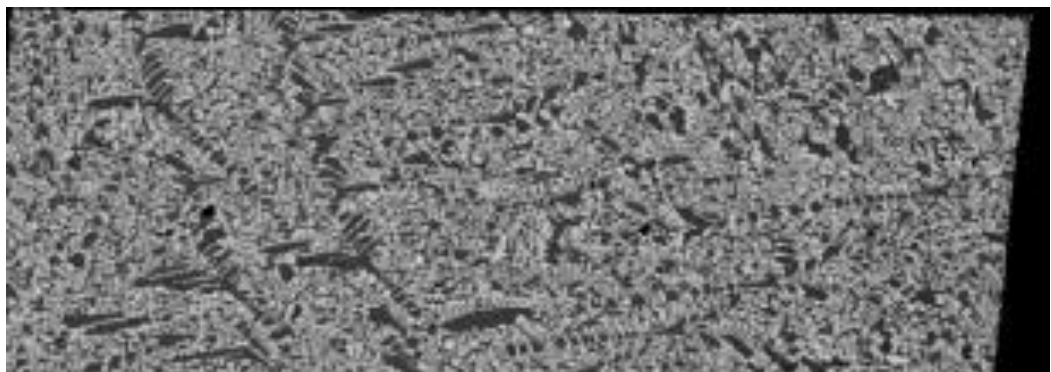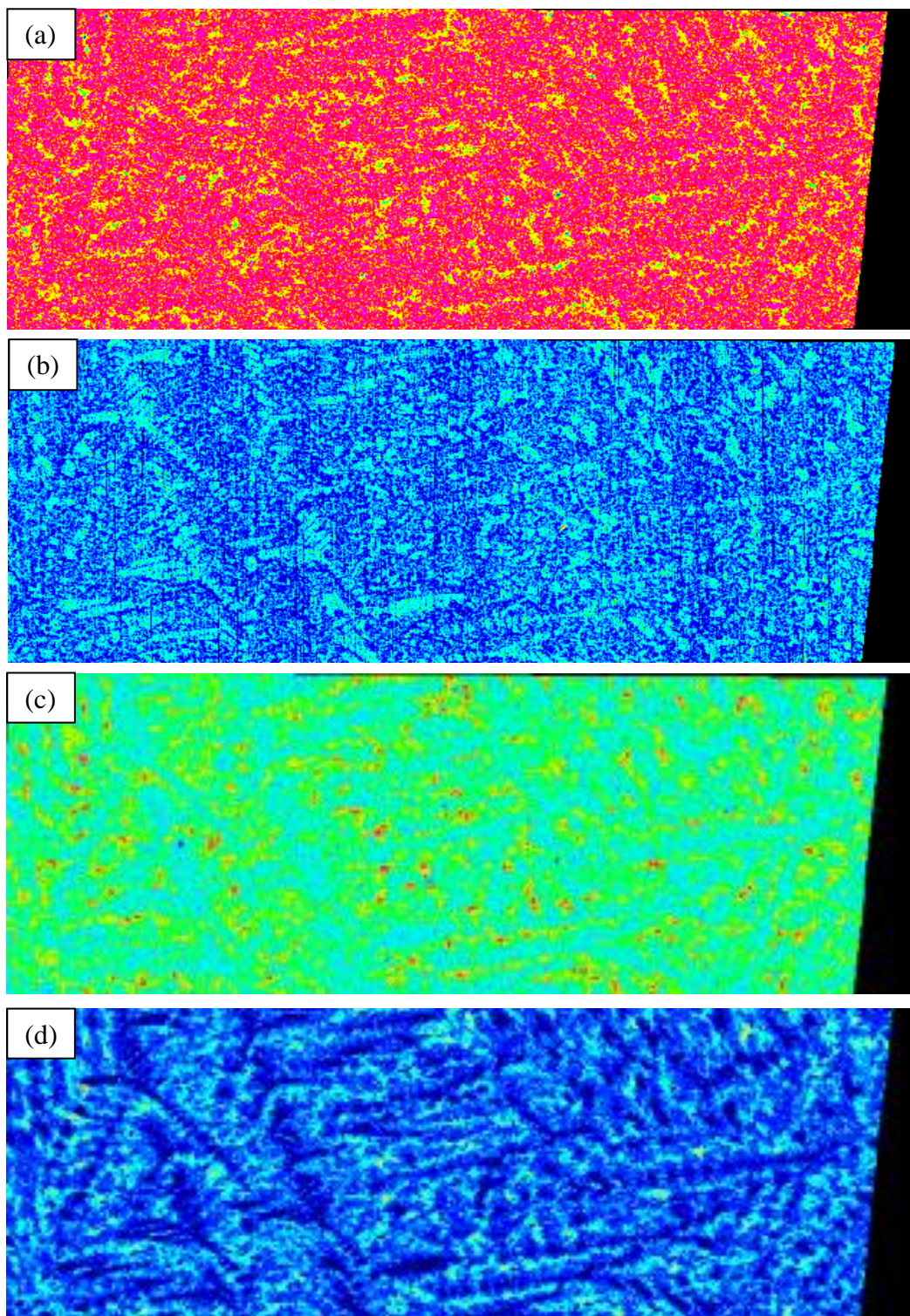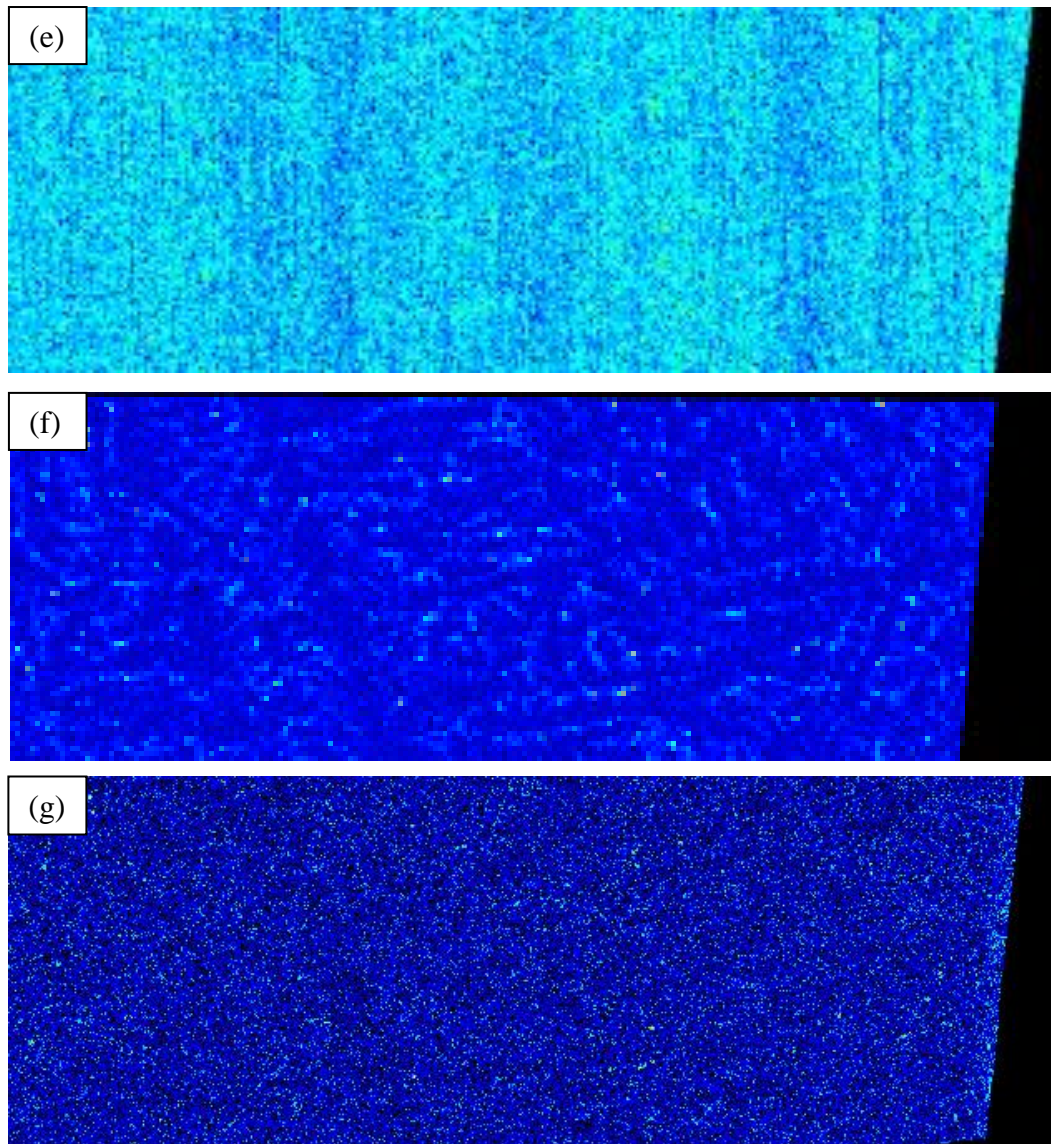
Figure 6.5 BSE image and X-ray maps of JN1 after oxidation at 800 °C Nb (a), Si (b), Ti (c), Cr (d), Al (e), Hf (f) and O (g). The surface of the specimen is on the RHS of the image.

Table 6.1 gives the EPMA data for the oxidised JN1-AC. Data was taken in the diffusion zone, 30 μm below the diffusion zone and the bulk of the alloy in order to determine how deep the contamination by oxygen was. The diffusion zone was comprised of Nb_5Si_3 and a mixed oxide of which the constituent phases are unknown. On the basis of the results reported in (Zelenitsas & Tsakiropoulos 2006a; Geng & Tsakiropoulos 2007) the oxides were likely to be niobates of Ti, Al and Cr and Nb_2O_5, SiO_2 and TiO_2. The composition of the missed oxide in JN1-AC was similar to that reported in (Geng & Tsakiropoulos 2007) for JG4-AC. Compared with the cast alloy (Table 4.4) the Nb_5Si_3

showed little to no affinity for oxygen, with a low (0.4 at%) concentration of oxygen in the diffusion zone and 0 at% oxygen below the diffusion zone and in the bulk. The latter is in agreement with the results reported in (Geng & Tsakiropoulos 2007) for JG4-AC. However the Nb_{ss} in JN1 had been contaminated and has an oxygen concentration of 1.4 at% in the diffusion zone, which dropped towards the bulk of the alloy where the oxygen content was 0.8 at%. This confirmed that oxygen had contaminated (reached the bulk of the alloy) and displayed higher levels than those seen in JG4-AC which might suggest that the synergy of Hf and Mo is effective for controlling contamination by oxygen at 800 °C. The oxygen content of the Nb_{ss} was below the maximum solubility of O_2 in Nb_{ss} (~9 at%) owing to the the formation of HfO_2 in the microstructure. The pesting of the specimen in some parts could suggest that over a prolonged period of time it is likely that the whole specimen might pest which would then suggest that Hf on its own (or in synergy with Ti, Al and Cr but not other TMs like Mo or simple metals like Sn) cannot supress pest oxidation.

Table 6.1 EPMA data for phases in JN1-AC oxidised at 800 °C (at%)

Area of interest	phase	Nb	Si	Ti	Cr	Al	Hf	O
Diffusion zone	Nb_5Si_3	39.1±0.9	35.3±1.2	17.2±0.5	0.9±0.1	2.8±0.3	4.3±0.1	0.4±0.9
		37.8-39.9	33.8-36.8	16.6-17.9	0.8-1.0	2.5-3.2	4.2-4.4	0-2.0
	Mixed oxide	34.3±1.2	0.8±0.4	17.8±0.6	4.6±0.3	3.9±0.3	2.8±0.1	35.9±1.7
		33.4-36.0	0.4-1.2	16.8-18.1	4.4-5.0	3.6-4.2	2.7-2.9	33.6-37.9
30 µm below the Diffusion zone	Nb_{ss}	50.2±3.5	1.7±1.5	28.4±1.5	8.1±2.4	5.7±0.2	4.4±0.5	1.4±1.6
		46.9-54.2	0.5-3.9	26.6-29.9	6.6-11.6	5.5-6.0	4.0-5.1	0-2.9
	Nb_5si_3	40.7±0.2	34.2±0.0	17.4±0.0	0.8±0.0	2.6±0.1	4.3±0.1	0.0±0.0
		40.4-40.9	34.2-34.2	17.4-17.4	0.8-0.9	2.5-2.7	4.2-4.4	0-0
Specimen Bulk	Nb_{ss}	50.6±1.8	1.7±1.3	29.0±0.7	8.1±2.5	6.2±0.2	3.5±0.4	0.8±1.4
		49.0-52.5	0.8-3.1	28.6-29.9	5.7-10.7	6.0-6.4	3.1-3.9	0-2.4
	Nb_5si_3	40.5±0.1	33.7±0.1	17.6±0.0	0.9±0.0	2.9±0.1	4.3±0.0	0±0
		40.4-40.5	33.6-33.8	17.6-17.6	0.9-1.0	2.9-3.0	4.3-4.4	0-0

6.2   Alloy JN2 (Nb-18Si-15Ti-10Cr-2Hf-5Mo-5W-2Sn) after oxidation at 800 °C

The isothermal oxidation study of JN2-AC was done as described in section 3.9. The same preparation procedure as JN1-AC was used for the TGA specimen of JN2-AC. Figure 6.6 shows the TGA data for JN2-AC, oxidised at 800 °C; unlike JN1 the TGA curve was not smooth but more similar in shape to that of the KZ alloys with Al and Cr additions (Zelenitsas & Tsakiropoulos 2006a). The roughness of the TGA curve confirmed that there were small changes in weight caused by stress relief as the oxide

scale cracked and pulled away from the substrate. This is supported by Figure 6.7 where it can be clearly seen that a non-adhesive oxide scale had formed with contact only along the edges of the specimen, as seen before in the oxidised alloy KZ5-HT and KZ6-HT (Zelenitsas & Tsakiropoulos 2006a). The weight gain of JN2-AC was 0.009 g/cm^2 and the data gave a linear oxidation rate constant of 3×10^{-8} gcm^{-2}s^{-1}. Both the weight gain and rate constant was higher compared with alloy JN1. In comparison the alloy JG6-AC had a mass gain of ~ 0.0023 g/cm^2 and a parabolic rate constant of 1.0×10^{-11} g^{2}cm^{-4}s^{-1} after oxidation at 800 °C which indicated better oxidation resistance than JN2. Before considering the oxidation of JN2 in more detail it is fair to say that the better oxidation behaviour of JG6 was due to the increased Ti and Sn concentrations in JG6. There was little beneficial effect gained from increasing the Cr content, and the presence of the Laves phase in JN2-AC, over the effects gained by simply adding more Ti and Sn.
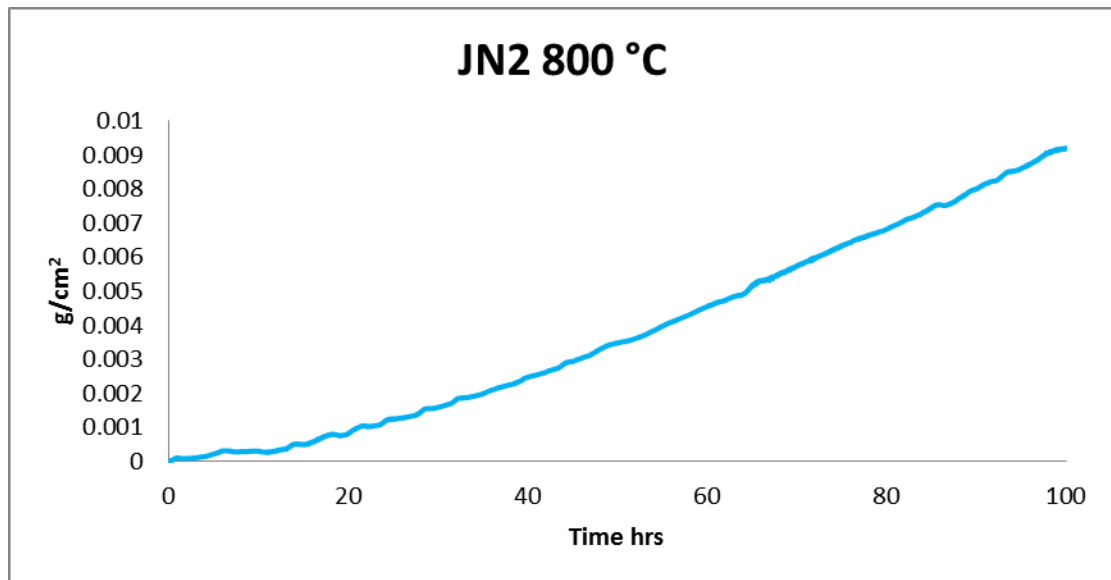
Figure 6.6 TGA data of JN2 AC after oxidation at 800 °C

Figure 6.7 shows the lack of scale adhesion at the scale/substrate interface. At higher magnification the scale appeared to show contrast differences indicating two different oxide phases.

Figure 6.7 image of JN2 800 °C after 100 h oxidation

Figure 6.8 shows typical SEM images of the surface of JN2-AC after 100h oxidation at 800 °C. The low magnification topographical image (Figure 6.8 a) showed that a relatively thick scale had formed on the outside of the sample, unlike JN1 and JN3. The Nb_5Si_3 phase can no longer be seen through the surface of the scale as the thick oxide scale has covered the entire sample surface. The oxide scale formed was non-protective and highly cracked along the surface (Figure 6.8 b). The higher magnification image also shows there was no presence of needle like oxide precipitates like those seen on JN1 (Figure 6.8 c)
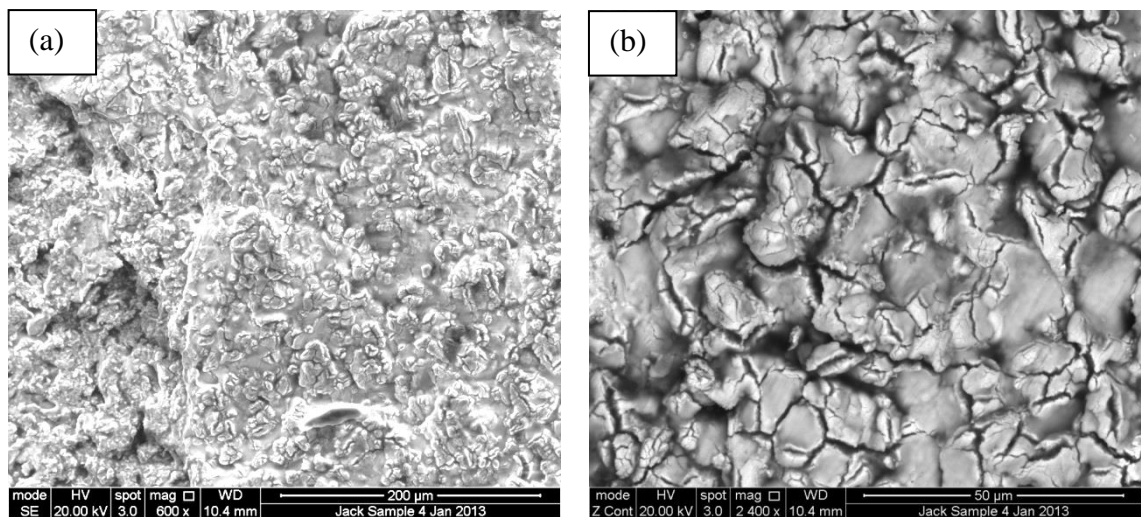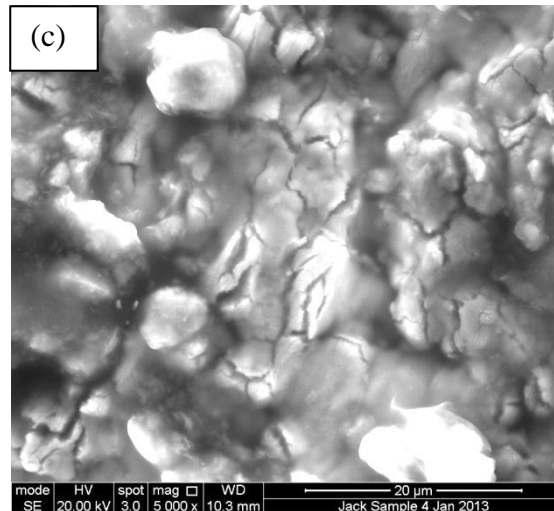
Figure 6.8 SE and BSE images of JN2 800 °C at different magnifications 600, 2400 and 5000 X

Figure 6.9 shows typical images of the cross sectional JN2-AC after oxidation at 800 °C. The low magnification images showed that there were pores of ~50 μm diameter in the sample (see Figure 6.9a). Higher magnification images confirmed the presence of HfO_2 precipitates at Nb_5Si_3 grain boundaries throughout the alloy, as reported in (Geng & Tsakiropoulos 2007). There was a diffusion zone formed below the scale with cracks running parallel to the surface (see Figure 6.9 b) as was seen in (Zelenitsas & Tsakiropoulos 2006a; Geng & Tsakiropoulos 2007). In some areas of the specimen significant parts of the diffusion zone were missing (see Figure 6.9 c), this was likely lost during the sample preparation. This was further evidence of the lack of adherence of the scale. This made it impossible to get an estimate of the extent of the diffusion zone in JN2-AC after oxidation at 800 °C. In the diffusion zone the Nb_5Si_3 silicide grains were severely cracked as was seen in JN1-AC (see Figure 6.2) and were surrounded by highly contaminated/oxidised Nb_{ss}. The 2000 X magnification image near the edge of the alloy displays a large degree of parallel cracking within the silicides close to the oxide/substrate interface. This cracking is visible in all other 800 °C samples and is caused by the stress induced by the volume expansion which occurs during oxidation.
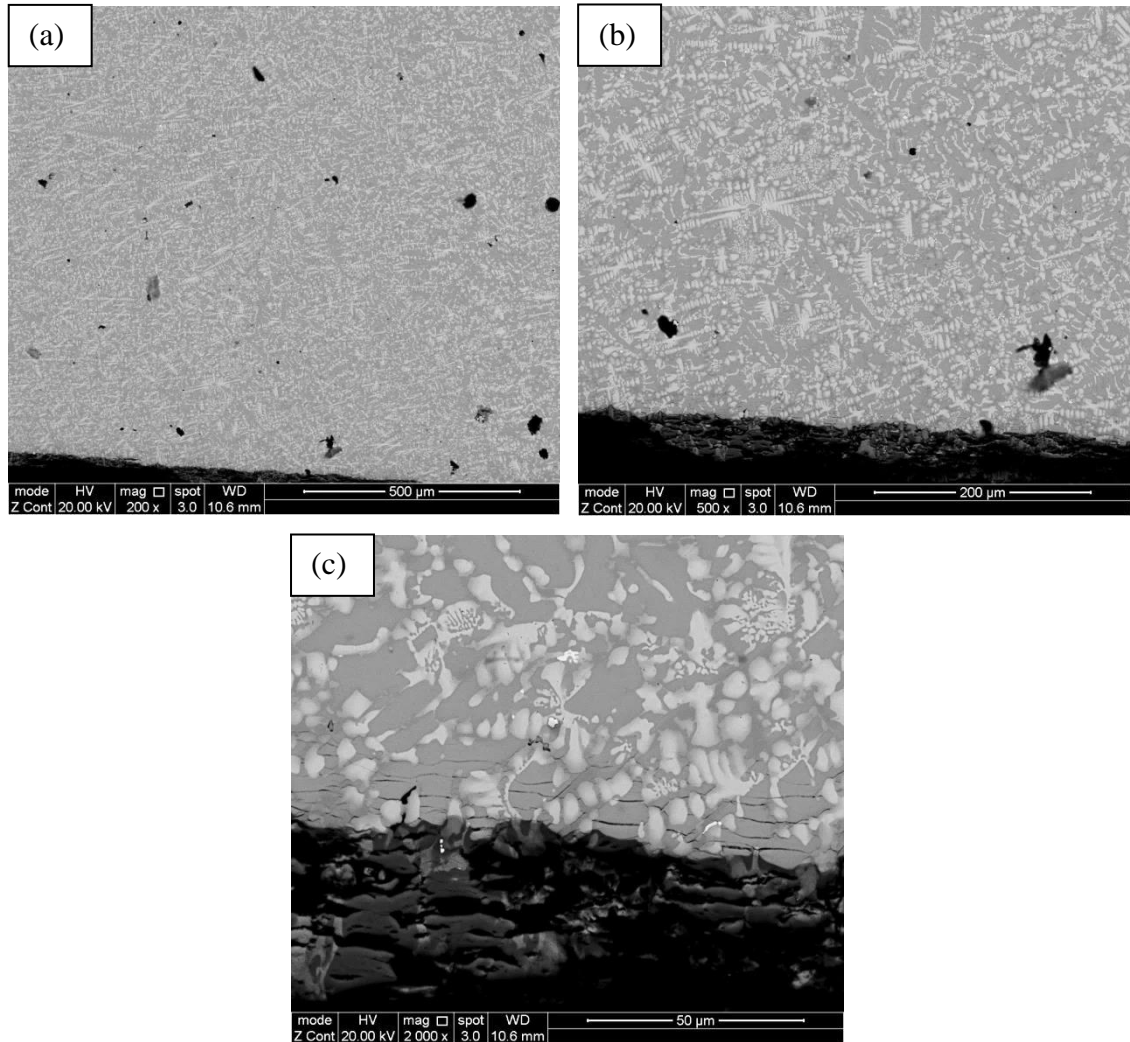
Figure 6.9 BSE cross sectional image of JN2 800°C at (a)200X, (b) 500X and (c) 2000X magnification

Figure 6.10 shows the BSE image of JN2 after oxidation at 800 °C. The scale outer scale has detached as is shown in Figure 6.7, the cracked diffusion zone extends ~20 μm from the surface of the substrate. The microstructure is similar to that of the cast alloy, all elements (apart from oxygen) show a relative depletion at the very edge of the surface, and the silicide and Nb_{ss} phases can be clearly seen with the positioning of the Laves phase being highlighted by the Cr map. The Sn map does not display any partitioning, indicating that no discernible Sn rich zone has formed at the surface (it is possible that any layer formed was attached to the spalled oxide layer).
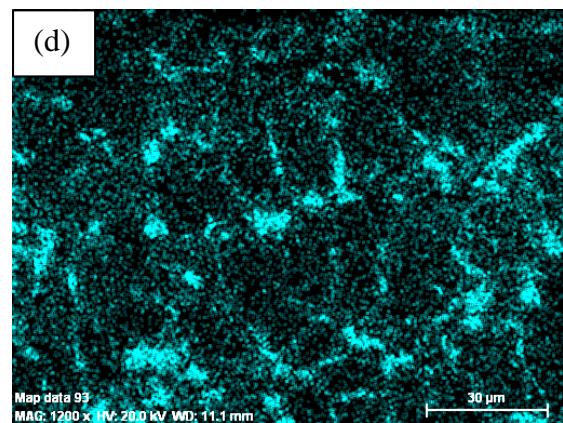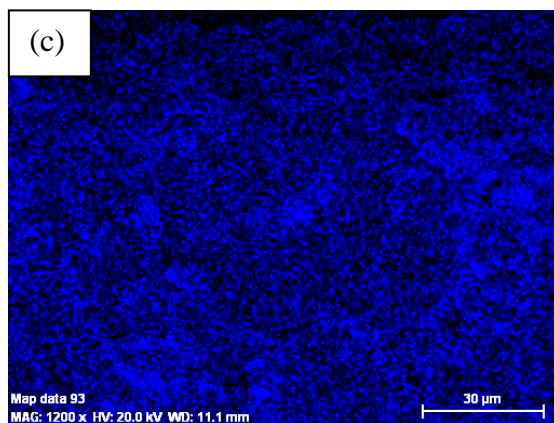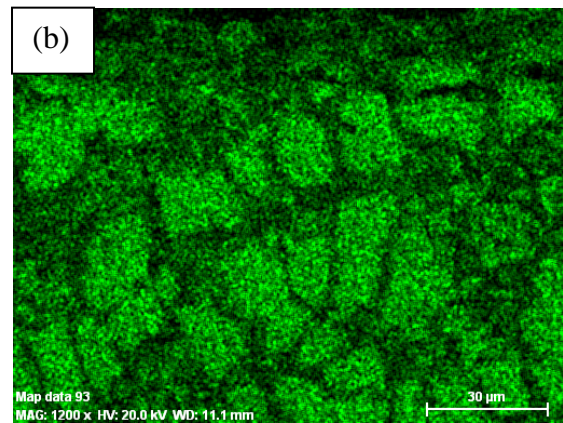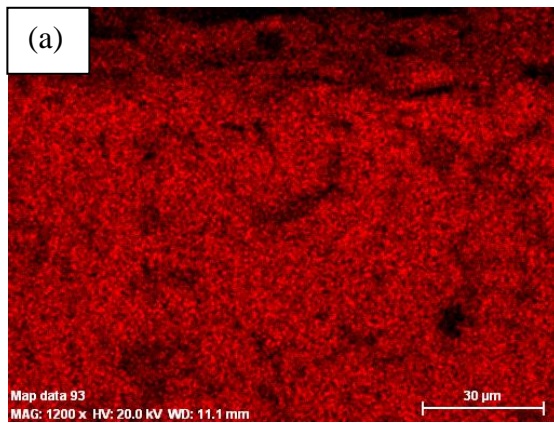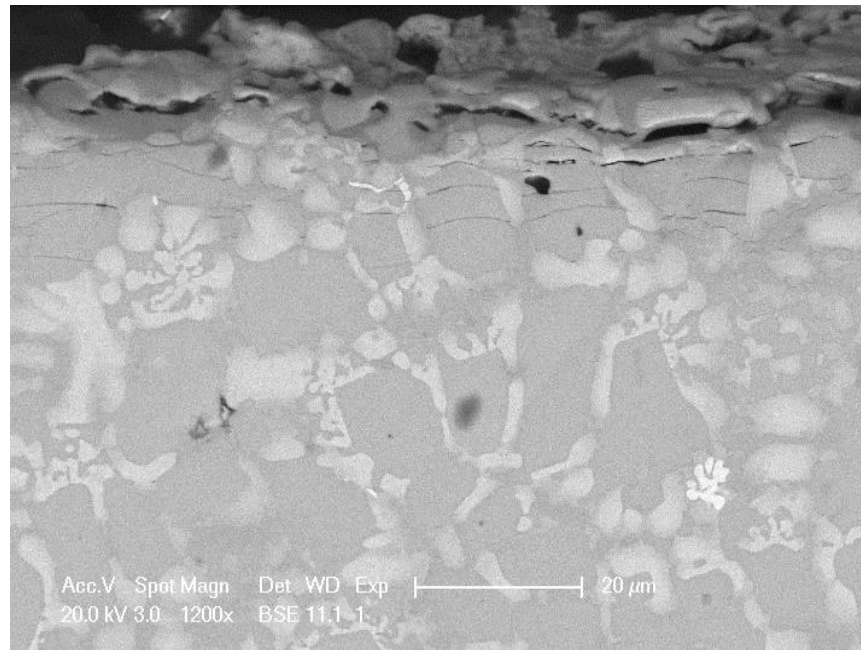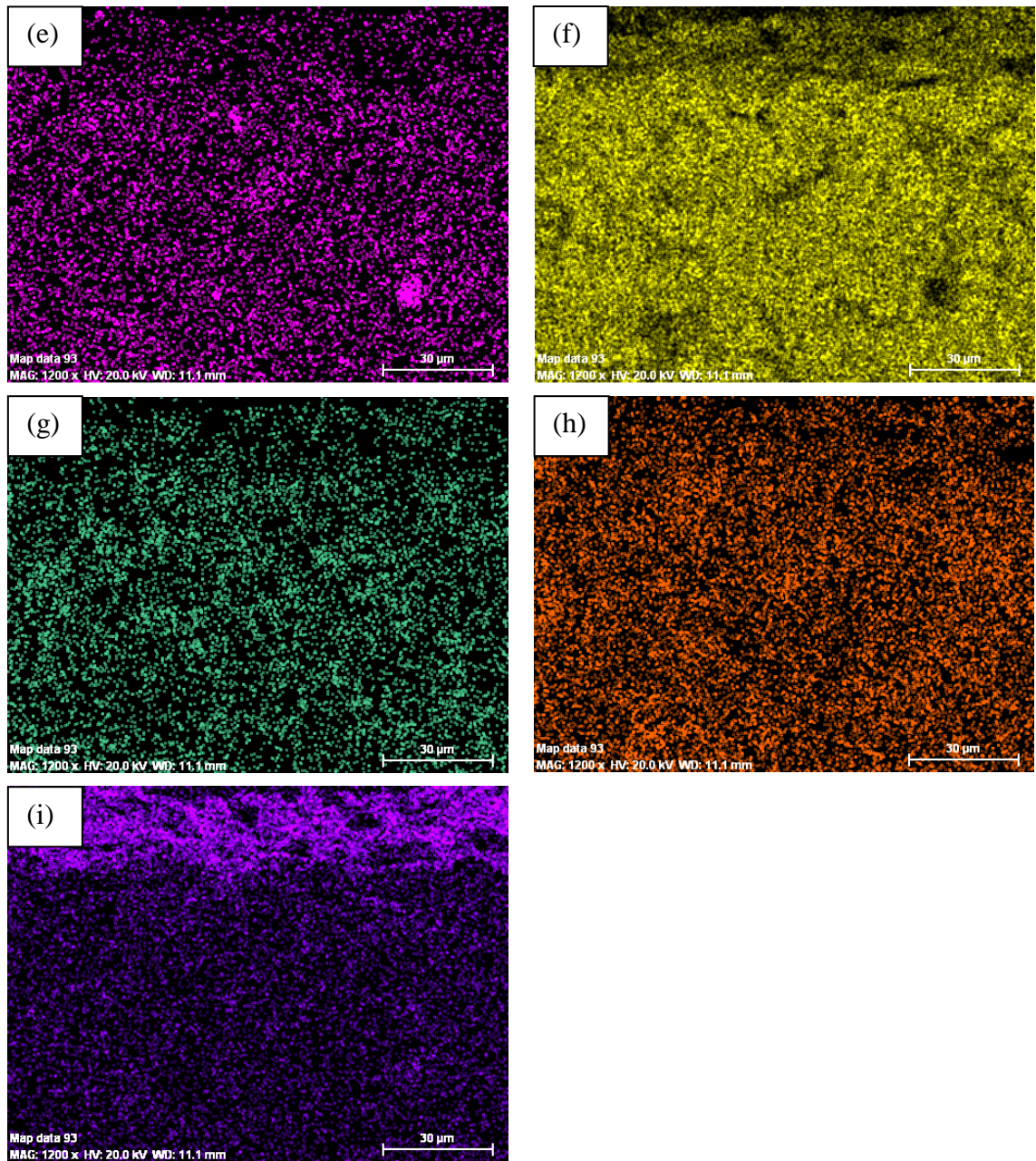
Figure 6.10 BSE image and X-ray maps of JN2 800 °C Nb (a), Si (b), Ti (c), Cr (d), Hf (e), Mo (f), W (g), Sn (h) and O (i).

Table 6.2 shows the EPMA phase analysis data from the diffusion zone, 60 μm from the edge of the sample and in the bulk of JN2-AC after oxidation at 800 °C. At the top of the diffusion zone the Nb_{ss} displayed an oxygen concentration of 2.1 at% but the oxygen contents both 60 μm from the edge of the sample and in the bulk of the alloy were 15.3 and 15.5 at% respectively. As significant parts of the scale and diffusion zone were lost, it is highly likely that the Nb_{ss} analysis at the top of the diffusion was remnant of

incompletely oxidised Nb_{ss} that could adhere to the rest of the alloy as it still had some toughness. The compositions of the high oxygen containing Nb_{ss} were slightly lower in Ti and Cr and slightly richer in W than the Nb_{ss} at the top of the diffusion zone, but all three compositions relate closely to that of JN2-AC (see Table 4.7). This would suggest either the homogenisation of the solid solution had occurred during the thermal expansion at 800 °C or that the "metastable" solid solution had oxidised preferentially.

There are many reasons why the solubility of oxygen in the Nb_{ss} below the diffusion zone and the bulk were higher compared with that of JN1 (see Table 6.1) The data in Table 6.2 also shows that both the Nb_5Si_3 and $NbCr_2$ Laves in JN2 were not immune to contamination by oxygen which, in the case of Nb_5Si_3, increased with depth below the diffusion zone. Compared with the cast alloy, the Nb_5Si_3 in JN2-AC after oxidation at 800 °C was leaner in Si but the concentration of the other elements were within the experimental error of EPMA. Compared with the cast alloy the composition of the $NbCr_2$ Laves phase in the JN2-AC after oxidation at 800 °C was essentially the same (within experimental error) regarding the concentration of all elements except oxygen. The assumption below will address some of the issues that might be responsible for the behaviour. Compared with the alloy JN1, the alloy JN2 had:

i.   Lower Ti and Hf and higher Cr contents and no Al.

ii. $NbCr_2$ Laves phase in its cast microstructure (owing to the higher Cr content of JN2).

iii. No microsegregation of Hf in the Nb_5Si_3 and thus only tetragonal Nb_5Si_3.

iv.   Strong partitioning of Cr, Sn and Ti in the Nb_{ss} which (a) had a strong effect on the solubilities (partitioning) of Mo and W in the Nb_{ss} and (b) led to the formation of three types of Nb_{ss}, see Table 4.7.

The vol% of solid solution was only slightly lower in JN2 than that in JN1 (see Table 4.4) and it is considered unlikely that the differences in isothermal oxidation between JN1 and JN2 at 800 °C can be solely attributed to the Nb_{ss}. The normal Nb_{ss} in JN2 was very rich in Mo (~ 11 at%) and W (~ 7.5 at%), as it had almost two and three times respectively the actual element content in the alloy (see Table 4.5 and Table 4.7) and slightly lower Ti content (~ 13 at%). The other two types of the solid solution were

significantly richer in Ti (up to 37 at%), and the average Ti content was similar to that in the Nb_{ss} in JN1. Furthermore, one of the solid solutions was even richer in Cr (up to ~ 25 at%). The increase in Cr content of the solid solution was accompanied by an increase in Si content, from ~ 1.8 at% in the normal Nb_{ss} to ~ 4.2 at% in the Cr and Ti rich Nb_{ss} (see Table 4.7). Compared with the alloy JN2 the alloy JG6 (Nb-24Ti-18Si-5Cr-5Al-5Hf-2Mo-5Sn) had:

i.   Higher Ti, Hf and Sn and lower Cr and Mo, and no addition of W.

ii.   Lower vol% of the $NbCr_2$ Laves phase (owing to the lower Cr content in JG6).

iii.   Strong partitioning of Sn that led to the formation of Nb_3Sn in the microstructure as well as Nb_{ss} (the former intermetallic was reported in (Geng, Tsakiropoulos & G. Shao 2007) as Sn rich Nb_{ss} but subsequent research in the group confirmed it to be the Nb_3Sn).

iv.   Microsegregation of Hf in Nb_5Si_3 that led to formation of tetragonal and hexagonal Nb_5Si_3, as was the case in JN1.

The "normal" Nb_{ss} in JG6-AC was rich in Ti, Cr and Hf, with similar contents of these elements as in one of the solid solutions in JN2 but leaner in Mo. The Nb_5Si_3 in JG6 was richer in Ti but leaner in Cr, Mo and Hf compared with JN2. Finally, the vol% Nb_{ss} in JG6 could not be estimated owing to the contrast of this phase under back scatter electron conditions, but it was thought to be significantly lower compared with the other JG series alloys (Geng, Tsakiropoulos & G. Shao 2007).

The diffusivity of oxygen in Nb increases with temperature, for example the diffusion distances at 800 °C and 1200 °C are about 0.6 and 6.2 mm, respectively (Ang 1953). The additions of Ti, Cr, Hf, Mo, W and Si in the alloys of this research were made to reduce the diffusivity of oxygen in Nb. It is thought that this effect of the aforementioned elements arises either from their strong interaction with oxygen or from their smaller atomic radii. For example, the diffusivity of oxygen in Nb-25 at% Ti solid solution alloy is about 5% that in unalloyed Nb (Kelly et al. 1949).

Even though there is no data for the effects of Hf, Mo and W on the solubility of oxygen in binary solid solution alloys of these elements with Nb at 800 °C, there is some data for higher temperatures. The data shows that all three elements reduce the

solubility of oxygen, but the behaviour of Hf is different from that of Mo and W. The solid solubility of oxygen in (Nb,Mo) and (Nb,W) solid solution binary alloys was studied by Taylor and Doyle (Taylor et al. 1967) at 1500 °C and 1000 °C who reported it to be lower compared with that in unalloyed Nb. According to these researchers, at 1500 °C the solubility of oxygen was about 1.75 at.% in Nb-10.5 at.% Mo, and about 2.3 at% in Nb-10.5 at% W. However, for binary (Nb,Hf) alloys the same authors reported a different behaviour, with the oxygen content increasing from ~ 4.75 at% in pure Nb to ~ 8.75 at% in Nb-2 at% Hf and then decreasing with further increase in Hf content to ~ 0.2 at% oxygen in Nb-10at%Hf where the HfO_2 was in equilibrium with the Nb_{ss}. Hf has a remarkably different effect on the solubility of oxygen in $(Nb,Hf)_{ss}$ when present in concentrations lower or higher than about 2 at%.

Zelenitsas and Tsakiropoulos (Zelenitsas & Tsakiropoulos 2006a) and Geng et al (Geng, Tsakiropoulos, et al. 2006a) reported that Nb_2O_5 formed on Nb silicide based alloys during oxidation at 800 °C. The Nb_2O_5 occurs in two forms of the same composition, a low temperature orthorhombic form, known as α Nb_2O_5, and a high temperature monoclinic form, known as $βNb_2O_5$. The α→β transformation occurs somewhere in the range 830 °C (Holtzberg et al. 1975) to 900 °C (Goldschmidt 1959). The $αNb_2O_5$ is considered metastable. Alloying additions are able to stabilise either form of Nb_2O_5. For example, Si progressively stabilises the $αNb_2O_5$ in preference to $βNb_2O_5$. The $βNb_2O_5$ can be stabilised by oxides of transition elements, e.g. TiO_2 and Cr_2O_3. The type of Nb_2O_5 formed can affect the oxidation rate of Nb alloys. For example, Argent and Phelps (Argent & Phelps 1960) attributed the decrease in the oxidation of (Nb,Ti) solid solution alloys at 700 °C to different diffusion rates of oxygen in the low and high temperature forms of Nb_2O_5.

Argent and Phelps (Argent & Phelps 1960) reported that Ti improves the oxidation of (Nb,Ti) solid solution alloys (at 800 °C the oxidation rate of Nb-20 at% Ti was ~ $2X10^{-7}$ gcm^2/s compared with ~ $6X10^{-6}$ gcm^2/s of Nb) and Sims et al (Sims et al. 1959) reported that there was minimum contamination by oxygen at 800 °C of the alloy Nb-25 at% Ti. According to Birks and Meir diffusion of oxygen in the Nb solid solution was reduced when the Ti content of Nb_{ss} was in the range 25 to 35 at%. The latter was thought to be related to the formation of $3Nb_2O_5•TiO_2$ in the scale (Birks & Meier 1982) and the influence of dissolved titanium on Nb_2O_5 (Sims et al. 1959).

Molybdenum is also reported to improve the oxidation of (Nb,Mo) solid solution alloys but its effectiveness decreases above a critical concentration(Kelly et al. 1949). According to Geng et al (Geng, Tsakiropoulos & G. Shao 2007) about 8 to 9 at.% Mo in the Nb_{ss} and about 1.5 to 2.5at.% Mo in the Nb_5Si_3 were high Mo concentrations leading to pest oxidation at 800 °C in Nb-18Si-5Cr-5Al-5Mo based alloys and suggested that the Mo content in the alloy should be lower than 5 at% to ensure avoidance of pest oxidation.

The oxidation of Nb has been discussed by Kofstad and Espevik (Kofstad & Espevik 1965) and Wilkinson (Wilkinson 1969). The oxidation proceeds by diffusion of oxygen into the metal, followed by the subsequent formation of NbO, NbO_2 and Nb_2O_5. At T < 400 °C the oxidation reactions do not proceed to the final formation of Nb_2O_5. Under normal atmospheric conditions, at T > 500 °C, the incubation period of the formation of Nb_2O_5 is too short to be detected in kinetic studies, with the result that the lower oxides are thought to play a negligible part in the oxidation process at T > 500 °C. Under these conditions a simultaneous oxygen dissolution and oxide formation takes place. This reaction occurs rapidly at 650 °C (at 1200 °C the kinetics were characterised as accelerated (extremely fast linear behaviour)). The results of Zelenitsas and Tsakiropoulos (Zelenitsas & Tsakiropoulos 2006a), Geng et al (Geng, Tsakiropoulos, et al. 2006a) and Chattopadhyay (Chattopadhyay et al. 2008) confirmed that Nb-base alloys oxidise mainly by anionic diffusion, with the rapid formation of stratified and porous scale which spalls off easily. The Nb_2O_5 scale is porous and non-protective, readily cracking and spalling due to stresses at the metal/oxide interface. This is a consequence of the Nb_2O_5 scale possessing a molar volume five times greater than the molar volume of Nb (Nb_2O_5: 58.8 cm^3mol^{-1}, Nb: 10.9 cm^3mol^{-1}(Kubaschewski & Hopkins 1960). Thus the oxidation of Nb_{ss} that is usually surrounded by Nb_5Si_3 and other phases (e.g. $NbCr_2$) in Nb silicide based alloys will generate high stresses that will deform the latter phases. Whether the aforementioned phases will crack or not will depend on their toughness.

The fracture toughness of unalloyed tetragonal Nb_5Si_3 is about 3 MPa√m and increases to an average value of about 10 MPa√m at ~ 30 at% Ti substituting for Nb. What the effect of substitution of Nb by Mo, Cr and W individually or in synergy with Ti is on the toughness of Nb_5Si_3 is unknown. For ~ 13 at% Ti in Nb_5Si_3 (this was the Ti

content in Nb_5Si_3 in JN2-AC) the toughness is expected to be ~ 7 MPa√m, according to data given by Chan (Chan 2002a). The fracture toughness of alloyed (but not with the same elements as those in JN2) C14 $NbCr_2$ is about 5 MPa√m (Chan & Davidson 2001; Chan 2002a). The fracture toughness of Nb-13Cr-37Ti (notice that similar Ti and Cr contents were measured for one of the solid solution types in JN2-AC) solid solution alloy is about 20 MPa√m (Chan & Davidson 2001). The brittle or ductile behaviour of Nb-Ti-Cr solid solution alloys depends on the relationship between the Ti/Nb ratio and the Cr content. The Ti content required for ductile behaviour increases with Cr content. For ~ 9 at% Cr the Ti/Nb ratio should be above 0.3, for ~ 14 at% Cr the ratio should be above 0.5 and for ~ 22 at% Cr the ratio should be above 0.9. The aforementioned Cr concentrations correspond to the three solid solution types in JN2-AC, for which the Ti/Nb ratios are 0.23, 0.9 and 0.6. Thus, only the Sn and Ti rich Nbss in JN2-AC(see Table 4.5) meets the criterion for ductility.

The Nb_5Si_3 silicide suffers from pest oxidation at 800 °C (and 1200 °C) when oxidised in static air, where it disintegrates completely into powder in less than 24 h (Vellios & Tsakiropoulos 2005). Refractory metals are also prone to pesting.

The above discussion points to the synergy of the many factors that might have contributed to the inferior oxidation at 800 °C of JN2-AC compared with JN1-AC and JG6-AC. It is not possible to isolate individual factors, as it is believed that more than one factor played significant role in the oxidation on JN2. For example, the diffusivity of oxygen in the different types of Nb solid solution varied at 800 °C (for example because of the different Ti, Mo, W, Hf contents, see above, or because of different forms of Nb_2O_5 formed in the scale, see above, but also because during this thermal exposure homogenisation of the solid solution occurred, as suggested by the phase analysis data given in Table 4.7 and Table 5.6) and oxygen contamination of the alloy occurred to different lengths depending on the distribution and chemistry of the solid solution types in the evolving (i.e., "dynamically" homogenising) microstructure at 800 °C. The different types of solid solution oxidised differently and deformed differently (owing to their "evolving" different chemistries) with most exhibiting brittle behaviour for the reasons given below, for example due to changes in the Ti/Nb ratio and Cr content. The stresses arising from the formation of oxidation products (because of differences in molar volumes, see above) led to the cracking of Nb_5Si_3, which was

severe as in the case of JN1 owing to the poor toughness of this phase, see above, and also to cracking of the $NbCr_2$ Laves phase owing to its poor fracture toughness, see above. The formation of cracks for the aforementioned reasons created more opportunities for contamination of the overall microstructure by oxygen and the penetration of oxygen to larger depths below the top of the diffusion zone and this resulted in further oxidation of the phases present.

Pest oxidation has been discussed in the literature. According to Grabke and Meier (Grabke & Meier 1995) the pest oxidation of intermetallics and intermetallic alloys is associated with oxide formation at g.bs, (pre-existing) cracks and pores and newly formed cracks (as discussed above) and occurs over a temperature range that is specific to the alloy system. In the case of Nb-Si based alloys pest oxidation can occur in the range 700 to 900 °C.

In this research porosity was found in the microstructure of the oxidised specimens of JN2-AC at 800 °C, see Figure 6.9. This porosity was most probably present in the cast alloy and the pores formed during the solidification of the alloy. The porosity present in JN2 and the cracking that resulted from the oxidation of phases in JN1 and JN2, as discussed above, must have contributed to the pest oxidation seen in parts of the JN1-AC and JN2-AC specimens oxidised at 800 °C.

Table 6.2 EPMA chemical analysis of JN2 800 °C (at%)

Phase and Area in sample	Nb	Si	Ti	Cr	Hf	Mo	W	Sn	O
Nb_{ss} diffusion zone	54.1±1.0 53.2-55.7	1.5±0.2 1.2-1.7	13.6±1.0 12.8-14.8	8.0±0.9 6.8-8.7	0.9±0.1 0.8-1.0	11.1±0.3 10.5-11.4	6.7±1.0 5.4-7.2	2.0±0.2 1.7-2.4	2.1±1.9 0.0-4.6
Nb_5Si_3 diffusion zone	45.7±1.2 43.9-46.7	27.4±1.4 26.1-28.7	14.1±1.4 12.9-16.1	1.3±0.8 0.7-2.3	2.5±0.6 1.8-3.2	1.2±0.5 0.8-1.8	0.5±0.2 0.4-0.8	0.9±0.2 0.8-1.2	6.3±1.7 4.2-8.1
Laves phase Diffusion zone	26.4±1.4 25.3-28.7	9.2±0.8 7.9-9.8	12.2±1.5 11.1-14.7	43.3±3.0 38.3-45.7	2.4±0.1 2.3-2.5	2.5±0.4 2.3-3.2	1.0±0.2 0.8-1.2	0.4±0.3 0.1-0.9	2.7±2.9 0.0-7.7
Nb_{ss} 60 µm from sample edge	47.1±3.3 44.0-52.1	1.4±0.1 1.3-1.7	10.4±1.5 8.8-13.2	5.7±1.1 4.6-7.8	0.7±0.1 0.7-0.9	10.1±0.5 9.7-11.2	7.9±1.0 6.6-9.7	1.4±0.3 1.0-1.9	15.3±6.3 5.3-20.5
Nb_5Si_3 60 µm from sample edge	40.6±1.1 39.7-42.5	29.4±0.2 29.2-29.7	12.6±1.4 11.6-14.8	1.7±0.4 1.7-2.1	1.7±0.4 1.5-2.3	1.5±0.4 0.8-1.8	0.7±0.2 0.3-0.8	0.7±0.2 0.6-0.9	11.2±1.8 8.3-12.8
Laves phase 60 µm from sample edge	25.8±1.4 24.6-27.3	10.2±0.2 10.0-10.5	11.4±0.9 10.8-12.4	44.8±0.9 43.7-45.2	2.3±0.0 2.3-2.3	2.4±0.3 2.2-2.7	1.0±0.1 0.9-1.1	0.2±0.2 0.1-0.4	1.8±1.7 0.0-3.4
Nb_{ss} bulk	47.4±1.3 47.3-48.4	1.8±0.6 1.4-2.7	10.1±0.4 9.8-10.7	5.2±0.2 5.0-5.5	0.8±0.1 0.7-0.8	9.9±0.4 9.3-10.1	8.1±0.6 7.2-8.7	1.2±0.0 1.2-1.3	15.5±1.1 14.5-16.9
Nb_5Si_3 bulk	38.8±3.4 35.0-40.7	27.4±1.4 25.7-28.3	14.3±3.5 12.2-18.4	3.1±2.1 1.9-5.6	1.9±0.7 1.5-2.8	1.6±0.4 1.1-1.8	0.7±0.4 0.2-0.9	1.0±0.5 0.7-1.6	11.1±1.3 9.6-12.0
Laves bulk	26.2±3.9 22.8-30.1	9.7±2.0 7.1-11.8	15.3±5.3 11.4-15.2	37.6±7.3 29.7-44.2	3.4±0.2 3.2-3.5	2.2±0.6 1.8-3.0	0.7±0.1 0.6-0.8	1.1±1.3 0.2-2.9	3.8±2.7 0.0-6.2

6.3   Alloy JN3 (Nb-18Si-15Ti-5Cr-2Hf-5Mo-5W-2Sn) after oxidation at 800 °C

Figure 6.12 shows the TGA data for the alloy JN3 AC after oxidation at 800 °C for 100h. The alloy had a weight gain of 0.007 g/cm^2, which was lower than that gained by JN2 (0.009 g/cm^2). The weight gain curve itself was smooth, as was the case for JN1-AC but the weight gain was different from that of JN2 and KZ5-HT (Zelenitsas & Tsakiropoulos 2006a). The TGA data indicated a steady growth rate of the scale, with no sudden increases in weight gain. The data showed a mix of both a linear and parabolic oxidation rate with constants of 2×10^{-8} gcm^{-2}s^{-1} from 0-50 h and 2×10^{-10} g^{2}cm^{-4}s^{-1} from 50-100 h, which was in between the value of JN2 (3×10^{-8} gcm^{-2}s^{-1}) and JN1 (1×10^{-8} gcm^{-2}s^{-1}). The alloy JN3 did not clearly show cracks on the scale near the edge but there was evidently a small amount of pesting at the edges forming an oxide
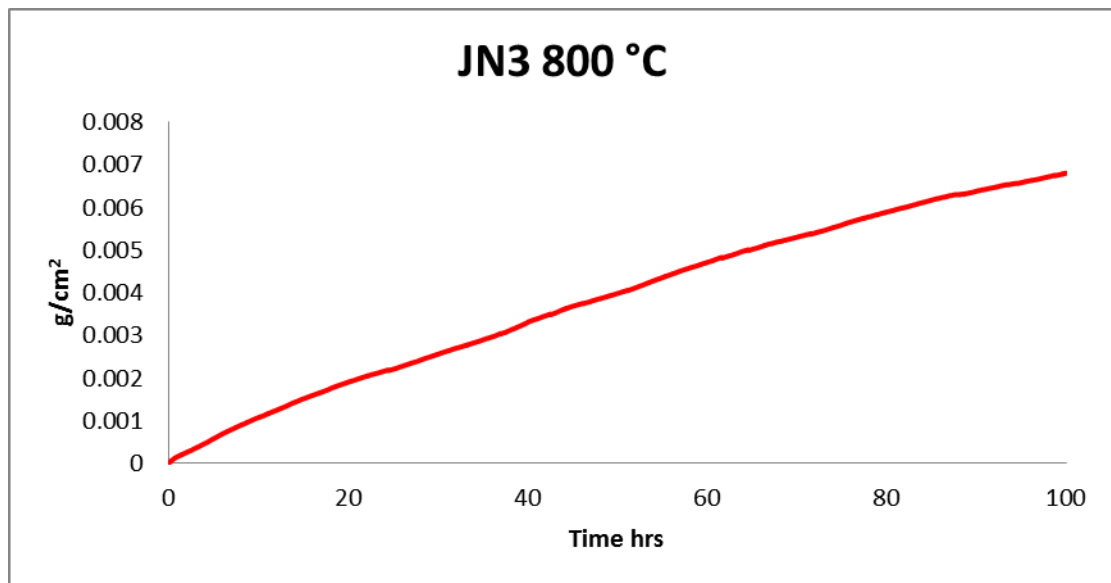
Figure 6.11 TGA data of JN3 AC after oxidation at 800 °C

Figure 6.12 image of JN3 800 °C after 100 h oxidation

Figure 6.13 shows typical images the oxide scale formed on JN3 AC at 800 °C; Nb_5Si_3 grains can still be clearly seen below the scale, along with the polishing lines. The ability to see these features indicated slow oxide kinetics and the inability of thick scale to form as was the case at 1200 °C. The BSE images show three different contrasts at low magnification, which correspond to Nb_5Si_3 and oxides, see Figure 6.13 (a). At medium and high magnification (Figure 6.13 b and c) oxides can be seen on the surface of the Nb_{ss} and Nb_5Si_3 grains respectively. In the case of the Nb_5Si_3 the oxides form as small, bright contrast, oxide crystals where the Nb_{ss} was the oxides were less defined. The degree of cracking on the surface is not as severe as that seen in JN2 which in itself would lead to less oxygen ingress through surface cracks.
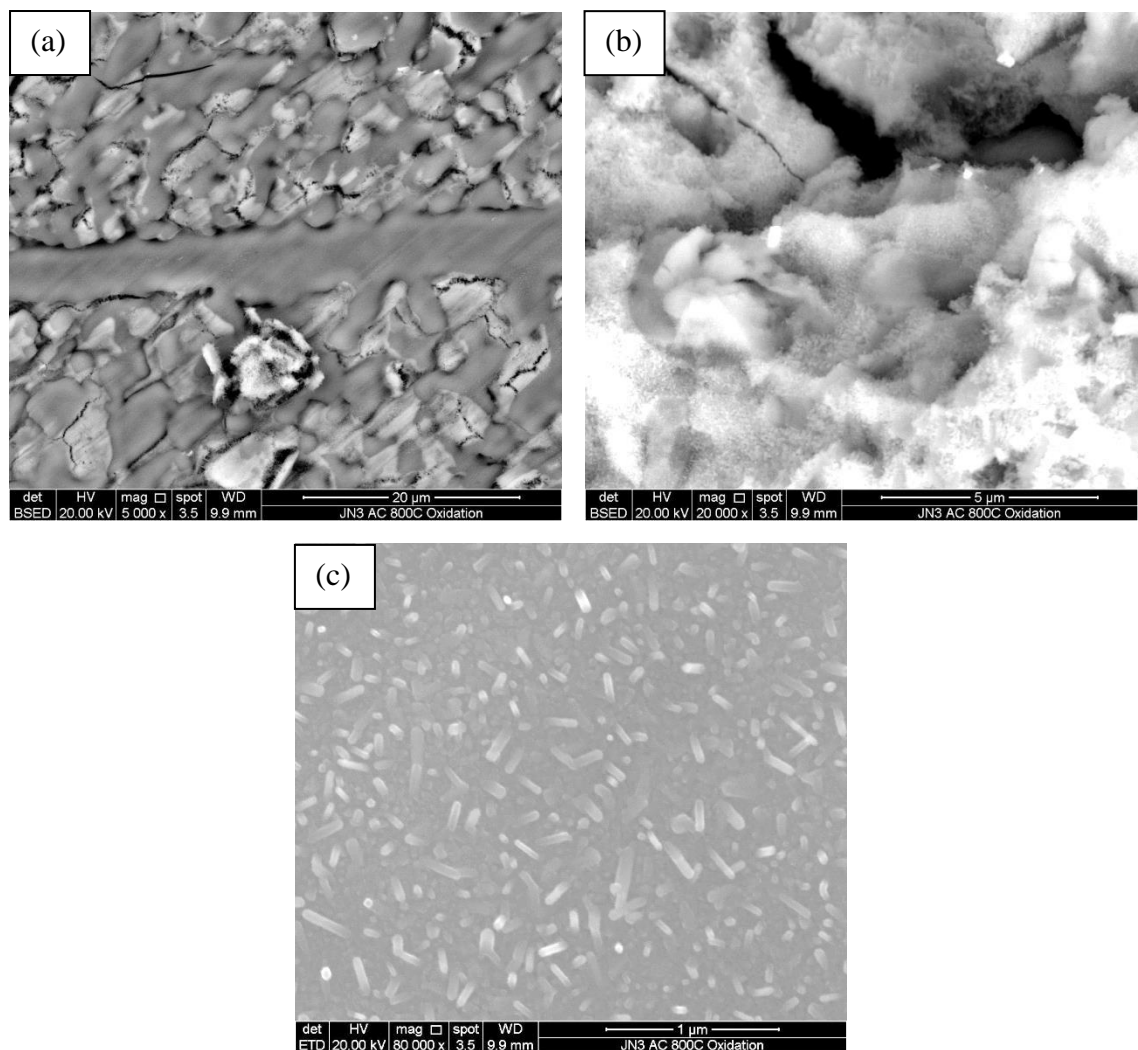
Figure 6.13 topographical images of JN3 AC oxide surface at 5000X, 20,000X and 80,000X magnification

Figure 6.14 shows cross section images of JN3 AC after oxidation at 800 °C. Figure 6.14 (a) shows the presence of porosity distributed throughout the sample, formed during solidification, separation of the scale from the surface can be seen at the bottom of the image. Due to the small amount of material that was available for the TGA, a specimen solely from the bulk was not possible, this lead to a difference in microstructure between the top and bottom of the image. The high magnification images (Figure 6.14 b and c) show that at the edge of the sample there is cracking in the silicides running parallel to the surface. HfO_2 precipitates can be seen at the edges of the silicide grains.
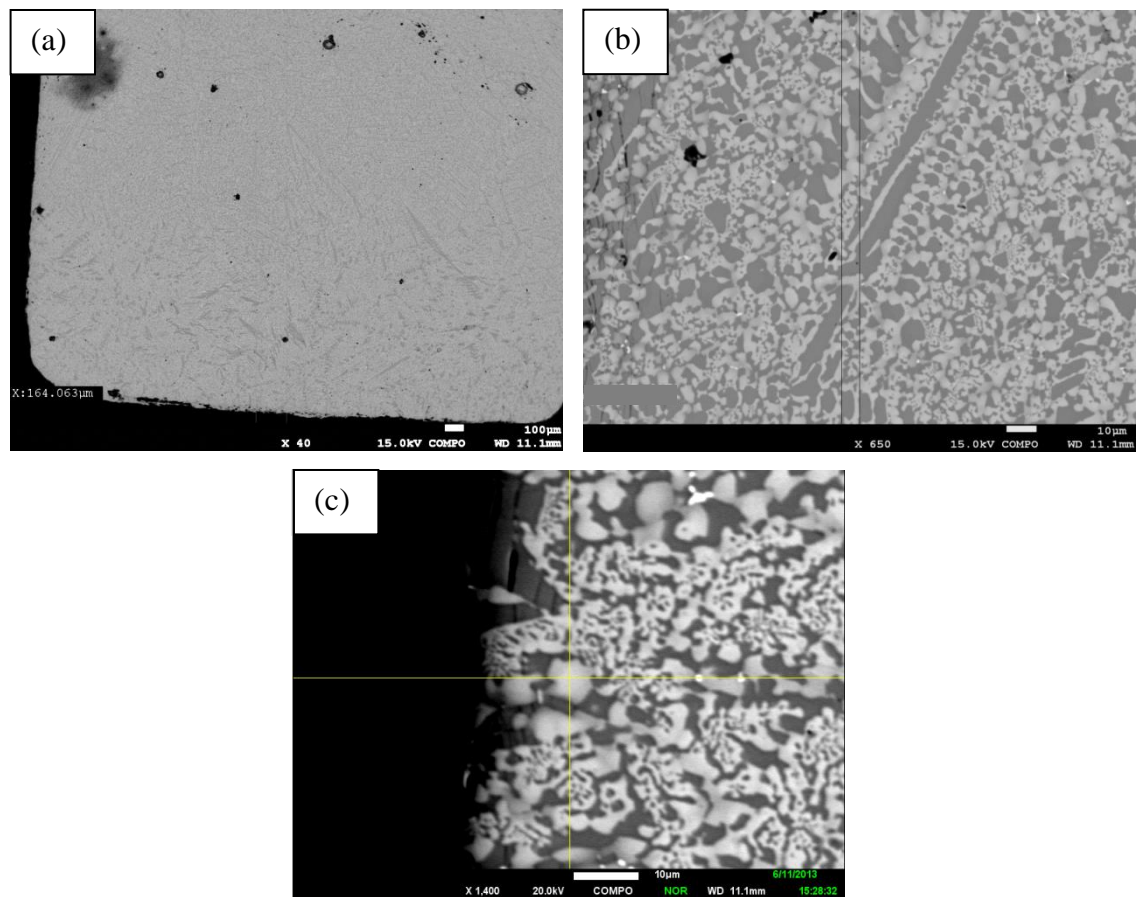
Figure 6.14 BSE cross sectional image of JN3 AC 800°C at (a)40X, (b) 450X and (c) 1400X magnification.

Figure 6.15 shows a BSE image at the surface of the oxidised specimen and the x-ray maps. It clearly shows the porosity and the cracks running parallel to the surface. The diffusion zone seems to extend at least 60 μm below the surface of the scale. The element maps show a very similar element distribution to that seen in the cast alloy. The oxygen map shows higher oxygen intensity at the edge of the sample than the bulk. In

these areas the Si, Cr, Hf, Mo and Sn maps show a decrease in concentration at the edge of the sample where the oxide scale has formed as they are in relatively low concentrations when compared to the un-oxidised bulk of the sample.
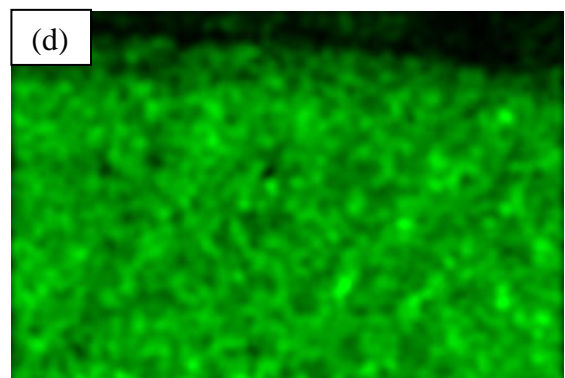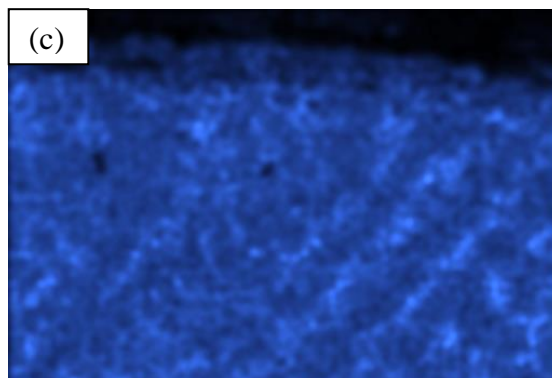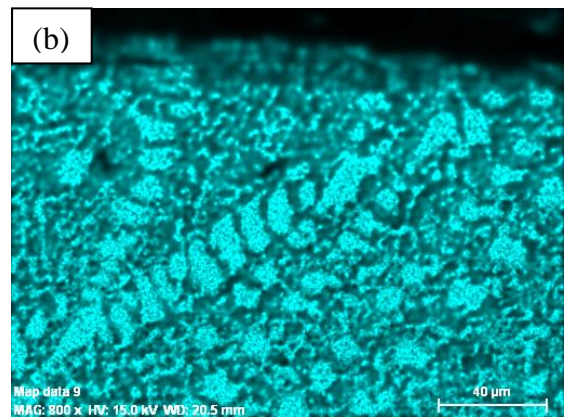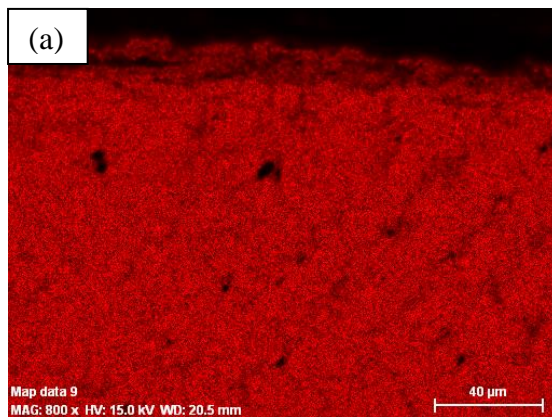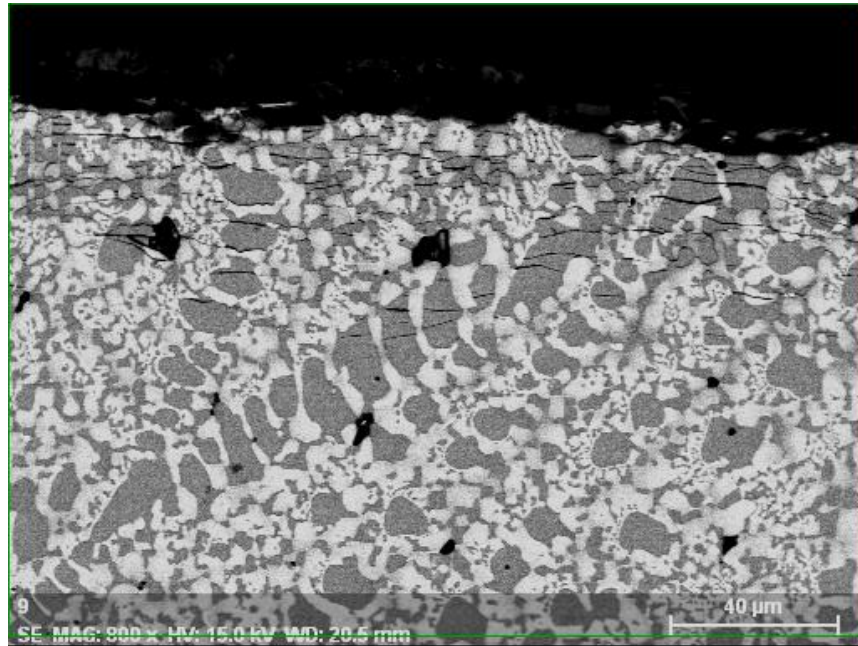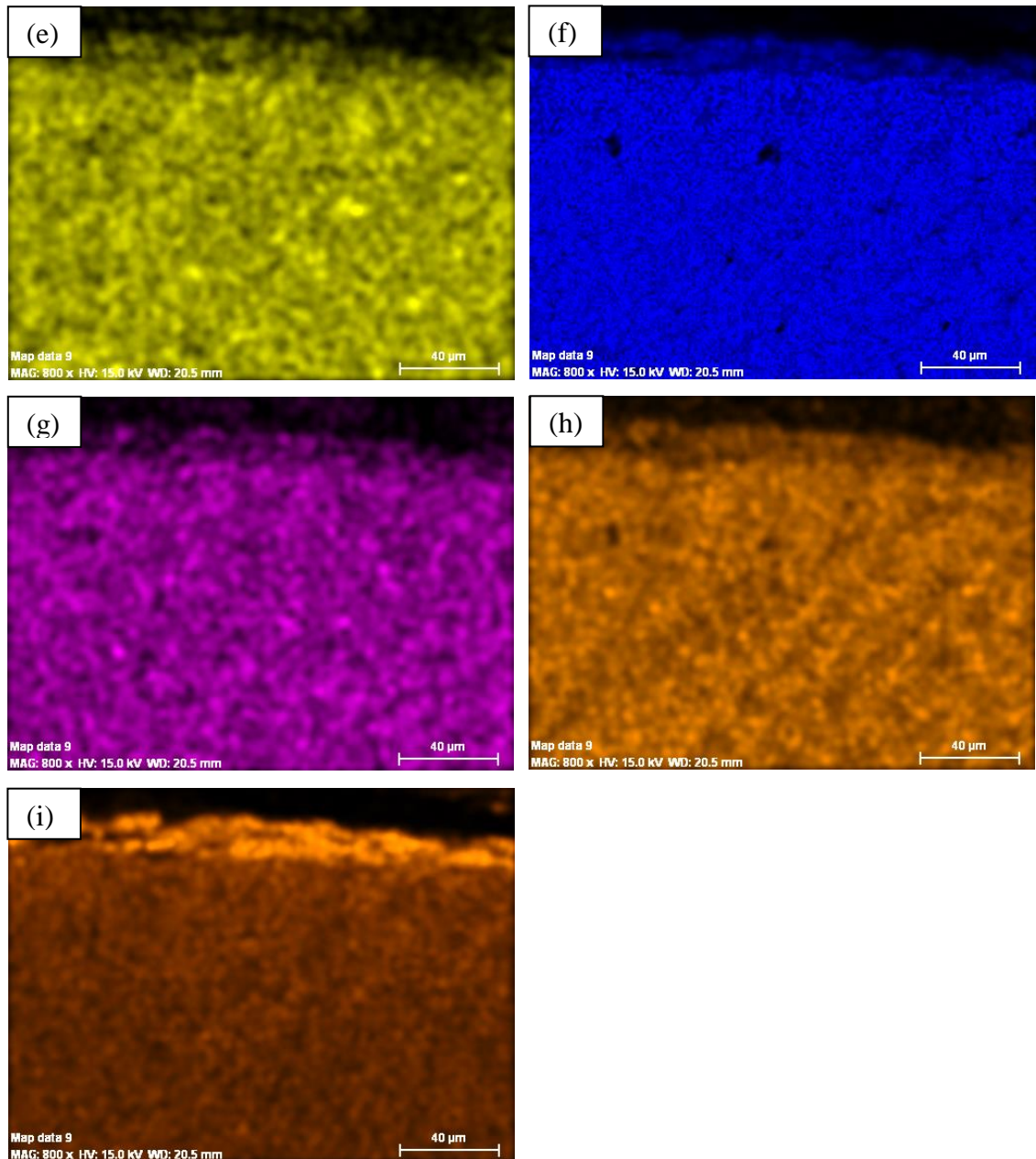
Figure 6.15 BSE image and X-ray maps of JN1 800 °C Nb (a), Si (b), Ti (c), Cr (d), Hf (e), Mo (f), W (g), Sn (h) and O (i).

Table 6.3 shows the EPMA data for JN3-AC after oxidation at 800 °C, data was taken from the edge, bulk and intermediate regions. At the top of the diffusion zone mixed oxide was formed, most likely Ti niobate. Further in the diffusion zone, the mixed oxide was no longer present and (50 μm below the diffusion zone) the Nb_{ss} had an oxygen concentration of 10.2 at% which is ~5 at% less than that observed in JN2. In the bulk the oxygen content of the Nb_{ss} dropped to 7 at%, the Nb_5Si_3 phase was not immune to contamination by oxygen like JN2. In the diffusion zone the oxygen level in Nb_5Si_3 is

15.8 at%, but this drops to 12.4 at% 50 μm below the diffusion zone. It is highly likely that the increased solubility of oxygen in Nb_5Si_3 was increased by its lower Ti and Cr content compared with JN2. The oxygen content in the silicide was reduced closer to the bulk but was still high compared with JN2 with exception of Nb and oxygen. The concentration of the other elements in the Nb_5Si_3 essentially did not change with depth below the scale which would suggest that the Nb in Nb_5Si_3 was consumed during oxidation.

When considering weight gain and oxidation rate constant the alloy JN3 exhibited marginally better and worse oxidation behaviour compared with alloys JN2 and JN1, respectively. Regarding alloy chemistry the alloy JN3 had the same alloying elements as JN2, but with lower Cr content. Direct comparison of JN3 and JN2 is thus reasonable.

The vol% of Nb_{ss} was higher in JN3 (51%) than in JN2 (40%), see Table 4.1, and there was no $NbCr_2$ Laves present in JN3. The former should be expected to have a negative contribution and the latter a positive one (owing to less damage (cracks) in the microstructure during oxidation, see previous section) on the oxidation of JN3.

In terms of phase chemistry, in the alloy JN3 the Nb_{ss} was richer in Ti and leaner in Cr and W with Mo+W ≈ 11 at% and 2 < Mo/W < 2.5 and below the diffusion zone the Ti/Cr ratio and Ti+Cr sum were about 7 and 18 at%, respectively, compared with the Nb_{ss} in JN2 where Mo+W ≈ 18 at% and 1 < Mo/W < 1.6, and Ti/Cr ≈ 2 and Ti+Cr ≈ 16 at%. If we were to assume, on the basis of the report of Taylor and Doyle for the effects of Mo and W on the solubility of oxygen in Nb (see previous section), that at the same concentration of Mo or W the former resulted in a lower oxygen content in the solid solution at 800 °C, then we would expect higher oxygen content in the Nb_{ss} in JN2 where the W concentration was higher (i.e., worst embrittlement of the Nb_{ss} in JN2 compared with JN3). The same would be the case regarding the effect of Ti, as the higher Ti content in the solid solution in JN3 would be expected to result to a lower oxygen concentration in the solid solution (see previous section). Furthermore, for the Cr content of the Nb_{ss} in JN3 ductile behaviour would require Ti/Nb > 0.2, which was indeed the case. It is thus suggested that the Nb_{ss} was more ductile and less embrittled in JN3 compared with JN2 and that these two factors contributed to having less cracking in the microstructure of JN3. On the other hand, the Nb_5Si_3 was leaner in Ti compared with JN2 and thus would be expected to be less tough.

In conclusion, the negative effects of pores, higher vol% of Nb_{ss} and Ti lean Nb_5Si_3 in JN3 were balanced by the more ductile and less embrittled Nb_{ss} in this alloy and this led to slightly less cracking in its microstructure and to a marginally better oxidation behaviour than the alloy JN2. However, pest oxidation could not be eliminated completely. The above argument regarding the roles of Ti and W in oxidation would point to the need to understand what the effects of increasing Ti content and avoiding W addition is on the oxidation of Nb silicide based alloys with addition of Sn.

Table 6.3 EPMA chemical analysis of JN3 800 °C (at%)

Phase and area in sample	Nb	Si	Ti	Cr	Hf	Mo	W	Sn	O
Mixed oxide	46.3±3.7	0.8±0.4	11.8±1.3	1.7±0.4	1.2±0.2	6.6±0.6	2.9±0.6	1.8±0.2	26.8±5.3
	40.0-48.9	0.6-1.4	11.0-14.0	1.4-2.2	1.1-1.6	6.5-7.2	2.2-3.5	1.7-2.2	21.6-35.7
Nb_5si_3 in crack zone	39.0±0.9	30.4±1.4	10.5±0.2	0.4±0	1.5±0	1.4±0.1	0.5±0	0.6±0	15.8±2.6
	38.2-39.9	28.9-31.8	10.3-10.6	0.4-0.4	1.4-1.5	1.3-1.4	0.5-0.6	0.6-0.6	13.2-18.3
Nb_{ss} 50 µm below diffusion zone	54.8±5.5	1.2±0.5	16.6±3.3	2.3±0.6	1.7±0.4	7.6±0.8	3.1±0.9	2.5±0.5	10.2±6.5
	54.2-62.0	0.7-1.9	12.1-20.3	1.5-3.2	1.2-2.2	6.6-8.7	2.1-4.7	1.8-3.0	0-18.4
Nb_5Si_3 50 µm below diffusion zone	41.3±0.5	30.8±0.3	11.0±0	0.4±0	1.5±0	1.4±0	0.6±0	0.6±0	12.4±0.8
	40.9-41.6	30.6-31.0	11.0-11.0	0.4-0.4	1.5-1.5	1.4-1.4	0.6-0.6	0.6-0.6	11.9-13.0
Nb_{ss} bulk analysis	59.0±4.4	0.7±0.2	15.5±1.6	2.4±0.9	1.6±0.2	7.8±0.8	3.7±0.5	2.3±0.2	7.0±3.0
	54.0-62.3	0.5-0.9	14.4-17.3	1.9-3.4	1.5-1.9	6.9-8.4	3.2-4.0	2.2-2.5	4.5-10.3

6.4   Alloy JN4 (Nb-20Si-20Ti-2Cr-2Hf- 6Mo-5Sn) after oxidation at 800 °C

Figure 6.16 shows the TGA data for JN4-AC, oxidised as 800 °C for 100 h. Unlike the other alloys discussed in this research, the alloy JN4 did not display a smooth TGA curve. The sudden weight change, especially after 60h were likely due to the release of stress in the form of small cracks leading to accelerated break away oxidation and an increase in mass measurements. This peak/trough formation through cracking and spallation has been reported by other work on alloys with similar Mo concentrations. It is assumed that any mass loss through Mo loss via MoO_3 evaporation was minimal if any at all (Chattopadhyay et al. 2008) (Geng, Tsakiropoulos & G. Shao 2007). The overall lower mass gain of 0.0014 g/cm^2 also resulted in higher sensitivity of the data to mass change as any small fluctuations in mass appear larger in relation to the overall curve. The data in Figure 6.16 corresponded to a parabolic oxidation rate constant of $2X10^{-11}$ g^2/cm^4s^{-1}, lower than that of the alloy JG4-AC and slightly higher than that of the alloy JG6-AC. It should be noted that the latter alloy had the same Sn content but higher and lower Hf and Mo contents respectively, compared to JN4.

Figure 6.17 shows a specimen of JN4-AC after isothermal oxidation at 800 °C for 100h, there were no surface cracks or signs of spallation of the scale.
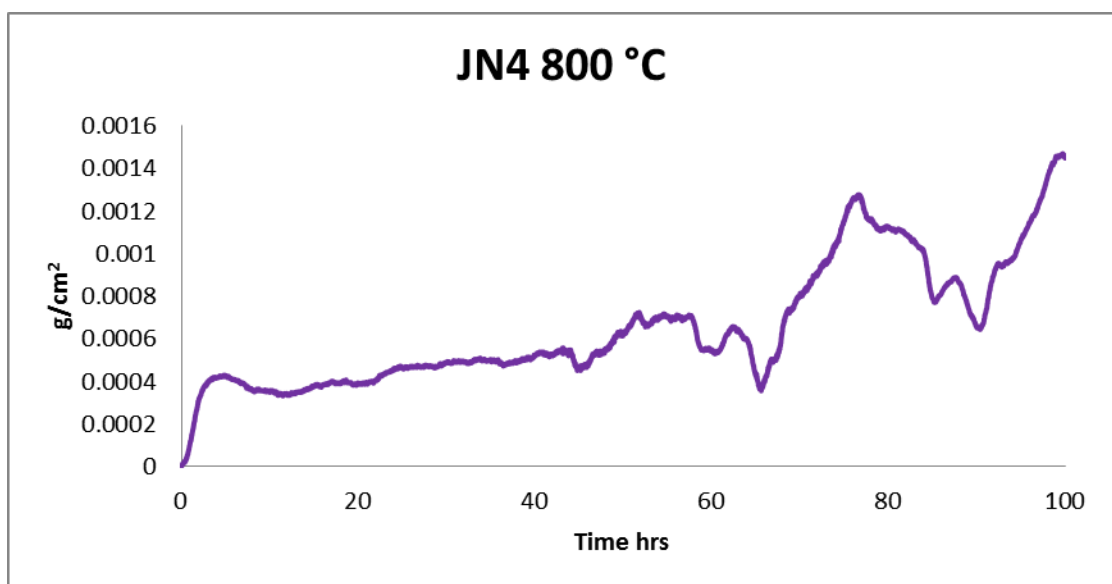
Figure 6.16 TGA data for JN3 AC after oxidation at 800 °C for 100h

Figure 6.17 image of JN3 after oxidation at 800 °C for 100 h

Figure 6.18 shows typical backscatter and secondary electron images of the surface of JN4-AC after oxidation at 800 °C. The scale surface seemed to be very similar to that of the alloys JN1 and JN3 in that the underlying Nb_5Si_3 phase was still visible and not yet covered by a thick oxide, the Nb_{ss} however showed the precipitation of oxides on the surface. Unlike the alloys JN1 and JN3 however, the alloy JN4 showed less cracking along the silicide boundaries. This this may be due to the oxides ability to grow into these cracks. As was the case in the alloy JN3, an oxide was visible at the surface of the Nb_5Si_3 grains.
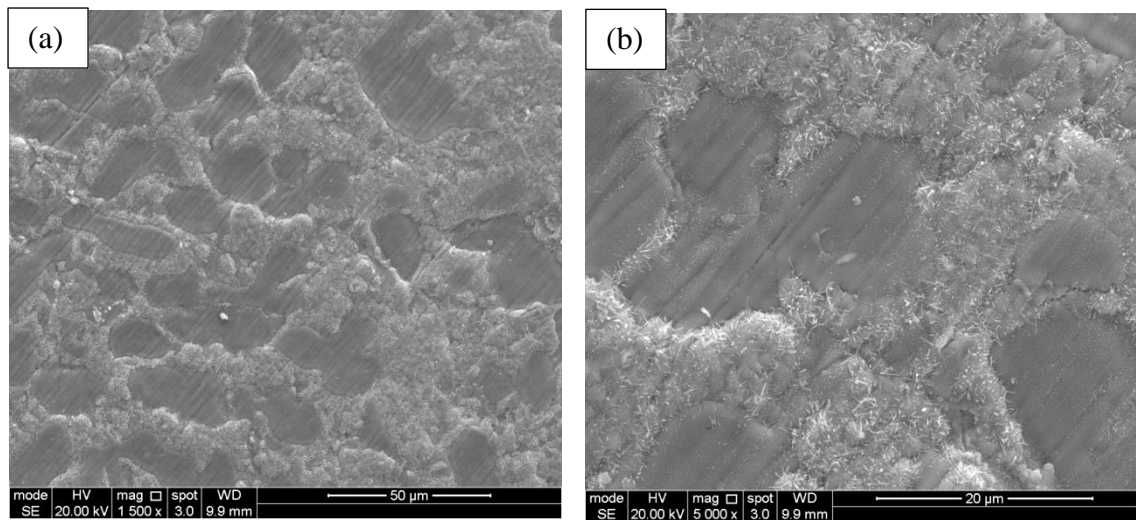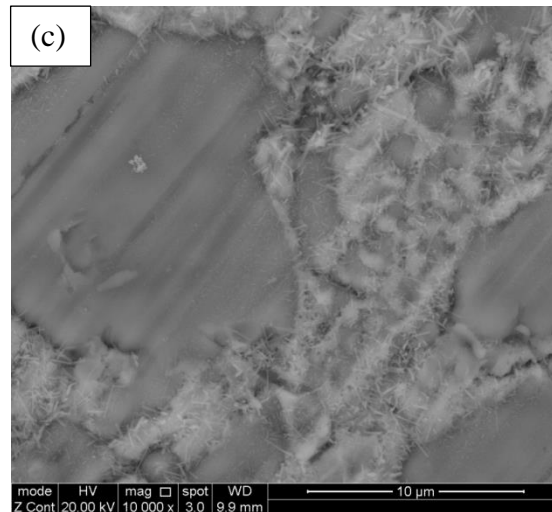
Figure 6.18 SE and BSE images of JN4 AC oxide surface at (a)1500, (b)5000 and (c)10,000 X magnification

Figure 6.19 shows typical images of cross sections of JN4-AC oxidised sample at 800 °C, in the images the surface of the sample is on the LHS. The low magnification image Figure 6.19 (a) shows the diffusion zone along the edge of the sample. Within this area there was significant cracking. The Figure 6.19 (b) shows few HfO_2 particles adjacent to Nb_5Si_3 grains. Figure 6.19 (a and b) shows that the thickness of the diffraction zone was much smaller in JN4 compared with the other alloys in this research. Figure 6.19 (c) clearly shows the cracks in Nb_5Si_3 running parallel to the oxide surface, as observed in the other alloys after oxidation at 800 °C.
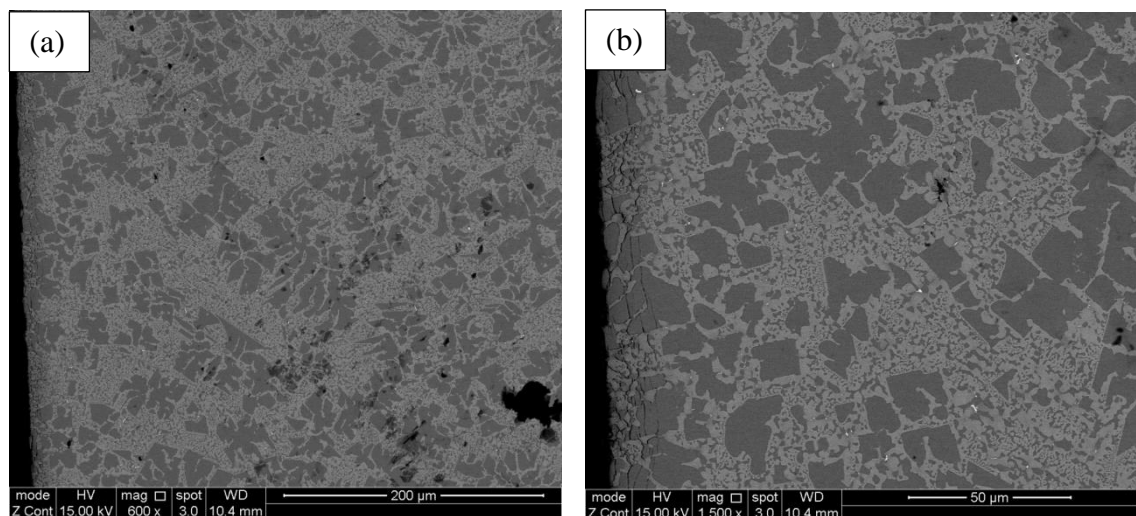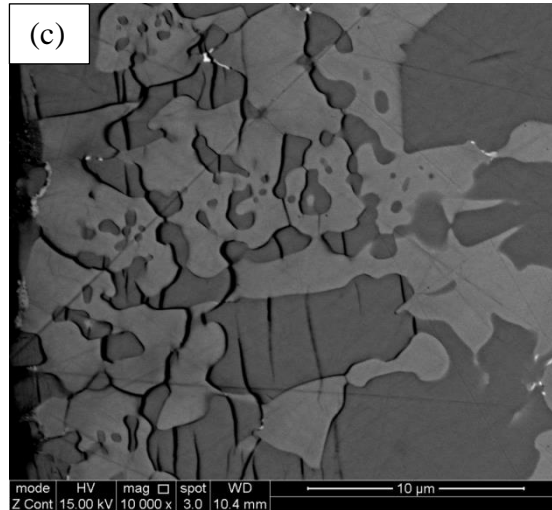
Figure 6.19 cross sectional image of JN4 AC 800 °C at (a) 600X, (b) 1500X and (c) 10,000X magnification

Figure 6.20 shows a BSE image of the cross section and the x-ray maps for JN4 after oxidation at 800 °C. All elements show a relatively unchanging concentration throughout the alloy, with the oxygen content being fairly constant. The Sn map shows no evidence of the formation of a Sn rich intermetallic like Nb_3Sn at the oxide/substrate interface. The edge of some of the maps show a decrease in element concentration, this is due to the specimen being mounted in resin and is therefore not a feature of oxidation.
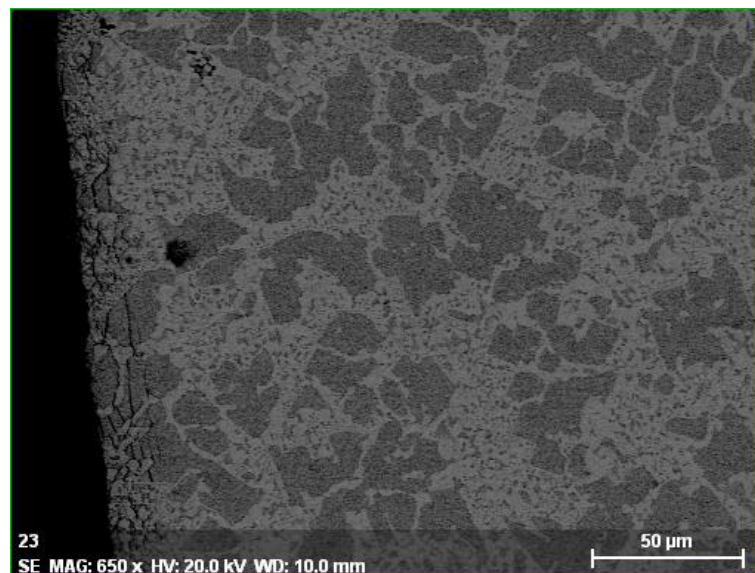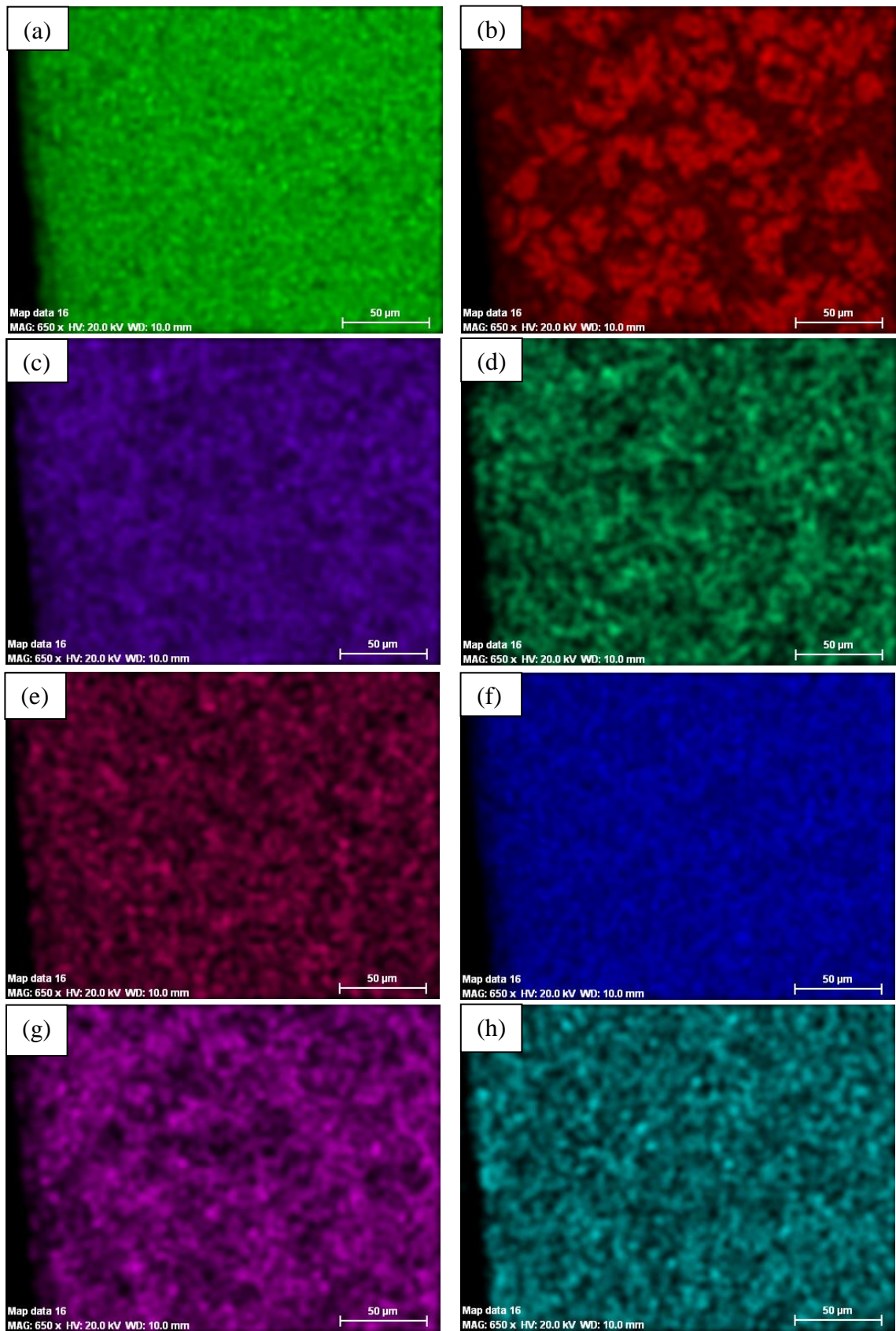
Figure 6.20 BSE image and X-ray maps of JN4 800 °C Nb (a), Si (b), Ti (c), Cr (d), Hf (e), Mo (f), Sn (g) and O (h).

Table 6.4 shows the EPMA data for the phases in JN4 after oxidation at 800 °C in the diffusion zone, bulk and 100 μm below the surface. The Nb_{ss} in the diffusion zone had an oxygen concentration of 1.4 at%, below the diffusion zone and in the bulk the oxygen content in the Nb_{ss} dropped to 0 at%. The Nb_{ss} in these areas had a slightly different composition but ultimately the data showed that the oxygen solubility in the Nb_{ss} has become negligible by a depth of 100 μm below the scale.

      Compared with the other Sn containing alloys, JN2 and JN3, the Nb_5Si_3 phase was still contaminated by oxygen, unlike the Sn free alloy JN1. In the diffusion zone the oxygen content in the Nb_5Si_3 was 1.2 at%, however 100 μm below the surface the oxygen concentration was 8.2 at%. This increase was similar to that seen in JN2 where a decrease in Ti, Hf and Sn had led to an increase in oxygen solubility in the silicide.

Table 6.4 EPMA data for phases in JN4 after oxidation at 800 °C (at%)

Area of interest	Nb	Si	Ti	Cr	Hf	Mo	Sn	O
Nb_{ss} diffusion zone	51.8±3.8 47.3-56.4	1.6±0.2 1.4-1.8	23.4±4.6 20.0-28.5	2.6±1.0 1.8-3.9	1.6±0.4 1.3-2.2	11.4±1.5 9.8-13.1	6.2±0.8 5.3-6.9	1.4±2.9 0.0-5.7
Nb_5Si_3 diffusion zone	42.9±3.6 38.8-45.4	31.6±1.6 30.6-33.5	17.7±0.6 17.3-18.3	0.5±0.0 0.5-0.6	1.8±0.1 1.6-1.9	2.4±0.2 2.2-2.5	2.0±2.0 1.8-2.1	1.2±2.0 0.0-3.5
Nb_{ss} 100 μm from sample edge	49.7±4.3 45.2-53.7	2.8±0.8 2.2-3.7	26.6±4.1 22.7-30.9	2.9±0.7 2.2-3.6	2.1±0.4 1.7-2.5	10.0±1.2 8.7-11.1	5.9±1.0 5.0-6.9	0±0.0 0.0-0.0
Nb_5Si_3 100 μm from sample edge	40.9±1.4 39.9-42.5	30.4±0.5 30.0-31.0	15.3±0.8 14.5-16.2	0.4±0.0 0.3-0.4	1.5±0.1 1.4-1.6	2.2±0.0 2.2-2.2	1.1±0.2 1.0-1.3	8.2±2.0 5.8-9.6
Nb_{ss} bulk	45.8±5.5 37.8-49.6	3.1±1.9 1.5-5.6	29.4±3.4 27.1-34.4	3.5±0.7 3.0-4.5	2.5±0.6 2.1-3.5	9.0±1.7 6.6-10.3	6.6±0.7 6.1-7.6	0.0±0.0 0.0-0.0

Considering weight gain and oxidation rate constant, the alloy JN4 was the best in terms of its oxidation at 800 °C compared with the other alloys of this research. Its oxidation behaviour at 800 °C was comparable with that of the alloy JG6-AC and better than the alloy JG4-AC (Geng, Tsakiropoulos & G. Shao 2007) and it showed no signs of pesting. Furthermore, the vol% of Nb_{ss} in JN4 was essentially the same as that in JN1 and JG4 (Geng, Tsakiropoulos, et al. 2006a), and higher than the vol% Nb_{ss} in JN2 and JG6 but lower than that in JN3. The better oxidation behaviour of JN4 cannot be attributed to its vol% of Nb_{ss}.

The microstructure of JN4-AC consisted only of the Nb_{ss} and Nb_5Si_3 phases, with no $NbCr_2$ Laves phase and Nb_3Sn being present. Considering that both the latter two phases were present in JG6-AC, it is unlikely that their absence in JN4 could have been responsible for its significantly improved oxidation behaviour. However, the absence of $NbCr_2$ in the microstructure of JN4 should have resulted in less damage (cracks) in the microstructure during oxidation (see previous section).   There is no data on the fracture toughness of unalloyed and alloyed Nb_3Sn. This intermetallic is however very brittle, like the Laves phase, and thus its absence in the microstructure would be expected to have also resulted to less damage during oxidation.

Compared with JG6-AC (Nb-24Ti-18Si-5Al-5Cr-5Hf-2Mo-5Sn) the alloy JN4 had no Al, lower Ti and Cr contents, the same Sn content and respectively higher and lower Mo and Hf concentrations. Compared with JG4-AC (Nb-24Ti-18Si-5Al-5Cr-5Hf-2Mo) the alloy JN4 had the addition of Sn, lower Ti and Cr contents, no Al, and respectively higher and lower Mo and Hf concentrations. Thus, the increase in the concentration of Sn in the alloy JN4 had a positive effect on its oxidation at 800 °C as did the addition of Sn in JG6 but in the case of JN4, this improvement cannot be linked with the formation of Nb_3Sn in the microstructure.

The chemistry of the Nb_{ss} in JN4-AC was given in Table 4.11. In the alloys JN4 and JG6, the Nb_{ss} had essentially the same Si+Sn content and the Ti/Nb ratios. The latter corresponded to ductile behaviour for the Nb_{ss} when considering its Cr content in JN4 and its Cr or Al+Cr contents in JG6.

Compared with the alloys JN2 and JN3 the oxygen content of the Nb_{ss} in the diffusion zone, 100 µm below the surface and in the bulk of JN4 was significantly lower. This can be attributed to the high Ti content of the Nb_{ss} in these areas and the

Ti/Nb ratio in the Nb_{ss} being in the range 0.45 to 0.64, which for the corresponding Cr concentrations (see Table 6.4) would suggest ductile behaviour of the Nb_{ss} and thus less cracking compared with the other alloys. The higher Mo concentration in the Nb_{ss} and the absence of W in JN4 compared with the alloys JN2 and JN3 should also have contributed to its lower contamination by oxygen (see above).

The Nb_5Si_3 was not immune to contamination by oxygen in the diffusion zone and below it in the oxidised JN4 at 800 °C, as was the case in JN2 and JN3 but compared with the latter two alloys the oxygen content of the Nb_5Si_3 was lower in JN4. The Ti content of Nb_5Si_3 was slightly higher in JN4-AC compared with JN2-AC and JN3-AC (both of which had lower Ti concentrations than JN4) but lower than in JG4-AC and JG6-AC (both of which had higher Ti concentrations than JN4). Thus, the toughness of Nb_5si_3 in JN4 should be expected to be slightly better than in JN2 and JN3 but inferior to that in JG4 and JG6. Furthermore, the Ti contents in the Nb_5Si_3 in the diffusion zone and below it in the oxidised JN4 at 800 °C must have also contributed to the lower oxygen contamination than in JN2 and JN3. Finally, the concentration of Sn in the Nb_5Si_3 in JN4 was the same as in JN2 and JN3 (which would suggest that the contamination by oxygen cannot be attributed solely to Sn) but the Mo concentration was slightly higher in JN4 and of course there was no W in solution.

In conclusion the effects of, (i) the chemistry of the Nb_{ss} (Si+Sn, Cr and Mo concentrations, Ti/Nb ratio and absence of W), (ii) the vol% of Nb_{ss}, the Ti and Mo contents (and absence of W) in the Nb_5Si_3, (iii) the absence of $NbCr_2$ Laves phase and Nb_3Sn in the microstructure and the anticipated ductile (and less embrittled) Nb_{ss} and slightly tougher Nb_5Si_3 in JN4 that led to; slightly less cracking in its microstructure, balanced out the negative effect of porosity, eliminated pest oxidation and resulted to essentially the same oxidation behaviour as the alloy JG6-AC at 800 °C. The fact that the improvement was achieved without Nb_3Sn forming in the microstructure (even though 5 at% Sn was added in JN4) would suggest that formation of the latter intermetallic might not be necessary for avoiding pest oxidation. If this conclusion were proved (by subsequent research) to be correct, it is an important discovery, as the Nb_3Sn has an adverse effect on alloy toughness.

Geng et al (Geng, Tsakiropoulos, et al. 2006a) reported what the Mo effect is on the oxidation of Nb-24Ti-18Si-5Cr-5Al based alloys and showed that oxidation was

improved significantly when the Mo concentration was reduced to 2 at%. Given the strong solid solution strengthening effect of Mo on Nb_{ss} and that twice as much Mo is required to get the same strengthening effect at high temperatures as W, the discovery in this research that oxidation similar to that of the alloy JG6-AC can be achieved with 6 at% Mo and with a significantly higher vol% Nb_{ss} compared with JG6-AC, is extremely important.

6.5   Conclusions

The isothermal oxidation of the alloys JN1, JN2, JN3 and JN4 at 800 °C in air was studied for 100 h using thermo-gravimetry, a summary of these results can be seen in Figure 6.21. The results presented in this chapter showed that the choice of alloying elements and their concentrations, and the types and compositions of phases present in the cast microstructure had strong influence on the oxidation behaviour of the studied alloys. The alloys JN1, JN2 and suffered from pest oxidation and exhibited linear oxidation kinetics. The alloy JN3 showed slight signs of pesting and displayed mixed oxidation kinetics, JN4 did not pest and followed parabolic oxidation kinetics.

All three alloys exhibited the typical damage observed in many Nb silicide based alloys, which consists of an area below the scale/substrate interface where the substrate is cracked, with the cracks running parallel to the interface and through the Nb_5Si_3 grains. In all alloys there was a diffusion zone formed below the scale/substrate interface. The chemical compositions of the phases in the oxide scale (when possible), in the diffusion zone, below it and in the bulk were analysed. It was found that depending on alloy, the Nb_{ss} and Nb_5Si_3 were contaminated by oxygen and the severity of this effect varied between alloys.

The Nb_{ss} was not contaminated by oxygen below the diffusion zone in JN4, and in the bulk in JN1 and JN4. The Nb_5Si_3 was not contaminated by oxygen below the diffusion zone in JN1, and in the bulk in JN1 and JN4. The oxidation behaviour of the alloys has been discussed by considering the "ductile" and brittle behaviour of Nb_{ss} and the toughness of Nb_5Si_3 using data from the literature linking these behaviours with specific alloying additions in Nb_{ss} (Cr or Al+Cr) and Nb_5Si_3 (Ti) and the effects of Mo and W on oxygen content of the Nb_{ss}.
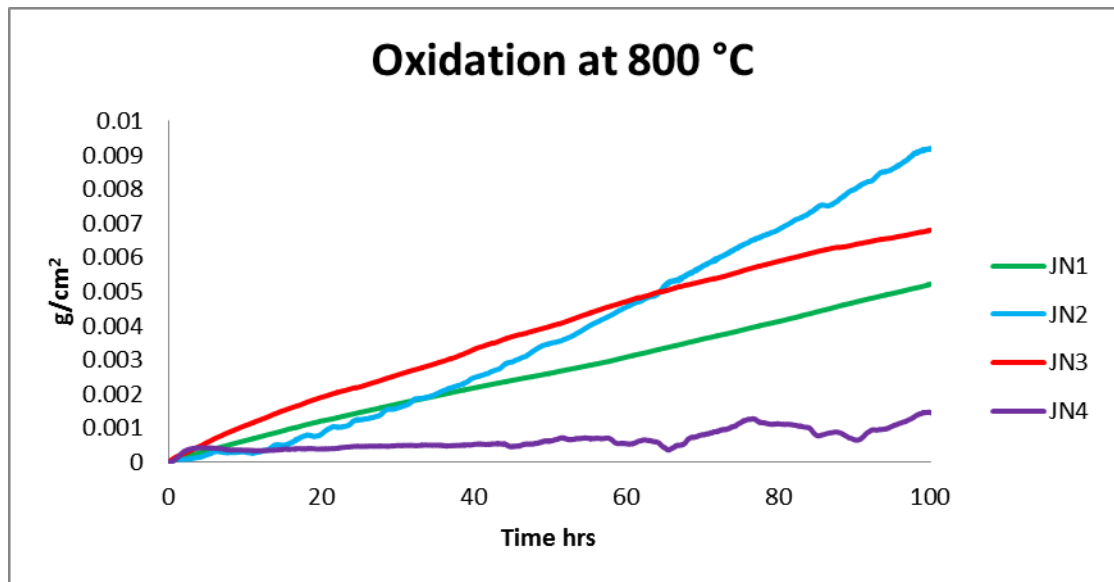
Figure 6.21 Summary of oxidation at 800 °C for JN1, 2, 3 and 4.

Oxidation at 1200 °C: Results and Discussion

This chapter studies the oxidation of the alloys of this research at 1200 °C. The isothermal oxidation experiments were done as described in section 3.9. The temperature was chosen to allow comparison of the present alloys with those studied within the research group and other research groups. Another reason for choosing this temperature is because an oxidation goal for polycrystalline Nb silicide based alloys is to "match" the oxidation of single crystal Ni superalloys at the same temperature (even though the latter are not used at 1200 °C), with the reference alloy being the CMSX4. Leaving aside whether such a comparison is reasonable, the oxidation of CMSX4 at 1200 °C is parabolic with rate constant equal to 4×10^{-12} $g^2 cm^{-4} s^{-1}$ and weight gain of 0.002 g/cm^2 after 50 h at 1200 °C. As we shall see in this chapter, none of the alloys studied matched the oxidation of CMSX4.

7.1   Alloy JN1 (Nb-18Si-24Ti-5Cr-5Al-5Hf) after oxidation at 1200 °C

Figure 7.1 shows the mass gain of JN1 AC after 100h at 1200 °C in air. The total mass gain was 0.05 g/cm^2. The curve itself is smooth, with no drastic weight gains or losses; this indicates a stable oxide growth with no sudden spallation of material or breakaway oxidation during testing. Compared with the "similar" alloys KZ5 HT and JG4 AC which had mass gains of 0.085 and 0.12 g/cm^2 respectively, the alloy JN1 performed much better at 1200 °C. This indicated a beneficial effect on high temperature oxidation from the addition of Hf to the alloy (KZ5 vs JN1 and the detrimental effect of low Mo additions) on high temperature oxidation (JG4 vs JN1).

Figure 7.2 shows a specimen after 100 h oxidation at 1200 °C; it can be clearly seen that the oxide scale readily spalled off. The pattern of cracking indicates that the scale formed near the edge of the specimen. Some parts of the oxide remained attached, particularly near the edge of the specimen.
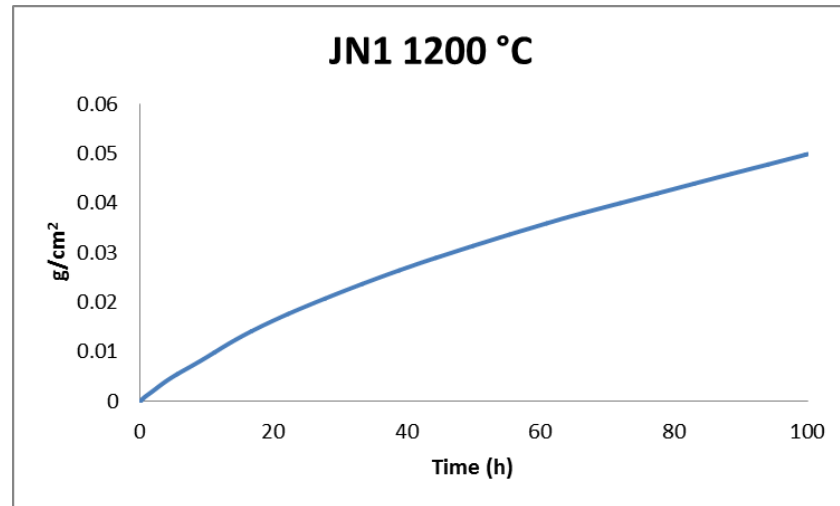
Figure 7.1 TGA data for JN1 after oxidation at 1200 °C for 100 h in air

Figure 7.2 A specimen of JN1 after oxidation at 1200 °C for 100h

Table 7.1 shows the oxidation rate constant for JN1 and includes data for JG4 at 1200 °C. The alloy JG4 had a linear oxidation rate constant, which changed half way through the 100 h test. The alloy JG4 showed a steadily increasing mass gain with little sign of tapering off. The alloy JN1 showed parabolic weight gain over the majority of the experiment, with two different oxidation rates, the weight gain is linear in the first 14h. Compared with the alloy JG6-AC, which exhibited parabolic oxidation only for the first 9h at 1200 °C ($K_p = 1.4 \times 10^{-9}$ $g^2 cm^{-4} s^{-1}$) the oxidation behaviour of JN1 was better. The same was the case when compared with the oxidation of JG6-HT at 1200 °C.

Table 7.1 Oxidation rate constants for JN1 and JG4 at 1200 °C.

Alloy	K_p ($g^2 cm^{-4} s^{-1}$)	K_L ($gcm^{-2} s^{-1}$)
JN1 AC	7×10^{-9} (14-50 h) 7×10^{-9} (50-100 h)	2×10^{-7} (0-14 h)
JG4 AC	-	4.4×10^{-7} (0-56 h) 2.4×10^{-7} (56-100 h)

Figure 7.3 shows images of the surface of the oxide scale formed on JN1 at low and high magnifications. Under low magnification, Figure 7.3 (a and b) unlike JN1 oxidised at 800 °C, the Nb_5Si_3 grains could no longer be clearly distinguished and appeared to have some porosity and cracks and it seemed to consist of the same oxide. High magnification images exhibited globular morphology Figure 7.3 (c and d), the scale consisted of Ti and Cr Niobates and Nb_2O_5, see Figure 7.6.
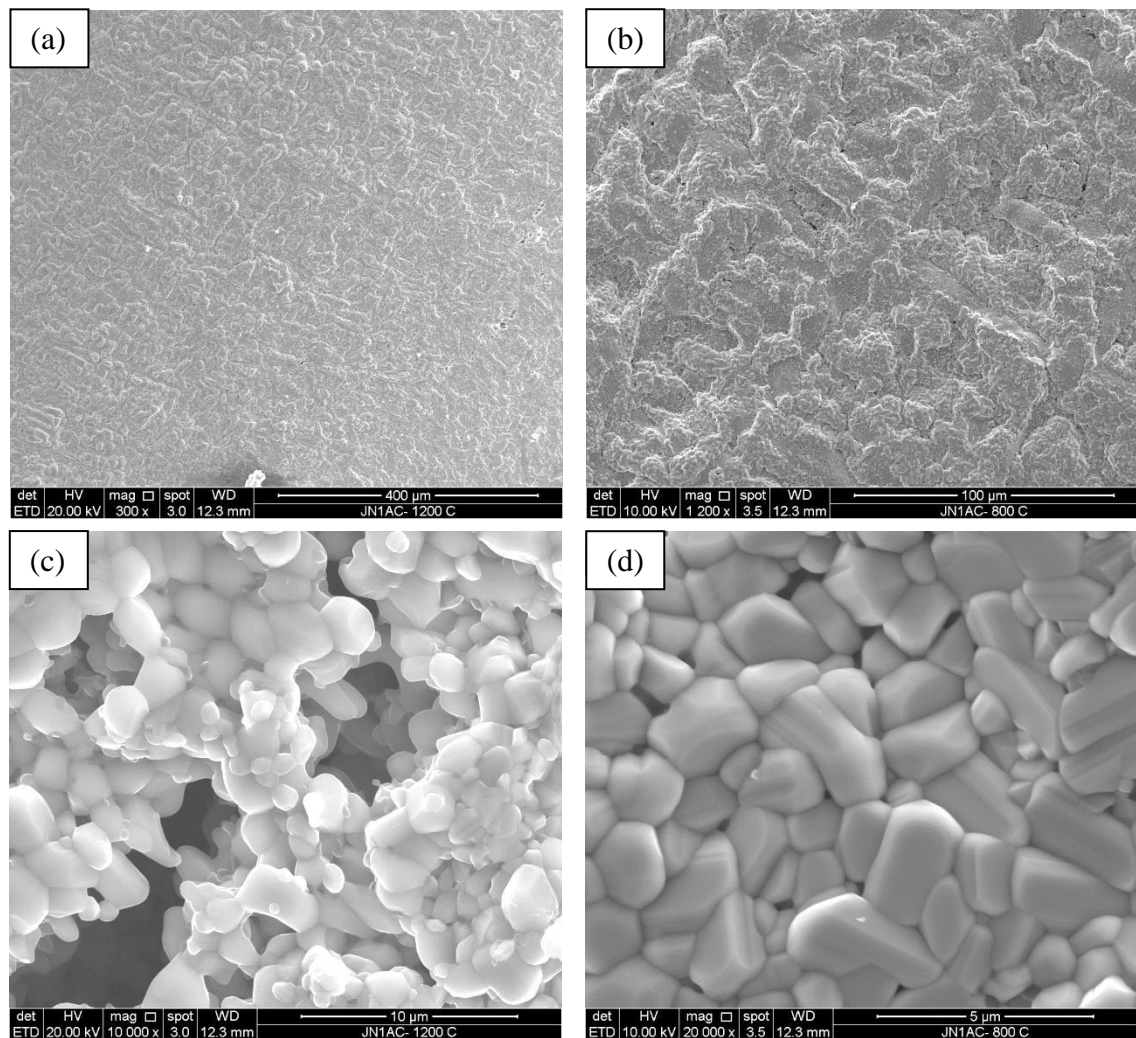
Figure 7.3 SEI images of JN1-AC oxide surface after 100h at 1200 °C (a) 300, (b) 1200, (c) 10,000 and (d) 20,000 X magnification

Figure 7.4 shows typical images of cross sections of JN1-AC after oxidation at 1200 °C, showing the depth of the diffusion zone (~ 600 μm, Figure 7.4 a), different phases in the diffusion zone (Figure 7.4 b and c) and details of the diffusion zone/oxide layer interface (Figure 7.4 d). The diffusion zone extended ~600 μm below the surface of the alloy and consisted of three distinct regions. Closest to the oxide layer was region A

which was up to ~100 μm deep, this was a dense region of oxides/nitrides and silicide grains. Next was region B which was ~100-350 μm deep and contained Nb_{ss}, Nb_5Si_3, TiO/TiN (black phase) and HfO_2 (white phase), and finally region C was ~250-800 μm deep and consisted of Nb_{ss}, Nb_5Si_3 and HfO_2. The phases in region A could not be accurately analysed using WDS, though similarities in contrast would suggest that it comprised of TiO/TiN and HfO_2. There are several regions of different contrast which are likely to be the formation of a third oxide but as previously mentioned it was not possible to analyse these phases to confirm this. Due to the low Nb concentrations in the TiO/TiN and the HfO_2, it is likely that an Nb-based oxide formed in this region. This is supported by the XRD that showed that the oxide comprised of Nb_2O_5 and $TiNb_2O_7$, amongst other oxides, see Figure 7.6.
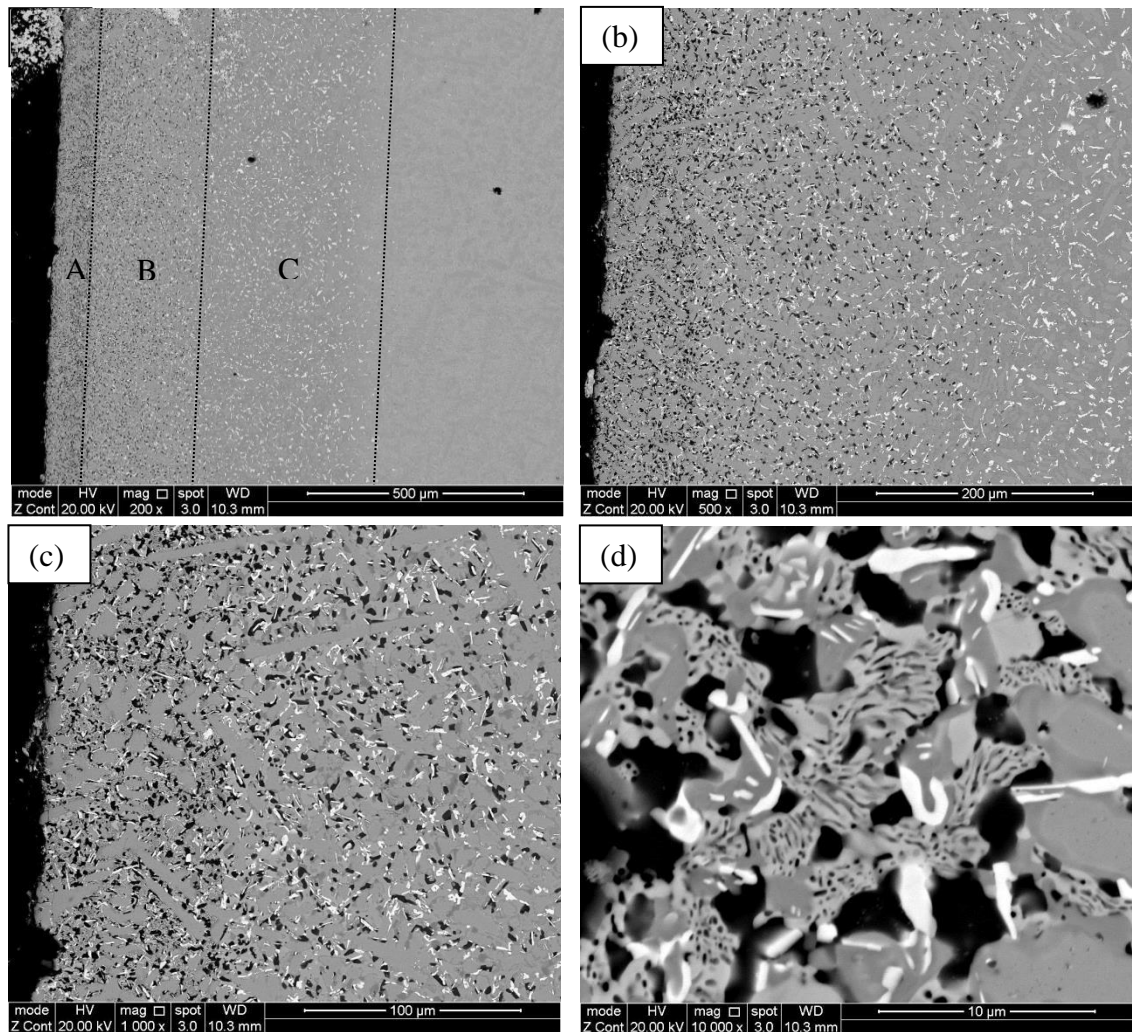
Figure 7.4 BSE images of cross section of JN1-AC oxidised at 1200 °C at (a) 200, (b) 500, (c) 100 and (d) 10,000 X magnification

Figure 7.5 shows X-ray maps taken at the edge of the oxidised JN1 specimen. The Si map shows the significant "damage" of the Nb_5Si_3 grains closer to the surface where significant vol% of HfO_2 is also formed, as confirmed by the O_2 and Hf maps. The Hf map clearly correlates with the very bright oxides that are predominantly adjacent to the silicide grains. The black contrast areas that are visible in the BSE image are predominantly comprised of Ti and are either Ti oxides or nitrides. The Cr maps show discrete Cr rich regions which are dispersed evenly in the interdendritic regions between the silicide grains. The Al and Nb maps show these elements to be in the same areas that appear to be adjacent to the silicide grains within the lamellar regions.
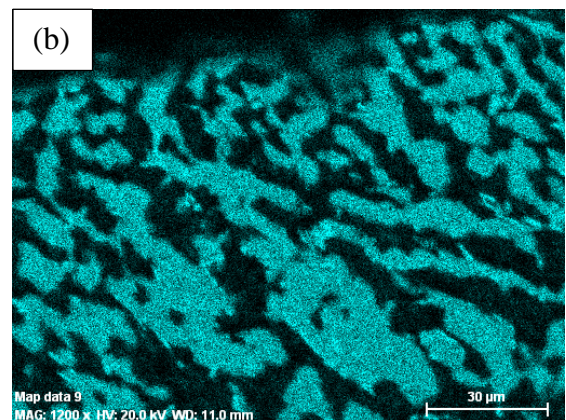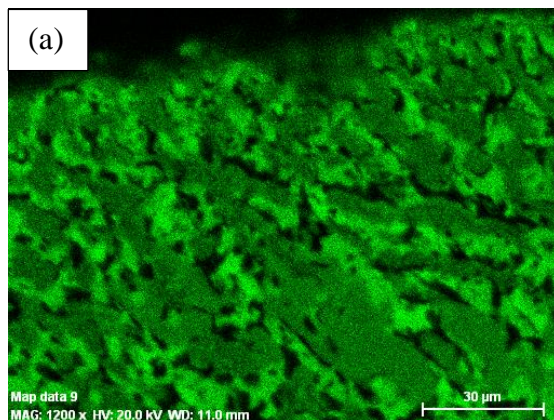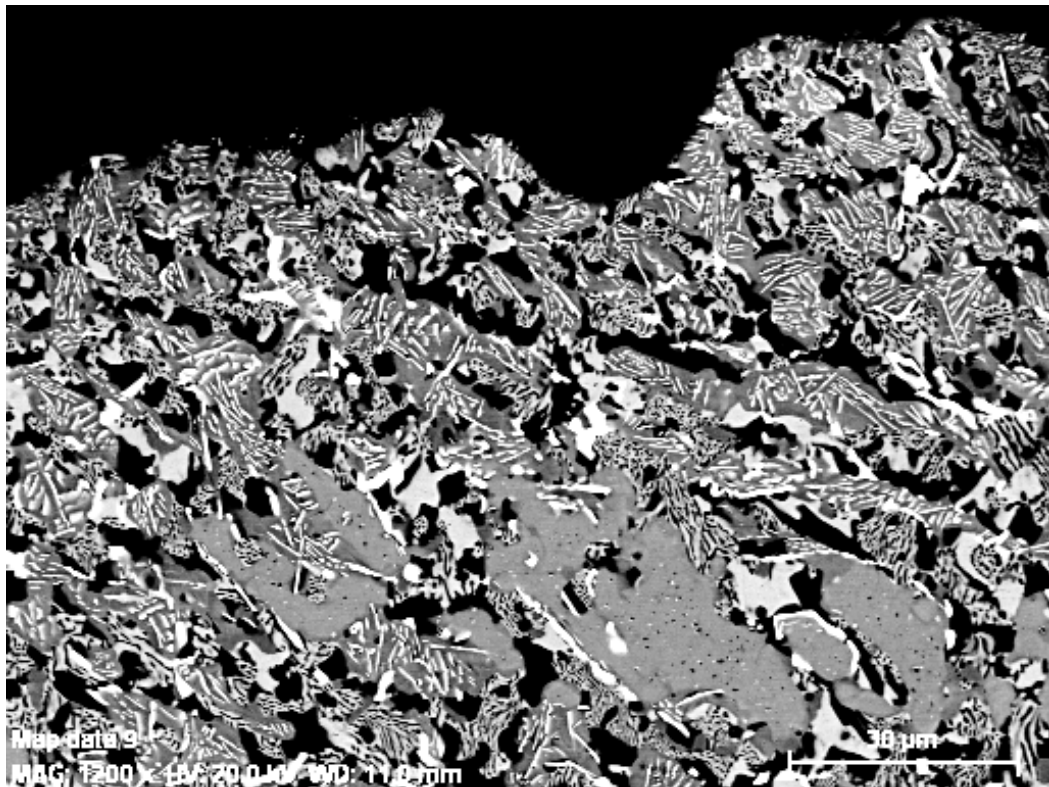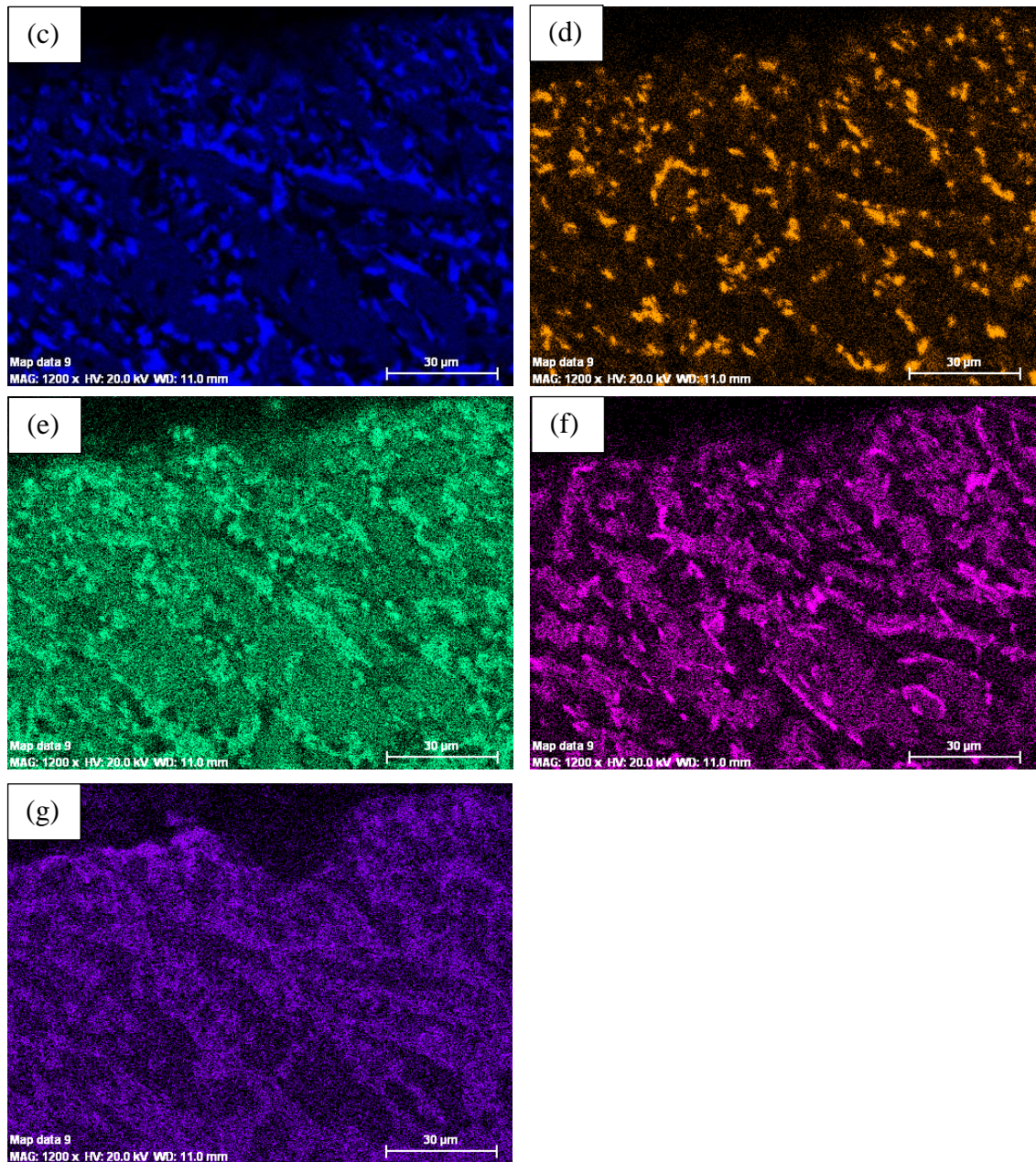
Figure 7.5 X-ray maps for JN1 1200 C Nb (a), Si (b), Ti (c), Cr (d), Al (e), Hf (f) and O (g)

Figure 7.6 shows the XRD pattern for the oxide of JN1 AC 1200 °C, the characteristic peaks suggest the presence of 4 different oxides, Nb_2O_5, HfO_2 $TiNb_2O_7$ and $TiNbCrO_6$.
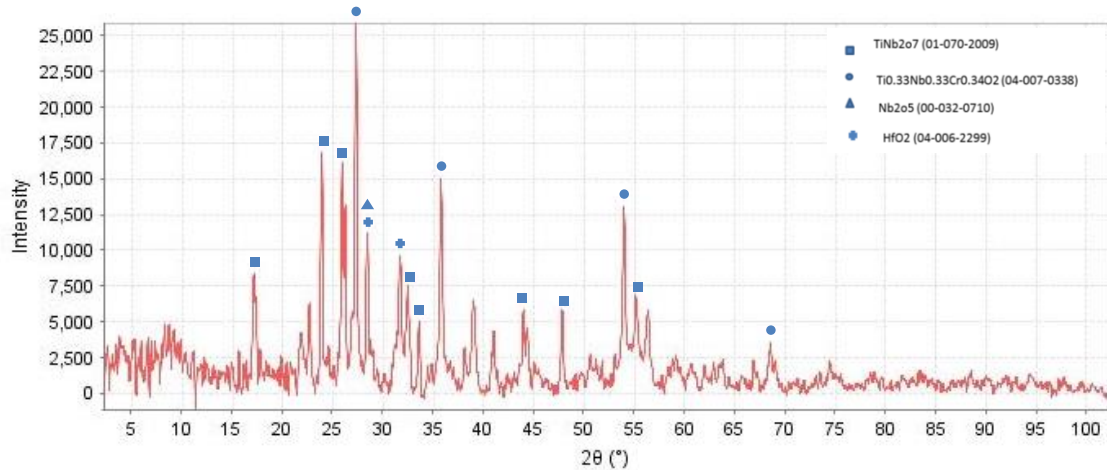
Figure 7.6 Transmission XRD diffractogram of powdered oxide formed on JN1 AC after oxidation at 1200 °C.

Table 7.2 shows the chemical compositions of the phases in the bulk and the diffusion layer as analysed using WDS. Unfortunately the oxide scale was not analysed as it had spalled off. The small oxide particles that are visible in the BSE images were too small to be analysed using point analysis. The composition of the silicide was similar to that seen in the as-cast and heat treated alloy. Both the normal and Hf rich Nb_5Si_3 showed little affinity for oxygen with a maximum solubility of 0.7 at%. The Nb_{ss} close to the surface was contaminated by oxygen and in the diffusion zone the oxygen content was 3.3 at%. In the bulk of the sample the Nb_{ss} was free of oxygen suggesting that the oxide formation at the surface and the scavenging of oxygen by Hf were enough to stop the oxygen ingress to the centre of the sample within the confines of the oxidation experiment. The bright and black regions were large enough to be analysed using point analysis; the bright areas were HfO_2 with a composition close to the stoichiometric ratio. The black precipitates were TiN or TiO, according to previous work it is most likely that they were TiN (Geng, Tsakiropoulos & G. Shao 2007; Grammenos & Tsakiropoulos 2010a).

Table 7.2 EPMA data for JN1 after oxidation at 1200 °C for 100h

Phase	Nb	Si	Ti	Cr	Al	Hf	O
Nb$_5$Si$_3$ DZ	40.3±0.9 38.5-41.8	32.1±1.9 29.5-34.2	18.6±0.9 17.8-19.8	0.7±0.3 0.3-1.2	3.1±0.3 2.4-3.5	4.5±0.1 4.3-4.7	0.7±1.1 0.0-2.2
Hf rich Nb$_5$Si$_3$ DZ	25.2±2.4 22.2-28.2	29.3±2.6 25.7-32.8	27.8±1.4 26.2-29.4	2.0±0.8 0.9-2.9	3.7±0.4 3.2-4.2	11.9±1.1 10.5-13.5	0.1±0.3 0.0-0.6
Nb$_{ss}$ DZ	45.3±0.7 44.7-46.1	0.3±0.0 0.3-0.3	32.6±0.5 32.1-33.1	10.5±0.2 10.3-10.8	7.7±0.1 7.5-7.7	0.2±0.0 0.2-0.3	3.3±1.5 1.8-4.9
HfO$_2$	0.7±1.2 0.1-2.7	0.0±0.0 0.0-0.0	1.3±0.9 0.5-2.7	0.3±0.2 0.2-0.6	0.0±0.0 0.0-0.0	37.7±1.0 36.0-38.5	60.0±1.9 56.7-61.3
TiO/TiN*	3.9±2.8 1.9-5.9	0.0±0.0 0.0-0.0	47.7±1.5 46.6-48.8	0.2±0.2 0.1-0.3	0.3±0.2 0.2-0.4	0.1±0.0 0.1-0.1	47.8±4.3 44.7-50.8
Nb$_{ss}$ bulk	52.2±0.1 52.1-52.3	0.3±0.0 0.3-0.3	29.5±0.1 29.5-29.4	9.2±0.0 9.2-9.3	6.9±0.1 6.8-6.9	1.9±0.0 1.9-1.9	0.0±0.0 0.0-0.0
*the atomic numbers of O and N, this could be either phase							

7.2   Alloy JN2 (Nb-18Si-15Ti-10Cr-2Hf-5Mo-5W-2Sn) after oxidation at 1200 °C

Figure 7.7 shows the mass gain for JN2-AC oxidised at 1200 °C. Unfortunately, due to equipment error the experiment was stopped after ~ 60 h. The overall mass gain of this alloy after 60 h was 0.076 g/cm^2; compared with 0.035 g/cm^2 for JN1 over the 60h period and the mass gain of JG6-AC after 60 h oxidation at 1200 °C was 0.061 g/cm^2. Thus the increase in Cr concentration to compensate for the decrease in the Ti, Hf and Sn content and the removal of Al, was not sufficient. To improve oxidation, even though the NbCr$_2$ Laves phase, which is reported as being beneficial to the oxidation resistance of these alloys (Chan 2004; Bewlay et al. 2003), was not present in the starting microstructure. The oxidation rate constant of JN2 was linear with a value of 4×10^{-7} gcm^{-2}s^{-1} between 0-17h, slightly worse than the rate constant of JG6-AC (K$_l$ =

3.1×10^{-7} gcm^{-2}s^{-1}) but better than the rate constant of JG6-HT ($K_l = 5.1 \times 10^{-7}$ gcm^{-2}s^{-1}). From 17-60h the oxidation rate was 3×10^{-8} g^{2}cm^{-4}s^{-2}. The TGA curve was smooth, indicating no abrupt change in weight gain.

Figure 7.8 shows a specimen of the alloy JN2 after oxidation at 1200 °C. The image shows pieces of the spalled off scale from the sides of the specimens and evidence that some of the scale adhered on the substrate in the centre. The spalled off pieces had raised edges which would indicate that a thicker oxide formed at the edge of the sample. The outer oxide layer had a similar colour of that formed on JN1-AC, suggesting that the scale may be comprised of similar oxides. The substrate had a much darker colour.
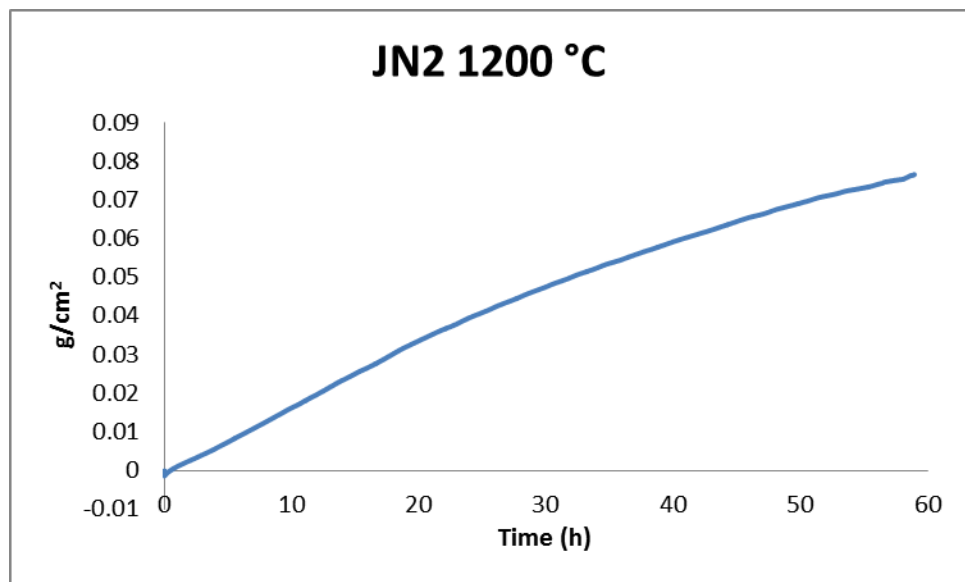
Figure 7.7 TGA data of JN2 after oxidation at 1200 °C in air
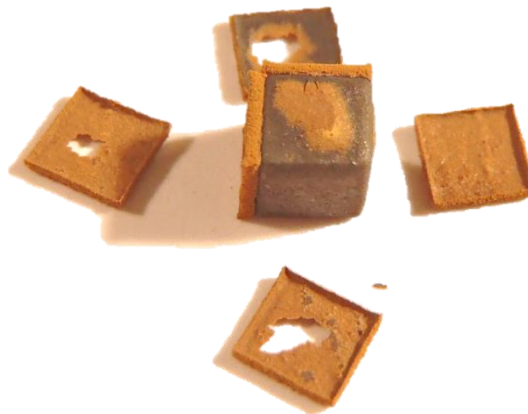
Figure 7.8 A specimen of JN2 after oxidation at 1200 °C

Figure 7.9 shows images of the oxide scale formed on JN2-AC at 1200 °C. The main feature to note is the visibility of the silicide grain positions (Figure 7.9 a) and the very thin oxide formed on them. The areas around the silicide grains are more heavily oxidised (Figure 7.9 a) and in some there is severe cracking (Figure 7.9 a and b), whilst the silicides themselves seem unaffected. The probable cause of this is the embrittlement of the underlying Nb_{ss} owing to its high oxygen content, causing it to crack rather than the Nb_5Si_3 due to the stresses imposed by the volume of the oxides. The high magnification images (Figure 7.9 b and c) show needle like oxide particles and smaller blocky oxides. These oxide morphologies were not seen on JN1-AC, after oxidation at 1200 °C. According to the transmission XRD data these oxides were Ti and Cr niobates, see Figure 7.12. There were other peaks that may be attributed to other oxides though no peaks could be matched.
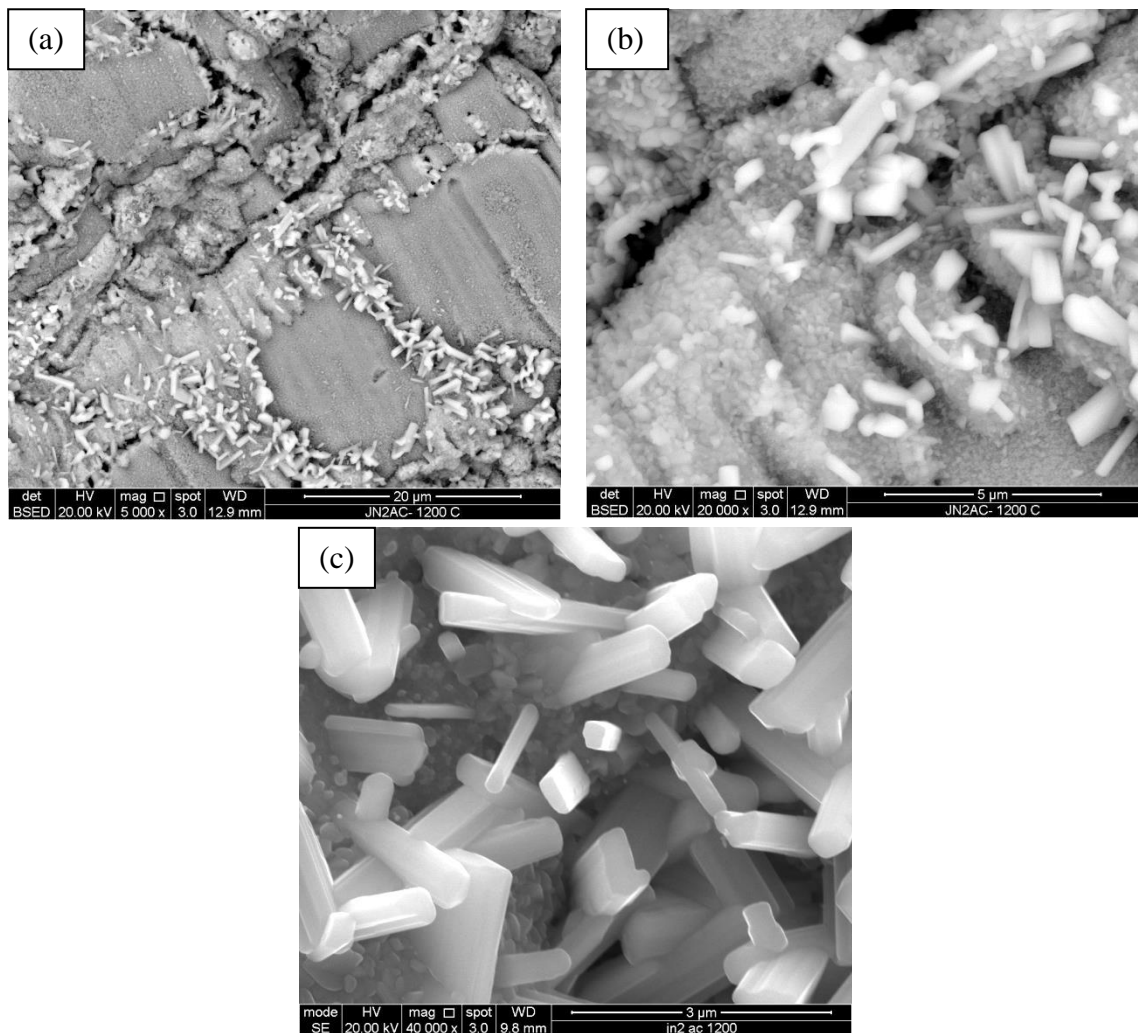
Figure 7.9 SEI and BSE images of oxide surface formed on JN2 at (a) 5000, (b) 20,000 and (c) 40,000 X magnification.

Figure 7.10 shows BSE images of the cross section of the JN2 sample oxidised at 1200 °C. The low magnification image seen in Figure 7.10 (a) shows that, unlike JN1, there was no distinct diffusion zone within the alloy. Figure 7.10 (b and c) show that the substrate that is adjacent to remnants of the oxide layer shows no oxide precipitation except for small HfO_2 grains. However there is a variance in contrasts at high magnification (Figure 7.10 c) at the edge of the sample which indicates the possibility of other phases forming, these particles were too small to analyse by WDS. Figure 7.10 (d) shows a high magnification image of the scale that was still attached to the substrate. It comprises of a mix of different phases including HfO_2 particles, small dark precipitates and silicide grains. This lack of a distinct diffusion zone in the substrate indicates the preferred formation of oxides at the edge of the substrate, i.e. the formation of a thick oxide scale incorporating the diffusion zone. This continuous oxide formation was responsible for the higher mass gain of JN2 compared with JN1.
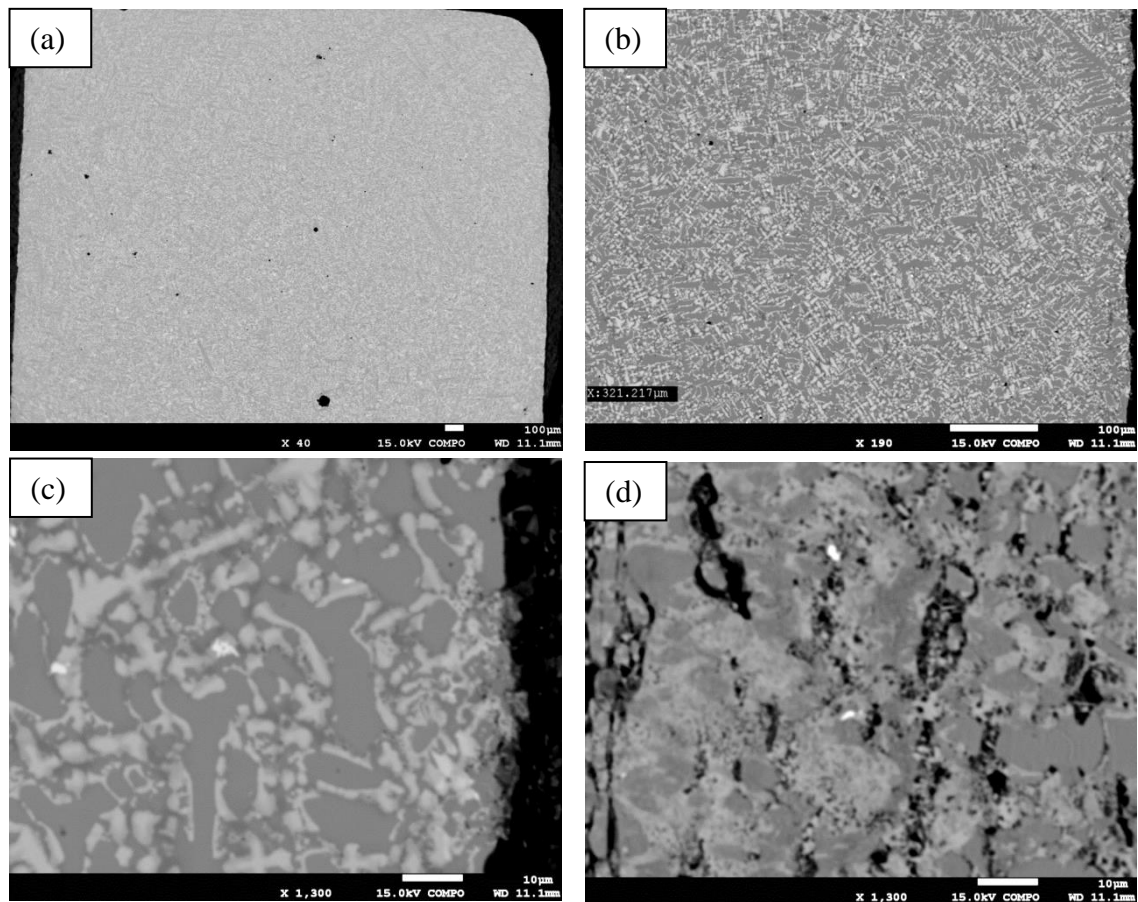
Figure 7.10 BSE images of the oxide cross section of JN2 after oxidation at 1200 °C at (a)40, (b)190, (c)1300 and (d)1300 X

Figure 7.11 shows the BSE image for JN2 after oxidation at 1200 °C and the X-ray maps for Nb, Si, Ti, Cr, Hf, Mo, Sn and O. The BSE image shows a distinct decrease in brightness between the oxide (top of sample) and the substrate. As in Figure 7.10 (d), small precipitates can be seen in the BSE image of the oxide scale. The Nb, Si, Ti, Cr and Mo maps show a distinct reduction in concentration between the substrate and the oxide. The Sn map shows an increase along the substrate edge, indicating a Sn rich region is very thin along the diffusion zone/scale boundary. The Sn-rich layer does not show continuity across the oxide/substrate interface and is interrupted by the presence of silicide grains. The concentration of Sn outside of this Sn-rich region appears low in both the substrate and the oxide layer. The O_2 map shows a high intensity in the scale, it does not however extend beyond the Sn-rich region, suggesting a protective effect of the Sn segregation.
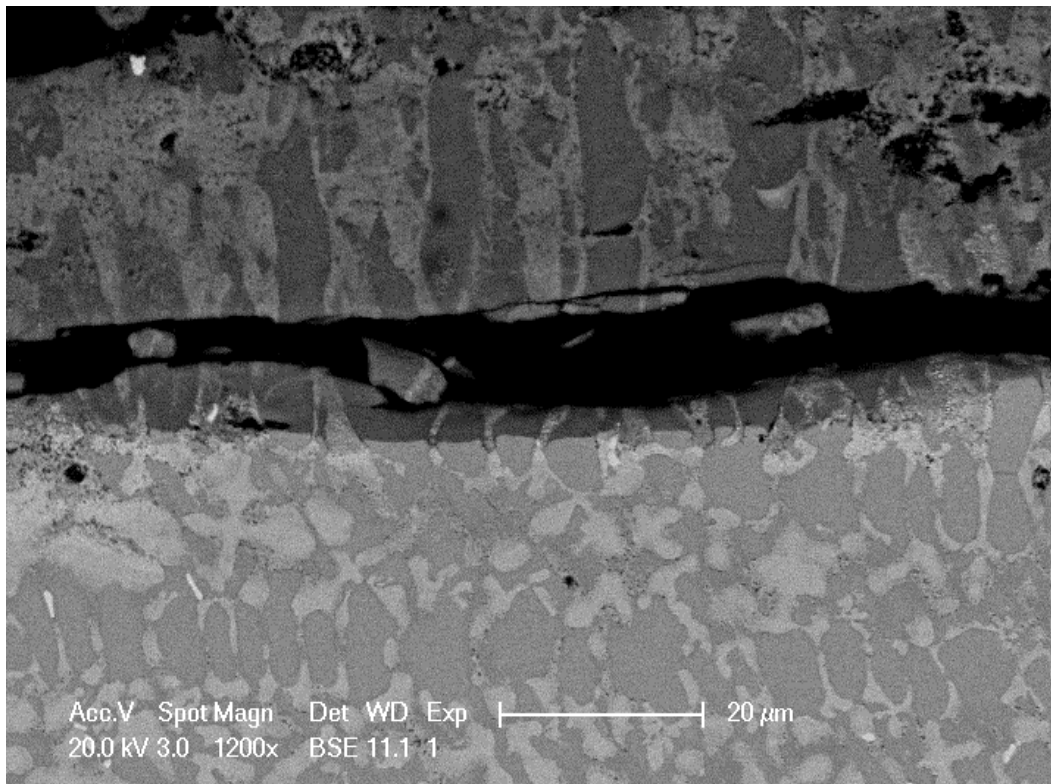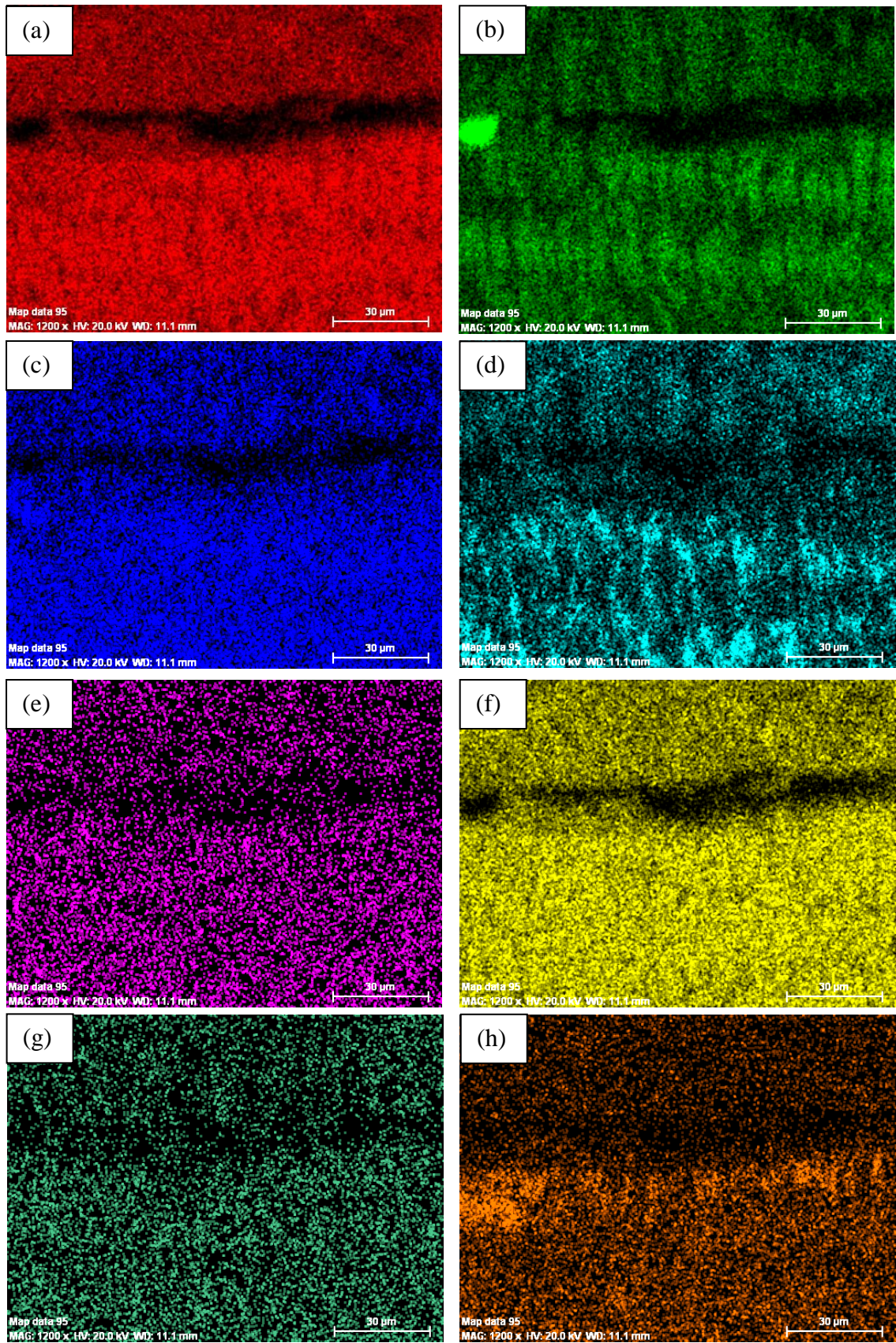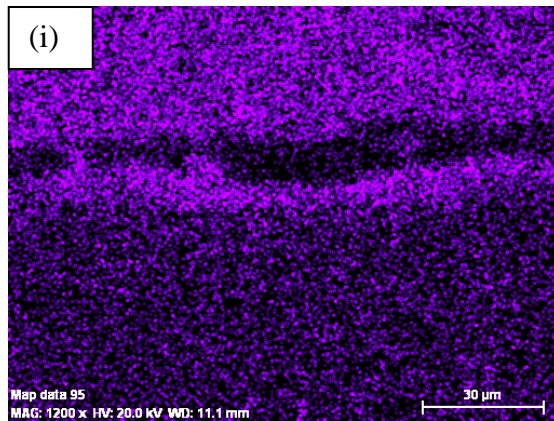
Figure 7.11 X-ray maps for JN2 after oxidation at 1200 °C Nb (a), Si (b), Ti (c), Cr (d), Hf (e), Mo (f), W (g), Sn (h) and O (i)

Figure 7.12 shows a transmission X-ray diffractogram of the scale from JN2 after oxidation at 1200 °C, the profile suggests that the oxides present in the scale are mixed Ti and Cr niobates.
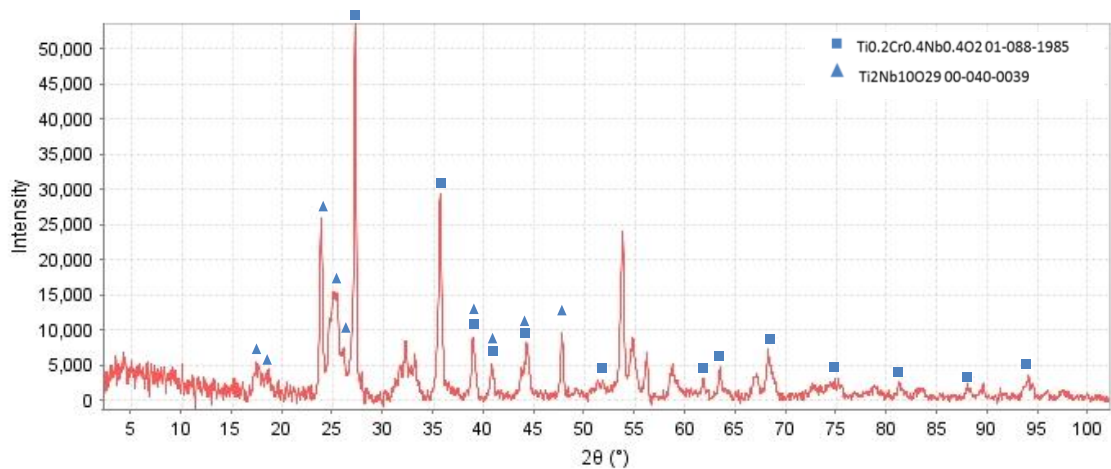
Figure 7.12 Transmission X-ray diffraction pattern of the scale from the JN2 oxide layer after oxidation at 1200 °C for 60 h

Table 7.3 shows the EPMA data for JN2 after oxidation at 1200 °C for 60h. The data suggests the presence of at least 2 different oxides in the oxide layer. One of the oxides would be a Ti and Cr niobates and the other is richer in Si and Nb than in Ti. The point analysis data of the oxide layer suggested the stoichiometry of $Ti_2Nb_{10}O_{29}$ which was supported by the XRD data. The other mixed oxide that was analysed comprised of two different contrasting phases and had high Si content, this is suggestive of it being either a mixture of oxide and Nb_5Si_3 or a mixture of silicate and an Nb based oxide. The data shows that the Nb_5Si_3 was not contaminated by oxygen at any point below the surface of the substrate; it also maintains an almost identical composition throughout the cross

section yet is richer in Si than that in JN2-AC. The Nb_{ss} was contaminated by oxygen even in the bulk, with the solubility of O at ~ 8 at%. The Ti and Cr content of the Nb_{ss} near the oxide were higher than that in the bulk and diffusion zone.

Table 7.3 EMPA data of JN2 after oxidation at 1200 °C for 60 h (at%)

Phase	Nb	Si	Ti	Cr	Hf	Mo	W	Sn	O
$Ti_2Nb_{10}O_{29}$ In oxide layer	15.6±0.9 14.7-16.8	0.8±1.1 0.0-2.3	5.7±1.1 4.1-6.7	4.6±1.0 3.4-5.4	0.6±0.1 0.4-0.7	1.1±0.4 0.6-1.6	1.1±0.2 0.9-1.4	0.1±0.1 0.0-0.2	70.4±0.4 70.2-71.1
Mixed oxide In oxide layer	13.8±0.4 13.3-14.1	10.6±0.4 10.2-10.9	4.1±0.7 3.6-4.9	0.9±0.4 0.6-1.3	0.5±0.0 0.5-0.5	0.6±0.1 0.5-0.6	0.3±0.0 0.3-0.3	0.1±0.0 0.1-0.1	69.3±0.2 69.1-69.5
Nb_{ss} at scale interface	50.8±2.1 48.4-53.2	0.1±0.2 0.0-0.4	14.1±1.4 12.4-15.6	8.3±2.2 6.8-11.6	1.0±0.1 0.9-1.1	9.8±0.6 9.1-10.4	6.4±1.2 5.4-7.8	1.4±0.4 1.2-2.0	8.0±3.0 4.8-11.8
Nb_5Si_3 at scale interface	44.9±0.2 44.7-45.0	36.3±0.2 36.1-36.5	11.8±0.1 11.7-12.0	1.9±0.0 1.9-2.0	1.6±0.0 1.6-1.7	1.9±0.0 1.8-1.9	1.0±0.0 1.0-1.0	0.7±0.0 0.6-0.7	0.0±0.0 0.0-0.0
Nb_{ss} 300 µm below the surface	52.3±0.3 52.1-52.7	0.0±0.0 0.0-0.0	12.8±1.0 12.2-14.0	6.3±0.4 5.8-6.7	0.9±0.0 0.8-0.9	10.5±0.1 10.4-10.6	8.1±0.2 7.8-8.3	1.1±0.1 1.1-1.2	7.9±0.5 7.9-8.5
Nb_5Si_3 300 µm below the surface	44.4±0.2 44.1-44.6	36.6±0.1 36.6-36.7	11.7±0.0 11.7-11.8	2.0±0.0 2.0-2.0	1.6±0.0 1.6-1.7	1.9±0.1 1.8-1.9	1.0±0.1 1.0-1.1	0.7±0.0 0.7-0.7	0.0±0.0 0.0-0.0
Nb_{ss} bulk	52.0±1.2 50.6-53.0	0.0±0.0 0.0-0.1	12.1±1.4 10.8-13.6	6.5±0.2 6.4-6.7	0.9±0.0 0.9-0.9	10.4±0.3 10.2-10.7	7.9±0.4 7.5-8.2	1.3±0.3 1.0-1.5	8.9±1.5 7.2-9.8
Nb_5Si_3 bulk	44.4±0.2 44.2-44.5	36.8±0.1 36.8-37.0	11.7±0.1 11.6-11.7	1.9±0.1 1.9-2.0	1.6±0.0 1.6-1.7	1.9±0.1 1.8-1.9	1.0±0.0 1.0-1.0	0.6±0.0 0.6-0.6	0.0±0.0 0.0-0.0

7.3   Alloy JN3 (Nb-18Si-15Ti-2Cr-2Hf-5Mo-5W-2Sn) after oxidation at 1200 °C

The TGA data, JN3 is shown in Figure 7.13. Unfortunately equipment failure after 40 h meant that the experiment had to stop, after the 40 h oxidation, the mass gain was 0.062 g/cm^2. This was higher than the mass gain of 0.04 g/cm^2 of JG6 AC (Nb-18Si-24Ti-5Al-5Cr-5Hf-2Mo-5Sn) and similar to that of JN2, after 40 h oxidation which was 0.06 g/cm^2. Comparison of the oxidation of JN2-AC and JN3-AC at 1200 °C brings to question the benefits of high Cr content in the alloy and the presence of NbCr$_2$ Laves phase in the microstructure. The linear oxidation rate constant of JN3 at 1200 °C was 4×10^{-7} gcm^{-2}s^{-1}; this is the same as that of JN2.

Figure 7.14 shows a specimen of the alloy JN3 after oxidation and that a substantial oxide layer was formed. The oxide formed as a Maltese cross; with a loss of substrate contact at all edges, this oxide was however highly adhered at each face and reasonable force was required to remove it for analysis. The oxide itself was dense rather than powdery, resulting in a visibly smooth surface appearance.
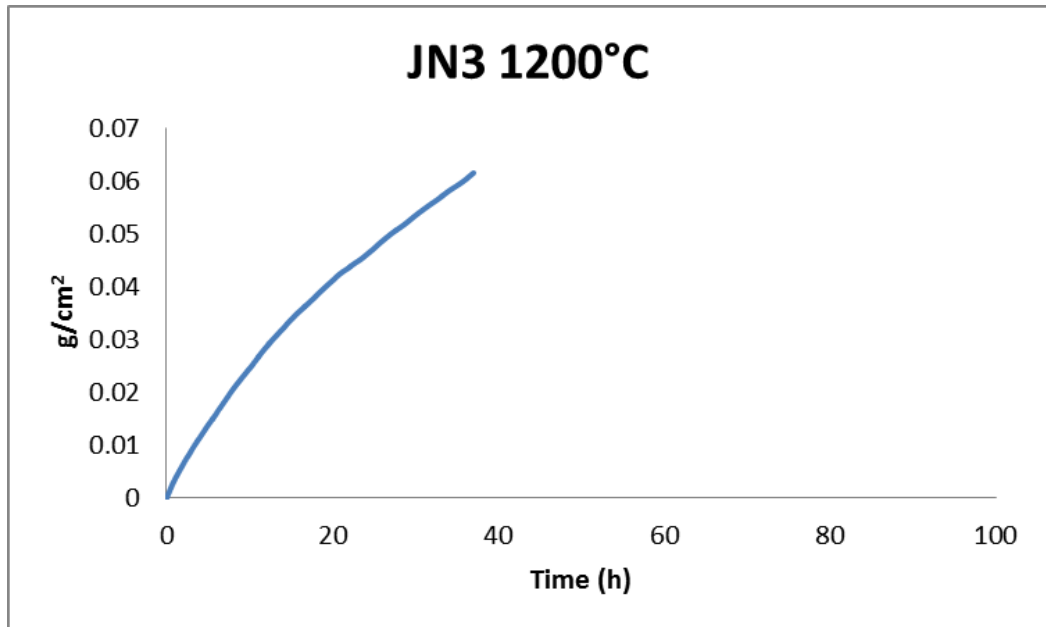
Figure 7.13 TGA data of JN3 after oxidation at 1200 °C in air

Figure 7.14 A specimen of JN3 AC after oxidation at 1200 °C

Figure 7.15 shows images of the oxide scale on JN3. The oxide displays almost continuous coverage with blocky and needle type oxides covering the majority of the surface (Figure 7.15 a), as seen in JN2, see Figure 7.9 but in this the needles were more defined. The recessed regions display a more refined oxide microstructure (Figure 7.15 b) to the majority of the oxide surface, which is coarser.
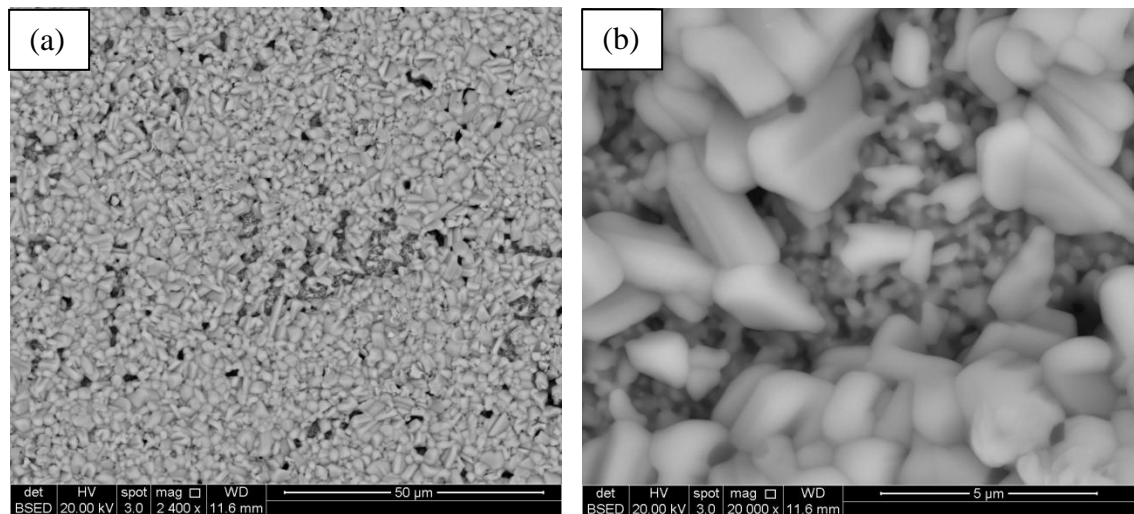
Figure 7.15 BSE images of JN3 after oxidation at 1200 °C at (a) 2400 and (b) 20,00 X magnification

Figure 7.16 shows the cross sectional images of JN3 at 1200 °C; unlike the alloy JN2, the JN3 did display a diffusion zone with noticeable precipitates, similar to those observed in JN1. Like the precipitates found in JN1 as they had similar a contrast, they are likely to be TiN and HfO_2, but in JN3 they were too small to analyse using EPMA. Like JN2, in JN3 there was a noticeable formation of a 20-30 μm thick protective Nb_3Sn phase at the substrate/oxide interface. Unlike JN1 and JN2 there was a damaged area below the substrate/scale interface (Figure 7.16 b to d) with dark contrast second phase particles, the "cracks" that run parallel to the interface. However this damage was

different to that seen at 800 °C. The oxide itself displays arced cracking parallel to the substrate surface (Figure 7.16 a), this is usually indicative of stress build-up during the oxide growth. The arcing nature of these cracks suggested the build-up of stress at the oxide edges and their release via the formation of the Maltese cross appearance of the oxide and resulting crack growth from the edges. Aside from the cracking there was a visible gap between the oxide layer and the substrate, indicating a lack of adherence between the two.
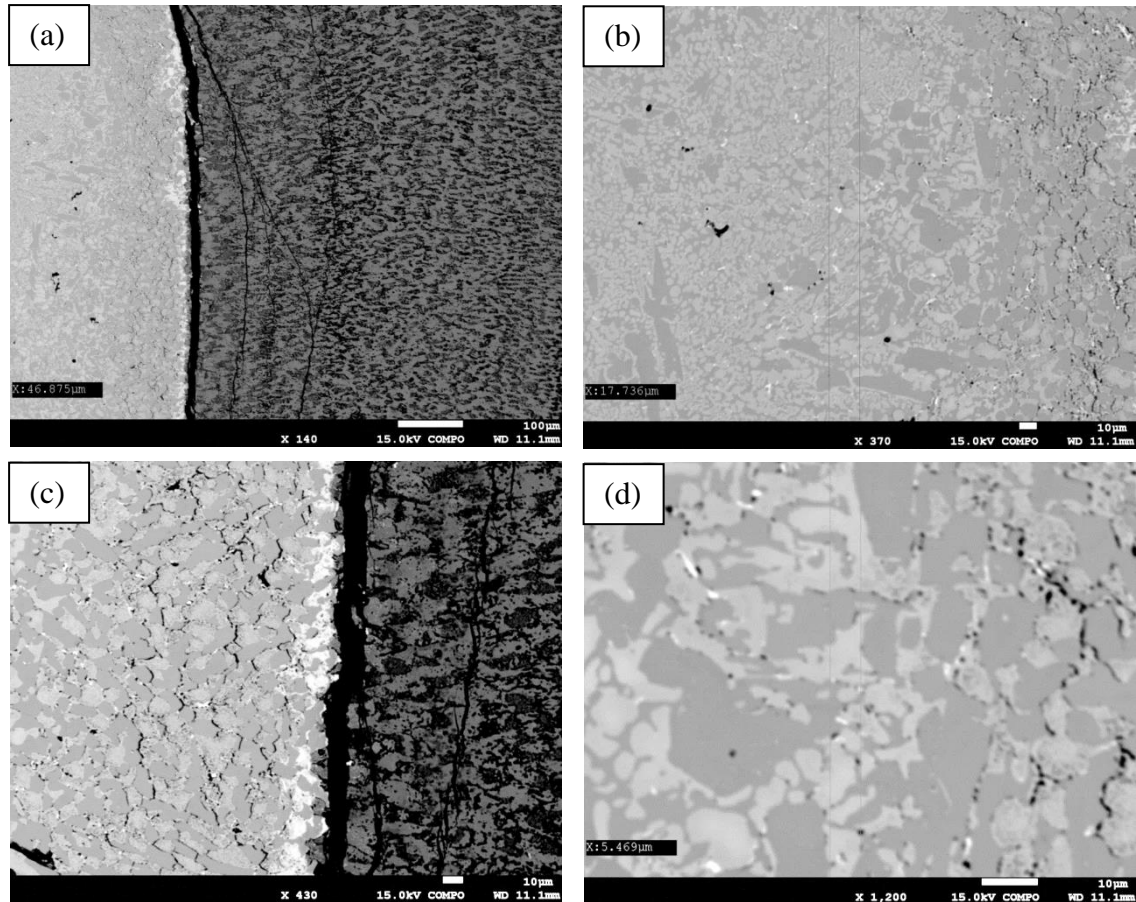
Figure 7.16 BSE Images of the oxide cross section of JN3 after oxidation at 1200 °C at (a) 140, (b) 370, (c) 430 and (d) 1200 X magnification

Figure 7.17 shows the X-ray maps for JN3 1200 °C, the maps clearly display the positioning of each phase within the substrate and the oxide. The Nb, Hf and W maps show a higher concentration in the substrate layer when compared to the concentration in the oxide with no evidence of any areas with dramatically increased concentrations. The Ti and Cr maps show a presence of Ti and Cr in both the substrate and the oxide layer, with a possible area of higher Ti concentration at the oxide interface along with

Sn. The Sn map shows a dramatic increase in concentration along the edge of the oxide interface; this is due to the formation of a protective Sn layer forming adjacent to the oxide. The Mo, unlike the W, shows a degree of banding within the oxide layer. The O_2 map shows the majority of the oxygen lies within the oxide layer and the rest of the alloy has a fairly uniform oxygen concentration. Figure 7.18 indicates that the oxide layer, as with JN1 and JN2, is comprised of a mixture of oxides, including Cr/Ti niobates and Nb_2O_5.

(a)

(b)
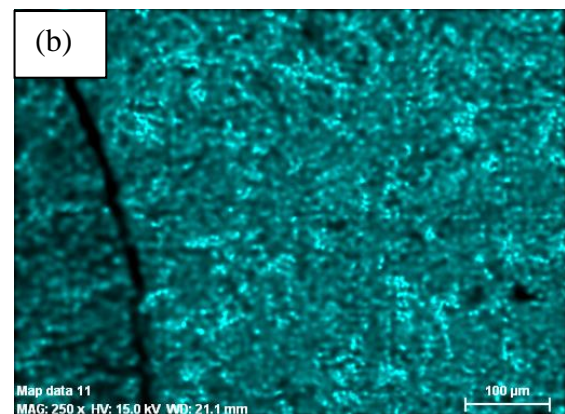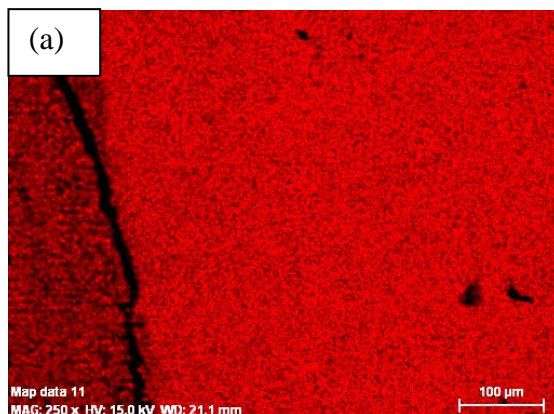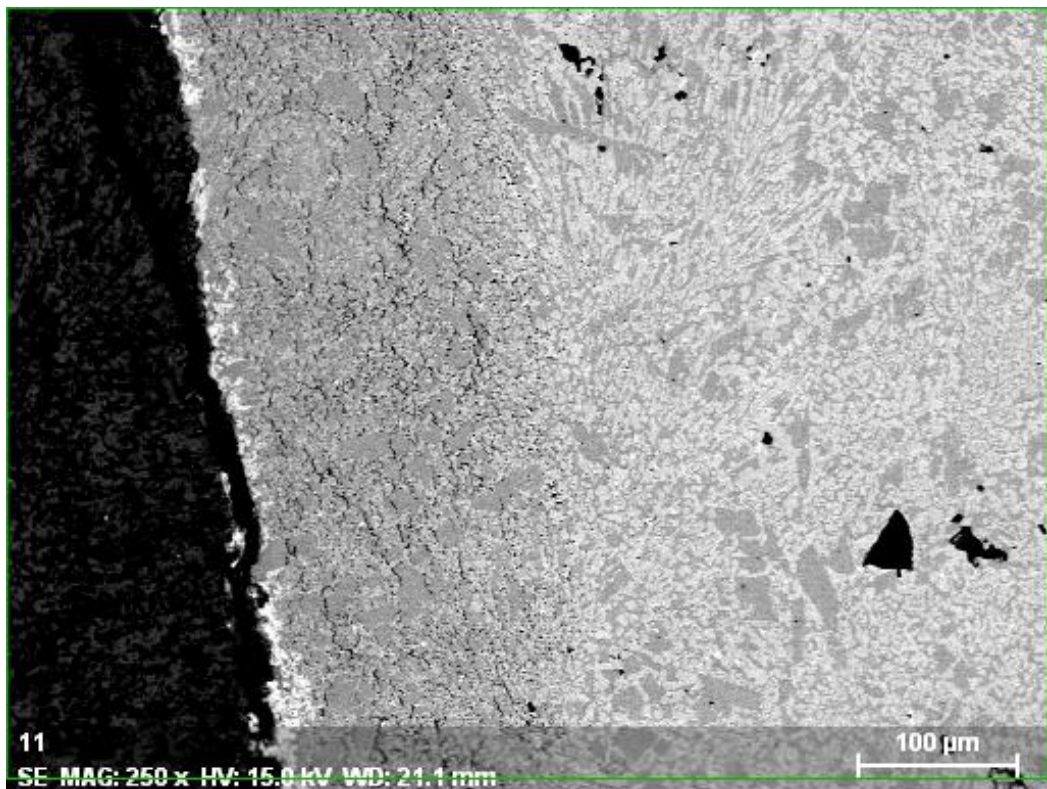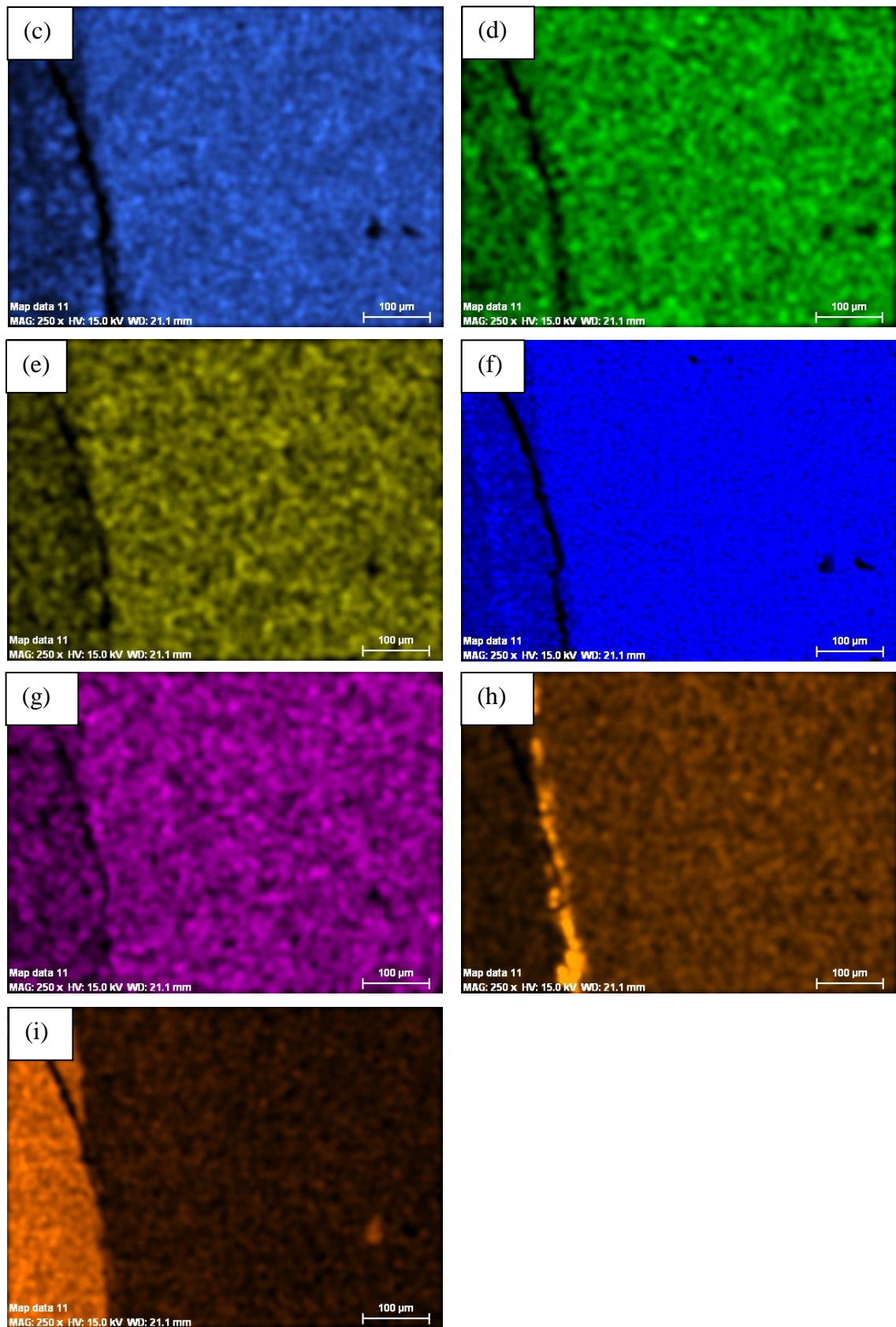
Figure 7.17 X-ray maps for JN3 1200°C Nb (a), Si (b), Ti (c), Cr (d), Hf (e), Mo (f), W (g) and Sn (h), O (i)
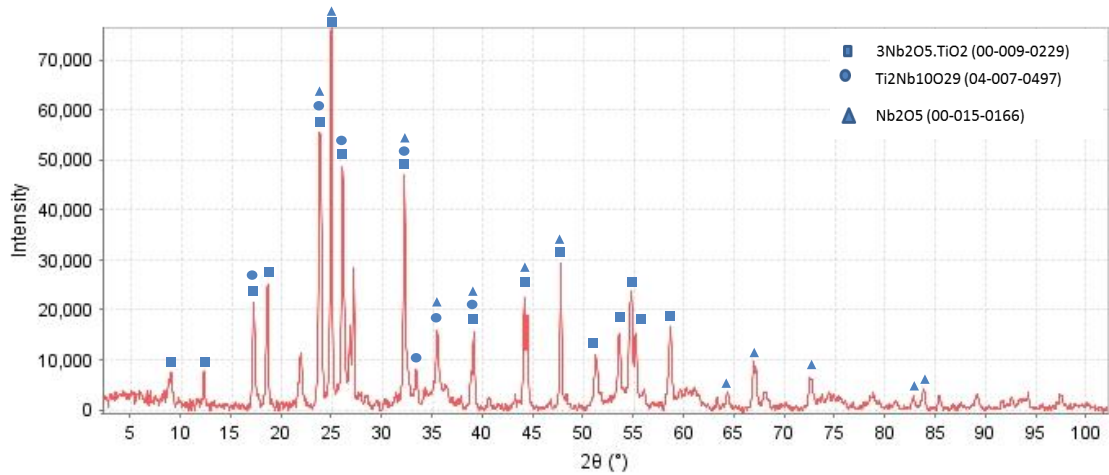
Figure 7.18 Transmission X-ray diffraction pattern of the scale from the JN3 oxide layer after oxidation at 1200 °C for 40 h

Table 7.4 shows the EPMA data for JN3 after oxidation at 1200 °C for 40 h. In the scale, $Ti_2Nb_{10}O_{29}$ and a mixed oxide were analysed. The former was richer in Nb compared with the Ti niobates in JN2 and the latter had a similar composition to the mixed oxide in the scale of JN2. The analysis is also backed up with the powder XRD analysis from the scale (Figure 7.18). Overall the main effect that Cr appears to have at 1200 °C is to alter the thickness of the scale. The scale formed on JN2 (high Cr) was thin and had low adherence whilst the scale on JN3 (low Cr) was thicker, and remained attached to the substrate. The Cr content in the alloy had very little effect on the overall mass gain or the rate constant, which was linear for both alloys. The Nb_{ss} was contaminated by oxygen, even in the bulk, and towards the surface of the substrate the oxygen concentration was ~ 16.2 at%. In the bulk of the alloy the oxygen concentration of the Nb_{ss} was ~ 5.2 at%. The Nb_5Si_3 in the diffusion zone of the alloy showed a small amount of oxygen contamination, though given the high oxygen content of the surrounding phases it is likely due to contamination from another phase, detected in the interaction volume. The composition of the Nb_5Si_3 in the bulk was similar to that of the normal Nb_5Si_3 however, like JN2; it displayed an increase in Si and a decrease in Nb. The Nb_5Si_3 in the bulk showed no affinity for oxygen, this may be due to the increased depth from the edge of the sample or the Nb_5Si_3's lack of solubility for oxygen.

Table 7.4 point EPMA data for JN3 1200 °C (at%)

Phase	Nb	Si	Ti	Cr	Hf	Mo	W	Sn	O
$Ti_2Nb_{10}O_{29}$	22.1±0.6	0.0±0.0	4.6±0.5	0.2±0.1	0.6±0.1	0.1±0.1	0.6±0.2	0.0±0.0	71.7±0.6
	21.5-22.7	0.0-0.0	4.0-5.1	0.1-0.3	0.5-0.6	0.1-0.2	0.4-0.7	0.0-0.1	71.1-72.2
Mixed oxide	10.3±2.5	10.4±3.5	3.4±0.9	0.2±0.1	0.5±0.2	0.4±0.5	0.3±0.1	0.0±0.0	74.5±5.7
	7.9-12.9	8.2-14.5	2.8-4.5	0.1-0.3	0.3-0.6	0.0-0.9	0.2-0.4	0.0-0.1	68.9-80.2
Nb_3Sn	47.5±4.2	0.0±0.1	0.4±0.4	0.1±0.1	1.2±0.3	11.4±0.6	5.9±2.4	30.1±6.1	3.4±4.0
	41.6-51.6	0.0-0.2	0.1-1.0	0.0-0.2	0.7-1.4	10.8-11.9	3.1-8.5	26.5-37.5	0.0-7.8
Nb_{ss} **Diffusion zone**	55.1±1.8	0.8±0.7	10.9±1.0	2.4±0.4	0.7±0.2	8.1±0.2	4.4±0.9	1.4±0.2	16.2±1.9
	52.5-56.7	0.1-1.6	9.9-12.2	1.8-2.9	0.4-0.8	7.9-8.5	3.1-5.4	1.1-1.6	14.4-18.5
Nb_5Si_3 **Diffusion zone**	48.5±0.5	35.6±1.2	11.2±0.6	0.1±0.1	2.3±0.1	0.7±0.1	0.3±0.0	0.6±0.0	0.7±1.2
	47.9-49.0	34.3-36.4	10.6-11.8	0.1-0.2	2.1-2.4	0.6-0.8	0.2-0.3	0.6-0.7	0.0-2.1
Nb_{ss} **bulk**	58.5±1.6	0.3±0.4	17.1±0.8	3.5±0.2	1.1±0.3	8.4±0.5	4.0±1.0	1.9±0.3	5.2±2.3
	56.7-60.4	0.0-1.1	15.5-17.9	3.3-3.8	0.7-1.5	8.0-9.0	2.9-5.7	1.4-2.2	2.5-8.2
Nb_5si_3 **Bulk**	47.9±0.5	36.4±0.2	11.6±0.5	0.3±0.1	1.8±0.3	1.0±0.3	0.4±0.1	0.6±0.0	0.0±0.0
	47.3-48.3	36.2-36.6	11.2-12.2	0.1-0.3	1.6-2.1	0.7-1.3	0.3-0.5	0.6-0.7	0.0-0.0

7.4   Alloy JN4 (Nb-20Si-20Ti-2Cr-2Hf- 6Mo-5Sn) after oxidation at 1200 °C

The total mass gain JN4 after oxidation at 1200 °C was 0.03 g/cm^2. The alloy itself was developed to balance the negative effect on oxidation caused by the addition of a refractory metal, Mo (6 at%), and the decreased Ti (20 at%) and Hf (2 at%) content (compared with JG6) to improve the oxidation. With an increase in Si (20 at%) and Sn (5 at%) content and an increase in Ti concentration compared with JN2 and JN1. When compared with the Sn containing alloy JG6 (weight gain of 0.09 g/cm^2 at 1200 °C), the alloy had superior oxidation resistance. The smooth TGA curve in Figure 7.19 indicates no spallation or breakaway oxidation and is significantly different from that after oxidation at 800 °C. The parabolic oxidation rate constant for JN4 was 9x10^{-10} g^{2}cm^{-4}s^{-1} for the first 14 h and decreased to 3x10^{-9} g^{2}cm^{-4}s^{-1} for the rest of oxidation, better than both JG6-AC (K$_p$= 4.1x10^{-9} g^{2}cm^{-4}s^{-1}) and JN1 (7x10-9 g^{2}cm^{-4}s^{-1}).

Figure 7.20 shows the specimen after 100 h oxidation at 1200 °C. It can be seen there is evidence of a Maltese cross formation but no powder oxide or scale spallation. The oxide scale itself was highly adhered and required chipping off to remove for

analysis; the scale was very thin and dense, particularly when compared with the alloys JN1 and JN3. This is likely due to the formation of an Nb_3Sn rich layer at the scale/oxide interface and reduction of the oxygen ingress and the outward mobility of metal ions into the scale.
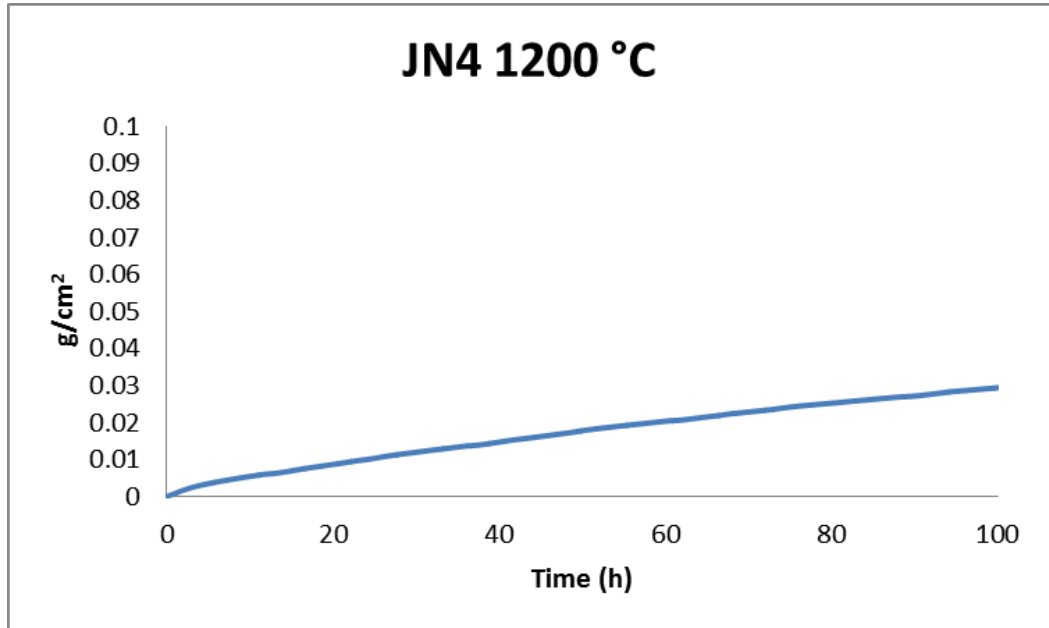
Figure 7.19 TGA data of JN4 after oxidation at 1200 °C in air

Figure 7.20 A specimen of JN4 after oxidation at 1200 °C

Figure 7.21 shows BSE images of the surface of the oxide formed on JN4 after 100 h oxidation at 1200 °C. The outlines of silicide grains in the substrate can be clearly seen amongst areas of dense, oxides. The areas above the silicides are covered by a fine oxide, very similar to what was seen in JN2 and 3. Figure 7.25 shows the XRD diffractogram of JN4 after oxidation at 1200 °C. The diffraction pattern shows the presence of 4 possible phases; namely $TiNb_2O_7$, Nb_2O_5, TiO_2 and $Ti_2Nb_{10}O_{29}$. The latter

have been previously reported to form on oxidised Nb-silicide based alloys. Though all oxides show peak matches, the $TiNb_2O_7$ and TiO_2 oxides show peak correlation to higher and lower angles which the other alloys only show possible matches at lower angles. This means that the presence of these two oxides is highly likely.
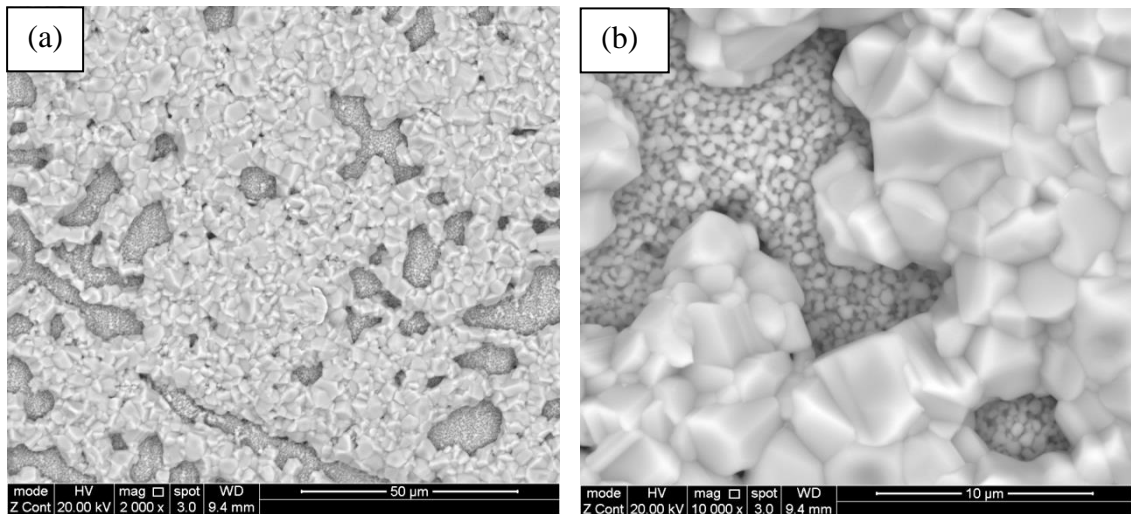
Figure 7.21 BSE images of the surface of JN4 AC after oxidation at 1200 °C at (a) 2000 and (b) 10,000 X magnification

Figure 7.22 shows the images of the cross section of JN4 after oxidation at 1200 °C at low and high magnifications. It can be seen that the oxide itself was cracked, though as mentioned earlier, it was highly adherent (Figure 7.22 a). Unlike the previous alloys however there were large regions of the oxide which remained fully adhered to the substrate. There was a visible Sn-rich layer at the very edge of the substrate which was ~ 50-100 μm thick (Figure 7.22 b). As was the case in JN3, there was also a discernible diffusion zone that was primarily comprised of both black and white precipitates which are likely to be TiN and HfO_2. The cross section of the oxide clearly displays the different sized grains that were seen in Figure 7.22 c. The fine grained regions were rich in Si, indicating they were previously Silicides and the larger oxide grains were poor in Si, indicating they were formed from the oxidation of the Nb_{ss}.

Oxidised Nb$_{ss}$

Oxidised Nb$_5$Si$_3$

Sn-rich layer
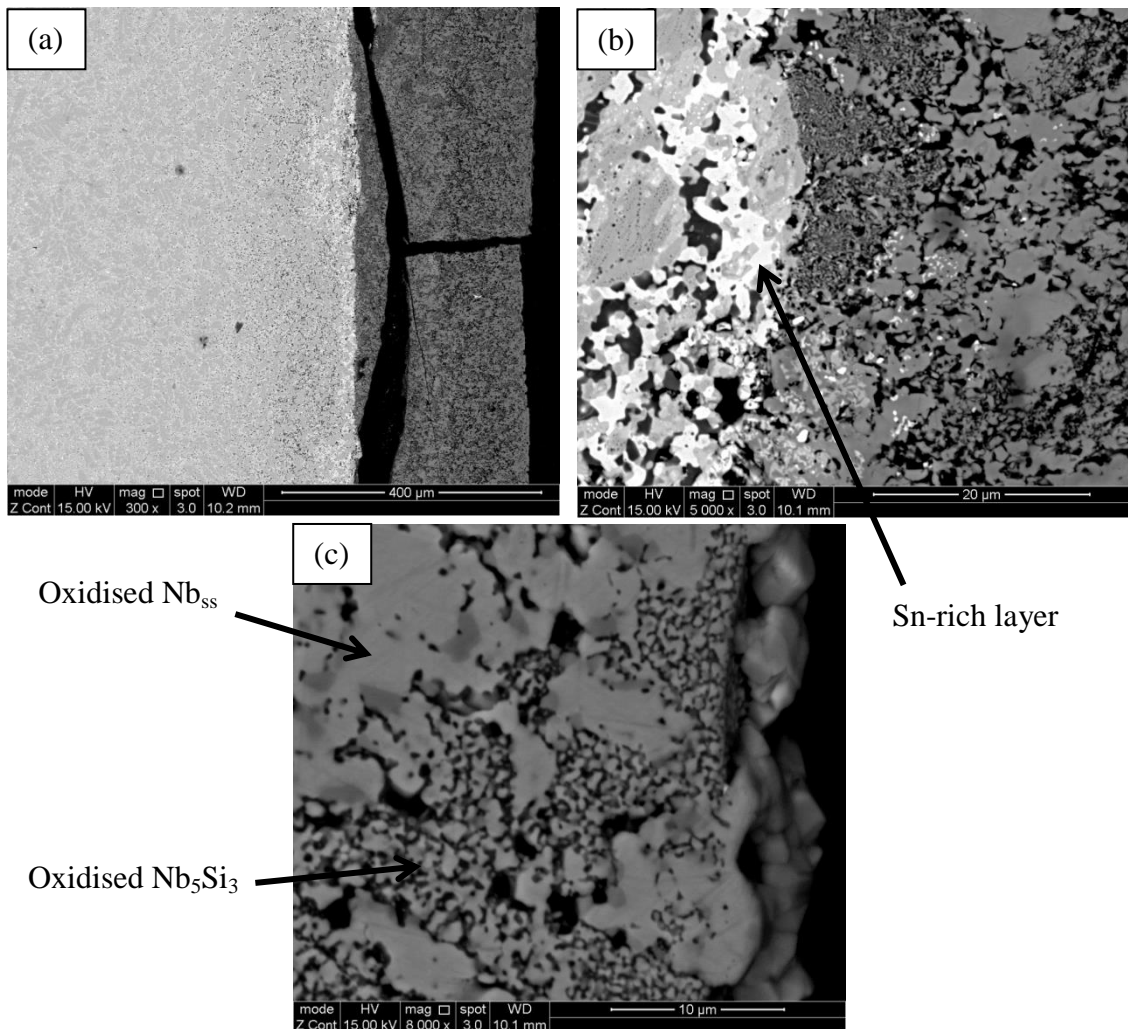
Figure 7.22 BSE images of the cross section of JN4 AC after oxidation at 1200 °C (a) 300, (b) 5000 and (c) 8000 X magnification

Figure 7.23 shows large bright contrast areas in a cross section of JN4. These areas were Sn rich and comprised of Nb$_3$Sn, HfO$_2$ and Nb$_5$Si$_3$; large Sn rich regions such as these had not been observed in the cast alloy JN4. The round shaped Sn-rich regions are found surrounding faults such as cracks in the substrate and small notched areas, which must have existed prior to oxidation yet not been visible. The Sn-rich areas must have formed by the diffusion of Sn towards the surface and show a propensity for Sn atoms to migrate to oxygen rich regions. This migration behaviour of Sn atoms may lead to a degree of self-healing in these alloys, improving their oxidation resistance.

Sn-rich layer
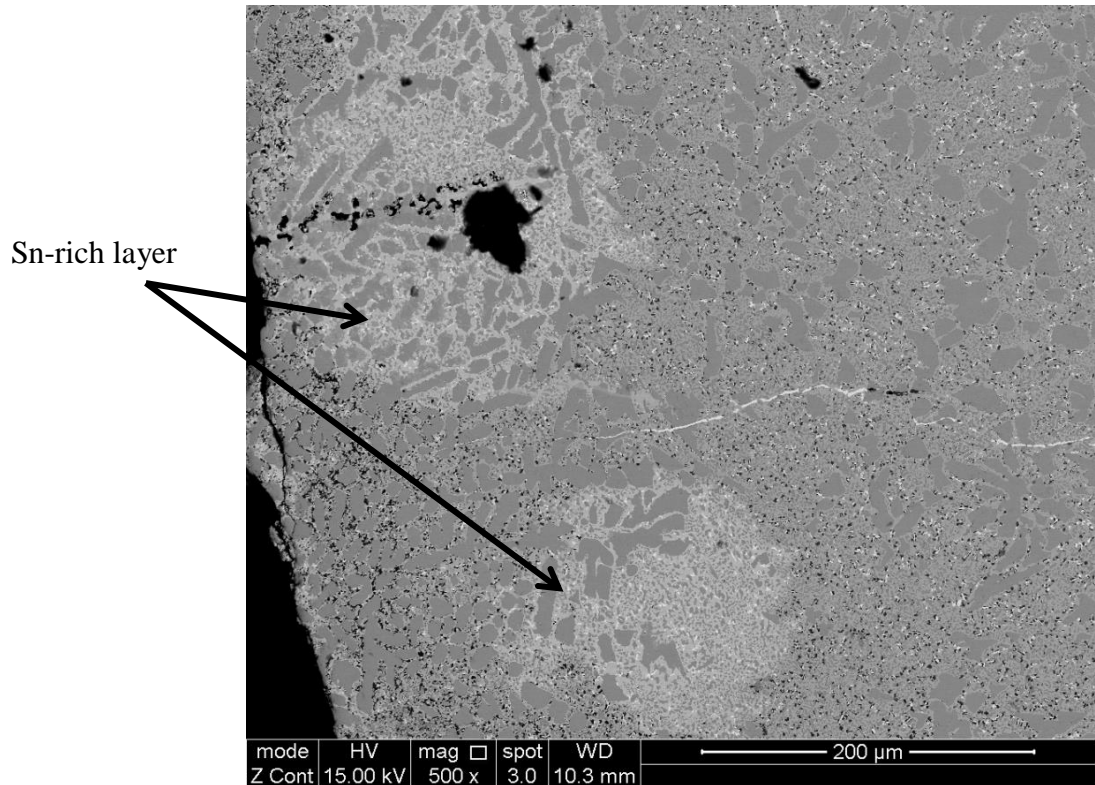
Figure 7.23 Cross section images showing Sn rich regions near the scale/substrate interfaceof JN4 after oxidation at 1200 °C

Figure 7.24 shows the cross section BSE image and X-ray maps of JN4 after oxidation at 1200 °C that were taken at the oxide/substrate interface. The Si map shows that the Si content is fairly even throughout the sample and oxide. The Nb, Hf and Mo maps are all similar as they all show a higher concentration of each element in the substrate with a drop of Mo content in the oxide layer. The Ti map shows a drop in Ti content along the oxide/substrate interface and areas of a high Ti content adjacent to the depleted zone. These bright areas correspond to dark phases and are likely Ti oxides, nitrides or niobates. The Cr map shows no distinct bright regions in the map so in this region of the alloy there are no Cr rich oxides (these may reside closer to the edge of the oxide scale) however there does appear to be a gradient where the Cr level drops as it gets closer to the oxide interface. Importantly, like JN3, the JN4 formed a Sn-rich area near the scale/substrate interface. Given the higher Sn content in JN4, the Sn-rich layer was much thicker than that found in JN2 and JN3. The oxygen map shows that the majority of the oxygen in the alloy is in the oxide itself, the Sn rich region shows a lower oxygen concentration.
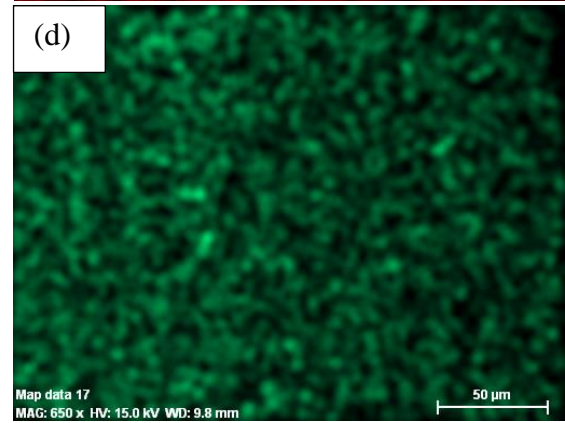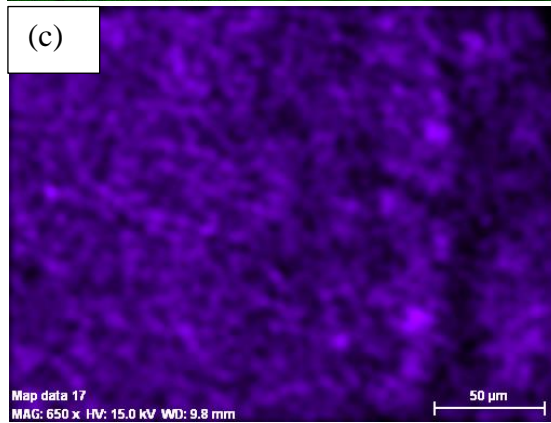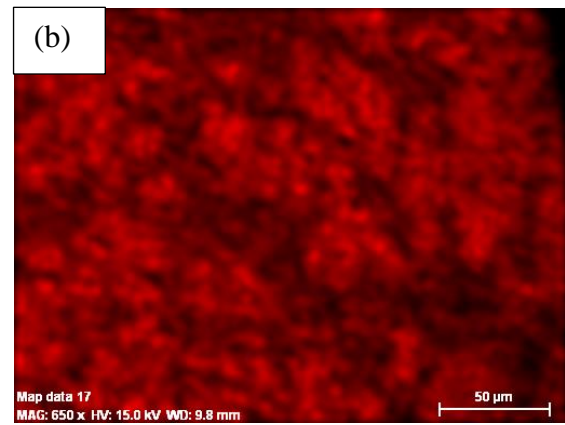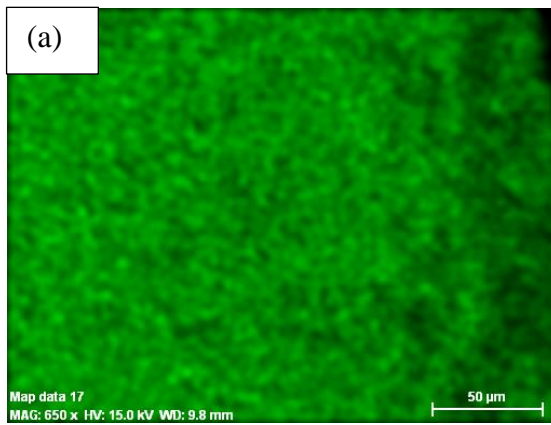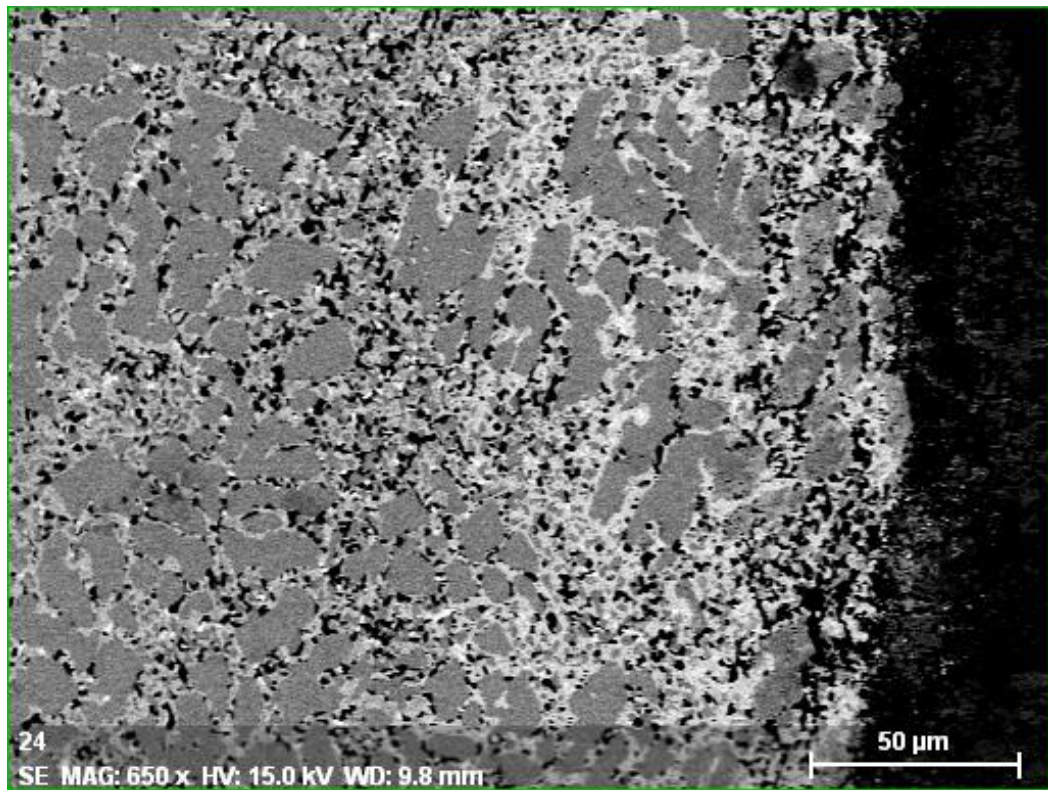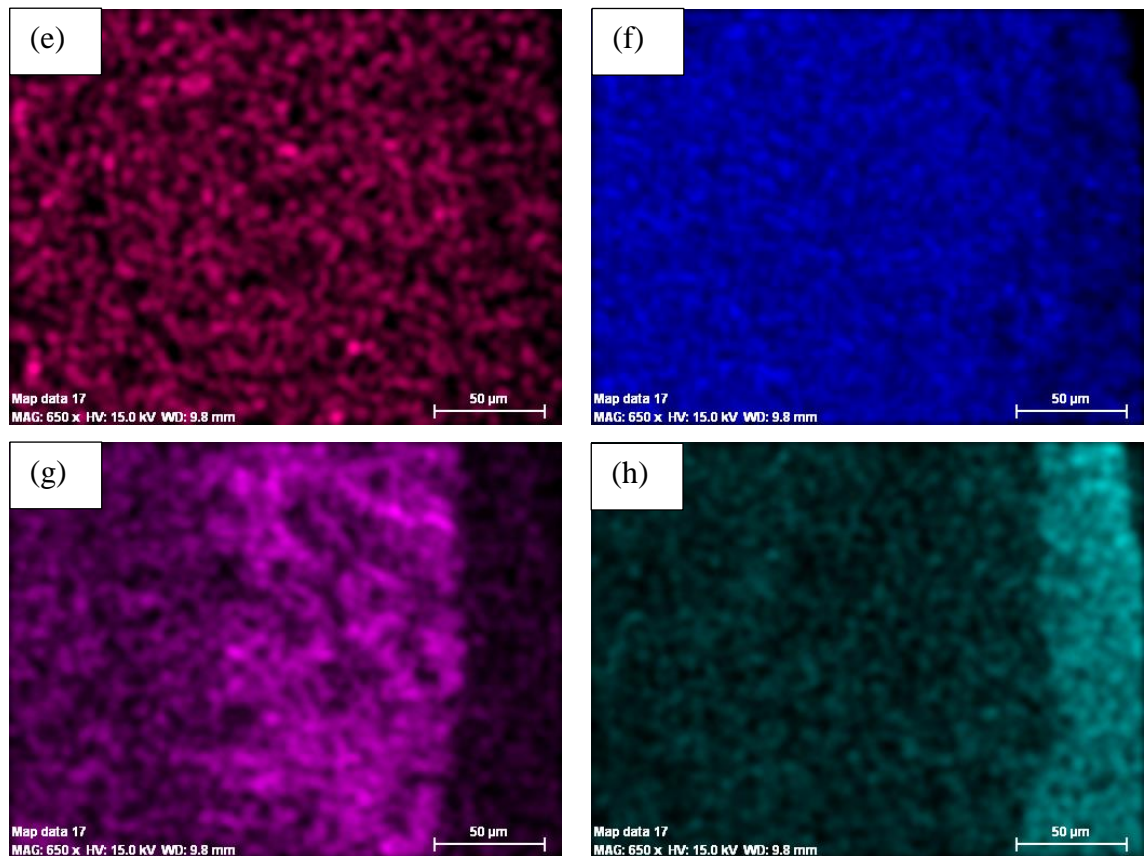
Figure 7.24 X-ray maps for JN4 1200°C Nb (a), Si (b\), Ti (c), Cr (d), Hf (e), Mo (f), Sn (g) and O (h).

Figure 7.25 shows the powder transmission X-ray diffractogram and JN4 after oxidation at 1200 °C, it shows the existence of niobium pentoxide, Titanium dioxide and Titanium niobates.
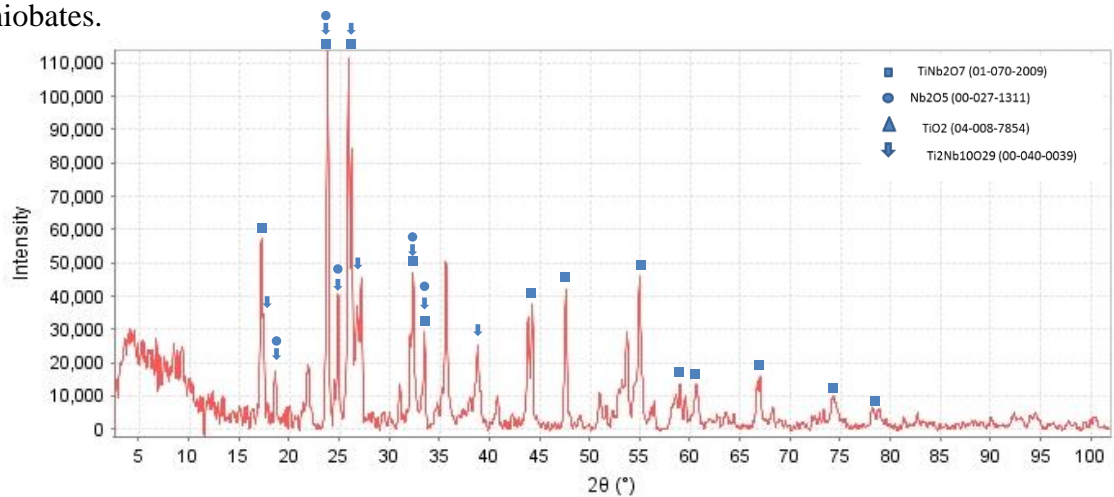
Figure 7.25 Powder transmission XRD diffractogram of JN4 oxidised at 1200 °C

Table 7.5shows the EPMA data for phases in the alloy JN4 after oxidation at 1200 °C. Unlike the other alloys of this research the Nb_5Si_3 was contaminated by oxygen. This is

also seen for the oxidised samples at 800 °C. The Nb_5Si_3 (in the Sn rich layer) closest to the oxide showed a solubility for oxygen of 8.7 at% and the oxygen content dropped to 5.9 at% in the silicides in the bulk. In the diffusion zone the concentration of O_2 in the Nb_5Si_3 was ~2.3 at% compared with 5.9 at% in the bulk. The higher oxygen content in the bulk rather than in the diffusion zone may be due to a slightly different chemical composition with the diffusion zone silicide containing a higher amount of Si and Ti. The Nb_{ss} in the diffusion zone was too small to analyse accurately but accepting the influence of the surrounding oxides the oxygen level of the Nb_{ss} was low at 3.9 at%. The solubility of oxygen in the bulk Nb_{ss} dropped to zero. Comparably the main difference between the Nb_{ss} in the bulk and the diffusion zone is the large decrease in Ti content in the diffusion zone. The other elements remain similar in concentration but the Ti is depleted, likely to form the $TiNb_2O_7$ phase in the scale.

The EPMA of the oxides is in good agreement with the XRD data. The stoichiometry shows the $TiNb_2O_7$ oxide. The $TiNb_2O_7$ corresponds to the bright phase in Figure 7.22 c; it can be clearly seen that this phase corresponds to the large oxide phases seen in Figure 7.21, and was formed from oxidised Nb_{ss}. The data for the mixed oxide phase corresponded to the finer oxide that can be seen in Figure 7.21 and is the product of the oxidation of the Nb_5Si_3 phase.

The data taken from the bright regions close to the edge of the alloy correspond to a Sn rich region comprised of Nb_3Sn and Nb_5Si_3 as can be seen in Figure 7.23. The oxygen content of the Nb_5Si_3 is the same as that in the Sn rich zone at the edge of the sample. This indicates that either the oxidation occurs before the protective Nb_3Sn layer has time to form, or the Nb_3Sn does not totally shield the Nb_5Si_3 from oxidation. Given the similarities between the Nb_5Si_3 in the protective Nb_3Sn layer that surrounds the sample and that found in the Nb_3Sn region which surrounds the cracks; it can be deduced that the Sn itself has a negative effect on the oxygen resistance of the Nb_5Si_3 and increases its affinity for oxygen.

Table 7.5 EPMA data for JN4 after oxidation at 1200 °C for 100 h (at%)

phase	Nb	Si	Ti	Cr	Hf	Mo	Sn	O
$TiNb_2O_7$ In scale	20.7±3.9 16.5-24.7	1.3±1.5 0.03-3.2	7.8±2.5 4.9-11.1	0.4±0.4 0.1-1.0	0.7±0.2 0.5-0.9	0.4±0.5 0.1-1.1	0.0±0.0 0.0-0.1	68.6±1.4 66.9-70.1
mixed oxide	15.1±1.6 13.8-18.6	14.1±2.7 8.6-16.7	4.7±1.4 3.3-7.6	0.3±0.2 0.1-0.6	0.5±0.0 0.5-0.6	1.0±0.9 0.0-2.9	0.0±0.0 0.0-0.0	64.3±1.3 62.0-66.5
Nb_3Sn/ Nb_5Si_3 mix	50.1±2.7 47.1-52.5	17.7±4.8 13.4-23.5	4.5±1.9 2.1-6.4	0.2±0.1 0.1-0.3	1.4±1.0 0.7-2.8	8.7±3.8 4.8-12.0	17.4±3.4 14.2-19.6	0.0±0.0 0.0-0.0
Nb_5Si_3 In Sn layer	42.1±2.3 39.6-43.9	29.1±1.1 27.9-30.0	13.9±1.6 12.1-15.2	0.2±0.0 0.2-0.2	1.4±0.1 1.3-1.5	2.2±0.0 2.1-2.2	2.4±1.3 1.5-3.9	8.7±5.4 4.7-14.9
Nb_{ss} DZ	56.9±3.5 53.2-62.4	3.5±2.3 1.7-7.2	8.8±2.9 5.6-12.4	5.7±3.4 4.3-11.7	0.3±0.2 0.2-0.3	14.2±3.2 10.5-17.1	6.7±3.0 3.4-11.1	3.9±3.8 0.0-8.5
Nb_5Si_3 DZ	43.6±0.3 43.3-44.0	31.1±0.6 30.5-31.6	16.5±0.3 16.3-16.8	0.4±0.1 0.3-0.4	1.6±0.0 1.6-1.7	2.4±0.2 2.3-2.6	1.5±0.2 1.3-1.6	2.8±0.3 2.5-3.1
Nb_{ss} bulk	51.4±2.0 49.0-53.3	1.5±0.4 1.1-2.1	23.8±2.6 21.4-26.8	4.4±0.4 4.0-4.8	0.2±0.0 0.1-0.2	12.4±1.5 10.9-13.8	6.3±1.7 4.3-7.9	0.0±0.0 0.0-0.0
Nb_5Si_3 bulk	42.2±0.5 41.6-42.5	30.7±0.4 30.4-31.1	15.9±0.4 15.4-16.2	0.3±0.0 0.3-0.3	1.6±0.0 1.5-1.6	2.2±0.2 2.0-2.4	1.2±0.1 1.1-1.3	5.9±1.3 5.0-7.4
Nb_3Sn bright area	50.9±1.6 47.9-52.4	2.0±1.6 1.0-5.1	8.7±1.7 7.2-12.0	1.3±0.2 1.1-1.6	0.3±0.2 0.1-0.5	11.3±1.0 9.4-11.7	25.5±2.4 21.1-27.8	0.0±0.0 0.0-0.0
Nb_5Si_3 Bright area	40.9±0.2 40.7-41.2	29.4±0.0 29.4-29.5	15.8±0.3 15.4-15.9	0.4±0.0 0.3-0.4	1.5±0.0 1.5-1.6	2.1±0.1 2.0-2.2	1.4±0.1 1.3-1.5	8.5±0.5 8.0-9.0

The oxidation of the two "best" alloys, namely JN1 and JN4, compared with that of the alloys JN2 and JN3 cannot be explained by, or attributed, to only one of the following factors (i) the vol% of the Nb_{ss} in the alloys, as in the as cast condition (which is the starting condition of the specimen oxidised at 1200 °C) the vol% of Nb_{ss} in JN2 was the lowest and the "tendency" was for the vol% of Nb_{ss} to decrease after heat treatment in JN2 and JN3, see Table 5.6, (ii) the absence of Laves phase in JN1 and JN4 as the $NbCr_2$ Laves was also not observed in JN2 and was not stable in JN3, (iii) the "ductile" or brittle behaviour of the Nb_{ss} in the starting microstructure (i.e., the cast condition) as the Nb_{ss} could be expected to be less ductile in the sequence ("ductile") JN4>JN1>JN2/JN3 (brittle) and in the bulk after oxidation in the sequence ("ductile")

JN4>JN1/JN3>JN2 (brittle), (iv) the toughness of the Nb_5Si_3 in the starting microstructure as this silicide was less tough in the sequence JN1>JN3>JN4>JN2 and in the bulk after oxidation in the sequence JN1>JN4>JN2/JN3 and (v) the formation of Sn rich layer at the scale/substrate interface, as such a layer was formed in the alloys JN2, JN3 and JN4 but not in JN1 and the layer was "more continuous" and thicker in JN4 than in JN2 and JN3. It should be noted that Sn rich areas below the scale/substrate interface were observed in JG6 after oxidation at 1200 °C (Geng & Tsakiropoulos 2007).

Furthermore, the chemistry of the alloys was important regarding the role played by specific additions. In JN1 the Hf acted as an effective scavenger of oxygen forming high vol% of HfO2 in the diffusion zone and below it in the Hf rich areas on the starting (as cast) microstructure (i.e., the Hf rich Nb_5Si_3 and the Hf rich Nb_{ss}) and thus "protected" the Nb_{ss} and Nb_5Si_3 in the bulk from contamination by oxygen and embrittlement. The addition of Hf was effective when the oxidation of JN1 is compared with KZ5-HT. In JN4 the absence of W and the increase of Ti content led to a higher solubility of Mo in the Nb_{ss} and thus lowered the oxygen content in the latter (as discussed in the previous chapter) and therefore there was less embrittlement of the microstructure.

7.5   Conclusions

The isothermal oxidation of the alloys JN1, JN2, JN3 and JN4 at 1200 °C in air was studied for 100 h using thermo-gravimetric analysis, a summary of this data can be seen in Figure 7.26. The alloys JN1 and JN4 exhibited best oxidation with parabolic kinetics. The alloys JN2 and JN3 followed linear oxidation kinetics. There was spallation of the scale formed on JN1and JN2, and the alloy JN3 formed a "Maltese cross". In JN3 and JN2 a Sn rich layer formed below the scale/substrate interface, this layer was more continuous and thicker in JN4 and contained Nb_3Sn. The latter intermetallic was also formed in JN3. In all alloys there was a diffusion zone formed below the scale/substrate interface. The chemical compositions of the phases in the oxide scale (when possible), in the diffusion zone, below it and in the bulk were analysed. Ti niobates and a mixed oxide rich in Nb and Si was confirmed by WDS analysis and XRD. It was found that

depending on the alloy composition, the Nb_{ss} and Nb_5Si_3 were contaminated by oxygen and the severity of this effect varied between alloys. The Nb_{ss} was not contaminated by oxygen in the bulk in JN1 and JN4. The Nb_5Si_3 was not contaminated by oxygen in the bulk in JN1. The Nb_3Sn was not contaminated by oxygen in JN4. Various factors that could have contributed to the oxidation behaviour of the alloys were discussed, including consideration of the "ductile" and brittle behaviour of Nb_{ss} and the toughness of Nb_5Si_3 using data from the literature linking these behaviours with specific alloying additions in Nb_{ss} (Cr or Al + Cr) and Nb_5Si_3 (Ti) and the effects of Mo and W on the oxygen content of the Nb_{ss}.
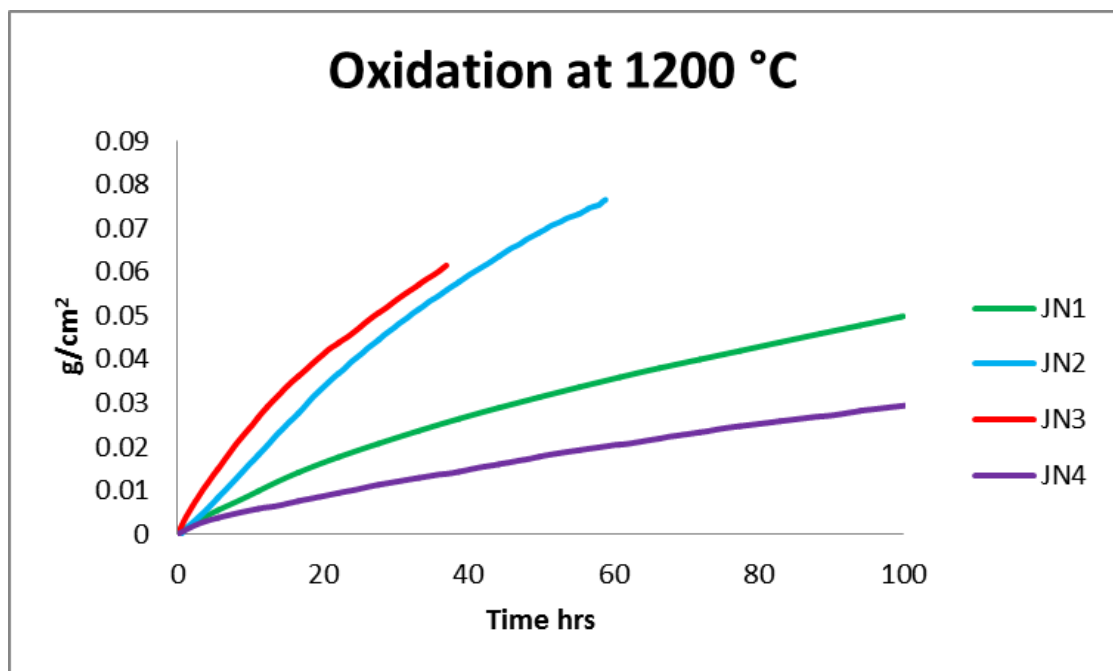
Figure 7.26 Summary of oxidation results at 1200 °C for JN1, 2, 3 and 4.

Nano indentation

8.1　Introduction

Hardness is a "convenient" property for ranking alloys and phases in terms of their "mechanical" behaviour and a useful tool in alloy development as it can point to the effects that alloying elements can (might) have on properties. Measurement of Vickers hardness is based on the measurement of the dimensions of the plastic indentation diagonal. In the nano-indentation technique the hardness (often referred to as nano-hardness, and presented here as nH) and modulus of elasticity are calculated from the load displacement curve that is recorded during indentation. In both methods it is essential to see the microstructure. Measurement of Vickers hardness uses light microscopy to image the microstructure. When a difference in contrast between phases is not strong, differentiation of phases is tricky and results in errors, particularly when more than two phases are involved and their Vickers hardness values do not differ significantly. In nano-indentation, indenting is done on areas selected with the help of atomic force microscopy that gives a topographic image of the surface of the specimen. Differentiating between phases can be easier compared with the use of light microscopy when only two phases are present in the microstructure. However, when three or more phases are present differentiating between them is extremely difficult. Both techniques for measuring hardness cannot provide data about the chemical composition of the indented grain. Nano-indentation was done as described in the experimental 3.10, the elastic modulus of the phases was calculated from the reduced modulus values as described in 3.10

Nano indentation was performed on the alloys to ascertain the effects of alloying on the hardness of Nb_{ss} and Nb_5Si_3. Nano indentation made the study of individual phases possible, regardless of their small size; whilst micro indentation may have been possible in some of the larger silicide grains, the plastic zone would have likely extended beyond the intended area of interest. Whilst nanoindentation was best for this work, compared with micro hardness; it was still not good enough to measure nano-properties of the highly microsegregated, and finer microstructures, such as the eutectics present in the cast alloys. Thus only the HT alloys were studied.

8.2   Nano indentation of JN1-HT

The microstructure of alloy JN1-HT is comprised of, Nb_{ss}, Hf-rich Nb_5Si_3 and Nb_5Si_3. In order to discriminate between phases, the specimen was prepared with an extended polishing duration that gives preferential polishing of the softer Nb_{ss}, leaving the harder silicide phases raised. The imaging system used to image the surface before and after indentation was atomic force microscopy (AFM) which uses height differences in the sample to produce a topographical image. The Hf-rich and "normal" Nb_5Si_3, whilst patently different under BSE imaging were indistinguishable using this method. Attempts were made to find the indents using a high resolution SEM (Inspect F); however this was futile, as the total area of the indent array was 50 μm^2 (slightly larger than a large silicide grain) and the indents were ~ 2 μm across. Considering this problem the hard phases were all treated equally, meaning we could not determine between tetragonal Nb_5Si_3 and hexagonal Nb_5Si_3, an appropriate constant was used for the calculations, however the presence of multiple morphologies is partially responsible for the high standard deviation in Table 8.1. Another cause of the large spread in data is likely to be a composite effect of indent proximity to the grain edge, depth of grain being indented and to a lesser extent the distance of the rastered indent from the centre of the array. Table 8.1 shows the nano hardness in GPa, the corresponding Vickers hardness value and the elastic modulus for each phase. Figure 8.1 shows the AFM image of the indents in JN1-HT; it can be seen that indents clearly lie within individual phases, and on their edges, measurements from the latter area were subsequently discounted.

The results gained in this work are similar in comparison with other work on the nano indentation of Nb silicide based alloys, which gave Hv values for Nb_{ss} and Nb_5Si_3 ranging from 340-700 and 1470-1670 respectively (Yu et al. 2010; Kim et al. 2003; Kim et al. 2004). The hardest Nb_{ss} was in the alloy Nb–18Si–10Mo–10Ti–15W and the alloy with maximum Nb_5Si_3 hardness was the alloy Nb–18Si–5Mo–5Hf (Kim et al. 2004).

Table 8.1 Nano indentation data for JN1-HT

Phase	Nb_{ss}	Nb_5Si_3
Nano hardness Hv	597.4±35.8	1775.3±153.0
	690.8-548.4	2079.5-1490.3
Hardness GPa	5.9	17.4
Elastic modulus	137.6	241.4
	174.0-127.3	284.4-206.1
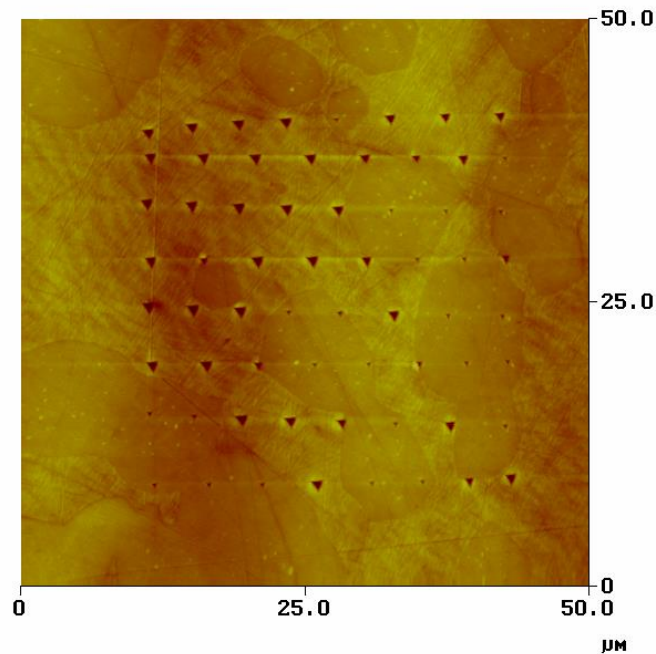
Figure 8.1 AFM image of JN1-HT after nano- indentation.

8.3   Nano indentation of JN2-HT

The microstructure of the alloy JN2-HT, consisted of; Nb_{ss}, Nb_5Si_3 and $NbCr_2$. Unlike JN1-HT however, the phases were not evenly distributed within the alloy, thus allowing an educated separation between possible areas where the Laves phase was present. The individual indents were treated the same as with JN1-HT, separating those indents which lay within the centre of grains and those that lay on their edges. Indents which lay in small raised areas adjacent to large (assumed to be silicide) grains are treated as $NbCr_2$ and also discounted. Table 8.2 shows the nano indentation data for JN2 HT; the addition of refractory metals to the alloy has caused a distinct and expected increase in

the elastic moduli and hardness values of each phase. When compared with other refractory metal containing alloys (Kim et al. 2004) JN2-HT displayed a marked increase in both Nb_{ss} and Nb_5Si_3 nano hardness, with a hardness value of 819.9 Hv and 2025.1 Hv respectively.

Figure 8.2 shows the AFM image of JN2 HT after indentation; the majority of indents which lie in the Nb_5Si_3 grains are close to the centre of the large grains as opposed to the small interdendritic grains. The positioning of the indents at the centre of the grains indicates a high probability that they had likely landed in Nb_5Si_3 rather than $NbCr_2$ Laves phase.

Table 8.2 Nano indentation data for JN2-HT

Phase	Nb_{ss}	Nb_5Si_3
Nano hardness Hv	819.9±38.4	2025.1±83.6
	940.1-763.5	2174.7-1818.8
Hardness GPa	8.0	19.8
Elastic modulus	166.3	290.2
	215.0-153.2	312.8-230.5
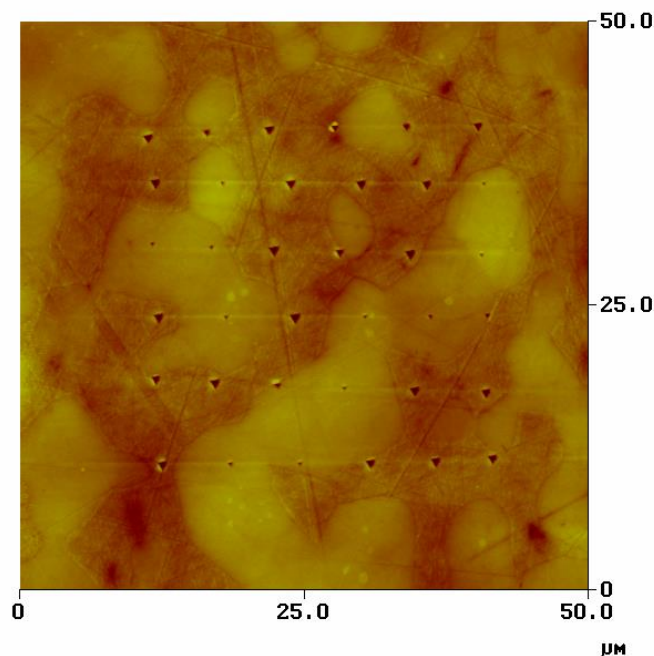
Figure 8.2 AFM image of JN2-HT after nano-indentation.

8.4   Nano indentation of JN3-HT

The microstructure of JN3-HT is comprised of, Nb_{ss} and Nb_5Si_3; this relatively simple microstructure made measurements easier as there was no fear of indenting a wrong phase. An image of the nano-indent positioning can be seen in Figure 8.3. Table 8.3 shows the nano indentation data for JN3 HT; like JN2, the alloy JN3 had a higher Nb_{ss} and Nb_5Si_3 hardness than that of JN1-HT. The Hv value for the Nb_5Si_3 phase was almost identical to that of JN2-HT, 2025.1 and 2005.2 Hv respectively, as both had similar compositions. The nano-hardness of the Nb_{ss} was closer to that of the Nb_{ss} in Nb–18Si–10Mo–10Ti–15W (Kim et al. 2004; Kim et al. 2003).

Table 8.3 Nano indentation data for JN3-HT

Phase	Nb_{ss}	Nb_5Si_3
Nano hardness Hv	725.0±64.6	2005.2±84.0
	885.3-669.5	2156.6-1818.0
Hardness GPa	7.1	19.7
Elastic modulus	153.3	260.4
	277.1-225.2	183.1-131.2
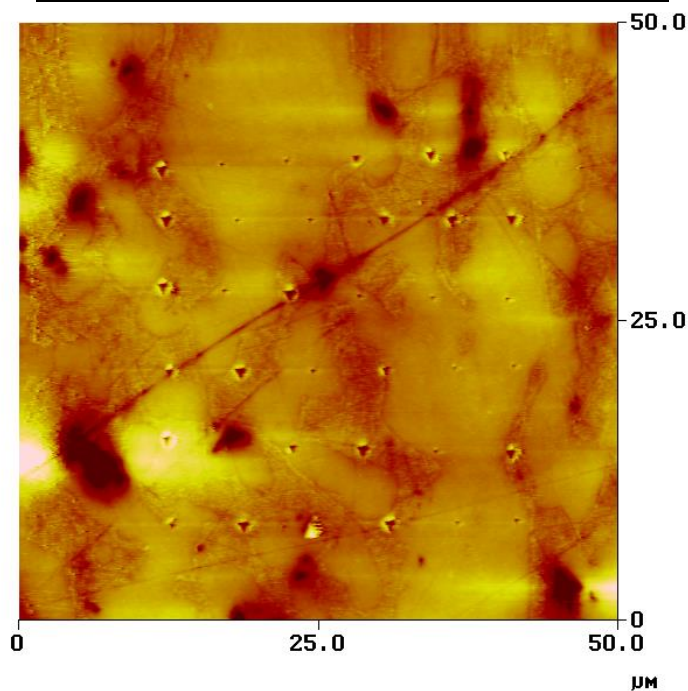
Figure 8.3 AFM image of JN3-HT after nano-indentation

213

8.5   Nano indentation of JN4-HT

The microstructure of JN4-HT comprised of, Nb_{ss}, Nb_5Si_3 and Nb_3Sn, with the latter phase confirmed by x-ray mapping and XRD. Due to the indiscernible nature of Nb_{ss} and Nb_3Sn with regards to BSE imaging and AFM, the alloy was treated as a binary alloy of Nb_{ss} and Nb_5Si_3. An image of a nano-indent array is shown in Figure 8.4, the closest alloys to JN4 HT were JN2 HT and JN3 HT, both had similar elemental addition though JN4 does not contain W. The Nb_{ss} in JN4 had a nano hardness of 825.6 Hv, compared with 819.9 Hv and 725.0 Hv found in JN2 and JN3. The nano hardness of the Nb_5Si_3 is also greater than that in JN2-HT and JN3-HT with a value of 2306.9 Hv.

Table 8.4 Nano indentation data for JN4-HT

Phase	Nb_{ss}	Nb_5Si_3
Nano hardness Hv	825.6±51.3	2306.9±162.6
	903.6-744.8	2545.0-2101.8
Hardness GPa	8.1	22.6
Elastic modulus	170.7	314.7
	189.5-155.6	362.5-247.8
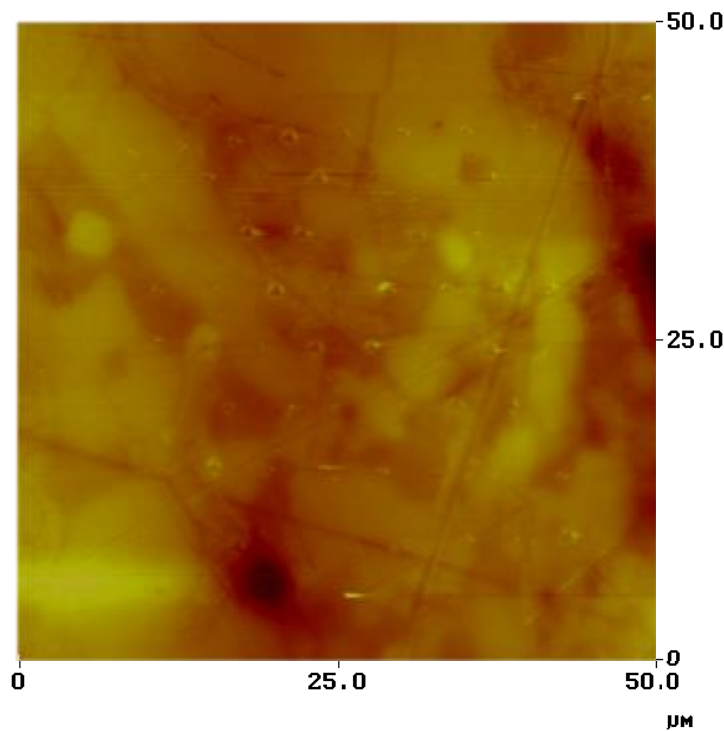
Figure 8.4 AFM image of JN4-HT after nano-indentation

Previous research in the Sheffield group has shown that the nanohardness (nH) values of the Nb_{ss} and Nb_5Si_3 measured in Nb silicide based alloys are different (larger) than the microhardness (mHv) values of the same phases and that this difference is sensitive to alloy system. For the KZ series of Nb silicide based alloys (i.e., Nb-24Ti-18Si based alloys without Sn additions (Zelenitsas & Tsakiropoulos 2006b; Zelenitsas & Tsakiropoulos 2005) and for measurements of nH using the same load as in this research, the relationship for the Nb_{ss} is mHv ≈ 0.68 nH and for the Nb_5Si_3 is mHv ≈ 0.6716 nH (see below). A linear relationship between mHv and nH has also been suggested by Kim et al (Kim et al. 2003).

Previous research in our group has also shown that there is a difference in the nH of both phases with depth below the surface, and that their nH values, up to some critical depth below the surface (which depends on alloy system), can vary compared with their values in the bulk of the alloy, these variations can be lower and/or higher compared with the area. Such variations in nH with depth below the surface have been attributed to contamination of both phases by interstitials, which is consistent with the WDS results for Nb_{ss} and Nb_5Si_3 discussed in the previous chapter for the oxidised alloys, and to slight variations in solute concentrations.

The nano-hardness values for the Nb_{ss}, in the heat treated alloys of this research, are consistent with solid solution hardening of Nb, when compared with published values for the hardness of "pure" Nb. In the alloys of this research, the solid solution hardening of Nb is attributed to interstitials in solid solution as well as the transition (including refractory) metal (i.e., Cr, Hf, Mo, Ti, W) and simple metal (i.e., Al, Si, Sn) alloying additions. The presence of the former (i.e., interstitials), even though it was not confirmed for the cast and heat treated alloys by the analysis method used in this research (WDS), is possible as the elements used to make the alloys were not of the highest possible purity (in other words interstitials were in solution in the starting elemental charges) and interstitial pick up cannot be avoided during alloy making and heat treatment. The presence of the latter was confirmed by the analyses of the Nb_{ss} in the cast and heat treated alloys.

The effect of interstitials such as oxygen and nitrogen individually or in synergy on the critical resolved shear strength (CRSS) of Nb single crystals has been studied. Changes in the CRSS were attributed to changes in the total concentration of solute(s)

as a result of specimen preparation (a common "problem" in many studies on Nb alloys) or, for the cases where contamination from specimen preparation was avoided, to interactions of solute atoms changing the number, effectiveness and spatial distribution of obstacles to the motion of dislocations (Gibala & Mitchell 1973).

The nano-indentation technique is more sensitive to the surface condition of the specimen than the measurement of microhardness. Studies of the CRSS of very high purity Nb single crystals with < 160 nm Nb_2O_5 surface films have confirmed that at room temperature the oxide films caused hardening (Sethi & Gibala 1977), in other words the mechanism of flow in Nb was altered by the presence of the surface film. The specimens used for nano-indentation were prepared using mechanical polishing. The latter can work harden the near surface areas of the alloy, which would lead to overestimation of the hardness of phase(s).

In the nano-indentation technique the depth of phase below the surface is not known and thus "shallow" indents might be "sampling" the properties of the underlying phase. Thus, even when a compromise is made for the surface roughness of the specimen, to have shallow indents to measure only single phase properties, we are not sure if the latter is indeed the case. This is particularly important when $NbCr_2$ and Nb_3Sn are present in the microstructure, as the microhardness values of these intermetallics are 790 to 970 Hv for the unalloyed Laves and ~ 1350 Hv for ~ 5 at% and 1300 Hv for 10 at% ≤ Hf ≤ 15 at% for $(Nb, Hf)Cr_2$ and 940 Hv for $Nb_3(Sn, Si)$ and 640 Hv for $(Nb, Ti)_3(Sn, Si)$ (Tsakiropoulos & Vellios 2009). These values are not significantly different from those of the Nb_{ss} and Nb_5Si_3 in some alloys. Furthermore the microhardness of HfO_2 is ~ 1760 Hv (Tsakiropoulos & Vellios 2009). Nano-indentation of a single grain of a phase might not give the properties only of the indented grain when the surrounding phase is softer as there will be an elastic component from the phase below.

The diffusivity of oxygen in Nb has been studied in recent years and in the past. (De Almeida et al. 2005; Ciovati 2006; Powers & Doyle 1959). For temperatures in the range 300 K to 485 K the newest diffusion distance of oxygen is about 200 to 300 nm, depending on the diffusivity value used to calculate $x = 2.4 \, (Dt)^{1/2}$. Older data gives $x \approx$ 23 nm for 150 °C. It is concluded that in the solid solution hardening represented by

the nH values reported for the Nb_{ss} in the alloys of this research, there are contributions arising from:

i.   Interstitial contamination during specimen preparation (meaning melting, casting, heat treatment, and possibly during cutting and polishing).

ii. Interactions of interstitials (O-O, O-N, N-N) in the solid solution.

iii. The thin surface oxide on the tested specimens. These are not the only contributions however, as we now need to consider the effects of transition metals (including refractory metals) on solid solution hardening.

The results for the heat treated microstructures of the alloys of this research showed that changes had occurred in the compositions of the Nb_{ss} after the heat treatment that resulted to the "homogenisation" of the solid solution (in JN1 there were Hf-rich areas in the Nb_{ss} in the cast alloy, 3 types of solid solution in the cast microstructure of JN2, Ti-rich areas in the Nb_{ss} in the cast JN3 and only one type of Nb_{ss} (the "normal" Nb_{ss}) after the heat treatment). The word homogenisation is within inverted commas to indicate that the data presented in this thesis can neither prove nor disprove the existence or absence of "clusters" of solutes in the Nb_{ss}. The "homogenisation" of the solid solution occurred because of the diffusion of solutes at 1500 °C. For example, regarding the diffusion of Mo or W or Ti in Nb at 1500 °C (the heat treatment temperature), the diffusivity data in Liu et al (Liu et al. 2012; Liu et al. 2013) (Liu et al. 2009) gives diffusion distances of about 4.5, 14.5 and 26 μm, respectively (the self-diffusion distance of Nb at the same temperature is ~ 14.5 μm (with the data in (Guthoff et al. 1994)) or 17 μm (with the data in (Resnick & Castleman 1961)), and the diffusion distance of Nb in Nb-25Ti (at%) solid solution is about 80 μm (Pontau & Lazarus 1979). The diffusion distance of Cr in Nb at 1500 °C is ≈ 56 μm (calculated using bulk diffusion data in (Li & Chou 1996). Furthermore, using data for diffusion of Al in Nb from Ogurtani (which should be considered questionable) the diffusion distance of Al in Nb at 1500 °C is about 11.5 cm (Ogurtani 1972).

Even though the hardness of solid solutions of Nb with interstitials and substitutional additions has been studied by different groups in the last 60 years, much less attention has been paid to the Nb_5Si_3 silicide. The research in our group has shown that:

   i.   The hardness of cast unalloyed Nb_5Si_3 is ~ 1360 Hv, (2) that Ti in solid solution decreases the hardness and that the latter increases as the concentration of Ti in $(Nb,Ti)_5Si_3$ decreases.

   ii.   Cr does not have a strong effect on the hardness of Nb_5Si_3 and the latter increases with Cr concentration in $(Nb,Cr)_5Si_3$.

   iii.   The hardness of Nb_5Si_3 increases with the Al concentration.

   iv.   Mo increases the hardness of Nb_5Si_3.

   v.   Sn has a very weak effect on the hardness of Nb_5Si_3.

   vi.   Hf in solid solution decreases the hardness and that the latter increases as the concentration of Hf in $(Nb,Ti)_5Si_3$ decreases.

The microhardness and nano-indentation hardness (nano-hardness) values of the Nb_{ss} in the alloy KZ5 (=Nb-24Ti-18Si-5Al-5Cr) have been measured. The data gives nH = 685, mHv = 466 and mHv = 0.6803 nH. Using the latter and the nano-hardness for Nb_{ss} in JN1-HT we get mHv ≈ 406, in other words the addition of Hf in JN1 resulted in a decrease in micro-hardness of 60 Hv or ~ 27 Hv per at% Hf in the Nb_{ss}. This would suggest that the synergy of Ti and Hf with Al and Cr in JN1 "softened" the solid solution.

The microhardness of the Nb_{ss} in the alloy EZ8 (=Nb-24Ti-18Si-5Al-5Cr-5Hf-5Sn) has also been measured. The data gives mHv = 677, which, when it is compared with the mHv of Nb_{ss} in JN1-HT (see above), suggests (a) that the addition of Sn in EZ8 increase the hardness of the Nb_{ss} by ~ 271 Hv or ~ 54 Hv per at% Sn and (b) that the synergy of Ti and Hf with Al, Cr and Sn has a strong hardening effect.

The microhardness and nano-indentation hardness (nano-hardness) values of the Nb_5Si_3 in the alloy KZ5 (=Nb-24Ti-18Si-5Al-5Cr) have also been measured. The data gives nH = 1684, mHv = 1131 and mHv = 0.6716 nH. Using the latter and the nano-hardness of Nb_5Si_3 in JN1-HT we get mHv ≈ 1192, in other words the addition of Hf in JN1 increased the hardness of Nb_5Si_3 by 62 Hv, which would suggest a weak hardening effect for Hf in $(Nb,Ti,Hf,Cr)_5(Si,Al)_3$.

The microhardness of Nb_5Si_3 in the alloy EZ8 was 1150 Hv. Comparison with the data for Nb_5Si_3 in JN1-HT would suggest a "softening" of the $(Nb,Ti,Cr,Hf)_5(Si,Al,Sn)_3$

by Sn. However, the difference of ~ 40 Hv between the two values is within the error of this type of measurement. This result is in agreement with the "conclusion" (vi) above. The difference between the nano-hardness values of the Nbss in JN2-HT and JN3-HT confirmed the solid solution strengthening effect of Cr. However, the difference between the nano-hardness values of the Nb_5Si_3 in JN2-HT and JN3-HT was significantly smaller owing to the weak effect of Cr on the hardness of Nb_5Si_3 (see "conclusion" (iii) above).

The nano-hardness of the Nb_{ss} in JN4 was essentially the same as in JN2. It is suggested that the loss of the solid solution hardening effects of Cr and W (lower Cr content and no W in the Nb_{ss} in JN4) was "balanced" by the actual Ti and Mo contents that were higher in the Nb_{ss} in JN4, even though the Ti/Mo ratio was essentially the same in the Nb_{ss} in JN2-HT and JN4-HT.

In the Nb-18Si-5Mo-5Hf alloy the microhardness of $(Nb,Mo,Hf)_5Si_3$ was 1610 Hv, which is higher than the microhardness of Nb_5Si_3 in JN2 and JN3, 1360 Hv and 1347, respectively, but much closer to that in JN4 (1549 Hv), which would suggest that the synergy of Mo and W "softens" the 5-3 silicide.

Data for the moduli of elasticity for the alloy KZ5-HT gave the average values E_{Nbss} = 141.4 GPa and E_{Nb5Si3} = 285.1 Gpa (Tsakiropoulos & Singh sethi 2012). Comparison of this data with that for the average values of the moduli of elasticity of the Nb_{ss} and Nb_5Si_3 in JN1-HT (see Table 8.1) would suggest that alloying of both phases with Hf resulted to a reduction of their elastic moduli. This is the _first time_ that such data has become available regarding the effect of Hf on the Young's modulus of $(Nb,Si,Ti,Cr.Al,Hf)_{ss}$ and $(Nb,Ti,Hf,Cr)_5(Si,Al)_3$.

The average values of the moduli of elasticity of the Nb_5Si_3 in JN2-HT and JN3-HT were significantly higher than those in JN1-HT and the average value for JN2-HT was higher than that for JN3-HT. Considering the chemical compositions of the Nb_5Si_3 in JN2-HT and JN3-HT (see Table 8.2, Table 8.3 and Table 8.4), the data would suggest that the synergy of Mo and W with Cr, Hf, Sn and Ti in the Nb_5Si_3 in JN2-HT had a stronger effect on the elastic modulus, probably because of the slightly higher concentrations of Cr, Mo and W in the Nb_5Si_3 in JN2-HT compared with JN3-HT. The significantly higher elastic modulus of Nb_5Si_3 in JN4-HT would suggest (a) that Mo has

a very strong effect on the elastic modulus of Nb_5Si_3 and (b) that this effect is compromised by synergy of Mo and W with Cr, Hf, Sn and Ti.

The higher average values of the elastic moduli of the Nb_{ss} in JN2-HT, JN3-HT and JN4-HT compared with that in JN1-HT would suggest a strong effect of the synergies of the alloying elements in the former three alloys on the Young's modulus of the Nb_{ss}. The higher elastic modulus of the Nb_{ss} in JN2-HT compared with that in JN3-HT is attributed to the higher Cr and W contents of these elements in the Nb_{ss} in the former alloy. The even higher elastic modulus of the Nb_{ss} in JN4-HT would suggest (i) that Mo has a strong effect on the elastic modulus and (ii) that the synergy of Mo with Sn and Ti also has a strong effect on the same property.

8.6   Conclusions

Nano-indentation was used to measure the hardness and elastic moduli of Nb_{ss} and Nb_5Si_3 in the alloys JN1, JN2, JN3 and JN4 in their heat treated condition (1500 °C for 100 h). The results would suggest that:

  i.   The synergy of Ti and Hf with Al and Cr in JN1 "softened" the solid solution.
 ii.   A weak hardening effect for Hf in $(Nb,Ti,Hf,Cr)_5(Si,Al)_3$.
iii.   The synergy of Mo and W "softens" the 5-3 silicide.
 iv.   Alloying of Nb_{ss} and Nb_5Si_3 with Hf results in a reduction of elastic moduli.
  v.   Mo has a very strong effect on the elastic modulus of Nb_5Si_3 and this effect is compromised by synergy of Mo and W with Cr, Hf, Sn and Ti.
 vi.   Mo has a strong effect on the elastic modulus of the Nbss as does the synergy of Mo with Sn and Ti.

Fracture toughness

9.1   Introduction

This chapter presents the results of a preliminary study (see below) of the fracture toughness of Nb silicide based alloys considered in this research. In the literature there is significant volume of work on the fracture toughness of "simple" alloys (binary Nb-Si alloys (Sekido et al. 2006), ternary and quaternary alloys, for example ternary Nb-Ti-Si alloys (Sekido et al. 2006; Li & Peng 2007), and quaternary Nb-Ti-Si-Al alloys (Murayama & Hanada 2002), Nb-Si-Mo-W alloys (Sha, H. Hirai, et al. 2003; Sha, Hisatoshi Hirai, et al. 2003; Kim & Tanaka 2002) and Nb-Si-Mo-Hf alloys (Kim et al. 2004) and significantly less work on the toughness of more "complex" alloys e.g. Nb-Ti-Si-Cr-Al- Hf-Ta (Tian et al. 2009) .

In the literature, "simple" binary, ternary and quaternary alloys and higher order alloys were studied to establish effects of alloying and/or processing (liquid route (AM, DS, OFZ), PM, thermo-mechanical processing (extrusion, HIP, forging), heat treatment (including environmental embrittlement) and loading rate on toughness. For example, it has been shown that "directionally" solidified alloys using OFZ have better toughness than AM alloys (Sekido et al. 2006), post solidification processing (Liu et al. 2010) improves toughness and that the latter can be sensitive to loading rate (Lewandowski & Rigney 1996b). Furthermore, alloys near eutectic compositions have improved fracture toughness (Kim et al. 2001).

Data about the fracture toughness of alloys based on the Nb-Ti-Si-Al-Cr-Hf system with $16 < \text{Si} < 20$ at%, $15 < \text{Ti} < 25$ at%, Hf < 8 at%, Al ≤ 6 at%, Cr ≤ 6 at% (i.e., the "basis" for developing Nb silicide based alloys with the potential to offer a balance of mechanical and environmental properties) is not easy to find, with the exception of toughness data (K_Q) for the MASC alloy, the composition of which is given in GE literatures as Nb-23Ti-16Si-8Hf-2Al-2Cr-xSn (+ sp elements). However, references to the toughness of MASC deliberately (?) ignore to mention if the alloy(s) studied had additions of Sn and other sp elements, for example Ge, and toughness data is given for the composition Nb-24.7Ti-16Si-8.2Hf-2Cr-1.9Al, for which the volume fraction of Nb_{ss} in the cast alloy is ~ 0.47 %. Data about the microstructure of MASC

has also been scarce, for example it is not clear whether the Nb_3Si is stable in its microstructure of this alloy or what the structure(s) of the Nb_5Si_3 (tetragonal and/or hexagonal given the high Hf concentration) is/are. In MASC type alloys eutectic microstructures are promoted by higher Al and Cr contents and result in improved strength.

The original objectives of the study of toughness of Nb silicide based alloys in this research were (a) to study the toughness of the "base" composition without Hf (i.e., the toughness of an alloy of composition as close as possible to that of the alloy KZ5 (Nb-24Ti-18Si-5Al-5Cr), this alloy will be called KZ5 (jn) in this chapter) (Zelenitsas & Tsakiropoulos 2005), (b) to consider the toughness of cast MASC (Nb-24.7Ti-16Si-8.2Hf-2Cr-1.9Al) ($18.2 < K_Q < 23.3$ MPa√m) as "indicative" of the toughness of alloys similar to JN1, (c) to study the toughness of an alloy with Ti+Hf the same as the concentration of Ti in KZ5 ($\approx$24 at%), with the ratio Si/(Al+Cr+Hf) the same as in MASC ($\approx$1.3) and with Al and Cr content as close to those in KZ5 as possible but with Ti/Hf ratio higher than that in MASC ($\approx$3.13) (to ensure formation of hexagonal and tetragonal Nb_5Si_3 in the microstructure), and select the composition Nb-19Ti-18Si-4Al-4.5Cr-5Hf (which in this chapter will be called alloy JN5) and (d) to study the toughness of the alloys JN1, JN2, JN3 and JN4 of this study, with the alloy JN4 being the priority owing to its superior oxidation behaviour.

The evaluation of the toughness was to be made according to ASTM E399 and the British standards for three point bend fracture toughness, see section 3.11 in the experimental chapter. This required "large" ingots to be available so that defect free (i.e., crack free and, as far as we could judge, porosity free) toughness specimens could be prepared (pre-existing cracks in silicide grains from processing are not unusual in Nb silicide based alloys, e.g. (Liu et al. 2010). As forging, HIP or extrusion facilities were not available in house and elsewhere in the UK (a serious handicap for ultra-high temperature alloy development) specimens of the cast alloys had to be used. Casting of "large" ingots in house was not possible because existing facilities were out of action for considerable length of time. An external facility was able to provide two cast alloys in 600 g ingots prepared using cold hearth (water cooled copper crucible) plasma melting. Thus, it was decided to modify the original objective and instead (new objective) concentrate the effort on the alloys KZ5 (jn) and JN5 (see above) and leave

the study of the toughness of JN4 (best in terms of oxidation behaviour, see section 6.4 and 0) to be done in the future. This "strategy" was the best for the time available.

9.2   Alloys KZ5 (jn) and JN5 results

The 600 g ingots were observed to crack as the melt solidified in the cold hearth after the plasma was switched off. The difference between the CTE values of unalloyed Nb and Nb_5Si_3 is $1X10^{-6}$/K, the tetragonal Nb_5Si_3 exhibits anisotropy of elastic moduli, which is more severe for βNb_5Si_3, alloying changes the CTE and moduli of each phase, including γNb_5Si_3. The cracking of the ingots upon cooling, which has been observed in alloys based on other Nb-Ti-Si based systems, was thus attributed to residual stresses due to differences in CTE and moduli of elasticity.

The cracking of the ingots meant that less useful material was available for preparing specimens for fracture toughness experiments. Because of the susceptibility to cracking of the cast alloys, the notches were not fatigue cracked prior to testing. The toughness values obtained from the tests were not true K_{IC} values but instead were K_Q values. It should be noted that most of the available literature on the fracture toughness of Nb silicide based alloys report K_Q values as obtained from specimens prepared as in this work (Kim et al. 2002; Tian et al. 2009; Yu et al. 2010).

Table 9.1 gives the large area analyses of the cast alloys KZ5 (jn) and JN5 prepared in this research. The actual Si and Ti contents of KZ5 (jn) was essentially the same as in KZ5-AC and the Al and Cr concentrations were slightly lower (Zelenitsas & Tsakiropoulos 2005). In JN5 the Ti+Hf (23.4 at%), Si/(Al+Cr+Hf) (1.2 at%) were close to the designed values, 24 at% and 1.3, respectively. Macrosegregation of Si was not strong in KZ5 (jn) and JN5.

Table 9.1 composition of 600 g ingot for fracture toughness testing (at%)

Alloy	Nb	Si	Ti	Cr	Al	Hf
KZ5	49.0±0.3	16.2±0.6	25.8±0.5	5.0±0.2	4.0±0.2	-
	48.5-49.4	15.4-17.1	25.2-26.4	4.7-5.2	3.7-4.3	-
JN5	48.0±0.8	18.1±0.4	18.3±0.4	4.8±0.1	5.7±1.2	5.1±1.2
	47.3-48.9	17.8-18.6	18.1-18.8	4.7-5.0	4.3-6.4	4.2-6.5

The XRD data for the cast alloys is shown in Figure 9.1. The figure shows powder diffractograms, the powders were produced by crushing pieces of the ingot of each alloy. The XRD data was fitted using Sieve+ software. The data shows that the microstructure of KZ5-AC (jn) consisted of Nb_{ss} and βNb_5Si_3, which is in agreement with (Zelenitsas & Tsakiropoulos 2005). The microstructure of JN5-AC consisted of Nb_{ss} and Nb_5Si_3 (as required by alloy design) and the evidence was that the latter was present in its tetragonal and hexagonal forms (as required by alloy design).
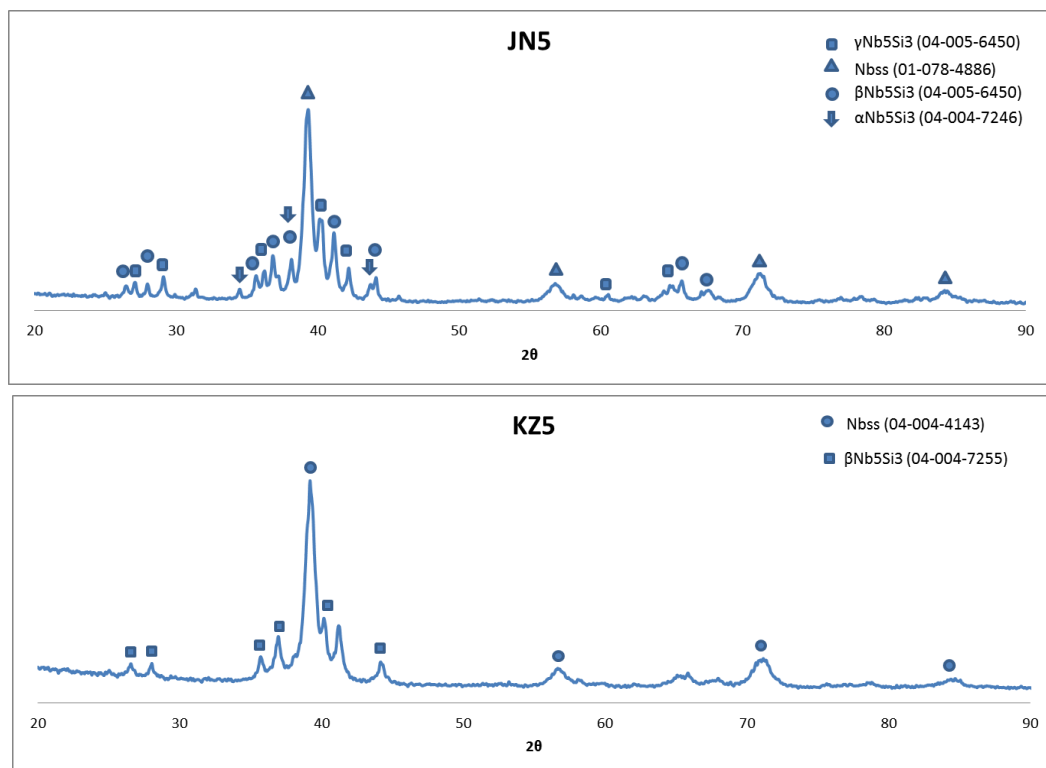
Figure 9.1 Powder X-ray difractograms for KZ5 and JN5 fitted using Sieve+ software.

The K_Q values of KZ5 (jn) and JN5 can be seen in Table 9.2 and were 21.3 and 19.7 MPa√m respectively, this was in the range ($18.2 < K_Q < 23.3$ MPa√m) reported for cast MASC alloy.

Table 9.2 K_Q values for JN5, KZ5 and MASC alloys

Alloy	KZ5	JN5	MASC
Fracture toughness (K_Q) $MPa\sqrt{m}$	21.27	19.69	18.2 - 23.3

Figure 9.2 (a) shows the crack path in KZ5 (jn) and (b) a close up image of the microstructure at the crack initiation point. The image displays branching at the point of crack emanation; however the branching crack terminates in the Nb_{ss}. The crack path continues to travel through the eutectic region adjacent to the βNb_5Si_3 grains. As well as the inter-granular fractures within the eutectic, there are also trans-granular fractures across the larger silicide grains with further evidence of crack branching within these silicides. In Figure 9.2 (a), evidence of crack deflection can be seen with the crack tip hitting a eutectic region with a high area of Nb_{ss}. At this point the crack branches and is arrested by surrounding Nb_{ss}, it is ultimately deflected around the eutectic region and down the silicide-Nb_{ss} interface of a nearby large silicide grain. Figure 9.2 (b) also displays crack bridging after the region of deflection with the Nb_{ss} forming a ligament across the fracture path.

(a)
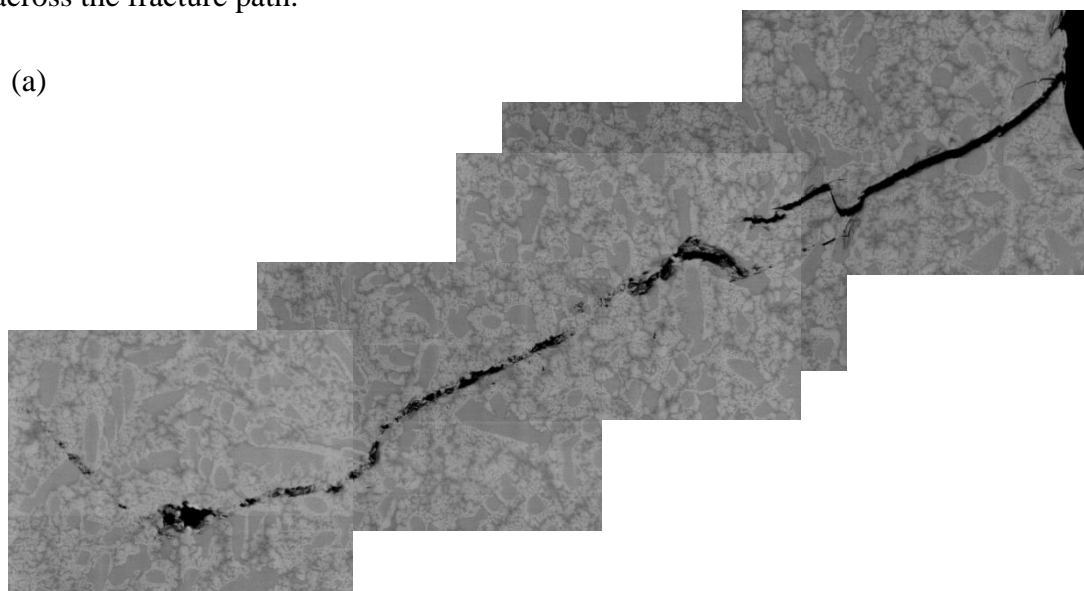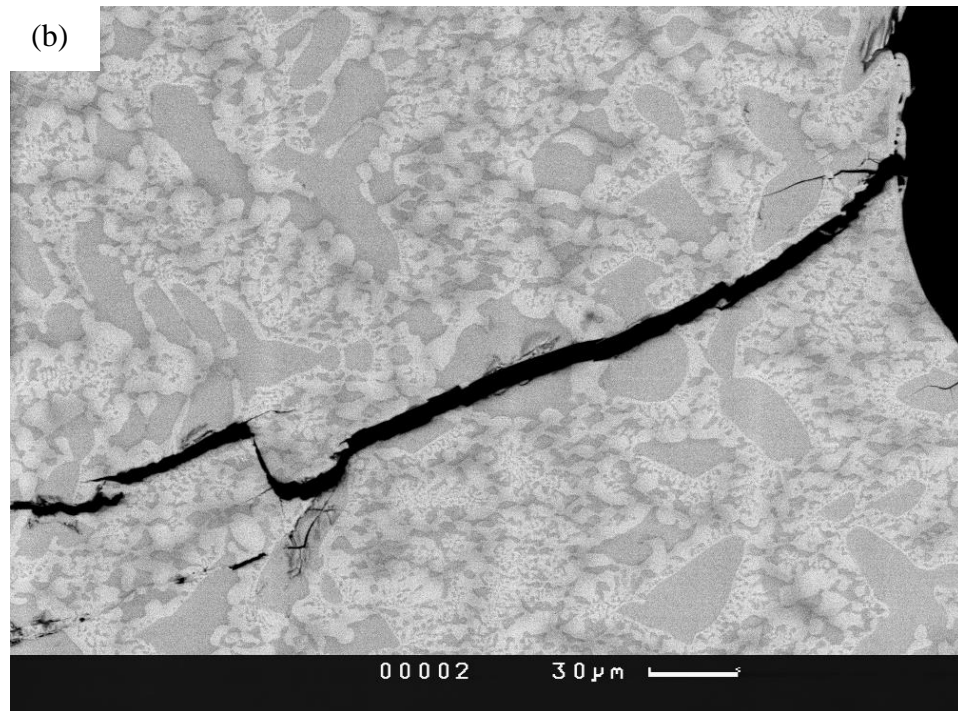
Figure 9.2 BSE images of the fracture path of KZ5 AC

Figure 9.3 shows the crack path in JN5, it displays traits of a more brittle material. The crack initiates in an Hf rich γNb_5Si_3 grain and continues to propagate through the adjacent Nb_5Si_3 and Nb_{ss} phases. With a complex microstructure comparable with that of JN1-AC, it can be seen that the crack path is much more erratic than that seen in KZ5 (jn) which displays a constant crack direction. Due to the high number of intersecting silicide grains and the lack of a "definitive" solid solution (see JN1-AC), the crack path shows much more branching as it meanders through the more closely spaced silicide regions. Ultimately the ability for the relatively ductile Nb_{ss} to provide crack arrest is essential towards the fracture toughness of these alloys.
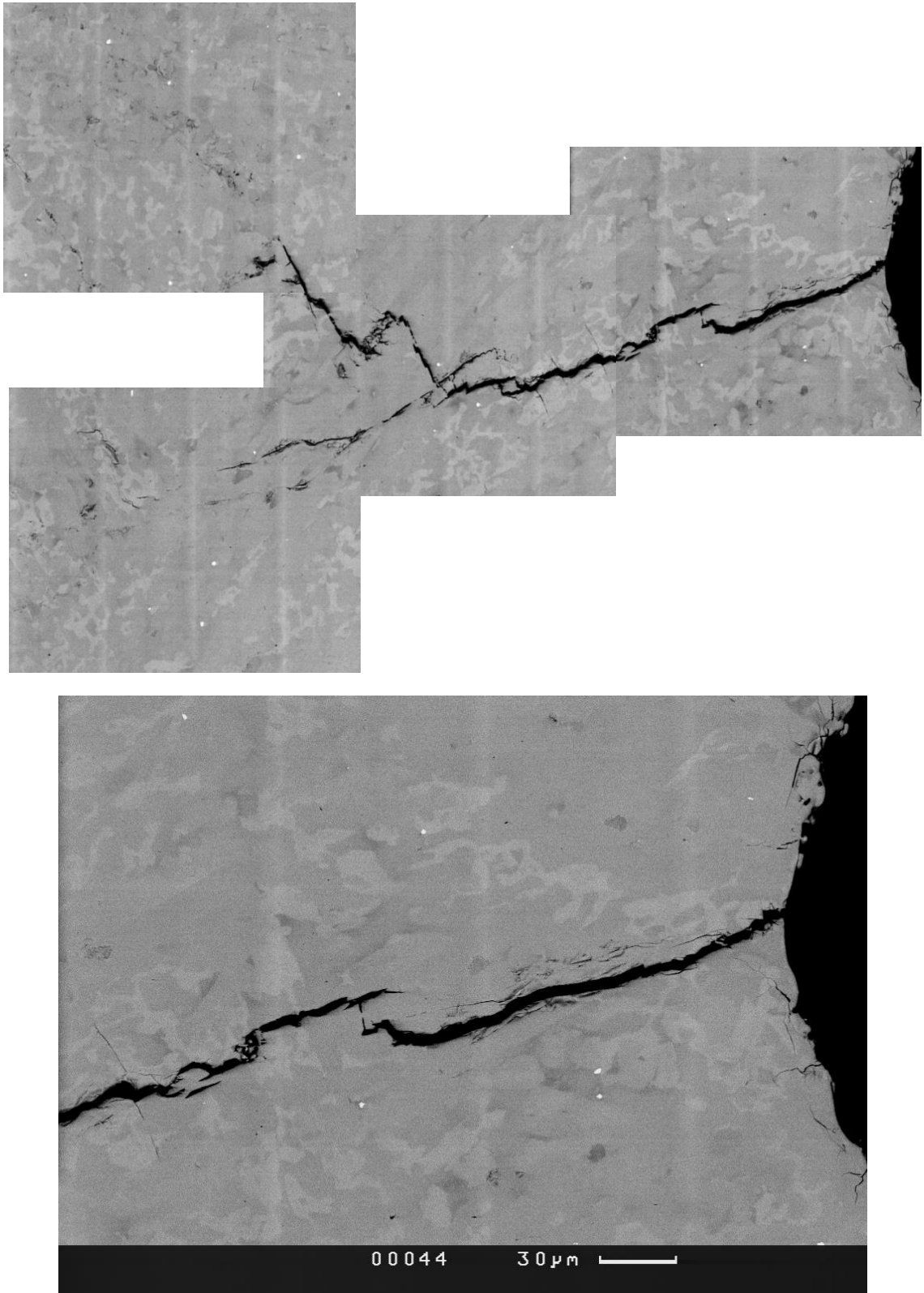
Figure 9.3 BSE images of the fracture path of JN5 AC

9.3   Discussion

Nb_5Si_3 fractures showing cleavage like features, large Nb grains fracture in a cleavage like mode and small Nb_{ss} grains in lamellar (eutectic or eutectoid) microstructures can exhibit ductile rupture (Chan 2002a; Davidson & Chan 1999). In the literature there is plenty of evidence that in Nb silicide based alloys crack tip blunting, crack deflection, micro-crack re-nucleation (i.e., micro-cracking ahead of the main crack), shear ligament formation and crack bridging by ductile Nb grains can be mechanisms responsible for toughening (Chan 2002a). Evidence for these mechanisms was found in the crack paths in both alloys of this study, for example Figure 9.2 and Figure 9.3 show that the crack was bridged by Nb_{ss} in the eutectic. This is in agreement with Li et al (Li & Peng 2007) The morphology of the ductile phase that provides extrinsic toughening to low intrinsic toughness intermetallics (like Nb_5Si_3 that has intrinsic toughness ~ 3 MPa√m) with crack tip shielding mechanisms described above is also important. For example, Bloyer et al (Bloyer et al. 1998) showed that high aspect ratio Nb improved the fracture of the low toughness Nb_3Al (~ 1 MPa√m) in Nb/Nb_3Al laminates with 20 vol% Nb. The improvement was significantly higher than that seen in particulate Nb/Nb_3Al with 40 vol% Nb. This would suggest that lower volume fraction of large ductile phase grains is required to increase the toughness compared with fine grains.

The toughening mechanisms discussed above cannot be quantified using the "data" about the crack paths in Figure 9.2 and Figure 9.3. Given that crack bridging by ductile Nb grains has been observed we can deduce the toughness of the alloys from Equation 8 and Equation 9 which are essentially the same equation (Mataga 1989) and Equation 8 is often used [e.g. (Subramanian et al. 1994)] as a "simpler" version to calculate a lower value of K_C, owing to lack of data about the Poisson ratio of the Nb_{ss} and Nb_5Si_3.

Equation 8

$$KC = \sqrt{\left[EC\,(1 - Vf)\,K^2m/Em\right] + \chi VfEC\sigma o\alpha o}$$

Equation 9

$$K_C = \sqrt{[E_C (1 - v^2_m) (1 - V_f) K^2_m/(1 - v^2_C) E_m] + \chi V_f E_C \sigma_o \alpha_o/(1 - v^2_C)}$$

where K_C is the alloy (in situ composite) fracture toughness, K_M is the fracture toughness of the Nb_5Si_3, E_C and E_M are the Young's moduli of the alloy (in situ composite) and Nb_5Si_3, v_C and v_m are the Poisson's ratios of the alloy (in situ composite) and Nb_5Si_3, V_f is the volume fraction of the Nb_{ss}, σ_o and α_o are the yield strength and the "radius" of Nb_{ss} grains and χ is a parameter "representing" the constraint of the Nb_{ss} by the Nb_5Si_3 (meaning χ is linked with the work of rupture of the Nb_{ss} (ductile phase) that is deformed and fractures under the constraint that is imposed on it by the surrounding Nb_5Si_3). The value of χ depends on the material (meaning it is specific to composite system) and usually $0.73 < \chi < 7.2$. For the Nb silicide based alloys (also known as Nb in situ composites) the values of $\chi = 1.6$ (Subramanian et al. 1994) and $\chi = 1.75$ (Kim et al. 2004) have been used.

As we have data for the volume fractions of phases in the alloys of this study and in KZ5 and data for the hardness and elastic moduli of Nb_{ss} and Nb_5Si_3 in the same alloys in the heat treated condition (see previous chapter) the Equation 8 and Equation 9 were used to calculate K_C values of the alloys JN1, JN2, JN3, JN4 and KZ5. The values of the parameters in Equation 8 and Equation 9 and the calculated fracture toughness values are given in Table 9.3. The calculated values for the indicated alloys are higher than those reported for simpler Nb-Ti-Si-Al alloys [(Subramanian et al. 1994)] and significantly higher than those for Nb-Si-Mo-Hf alloys (Kim et al. 2004). The K_C value for JN4-HT would suggest "exceptional" fracture toughness for this alloy, which also exhibited very good oxidation resistance. This is worth further investigation to verify the result of the simple calculation described above.

The calculated K_C values are not very sensitive to the chosen value for K_M (fracture toughness of alloyed Nb_5Si_3). For example, if the calculation for JN1-HT were to be repeated for K_M values 7.8 and 3 MPa√m the calculated K_C values are 26 and 25.5 MPa√m, respectively. However, the K_C values are very sensitive to the size of the Nb_{ss} grains. For example, if the calculation for JN1-HT were to be repeated for $2\alpha_o$ values of 20 μm and 5 μm the calculated K_C values are 36.4 and 18.8 MPa√m, respectively. This

is consistent with the conclusions of the work of Bloyer et al (Bloyer et al. 1998) reported above.

The higher calculated K_C value for the alloy JN3 (31.6 MPa√m) compared with that of JN2 (23.1 MPa√m) is attributed also to the higher toughness of the Nb_{ss} in the former alloy. Indeed, using the data for Mo and W concentrations in the Nb_{ss} in JN3-HT and JN2-HT and the data in figure 2 in (Fujikura et al. 2004) we get $K_Q^{NbssJN2}$= 12.5 MPa√m and $K_Q^{NbssJN3}$= 15 MPa√m.

The calculated K_C value for the alloy KZ5-HT was 28.7 MPa√m and its dependence on the grain size of Nb_{ss} shows that it increases to 40.2 MPa√m for $2\alpha_o = 20$ μm and decreases to 25, 20.7 and 13.8 MPa√m for $2\alpha_o$ of 7.5, 5 and 2 μm, respectively. The average of the latter three values is 19.8 MPa√m for an average grain size $2\alpha_o = 4.8$ μm, which is very close to the measured K_Q for KZ5 (jn).

In the microstructure of KZ5(jn) there was Nb/Nb_5Si_3 eutectic between the primary Nb_5Si_3 grains, the same as in KZ5-AC. Figure 1.2 shows that the crack encountered Nbss grains of different sizes as it moved in and out of areas of Nb/Nb_5Si_3 eutectic. Thus, it is suggested that the measured K_Q for KZ5(jn) can be attributed to Nbss grains of different size bridging the crack as it propagated in the alloy and to the presence of fine eutectic in its microstructure (see above).

We do not have data for the hardness and elastic moduli of phases in JN5. If we were to assume that the properties of the Nb_{ss} and Nb_5Si_3 in JN5 were the same as in JN1-HT, the calculation for $2\alpha_o = 5$ μm (which is the "average" size of the Nb_{ss} in the alloy) gives $K_C = 18.8$ MPa√m, which is very close to the measured K_Q for JN5 and falls within the range of reported toughness values for MASC (see above). Thus, it is suggested that the measured K_Q for JN5 can also be attributed to Nb_{ss} grains of different size bridging the crack as it propagated in the alloy and to the presence of fine eutectic in its microstructure (see above).

Solving Equation 9 for $\sigma_o \alpha_o \chi$ and using the measured K_Q value for the alloy KZ5(jn) for the value of K_C and the data for KZ5 in Table 9.3 we get $\sigma_o \alpha_o \chi \approx 4227$ J/m^2 i.e., the Nb_{ss} exhibits 4227 J per unit area as the work of fracture of the alloy (in situ composite). For $2\alpha_o = 4.8$ μm and $\sigma_o = 1118.4$ MPa we get $\chi = 1.56$. Repeating the same calculation using the measured K_Q value for the alloy JN5 for the value of K_C and

the data for JN1 in Table 9.3 we get $\sigma_o\alpha_o\chi \approx 3828$ J/m^2 i.e., the Nb$_{ss}$ exhibits 3828 J per unit area as the work of fracture of the alloy (in situ composite). For $2\alpha_o = 5$ μm and $\sigma_o = 975$ MPa we get $\chi = 1.62$. Both values are comparable with $\chi = 1.75$ (Kim et al. 2004).

The interface between the Nb$_{ss}$ and silicide is important in the fracture behaviour of Nb silicide based alloys (Nb in situ composites) (Chan 2005). As mentioned above, χ is a measure of the constraint of the Nb$_{ss}$ and thus its value depends on the Nb$_{ss}$/Nb$_5$Si$_3$ interface. A strong interface (meaning high constraint on the Nb$_{ss}$) promotes cleavage fracture (lowers the value of χ) (Mendiratta & Dimiduk 1993). The above calculations gave $\chi > 1$ for both alloys, in other words in KZ5 (jn) and JN5 the constraint operates positively into the ductile (Nb$_{ss}$) phase (meaning the work of fracture of the ductile phase in the composite is higher than that in the monolithic state with no constraint) (Kim et al. 2004).

Table 9.3 Calculated fracture toughness values for JN1, JN2, JN3, JN4 and KZ5

Note	Parameter	Alloy				
		JN1	JN2	JN3	JN4	KZ5
1	V_f	0.42	0.39	0.5	0.47	0.48
2	σ_0 (MPa)	975	1338.1	1183.2	1981.4	1118.4
3	$2\alpha_0$ (μm)	10	5	10	10	10
4	K_m (MPa√m)	8	7.4	7.4	8	8.5
5	E_m (GPa)	241.4	290	260.4	170.7	238.3
6	E_c (GPa)	197.8	241.9	206.7	247	186.6
7	ν_c	0.329	0.288	0.3075	0.3022	0.32
8	ν_m	0.281	0.219	0.219	0.219	0.25
9	K_c (MPa√m)	26	23.1	31.6	43	28.7
10	K_c (MPa√m)	28.7	25.1	34.7	47.6	

1. Calculated using image J, see Table 4.1
2. Calculated from $\sigma_0 = 2.4$ mHv (Subramanian et al. 1994)
3. Estimated from micrographs

4. Estimated from fracture toughness data in (Chan 2005) and Ti content in Nb_5Si_3

5. Data from nano-indentation experiments

6. Calculated using rule of mixtures

7. Calculated using rule of mixtures and data from (Tsakiropoulos & Papadimitriou 2015), $\nu_{Nb} \sim 0.396$

8. Data from (Tsakiropoulos & Papadimitriou 2015) for αNb_5Si_3 or $\beta Nb5Si_3$ with Ti in solution

9. Calculated from Equation 8 with $\chi = 1.6$

10. Calculated from Equation 9 with $\chi = 1.75$

9.4   Conclusions

The fracture toughness of two cast alloys with/out Hf addition, with nominal compositions Nb-24Ti-18Si-5Al-5Cr (KZ5 (jn)) and Nb-19Ti-18Si-4Al-4.5Cr-5Hf (JN5) was studied according to ASTM E399 and the British standards for three point bend fracture toughness. The K_Q values of both alloys were $\geq$ 19.5 MPa$\surd$m and in the range of values reported for the cast MASC alloy. In both alloys the Nb_{ss} provided effective crack blunting and the presence of lamellar Nb_{ss}/Nb_5Si_3 eutectic microstructure contributed to their toughness. Calculations of toughness for crack bridging by ductile Nb_{ss} grains (a) predicted exceptional toughness for the alloy JN4-HT and (b) suggested that the constraint operates positively into the Nb_{ss} phase.

Conclusions and suggestions for future work

The research described in this thesis was the study of:

i.   The microstructures of four alloys, namely JN1 (Nb-19.3Si-24.1Ti-4.1Cr-3.8Al-5.7Hf), JN2 (Nb-20.5Si-15.3Ti-10.0Cr-1.6Hf-5.6Mo-2.0W-1.9Sn), JN3 (Nb-22.1Si-15.8Ti-1.6Cr-1.7Hf-5.4Mo-1.2W-1.8Sn) and JN4 (Nb-21.9Si-20.9Ti-1.6Cr-2.0Hf-8.2Mo-3.9Sn in their cast and heat treated (1500 °C for 100 h) conditions.

ii.   The isothermal oxidation behaviour in air of the four alloys in the heat treated condition at 800 °C and 1200 °C using thermogravimetric analaysis.

iii.   The nano-indentation properties (nano-hardness and elastic moduli) of the two major phases, namely the Nb_{ss} and Nb_5Si_3, in the alloys.

iv.   The fracture toughness (K_Q) values of two cast alloys, with nominal compositions (at%) Nb-24Ti-18Si-5Al-5Cr (KZ5 (jn)) and Nb-19Ti-18Si-4Al-4.5Cr-5Hf (JN5).

The conclusions of this research were as follows.

10.1 Macrosegregation of Si and chemical inhomogeneity in microstructures

The addition of Hf in JN1 increased the macrosegregation of Si. This chemical inhomogeneity of Si persisted in JN1-HT, JN2-HT, JN3-HT and JN4-HT. In JN1-HT there was also chemical inhomogeneity of Al and Ti, which was attributed to the strong partitioning of Hf in the heat treated microstructure of JN1. It is thus suggested that:

• Alloying with ~ 5 at% Hf promotes chemical inhomogeneity in the microstructure of Nb silicide based alloys.

• Alloying with Cr affects the macrosegregation of Si. The latter increased with Cr concentration in the alloy JN2 compared with the alloy JN3.

• Alloying with Sn affects the macrosegregation of Si. The latter increased with the concentration of Sn in the alloy JN4.

- The chemical homogeneity of the microstructures alloyed with Mo, W and Sn depends on the Cr and Hf content of the alloy. Chemical inhomogeneity increases as Cr > 5 at% and Hf > 2 at%.

10.2 Solute partitioning

- Hafnium partitions to the Nb_{ss} and Nb_5Si_3 where it forms Hf rich areas in which its concentration depends on the Hf concentration in the alloy. In the alloy JN1, where the Hf concentration was the highest, the partitioning of Hf was enhanced in JN1-HT leading to homogenous Nb_{ss} and formation of Hf rich and Hf poor Nb_5Si_3.
- Molybdenum and W additions probably "control" the partitioning of Hf in the Nb_{ss} and Nb_5Si_3.
- Titanium partitions to the Nb_{ss} and Nb_5Si_3 and enhances the partitioning of Cr and Hf in the former and of Hf in the latter phase. The Ti rich areas in Nb_5Si_3 can persist after heat treatment. This is likely to depend on the concentration of Cr in the alloy.
- The partitioning of Ti in the Nb_{ss} and Nb_5Si_3 is enhanced by the synergy of the refractory metals Mo and W with Cr in the alloy. The role of W is probably strong in this synergy.
- Molybdenum and W partition to the Nb_{ss}
- Tin partitions to the Nb_{ss}
- The partitioning of Mo and W in the Nb_{ss} is opposite to that of Sn and Ti and Cr and Ti in the solid solution.
- The concentration of Cr in the alloy seems to be crucial for the partitioning of solutes when it is in synergy with Mo, Sn, Ti and W. High Cr concentrations promote strong partitioning of Sn and Ti in the Nb_{ss}.

10.3 Phase selection and stability

- The βNb_5Si_3 was the primary phase in the four alloys.

- The hexagonal γNb_5Si_3 was not formed during solidification in the four alloys.

- The synergy of Hf with Al, Cr and Ti stabilised the βNb_5Si_3 in JN1-HT.

- In JN1-HT, the Hf rich Nb_5Si_3 is likely to be the hexagonal γNb_5Si_3.

- The synergy of Hf with the refractory metals and Sn enhanced the transformation of βNb_5Si_3 to αNb_5Si_3.

- The formation of the C14 $NbCr_2$ Laves phase depended on the presence and concentration of Hf in the alloy and on the concentration of Cr in the alloy. The Laves phase was confirmed by XRD and WDS only in the cast and heat treated alloy JN2

- The Nb_3Sn was not formed in the alloy JN4-AC where its actual concentration was ~ 4 at%, but was stabilised in the heat treated microstructure.

- Nb_{ss} + Nb_5Si_3 eutectic was formed in all four alloys. The fine lamellar microstructure was not stable after the heat treatment.

- The addition of Hf stabilised the βNb_5Si_3 in JN1-HT and most likely suppressed the precipitation of Nb_{ss} in the Nb_5Si_3. However, the latter was observed in the alloys JN2-HT and JN3-Ht but the extent of Nb_{ss} precipitation was stronger in JN2-HT, which would suggest that the concentration of Cr in the alloy is important for this phase transformation.

10.4 Oxidation at 800 °C

The choice of alloying elements and their concentrations, and the types and compositions of phases present in the cast microstructure had strong influence on the oxidation behaviour of the studied alloys.

- The alloys JN1 and JN2 suffered from pest oxidation and exhibited linear oxidation kinetics.

- The alloy JN3 pested slightly and showed evidence of mixed oxidation kinetics, JN4 did not pest and followed parabolic oxidation kinetics.

- All four alloys exhibited the typical damage observed in many Nb silicide based alloys, which consists of an area below the scale/substrate interface where the

substrate is cracked, with the cracks running parallel to the interface and through the Nb_5Si_3 grains.

- In all four alloys there was a diffusion zone formed below the scale/substrate interface.

- The chemical compositions of the phases in the oxide scale, in the diffusion zone, below it and in the bulk were analysed. It was found that depending on alloy, the Nb_{ss} and Nb_5Si_3 were contaminated by oxygen and the severity of this effect varied between alloys. The Nb_{ss} was not contaminated by oxygen below the diffusion zone in JN4, and in the bulk in JN1 and JN4. The Nb_5Si_3 was not contaminated by oxygen below the diffusion zone in JN1, and in the bulk in JN1 and JN4.

10.5 Oxidation at 1200 °C

- The alloys JN1 and JN4 exhibited best oxidation with parabolic kinetics.
- The alloys JN2 and JN3 followed linear oxidation kinetics.
- There was spallation of the scale formed on the alloys JN1and JN2, and the scale of alloy JN3 formed in a "Maltese cross".
- The results confirmed that Sn tends to segregate below the scale/substrate interface during oxidation where it forms Sn intermetallics. In the alloys JN2, JN3 and JN4 a Sn-rich layer formed below the scale/substrate interface, this layer was more continuous and thicker in the alloy JN4 and contained Nb_3Sn. The latter intermetallic was also formed in JN3.
- In all alloys there was a diffusion zone formed below the scale/substrate interface.
- The chemical compositions of the phases in the oxide scale, in the diffusion zone, below it and in the bulk were analysed. Ti niobate and a mixed oxide rich in Nb and Si was confirmed by WDS analysis and XRD.
- Depending on the alloy, the Nbss and Nb_5Si_3 were contaminated by oxygen and the severity of this effect varied between alloys. The Nb_{ss} was not contaminated

by oxygen in the bulk in JN1 and JN4. The Nb_5Si_3 was not contaminated by oxygen in the bulk in JN1. The Nb_3Sn was not contaminated by oxygen in JN4.

- It would appear that alloying with W is detrimental to the oxidation of alloys of the Nb-Ti-Si-Al-Cr-Hf-Mo-W-Sn system.

10.6 Hardness and elastic moduli of Nb_{ss} and Nb_5Si_3

Nano-indentation was used to measure the hardness and elastic moduli of Nb_{ss} and Nb_5Si_3 in the alloys JN1, JN2, JN3 and JN4 in their heat treated condition (1500 °C for 100 h). It was found that:

- The synergy of Ti and Hf with Al and Cr in JN1 "softened" the solid solution.
- Hafnium has a weak hardening effect in $(Nb,Ti,Hf,Cr)_5(Si,Al)_3$.
- The synergy of Mo and W "softens" the 5-3 silicide.
- Alloying of Nb_{ss} and Nb_5Si_3 with Hf results in a reduction of elastic moduli.
- Molybdenum has a very strong effect on the elastic modulus of Nb_5Si_3 and this effect is compromised by synergy of Mo and W with Cr, Hf, Sn and Ti.
- Molybdenum has a strong effect on the elastic modulus of the Nbss as does the synergy of Mo with Sn and Ti.

10.7 Fracture toughness

- The K_Q values of the cast alloys Nb-24Ti-18Si-5Al-5Cr (KZ5 (jn)) and Nb-19Ti-18Si-4Al-4.5Cr-5Hf (JN5) were $\geq$ 19.5 MPa√m and in the range of values reported for the cast MASC alloy.
- The Nbss provided effective crack blunting.
- The presence of lamellar Nb_{ss}/Nb_5Si_3 eutectic microstructure contributed to their toughness.

- Calculations of toughness for crack bridging by ductile Nb_{ss} grains suggested exceptional toughness for the alloy JN4-HT and that the constraint operates positively into the Nb_{ss} phase.

10.8 Suggestions for future work

The research described in this thesis has shown that the cast alloy JN4 has promising oxidation properties at 800 °C and 1200 °C. It is thus suggested:

i.   First to evaluate the oxidation behaviour of the <u>heat treated</u> alloy JN4 at the same temperatures and, if the same or better oxidation behaviour is confirmed.

ii.   Second to expand the study to lower and higher temperatures in the pest regime, namely at 600 °C, 700 °C and 900 °C.

iii.   Third to study oxidation behaviour at 1100 °C and 1300 °C.

iv.   The research also pointed to an exceptional toughness for the heat treated microstructure of the alloy JN4.

v.   The fracture toughness of the alloy JN4 is evaluated in the cast and heat treated conditions and if the high toughness is confirmed then the high temperature mechanical properties of the alloy JN4 are evaluated.

Worldwide, the study of Nb silicide based alloys has been based on small quantities of cast alloys produced by arc melting or OFZ and there are very few processing-microstructure-property studies showing the effects of thermo-mechanical processing (e.g., forging, extrusion) on properties. Unfortunately, the latter were focused on "simple" binary, ternary or quaternary alloys. It is suggested that future research considers:

- The scaling up of alloy production
- The study of the effects of different methods of post solidification processing on microstructure and properties.

References

Abbaschian, R. & Lipschutz, M.D., 1997. Eutectic solidification processing via bulk melt undercooling. *Materials Science & Engineering A*, pp.13–21.

De Almeida, L.H. et al., 2005. No Title. *Materials Research*, 8, pp.239–243.

Ang, G.J., 1953. Activation energies and diffusion coefficients of oxygen and nitrogen in niobium and tantalum. *Acta Materialia*, pp.123–129.

Anon, 2010. BSI Standards Publication Metallic materials — Determination of plane-strain fracture toughness (ISO. , pp.1–28.

Argent, B. & Phelps, B., 1960. The oxidation of niobium-titanium and niobium-molybdenum alloys. *Less common metals*, 2, pp.181–190.

Ashby, M.F. & Jones, D.R.H., 2005. *Engineering Materials 1* 3rd ed.,

ASTM, 2013. Standard Test Method for Linear-Elastic Plane-Strain Fracture Toughness K Ic of. , pp.1–33.

Begley, R., 1994. COLUMBIUM ALLOY DEVELOPMENT AT WESTINGHOUSE. *EVOLUTION OF REFRACTORY METALS AND ALLOYS*, pp.29–48.

Behrani, V. et al., 2006. Microstructure and oxidation behavior of Nb–Mo–Si–B alloys. *Intermetallics*, 14(1), pp.24–32.

Bewlay, B.P. et al., 2003. A review of very-high-temperature Nb-silicide-based composites. *Metallurgical and Materials Transactions A*, 34(10), pp.2043–2052.

Bewlay, B.P. et al., 2004. Analyses of Eutectoid Phase Transformations in Nb–Silicide In Situ Composites. *Microscopy and Microanalysis*, 10(04), pp.470–480.

Bewlay, B.P., Zhao, J.C., et al., 1999. Determination of the effect of Hf additions on phase stability in Nb-silicide based in-situ composites. *Mat. Res. Soc. Symp, Proc*, 552.

Bewlay, B.P. et al., 2009. Experimental study of the liquid–solid phase equilibria at the metal-rich region of the Nb–Cr–Si system. *Intermetallics*, 17(3), pp.120–127.

Bewlay, B.P., Jackson, M.R. & Briant, C.L., 2001. *Deformation mechanisms in niobium silicide-based composites*,

Bewlay, B.P., Jackson, M.R. & Lipsitt, H.A., 1996. The Balance of Mechanical and Environmental Properties of a Multielement Niobium-Niobium Silicide-Based In Situ Composite. , 27(December), pp.3801–3801.

Bewlay, B.P., Jackson, M.R. & Subramanian, P.R., 1999. Processing high-temperature refractory-metal silicide in-situ composites. *JOM*, 51(4), pp.32–36.

Bewlay, B.P., Lewandowksi, J.J. & Jackson, M.R., 1997. Refractory metal-intermetallic in-situ composites for aircraft engines. *JOM*, 49(8), pp.44–45.

Birks, N. & Meier, G., 1982. *Introduction to High Temperature Oxidation of Metals*,

Bloyer, D.R., Ritchie, R.O. & Venkateswara Rao, K.T., 1998. Fracture toughness and R-Curve behavior of laminated brittle-matrix composites. *Metallurgical and Materials Transactions A*, 29(10), pp.2483–2496.

Cadek, J., 1988. *Creep in metallic materials* HRD., Elsevier publishing company.

Chan, K.S., 2002a. Alloying effects on fracture mechanisms in Nb-based intermetallic in-situ composites. *Materials Science and Engineering A*, 329-331, pp.513–522.

Chan, K.S., 2005. Alloying effects on the fracture toughness of Nb-based silicides and Laves phases. *Materials Science \& Engineering A*, 409(1-2), pp.257–269.

Chan, K.S., 2004. Cyclic oxidation response of multiphase niobium-based alloys. *Metallurgical and Materials Transactions A*, 35(2), pp.589–597.

Chan, K.S., 2002b. Modeling creep behavior of niobium silicide in-situ composites. *Materials Science and Engineering A*, 337(1-2), pp.59–66.

Chan, K.S., 2003. Relationships of Fracture Toughness and Dislocation Mobility in Intermetallics. *Metallurgical and Materials Transactions A*, 34(October), pp.2315–2328.

Chan, K.S. & Davidson, D.L., 2001. Delineating brittle-phase embrittlement and ductile-phase toughening in Nb-based in-situ composites. *Metallurgical and Materials Transactions A*, 32(11), pp.2717–2727.

Chan, K.S. & Davidson, D.L., 2003. Improving the Fracture Toughness of Constituent Phases and Nb-Based In-Situ Composites by a Computational Alloy Design Approach. *Metallurgical and Materials Transactions A*, 34.

Chattopadhyay, K., Mitra, R. & Ray, K.K., 2008. Nonisothermal and Isothermal Oxidation Behavior of Nb-Si-Mo Alloys. *Metallurgical and Materials Transactions A*, 39(3), pp.577–592.

Chen, Y. et al., 2009. Influence of vibrational entropy on structural stability of Nb − Si and Mo − Si systems at elevated temperatures. *Acta Materialia*, 57(9), pp.2657–2664.

Ciovati, G., 2006. Improved oxygen diffusion model to explain the effect of low-temperature baking on high field losses in niobium superconducting cavities. *Applied physics letters*, 89.

Dai, F. & Wei, B., 2009. Rapid solidification of Al-Cu-Ag ternary alloy under the free fall condition. *Science in China Series G: Physics, Mechanics and Astronomy*, 52(6), pp.848–855.

David, N. et al., 2006. Thermodynamic description of the Cr–Nb–Si isothermal section at 1473 K. *Intermetallics*, 14(4), pp.464–73.

Davidson, D.L. & Chan, K.S., 1999. The fatigue and fracture resistance of a Nb-Cr-Ti-Al alloy. *Metallurgical and Materials Transactions A*, 30(8), pp.2007–2018.

Dimiduk, D.M., 1995. Exploration of Nb-based advanced intermetallic materials. *Acta mettalurgica sinca*, 8(4-6), pp.519–530.

Fujikura, M. et al., 2004. Effect of Alloy Chemistry on the High Temperature Strengths and Room Temperature Fracture Toughness of Advanced Nb-Based Alloys. *Materials Transactions*, 45(2), pp.493–501.

Gale, W. & Totemeier, T., 2003. *Smithells metals reference book*, Oxford: Butterworth-Heinemann.

Geng, J., 2006. Development of Nbss/Nb5Si3 based in situ composites. *PHD thesis. The university of Surrey*.

Geng, J., Shao, G. & Tsakiropoulos, P., 2006. Study of three-phase equilibrium in the Nb-rich corner of Nb–Si–Cr system. *Intermetallics*, 14(7), pp.832–837.

Geng, J. & Tsakiropoulos, P., 2007. A study of the microstructures and oxidation of Nb–Si–Cr–Al–Mo in situ composites alloyed with Ti, Hf and Sn. *Intermetallics*, 15(3), pp.382–395.

Geng, J., Tsakiropoulos, P. & Shao, G., 2007. A study of the effects of Hf and Sn additions on the microstructure of Nbss/Nb5Si3 based in situ composites. *Intermetallics*, 15(1), pp.69–76.

Geng, J., Tsakiropoulos, P. & Shao, G., 2007. A thermo-gravimetric and microstructural study of the oxidation of Nbss/Nb5Si3-based in situ composites with Sn addition. *Intermetallics*, 15(3), pp.270–281.

Geng, J., Tsakiropoulos, P. & Shao, G., 2006a. Oxidation of Nb–Si–Cr–Al in situ composites with Mo, Ti and Hf additions. *Materials Science and Engineering: A*, 441(1-2), pp.26–38.

Geng, J., Tsakiropoulos, P. & Shao, G., 2006b. The effects of Ti and Mo additions on the microstructure of Nb-silicide based in situ composites. *Intermetallics*, 14(3), pp.227–235.

Geng, T. et al., 2010. Thermodynamic assessment of the Nb–Si–Mo system. *Calphad*, 34(3), pp.363–376.

Gibala, R. & Mitchell, T.E., 1973. Solid Solution Softening and Hardnening. *Scripta metallurgica*, (7), pp.1143–1148.

Gokhale, A.B. & Abbaschian, G.J., 1990. Mo-Si (Molybdenum-Silicon). *Binary Alloy Phase Diagrams, II Ed., Ed. T.B. Massalski*.

Goldschmidt, H., 1959. A High-Temperature X-ray Investigation Of Niobium Pentoxide And Some Problems Concerning The Oxidation Of Niobium. *Journal of the institute of metals*, 87, pp.235–239.

Goldschmidt, H. & Brand, J., 1961. The constitution of the chromium–niobium–silicon system. *Journal of the Less-Common Metals*, 3, pp.34–43.

Grabke, H.J. & Meier, G.H., 1995. Accelerated oxidation, internal oxidation, intergranular oxidation, and pesting of intermetallic compounds. *Oxidation of Metals*, 44(1-2), pp.147–176.

Grammenos, I. & Tsakiropoulos, P., 2010a. Study of the role of Al, Cr and Ti additions in the microstructure of Nb–18Si–5Hf base alloys. *Intermetallics*, 18(2), pp.242–253.

Grammenos, I. & Tsakiropoulos, P., 2011. Study of the role of Hf, Mo and W additions in the microstructure of Nb–20Si silicide based alloys. *Intermetallics*, 19(10), pp.1612–1621.

Grammenos, I. & Tsakiropoulos, P., 2010b. Study of the role of Mo and Ta additions in the microstructure of Nb–18Si–5Hf silicide based alloy. *Intermetallics*, 18(8), pp.1524–1530.

Grill, R. & Gnadenberger, a, 2006. Niobium as mint metal: Production–properties–processing. *International Journal of Refractory Metals and Hard Materials*, 24(4), pp.275–282.

Guthoff, F. et al., 1994. Lattice Dynamics and Self-Diffusion in Niobium at Elevated Temperatures. *J. Phys. COndensed matter*, 6, pp.6211–6220.

Han, X.J. & Wei, B., 2002. Microstructural Characteristics of Ni-Sb Eutectic Alloys under Substantial Undercooling and Containerless Solidification Conditions. , 33, pp.1221–1228.

Hennessey, T.P. & Morral, J.E., 1992. Oxidation and nitridation of niobium in air above 1150C. *Oxidation of Metals*, 38(1-2), pp.163–187.

Holtzberg, F. et al., 1975. Chemistry of the Group VB Pentoxides. VI:The Polymorphism of Nb2O5. *Journal of the American Chemical Society*, 79(9), pp.2039–2043.

Jéhanno, P. et al., 2005. Assessment of a powder metallurgical processing route for refractory metal silicide alloys. *Metallurgical and Materials Transactions A*, 36(3), pp.515–523.

Katsman, a., Grabke, H.J. & Levin, L., 1996. Penetration of oxygen along grain boundaries during oxidation of alloys and intermetallics. *Oxidation of Metals*, 46(3-4), pp.313–331.

Kelly, K.K., Prokoshkin, D.A. & Vasileva, E. V, 1949. Alloys of Niobium. *Bureau of mines*, 476, pp.22–29.

Kim, J. et al., 2004. Mechanical properties and fracture behavior of an NbSS/Nb5Si3 in-situ composite modified by Mo and Hf alloying. , 372, pp.137–144.

Kim, J., Tabaru, T. & Hirai, H., 2003. Evaluation Technique of the Hardness and Elastic Modulus of Materials with Fine Microstructures * 1. *Materials Transactions*, 44(4), pp.673–676.

Kim, W. et al., 2001. Microstructure and room temperature deformation of Nb ss / Nb 5 Si 3 in situ composites alloyed with Mo. , 9, pp.521–527.

Kim, W. & Tanaka, H., 2002. High temperature strength at 1773 K and room temperature fracture toughness of Nb ss / Nb 5 Si 3 in situ composites alloyed with Mo. , 7, pp.2885 – 2891.

Kim, W.-Y. et al., 2002. Effect of Cr Addition on Microstructure and Mechanical Properties in Nb-Si-Mo Base Multiphase Alloys. *Materials Transactions*, 43(12), pp.3254–3261.

Kimura, Y. et al., 2005. Processing, microstructure, and mechanical properties of (Nb)/Nb5Si3 two-phase alloys. *Metallurgical and Materials Transactions A*, 36(3), pp.483–488.

Kofstad, P. & Espevik, S., 1965. Low-Pressure oxidation of Niobium at 1200 Degrees - 1700 Degrees C. *Journal of the Electrochemical Society*, 112(2P1), p.153.

Kozlov, A., 2010. Molybdenum – Niobium – Silicon. , 1, pp.350–365.

Kubaschewski, O. & Hopkins, B.E., 1960. Oxidation mechanisms of niobium, tantalum, molybdenum and tungsten. *Journal of the institute of metals*, 2, pp.172–180.

Lewandowski, J.J. & Rigney, J.D., 1996a. Loading rate and test temperature effects on fracture of in situ niobium silicide-niobium composites. *Metallurgical and Materials Transactions A*, 27A, pp.3292–3306.

Lewandowski, J.J. & Rigney, J.D., 1996b. Loading rate and test temperature effects on fracture of in situ niobium silicide-niobium composites. *Metallurgical and Materials Transactions A*, 27A, pp.3292–3306.

Li, M. & Kuribayashi, K., 2003. Nucleation-Controlled Microstructures and Anomalous Eutectic Formation in Undercooled Co-Sn and Ni-Si Eutectic Melts. , 34(December), pp.2999–3008.

Li, M., Yoda, S. & Kuribayashi, K., 2006. Comments on the work by Wei and co-workers on free eutectic and dendritic solidification from undercooled metallic melts. *Scripta Materialia*, 54(7), pp.1427–1432.

Li, X. & Chou, Y., 1996. HIGH-ANGLE GRAIN-BOUNDARY DIFFUSION OF CHROMIUM IN NIOBIUM BICRYSTALS. *Acta Materialia*, 44(9), pp.3535–3541.

Li, Y. et al., 2013. Experimental study on phase relationships in the Si-rich portion of the Nb–Si–W ternary system. *Calphad*, 41, pp.60–70.

Li, Z. & Peng, L.M., 2007. Microstructural and mechanical characterization of Nb-based in situ composites from Nb–Si–Ti ternary system. *Acta Materialia*, 55, pp.6573–6585.

Liang, H., 1999. Thermodynamic modeling of the Nb–Si–Ti ternary system. *Intermetallics*, 7(5), pp.561–570.

Liu, Y. et al., 2012. Diffusion characteristics and atomic mobilities for bcc refractory Mo–Ta, Mo–W, and Mo–Nb alloys. *Calphad*, 36, pp.110–117.

Liu, Y. et al., 2009. Kinetic modeling of diffusion mobilities in bcc Ti–Nb alloys. *Journal of Alloys and Compounds*, 476, pp.429–435.

Liu, Y. et al., 2013. Mobilities and diffusivities for bcc Nb–W, Nb–Ta, Zr–Mo and Zr–Hf alloys. *Journal of Alloys and Compounds*, 555, pp.381–389.

Liu, Y. et al., 2005. Oxidation behavior of multiphase Nb-Mo-Si-B intermetallics. *Metallurgical and Materials Transactions A*, 36(3), pp.601–607.

Liu, Y., Shazly, M. & Lewandowksi, J.J., 2010. Microstructural effects on crack path selection in bending and fatigue in a Nb–19Si–5Cr–3.5Hf–24Ti–0.75Sn–1W alloy ☆. *Materials Science and Engineering: A*, 527(6), pp.1489–1500.

Lyutyi, E.M. et al., 1996. Mechanism and regularities of oxidation in Nb-Ti and Nb-Ti-Si systems. *Materials Science*, 31(1), pp.105–111.

Ma, C. et al., 2004. Microstructure and mechanical properties of Nb/NbSi in situ composites in Nb-Mo-Si and Nb-W-Si systems. *Materials Science and Engineering A*, 386(1-2), pp.375–383.

Ma, C.L. et al., 2000. Phase equilibria in Nb-Mo-rich zone of the Nb-Si-Mo ternary system.pdf. , pp.1329–1336.

Mataga, P.A., 1989. Deformation of crack-bridging ductile reinforcements in toughened brittle materials. *Acta Metallurgica*, 37(12), pp.3349–3359.

Mathieu, S. et al., 2012. On the oxidation mechanism of niobium-base in situ composites. *Corrosion Science*, 60, pp.181–192.

Mendiratta, M.G. & Dimiduk, D.M., 1993. Strength and toughness of a Nb/Nb5Si3 composite. *Metallurgical transactions*, 24A, pp.501–504.

Menon, E.S.K., OXIDATION BEHAVIOR OF COMPLEX NIOBIUM BASED ALLOYS. , (1), pp.1–25.

Mitra, R., 2006. Mechanical behaviour and oxidation resistance of structural silicides. *International Materials Reviews*, 51(1), pp.13–64.

Murayama, Y. & Hanada, S., 2002. High temperature strength, fracture toughness and oxidation resistance of Nb–Si–Al–Ti multiphase alloys. *Science and Technology of Advanced Materials*, 3(2), pp.145–156.

Naidu Negender, S.V., Sriramamurthy, A.M. & Rama Rao, P.J., 1990. SI-W. *Binary Alloy Phase Diagrams, II Ed., Ed. T.B. Massalski*, 3.

Ogurtani, T., 1972. Kinetics of diffusion in Nb-Al System. *Metallurgical transactions*, 3(2), pp.425–429.

Okamoto, H., 2000. Mo-Si phase diagram. *Phase diagrams for binary alloys, Desk handbook, ASM international*, p.580.

Okamoto, H., 2003. Nb-Sn (Niobium Tin). *J. Phase Equilib*, 24, p.380.

Okamoto, H., 1990. Nb-Sn (Niobium-Tin). *Binary Alloy Phase Diagrams, II Ed., Ed. T.B. Massalski*, 3, pp.2769–2771.

Olesinski, R.W. & Abbaschian, G.J., 1990. Si-Sn (Silicon-Tin). *Binary Alloy Phase Diagrams, II Ed., Ed. T.B. Massalski*, 3, pp.3361–3362.

Oliver, W.C. & Pharr, G.M., 1992. An improved technique for determining hardness and elastic modulus using load and displacement sensing indentation experiments. *J. Mater. Res*, 6(1), pp.1564–1583.

Pontau, A.E. & Lazarus, D., 1979. Diffusion of Titanium and Niobium in BCC Ti-Nb allloys. *Physical Review B*, 19, pp.4027–4037.

Powers, R.W. & Doyle, M. V, 1959. Diffusion of Interstitial Solutes in the Group v Transition Metals. *Applied physics*, 30, pp.514–520.

Resnick, R. & Castleman, L.S., 1961. The Self Diffusion of Columbium. *AIME*, p.4.

Rietveld, H.M., 1969. A profile refinement method for nuclear and magnetic structures. *Journal of Applied Crystallography*, 2(2), pp.65–71.

Rietveld, H.M., 1967. Line profiles of neutron powder-diffraction peaks for structure refinement. *Acta Crystallographica*, 22(1), pp.151–152.

Russ, J., 2007. Niobium-Silicon-Tungsten ternary alloy phase diagram (based on 1964 Dokukina N.V.). *ASM Alloy Phase Diagrams Center*, 9, pp.1031–1034.

Savitskii, E.M., 1965. Phase diagram and properties of Nb-Mo-Si alloys. *Russ. Metall*.

Sekido, N. et al., 2006. Fracture toughness and high temperature strength of unidirectionally solidified Nb–Si binary and Nb–Ti–Si ternary alloys. *Journal of Alloys and Compounds*, 425(1-2), pp.223–229.

Sethi, V.K. & Gibala, R., 1977. Surface oxide softening of niobium single crystals. *Acta Metallurgica*, 25, pp.321–332.

Sha, J., Hirai, H., et al., 2003. Mechanical properties of as-cast and directionally solidified Nb-Mo-W-Ti-Si in-situ composites at high temperatures. *Metallurgical and Materials Transactions A*, 34(1), pp.85–94.

Sha, J., Hirai, H., et al., 2003. Toughness and strength characteristics of Nb-W-Si ternary alloys prepared by Arc melting. *Metallurgical and Materials Transactions A*, 34(12), pp.2861–2871.

Shao, G., 2004. Thermodynamic modelling of the Cr–Nb–Si system. *Intermetallics*, 13(1), pp.69–78.

Sheasby, J.S. & Smeltzer, W.W., 1981. Oxygen tracer studies of the oxidation of niobium. *Oxidation of Metals*, 15(3-4), pp.215–229.

Shyrokov, V. V. & Rats'ka, N.B., 2009. Regularities of the oxidation of niobium with increased titanium content. *Materials Science*, 44(4), pp.581–588.

Sims, C., Klopp, W. & Jaffee, R., 1959. No Title. *Trans American Society of Metals*, 51, pp.256–262.

Soboyejo, W.O. et al., 1999. An investigation of the fatigue and fracture behavior of a Nb-12Al-44Ti-1.5Mo intermetallic alloy. *Metallurgical and Materials Transactions A*, 30(4), pp.1025–1038.

Subramanian, P.R., 1997. Advanced intermetallic alloys-beyond gamma titanium aluminides. *Materials Science and Engineering A*, 239-240, pp.1–13.

Subramanian, P.R., Mendiratta, M.G. & Dimiduk, D.M., 1994. High Temperature Suicides and Refractory Alloys. *Mat. Res. Soc. Symp, Proc*, 332, pp.491–502.

Taylor, A., Doyle, N.J. & Ioth, M., 1967. PART III: THE TERNARY SYSTEMS Nb-Mo-0 AND Nb-W-O*. , 33(657), pp.338–351.

Tian, Y.X. et al., 2009. Effect of growth rate on microstructure and mechanical properties in a directionally solidified Nb-silicide base alloy. *Materials and Design*, 30(6), pp.2274–2277.

Tian, Y.X. et al., 2008. Microstructure and room temperature fracture toughness of cast Nbss/silicides composites alloyed with Hf. *Materials Letters*, 62(17-18), pp.2657–2660.

Toffolon, C. et al., 2002. Reassessment of the Nb-Sn system. *Journal of Phase Equilibria*, 23(2), pp.134–139.

Tsakiropoulos, P. & Anazodo, B., 2015. MPhil thesis. *The University of Sheffield*.

Tsakiropoulos, P. & Grammenos, I., 2008. PhD thesis. *The University of Surrey*.

Tsakiropoulos, P. & Papadimitriou, I., 2015. PhD thesis. *University of Sheffield*.

Tsakiropoulos, P. & Singh sethi, J., 2012. MSC Dissertation. *The University of Sheffield*.

Tsakiropoulos, P. & Vellios, N., 2009. PhD thesis. *The University of Surrey*.

Vazquez, A. & Varma, S.K., 2011. High-temperature oxidation behavior of Nb–Si–Cr alloys with Hf additions. *Journal of Alloys and Compounds*, 509(25), pp.7027–7033.

Vellios, N. & Tsakiropoulos, P., 2010. Study of the role of Fe and Sn additions in the microstructure of Nb–24Ti–18Si–5Cr silicide based alloys. *Intermetallics*, 18(9), pp.1729–1736.

Vellios, N. & Tsakiropoulos, P., 2007a. The role of Fe and Ti additions in the microstructure of Nb–18Si–5Sn silicide-based alloys. *Intermetallics*, 15(12), pp.1529–1537.

Vellios, N. & Tsakiropoulos, P., 2007b. The role of Sn and Ti additions in the microstructure of Nb-18Si base alloys. *Intermetallics*, 15, pp.1518–1528.

Vellios, N. & Tsakiropoulos, P., 2005. Unpublished Work.

Ventura, J. & Varma, S.K., 2009. The Oxidation Resistance of Nb-20mo-15Si-5B-20Cr Up to 1,300°C. , pp.1–4.

Wang, X.L., Wang, G. & Zhang, K.F., 2010. Microstructure and room temperature mechanical properties of hot-pressed Nb − Si − Ti − Fe alloys. *Journal of Alloys and Compounds*, 502(2), pp.310–318.

Waterstrat, R.M. & Muller, J., 1977. TERNARY SYSTEMS A-15 PHASE REGIONS IN THE Nb-Sn-Si AND Nb-Sn-As. *Journal of the Less-Common Metals*, pp.271–277.

Wilkinson, W.D., 1969. *Properties of Refractory Metals*,

Xiong, B. et al., 2009. Effects of Si , W and W − Mo on isothermal oxidation behaviors of Nb / Nb 5 Si 3 in situ composites at high temperature. *Journal of Alloys and Compounds*, 486, pp.330–334.

Yang, Y. et al., 2009. Thermodynamic modeling of the Cr–Hf–Si System. *Intermetallics*, 17(5), pp.305–312.

Yang, Y., Bewlay, B.P. & Chang, Y. a., 2007. Liquid-solid phase quilibria in metal-rich Nb-Ti-Hf-Si alloys. *Journal of Phase Equilibria and Diffusion*, 28(1), pp.107–114.

Yang, Y., Bewlay, B.P. & Chang, Y.A., 2007. Thermodynamic modeling of the HfeTieSi ternary system. *Intermetallics*, 15, pp.168–176.

Yao, D. et al., 2009. Experimanetal studies and modelling of the oxidation of multiphase niobium-base alloys. *Corrosion Science*, 51, pp.2619–2627.

Yao, D. et al., 2009. Experimental study and modeling of high temperature oxidation of Nb-base in situ composites. *Corrosion Science*, 51(2), pp.364–370.

Yao, W., Cao, C. & Wei, B., 2006. Reply to comments on free eutectic and dendritic solidification from undercooled metallic melts. *Scripta Materialia*, 54(7), pp.1433–1437.

Yu, J.L. et al., 2010. Mechanical properties of multiphase Nb – Si – Fe in situ composites. *Materials Science & Engineering A*, 527(20), pp.5230–5233.

Yu-ren, W. et al., 2006. Undercooling and rapid solidification of Nb-Si eutectic alloys studied by long drop tube. , pp.2–5.

Zacharis, E., 2013. PhD Thesis. *University of Sheffield*.

Zelenitsas, K. & Tsakiropoulos, P., 2006a. Effect of Al, Cr and Ta additions on the oxidation behaviour of Nb–Ti–Si in situ composites at 800°C. *Materials Science and Engineering: A*, 416(1-2), pp.269–280.

Zelenitsas, K. & Tsakiropoulos, P., 2005. Study of the role of Al and Cr additions in the microstructure of Nb–Ti–Si in situ composites. *Intermetallics*, 13, pp.1079–1095.

Zelenitsas, K. & Tsakiropoulos, P., 2006b. Study of the role of Ta and Cr additions in the microstructure of Nb–Ti–Si–Al in situ composites. *Intermetallics*, 14, pp.639–659.

Zhao, J., Jackson, M. & Peluso, L., 2003. Determination of the Nb–Cr–Si phase diagram using diffusion multiples. *Acta Materialia*, 51(20), pp.6395–405.

Zhao, J., Jackson, M. & Peluso, L., 2004. Mapping of the Nb–Ti–Si phase diagram using diffusion multiples. *Materials Science and Engineering A*, 372(1-2), pp.21–27.

Zhao, J.C. et al., 2000. Hf-Si binary phase diagram determination and thermodynamic modeling. *Journal of Phase Equilibria and Diffusion*, 21(1), pp.40–45.

Zifu, L. & Tsakiropoulos, P., 2010. Study of the effects of Ge addition on the microstructure of Nb–18Si in situ composites. *Intermetallics*, 18(5), pp.1072–1078.

Appendix

During the study of the JN series of alloys it was noted that the concentration of some elements in the Nb_{ss} and Nb_5Si_3, namely Ti, Hf, Cr and Sn showed a trend with the amount of oxygen present in the respective phase. Based on this, data from other studies was compiled with that collected in this study and several plots were created to determine if any trend was present. Both the parabolic and linear lines of best fit were plotted to determine the type of relationship between oxygen and each respective element, be it a linear or power law relationship.

Data from the alloys studied in this research and the alloys JG3 and JG4 after oxidation at 800 °C have been used to estimate the concentrations of specific alloying additions required for "zero" oxygen content of the Nb_{ss} and the Nb_5Si_3.

Regarding the effect of alloying with Ti, the data shows for the first time that the solubility of oxygen in the Nb_{ss} in Nb silicide based alloys of the Nb-Ti-Si-Al-Cr-Hf-Mo-W-Sn system decreases with increasing Ti concentration. The best fit of the data gives the linear and quadratic equations Equation 10 and Equation 11, see also Figure 12.1.

Equation 10
$$\%O_2 = -0.7795(Ti\%) + 21.937, \qquad R^2 = 0.934$$

And

Equation 11
$$\%O_2 = 0.0283(Ti\%)^2 - 1.9309(Ti\%) + 32.192, \qquad R^2 = 0.9545$$

From which it is calculated that ~ 28 at% Ti is required in the Nb_{ss} for zero oxygen content for oxidation at 800 °C.

Regarding the effect of Hf, the data shows for the first time that the solubility of oxygen in the Nb_{ss} in Nb silicide based alloys of the Nb-Ti-Si-Al-Cr-Hf-Mo-W-Sn system decreases as the concentration of Hf in the solid solution increases. The best fit of the data is for the JN series alloys and JG4 after oxidation at 800 °C and gives the

linear and quadratic equations, see Equation 12 and Equation 13, see also Figure 12.2 for the plot.

Equation 12
$$\%O_2 = -5.3701(Hf\%) + 17.361, \qquad R^2 = 0.8111$$

And

Equation 13
$$\%O_2 = 2.2616(Hf\%)^2 - 15.314(Hf\%) + 26.267, \qquad R^2 = 0.8981$$

From Equation 12 and Equation 13 it is estimated that the Hf content in the Nb_{ss} must be ~ 3 at% to reduce to zero the solubility of oxygen in the Nb_{ss}.

The data for Sn also shows that an increase in the concentration of Sn in the Nb_{ss} in Nb silicide based alloys of the Nb-Ti-Si-Al-Cr-Hf-Mo-W-Sn system reduces the oxygen content of the solid solution. The best fit of the data is from the JN series alloys and gives the linear and quadratic Equation 14 and Equation 15, see also Figure 12.3.

Equation 14
$$\%O_2 = -2.5343(Sn\%) + 16.228, \qquad R^2 = 0.8845$$

And

Equation 15
$$\%O_2 = 0.7294(Sn\%)^2 - 8.0477(Sn\%) + 24.749, \qquad R^2 = 0.9378$$

From which it is estimated that ~ 6.3 at% Sn is required in solution in the Nb_{ss} to get zero oxygen solubility in it.

The data for Cr shows that the oxygen solubility in the Nb_{ss} in Nb silicide based alloys of the Nb-Ti-Si-Al-Cr-Hf-Mo-W-Sn system increases with the Cr content of the solid solution. The best fit of the data is for the JN series alloys and gives the linear and quadratic Equation 16 and Equation 17, see also Figure 12.4.

Equation 16

$$\%O_2 = 0.3844(Cr\%) - 0.7012, \qquad R^2 = 0.9012$$

And

Equation 17

$$\%O_2 = 0.0154(Cr\%)^2 + 0.1046(Cr\%) + 0.1367, \qquad R^2 = 0.9154$$

From which it is estimated that for zero oxygen content in the Nb_{ss} the Cr concentration in the latter should be ~ 2 at%.

The data for Mo and W was not enough to give a good fit, and thus estimates for the Mo and W concentrations in the Nb_{ss} that are required for zero oxygen content cannot be estimated.

The "critical" values for the concentrations of Cr, Hf, Sn and Ti that are required for zero solubility of oxygen in the Nb_{ss} are closely matched by the data for the Nb_{ss} in the alloy JN4, see Table 6.4, which, as we have seen, was the alloy that did not pest and exhibited best oxidation behaviour compared with the other alloys of this research. Regarding the effect of alloying Nb_5Si_3 with Ti, the data shows that the solubility of oxygen in the Nb_5Si_3 in Nb silicide based alloys of the Nb-Ti-Si-Al-Cr-Hf-Mo-W-Sn system decreases with increasing Ti concentration. The best fit of the data for the JN series alloys gives the linear and quadratic Equation 18 and Equation 19, see also Figure 12.5.

Equation 18

$$\%O_2 = -1.956(Ti\%) + 35.668, \qquad R^2 = 0.9064$$

And

Equation 19

$$\%O_2 = -0.0909(Ti\%)^2 + 0.6117(Ti\%) + 18.163, \qquad R^2 = 0.9152$$

From which it is calculated that ~ 18 at% Ti is required in the Nb_5Si_3 for zero oxygen content for oxidation at 800 °C. The fit of the data for the other elements was poor and

did not allow their concentrations for zero oxygen solubility in the Nb_5Si_3 to be estimated.

In the alloy JN1 the Nb_{ss} was slightly contaminated by oxygen below the diffusion zone and in the bulk. The Ti and Hf contents in the Nb_{ss} in the two areas of the oxidised specimen at 800 °C were in agreement with the values estimated above for zero oxygen content but not the concentration of Cr, which was significantly higher. Whether the contamination by oxygen of the Nb_{ss} in JN1 can be attributed solely to Cr is not clear, as there is no data for the effect of Al on the solubility of oxygen in the Nb_{ss}. The Al+Cr content of the Nb_{ss} would require Ti/Nb > 0.5 for ductile behaviour, which was satisfied by the concentrations of these elements in the Nb_{ss} below the diffusion zone and in the bulk. Furthermore, in JN1 the Ti concentration in the Nb_5Si_3, which was not contaminated with oxygen, was in agreement with the above estimated value, for which the toughness of the Nb_5Si_3 would be expected to be higher than that of the unalloyed silicide. Yet, the oxidation of the alloy JN1 was linear, there was cracking in the diffusion zone parallel to the surface of the specimen (as in all the alloys of this research) and there was evidence of pesting after 100 h oxidation at 800 °C in air. The evidence would thus seem to suggest that apart from the chemistry of the phases, which "determines" their deformation behaviour and the diffusivity of oxygen towards the bulk, other synergies (for example, between the elements and the phases) are important and that these are key to balancing out the detrimental effect of porosity. The alloying additions Mo and Sn are important in such synergies.
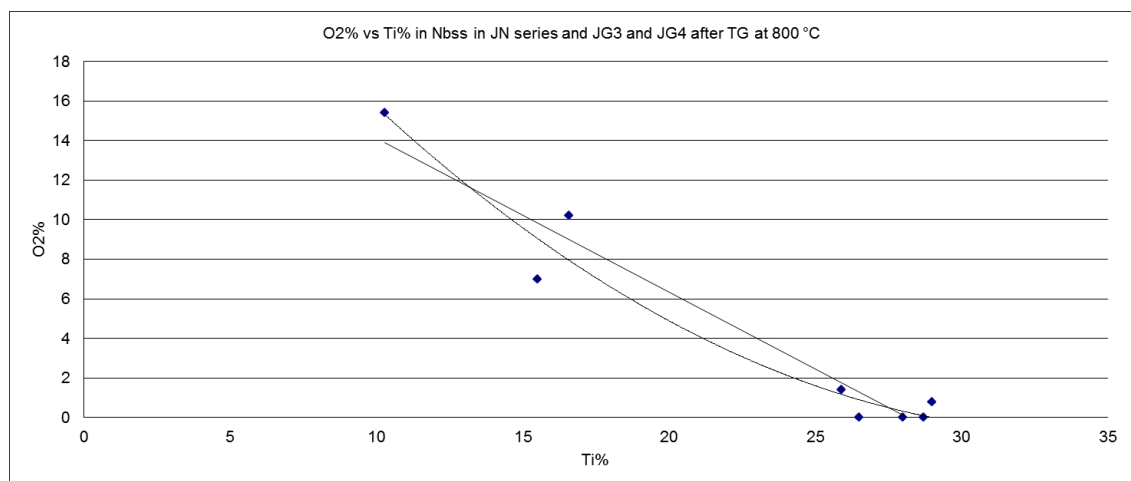
Figure 12.1 Oxygen versus Ti content in the Nb_{ss} of Nb silicide base alloys after oxidation at 800 °C in air for 100 h
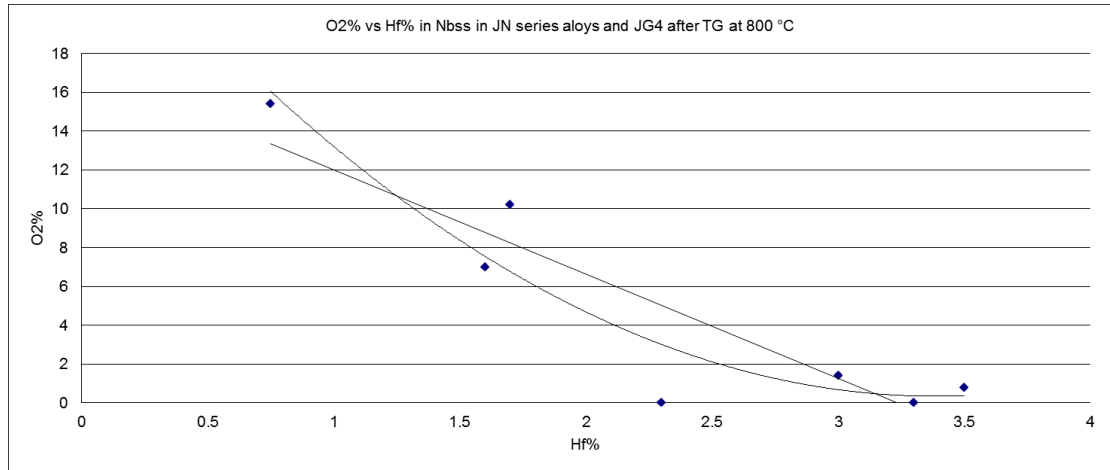
Figure 12.2 Oxygen versus Hf content in the Nb$_{ss}$ of Nb silicide base alloys after oxidation at 800 °C in air for 100 h
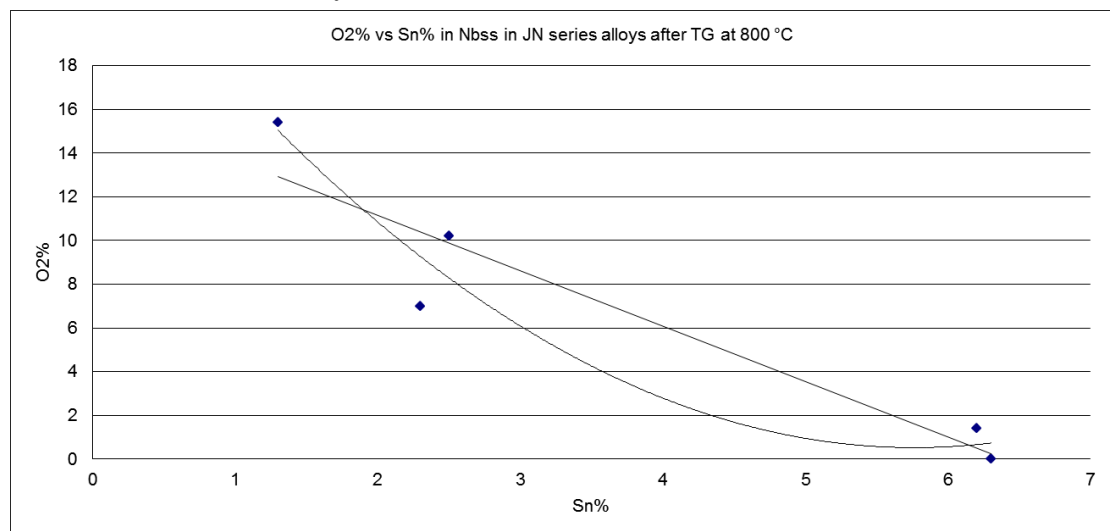
Figure 12.3 Oxygen versus Sn content in the Nb$_{ss}$ of Nb silicide base alloys after oxidation at 800 °C in air for 100 h
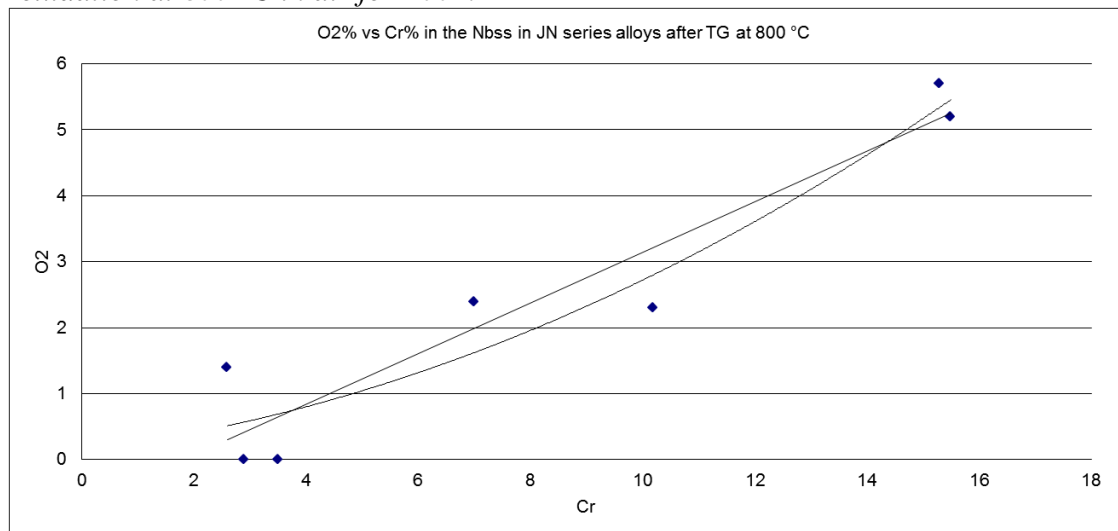
Figure 12.4 Oxygen versus Cr content in the Nb$_{ss}$ of Nb silicide base alloys after oxidation at 800 °C in air for 100 h
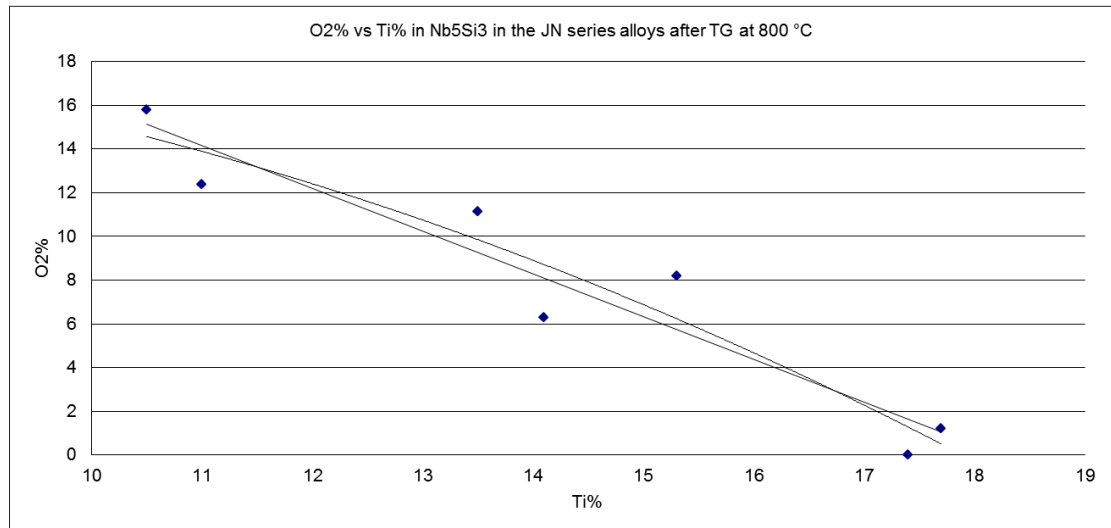
Figure 12.5 Oxygen versus Ti content in the Nb$_5$Si$_3$ of Nb silicide base alloys after oxidation at 800 C in air for 100 h

Data from the alloys studied in this research and the JG series alloys after oxidation at 1200 °C has been used to estimate the concentrations of specific alloying additions required for "zero" oxygen content of the Nb$_{ss}$ and the Nb$_5$Si$_3$.

Regarding the effect of alloying with Ti, the data shows <u>for the first time</u> that the solubility of oxygen in the Nb$_{ss}$ in Nb silicide based alloys of the Nb-Ti-Si-Al-Cr-Hf-Mo-W-Sn system at 1200 °C decreases with increasing Ti concentration. This trend is in agreement with previous research regarding the effect of Ti on the solubility of oxygen in solid solution binary Nb-Ti alloys. The best fit of the data includes the JN series alloys and JG4 and gives the quadratic Equation 20, see also Figure 12.6.

Equation 20
$$O2\% = 0.0674(Ti\%)2 - 3.3995(Ti\%) + 42.651, \qquad R2 = 0.9223$$

Which has a minimum oxygen content at ~ 25 at% Ti, which is the Ti concentration in the Nb$_{ss}$ for zero for oxidation at 1200 °C.

Regarding the effect of alloying Nb$_5$Si$_3$ with Ti, the data shows <u>for the first time</u> that the solubility of oxygen in the Nb$_5$Si$_3$ in Nb silicide based alloys of the Nb-Ti-Si-Al-Cr-Hf-Mo-W-Sn system at 1200 °C decreases with increasing Ti concentration. The best fit of the data for the JN series alloys gives the quadratic Equation 21, see also Figure 12.7.

Equation 21
$\%O2 = 0.1003(Ti\%)2 - 4.8181(Ti\%) + 56.844,$ $\quad\quad R2 = 0.8433$

Which shows that zero oxygen concentration in the Nb_5Si_3 can be achieved with ~ 21 at% and 28 at% Ti

Regarding the effect of Mo on the solubility of oxygen in Nb_5Si_3 at 1200 C best fit of the data only for JN4 shows O_2 decreasing with increasing Mo content and gives a linear and quadratic equation, Equation 22 and Equation 24 respectively, see Figure 12.8.

Equation 23
$\%O2 = -19.737(Mo\%) + 50.389,$ $\quad\quad R2 = 0.8084$

And

Equation 24
$\%O2 = -35(Mo\%)2 + 138.5(Mo\%) - 128,$ $\quad\quad R2 = 0.8287$

Data for the effect of Sn on the solubility of oxygen in Nb_5Si_3 in Nb silicide based alloys of the Nb-Ti-Si-Al-Cr-Hf-Mo-W-Sn system at 1200 °C shows <u>for the first time</u> that the oxygen content increases with increasing Sn content, see Equation 25, Equation 26 and Figure 12.9.

Equation 25
$\%O2 = 5.2918(Sn\%) - 2.7819,$ $\quad\quad R2 = 0.7238$

And

Equation 26
$\%O2 = -2.7684(Sn\%)2 + 13.196(Sn\%) - 7.2358,$ $\quad\quad R2 = 0.7901$

Zero oxygen content in Nb_5Si_3 requires ~ 0.5 at% Sn. It should be noted that the data for the effect of Sn on the solubility of oxygen in Nb_5Si_3 shows opposite trends at 1200 °C and 800 °C.

Data for the effect of Cr on the solubility of oxygen in Nb_5Si_3 in Nb silicide based alloys of the Nb-Ti-Si-Al-Cr-Hf-Mo-W-Sn system at 1200 °C shows for the <u>first ever time</u> that the oxygen content decreases with increasing Cr content, see Equation 27, Equation 28 and Figure 12.10

Equation 27
$$\%O_2 = -4.3589(Cr\%) + 6.841, \qquad R2 = 0.5446$$

And

Equation 28
$$\%O_2 = 7.2819(Cr\%)2 - 20.66(Cr\%) + 12.288, \qquad R2 = 0.7972$$

From which zero oxygen concentration requires about 0.9 and 1.7 at% Cr.
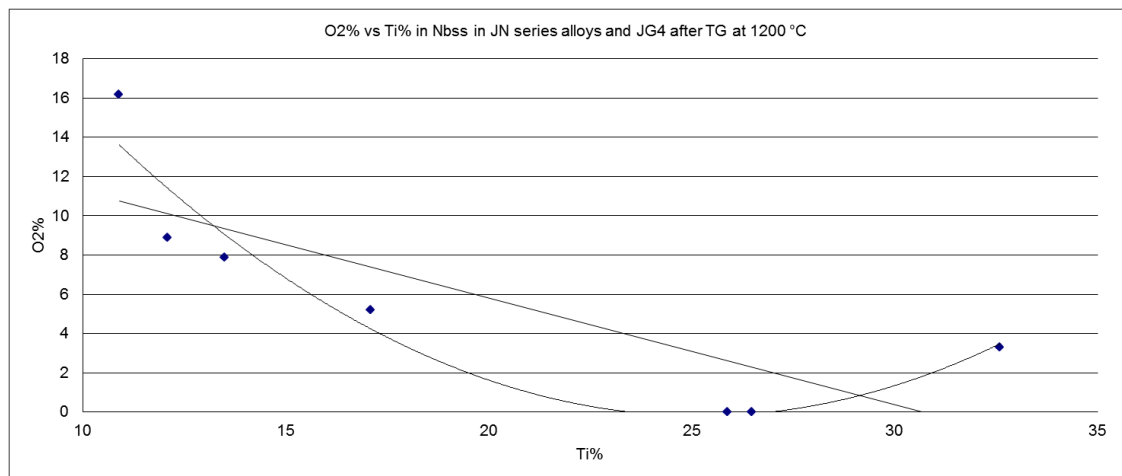
Figure 12.6 Oxygen versus Ti content in the Nb_{ss} of Nb silicide base alloys after oxidation at 1200 °C in air for 100 h
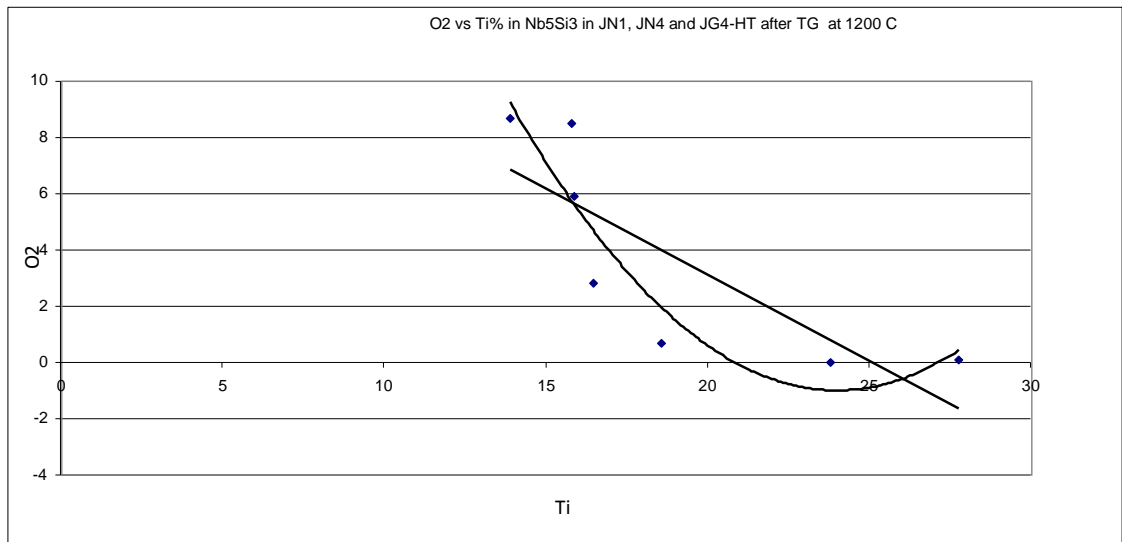
Figure 12.7 Oxygen versus Ti content in the Nb₅Si₃ of Nb silicide base alloys after oxidation at 1200 °C in air for 100 h
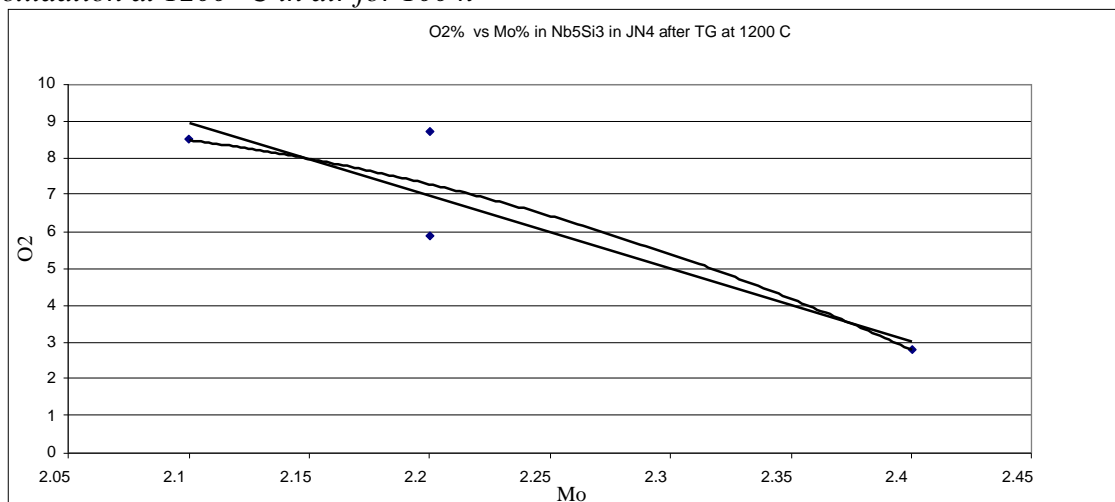
Figure 12.8 Oxygen versus Mo content in the Nb₅Si₃ of Nb silicide base alloys after oxidation at 1200 °C in air for 100 h
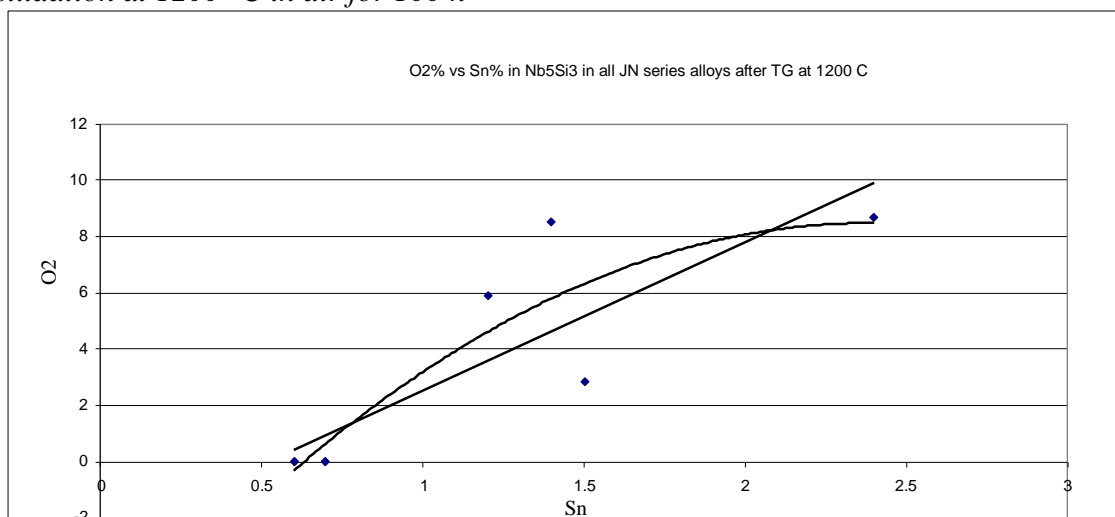
Figure 12.9 Oxygen versus Sn content in the Nb₅Si₃ of Nb silicide base alloys after oxidation at 1200 °C in air for 100 h

O2% vs Cr% in Nb5Si3 for JN1, JN4, average of JN2, JN3 and JG4-HT after TG at 1200 C
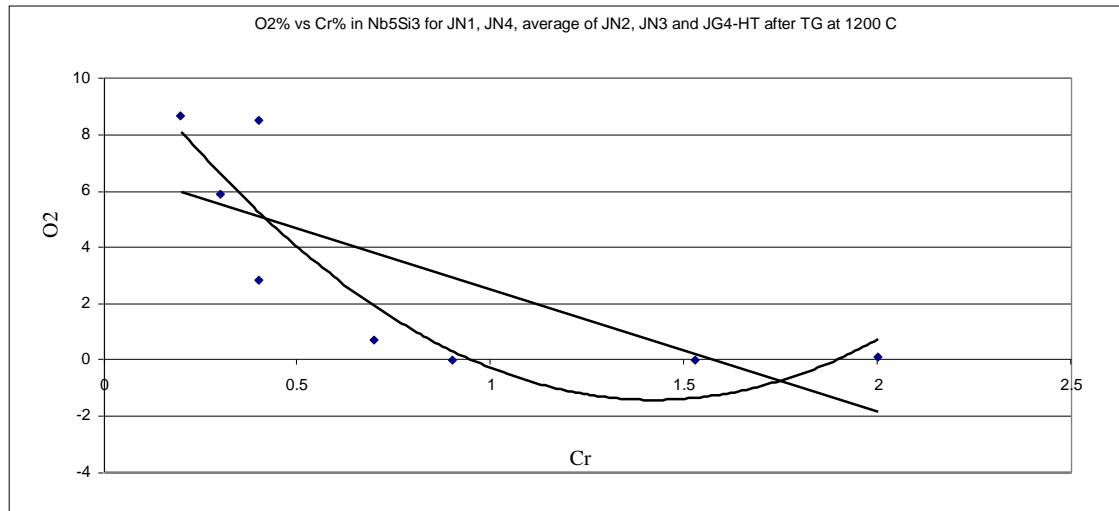
Figure 12.10 Oxygen versus Cr content in the Nb$_5$Si$_3$ of Nb silicide base alloys after oxidation at 1200 °C in air for 100 h

The plots and equations outlined above show a possibility for a trend between compositional control and oxygen content in the constituent phases. Whilst literature and study within the research group has allowed educated selection with regards to alloying elements, a better understanding of any trend that may exist will allow the prediction of properties and smarter alloying choices.